

Cranfield University

MELANIE PERERA

OPTIMAL DESIGN OF A COMPOSITE ACTIVE
AEROELASTIC WING

SCHOOL OF ENGINEERING
Department of Aerospace Engineering

PhD Thesis
Academic Year 2010 -2011

Supervisor: Dr. Shijun Guo
February 2011

Cranfield University

SCHOOL OF ENGINEERING
Department of Aerospace Engineering

PhD Thesis

Academic Year 2010-2011

MELANIE PERERA

Optimal Design of a Composite Active Aeroelastic Wing

Supervisor:

Dr. Shijun Guo

February 2011

This thesis is submitted in partial fulfilment of the requirements for
the degree of Doctor of Philosophy

© Cranfield University, 2011. All rights reserved. No part of this publication may be
reproduced without the written permission of the copyright holder.

Abstract

The primary aim of this research was to design a Seamless Aeroelastic Wing (SAW) structure applicable to a lightweight Unmanned Aerial Vehicle (UAV). Therefore the study focused on optimal design of a SAW structure by utilising the maximum aeroelastic beneficial effect. Although similar to the Active Aeroelastic Wing (AAW) and relevant to the Flapless Air Vehicle Integrated Industrial Research (FLAVIIR), the major difference from them is that a SAW will function as an integrated one piece lifting and control surface. It is designed to produce a desirable wing camber for control by deflecting a hinge-less flexible trailing edge (TE) part instead of a traditional control surface.

Attention was firstly paid on the design of a hinge-less flexible trailing edge control surface and the actuation mechanism applicable for a light-weight aircraft (UAV). The proposed mechanism in the SAW TE section has two innovative design features: an open sliding TE and a curved beam and disc actuation mechanism. This type of actuated TE section allows for the SAW having a smooth camber change in a desirable shape with minimum control power demand. This design concept has been simulated numerically and its feasibility has been demonstrated by a test model.

The wing structure for a small scale UAV is likely to be over designed in terms of strength, stiffness and weight due to manufacturing constraints. For the optimal wing design, the investigation was conducted in two stages. In the first stage, effort was made to design and model an optimised composite wing box for a minimum weight and maximum flutter speed. Both analytical and numerical methods were used for structural stress, vibration and aeroelastic analyses. In the second stage, the study focused on integrating the TE actuation mechanism with the optimised wing box for detailed understanding of the structure. A finite element analysis was conducted to simulate the SAW TE to ensure that structural strength requirements were satisfied. Furthermore, a study was carried out on the structural dynamic behaviour of the SAW TE section under the aerodynamic pressure to demonstrate its dynamic stability. Hence, the outcome of this research shows that a feasible SAW design for a UAV can be achieved.

Acknowledgments

This dissertation would not have been possible without the guidance and the help of several individuals who in one way or another contributed and extended their valuable assistance in the preparation and completion of this study. First and foremost I would like to thank Dr. Shijun Guo whose encouragement, supervision and support from the preliminary to the concluding level enabled me to develop an understanding of the subject.

I would also like to extend my gratitude towards UK EPSRC, BAE Systems and MBDA-Missile Systems for their financial support and the technical advice received from the industrial advisors Prof. C. Warsop, Prof. A. Hussain, A. Machell and M. Evans.

Dr. X. Zhang, for her unselfish and unfailing support. I am grateful to Prof. Ranjan Banerjee for his continuous encouragement from the very beginning. I also thank Dr. Chak-wa Cheung for all his help and support in pursuing a PhD after my undergraduate studies.

It is also a pleasure to acknowledge Barry Walker, Jim Hurley and Y. He for their help conducting the experimental tests and building the experimental model. It would have never been possible to complete the research without their contribution

My kindest regards also goes out to Ryoko Morishima, Natalia Di Matteo and Yang Da Qing who have spent countless late days at university helping me in my research.

I thank my father and mother for their continuous support throughout all my studies at University. My sister who discretely helped me get through tough times. Last but not least my husband Mishane Peiris, for giving me the strength and courage when I needed it the most.

Contents

Abstract	v
Acknowledgments	vi
Contents.....	viii
List of Figures.....	xii
List of Tables.....	xviii
List of Abbreviations, Nomenclature and symbols	xix
1 Introduction.....	1
1.1 Background	1
1.2 Research Aims and Objectives	5
1.3 Structure of Thesis	7
2 Literature Review.....	11
2.1 Aeroelastic Phenomena	11
2.2 AAW Concepts.....	13
2.2.1 Active Aeroelastic Wing (AAW)	15
2.2.2 Active Aeroelastic Aircraft Structures (3AS)	16
2.2.3 Belt-Rib Concept	21
2.2.4 Smart Structures	22
2.2.5 DARPA Smart Wing	28
2.2.6 Other AAW Concepts	29
2.3 Concluding Remarks on AAW Concepts	34
2.4 Aeroelastic Tailoring	36
3.2.5 Passive -Aeroelastic Tailoring.....	37
3.2.5 Active - Aeroelastic Control	38
2.5 AAW Benefits and Challenges.....	39
2.5.1 Benefits	40
2.5.2 Challenges	44
3 Theoretical Background	45
3.1 Hooke’s Law for Anisotropic Materials	46
3.1.1 Normal Stress and Strain.....	46
3.1.2 Stress and Strain for Specially Orthotropic Plates.....	47

3.1.3	Stress and Strain for Generally Orthotropic Plates.....	48
3.2	In-Plane modulus for the Laminate	52
3.3	Stress Analysis of Stiffened Thin-Walled Beams Using the TWbox Program	53
3.4	Finite Element Approach used in MSC NASTRAN/PATRAN	56
3.5	Anisotropic Thin-Walled Closed Section Beam Stiffness	57
3.6	Free Vibration analysis	59
3.6.1	Dynamic Stiffness Method.....	59
3.6.2	Evaluation of Natural Modes and Frequencies	59
3.6.3	Finite Element Approach used in MSC NASTRAN/PATRAN.....	64
3.7	Aeroelastic Analysis	66
3.7.1	Evaluation of Generalised Aerodynamic Matrix.....	66
3.7.2	Formation and Solution of the Flutter Determinant	68
3.7.3	Application to the SAW.....	68
3.7.4	Finite Element Approach used in MSC NASTRAN/PATRAN.....	69
3.7.5	Dynamic Analysis.....	74
3.8	Control effectiveness	79
3.8.1	Aerodynamic and Structural Integration.....	80
3.9	Gradient Based Design Optimisation.....	91
3.10	Methodology	93
4	SAW Actuation Mechanism	97
4.1	Aerodynamic Tools.....	97
4.1.1	ESDUpac A9931	97
4.1.2	JavaFoil	98
4.1.3	Unsteady Panel Method - USPM.....	98
4.1.4	Tool Selection.....	98
4.2	2-D Aerodynamics.....	99
4.2.1	Camber Effect.....	99
4.3	Two Dimensional Aerodynamic Analysis	102
4.3.1	Validation of Aerodynamic Tools	102
4.3.2	Effect of Trailing-edge Deflection.....	103
4.3.3	Pressure Distribution.....	109
4.3.4	Leading and Trailing Edge combinations	109

4.4	Actuation Mechanism	114
4.4.1	SAW Actuation Mechanism Design.....	115
4.4.2	SAW Open TE Design.....	120
4.4.3	Open TE Design Solutions	123
4.4.4	SAW Experimental Design	125
4.5	SAW Actuation Force Requirement	129
4.5.1	Actuation Force/Power Requirement.....	129
4.5.2	Available Actuators	132
5	Seamless Aeroelastic Wing box Design.....	134
5.1	DEMON	135
5.2	Wing Loading condition	136
5.3	SAW Structure Design.....	138
5.3.1	Wing Box FE Model.....	140
5.3.2	Analytical Results	141
5.3.3	Finite Element Results	142
5.4	Aeroelastic Tailoring	146
5.4.1	Wing Box Stiffness.....	146
5.5	Wing Box Aeroelastic Analysis	150
5.5.1	Wing Box Flutter Analysis.....	150
5.5.2	Control Effectiveness.....	155
5.6	Discussion of Results	157
6	SAW Structural and Dynamic Analysis	158
6.1	SAW FE Model	159
6.1.1	Finite Element model development of SAW	160
6.1.2	SAW Actuation Mechanism Creation	163
6.1.3	FE Model Cases.....	165
6.2	SAW Structural Analysis	166
6.2.1	Static Aerodynamic Loading Results	166
6.2.2	Actuation Results.....	173
6.3	SAW Vibration Analysis.....	175
6.4	SAW Flutter Analysis	182
6.4.1	Aerodynamic Modelling	183

6.4.2	Flutter Results.....	183
6.5	Dynamic Response Analysis	196
6.5.1	Dynamic Response Results	198
7	Concluding Remarks	202
7.1	Future Work	205
8	Reference	207
	Appendix A Aerodynamic Analysis	218
	Appendix B SAW Disc setting angle.....	226
	Equation of the beam curve	226
	Disc related equation.....	227
	Wing related equation	234
	Appendix C Eccentuator Concept Initial Calculations	239
	Force Requirements	239
	Appendix D Actuation Force/Power Calculation	241
	Appendix E.....	244
	Appendix F.....	246
	WINGLOADS Program.....	246
	TW-Box Program [122]	247
	BOXMEX Program.....	249
	OPTBOXFSC Program.....	250
	AERO-BEAM-SAW Program.....	252
	Appendix G	258
	Appendix H Mechanics of Laminated Composites	260
	Definition of Strains and Displacements	260
	Definition of Stress and Moments	262

List of Figures

Figure 2.1 Collar's Aeroelastic Triangle [9]	11
Figure 2.2 Change in Aerofoil section Pressure Distribution due to control Surface Deflection [10].....	14
Figure 2.3 Variable Camber Wing [11]	14
Figure 2.4 Morphing Aerofoil Patents [12-15].....	15
Figure 2.5 (a) AAW Technology; (b) Conventional Control Surface [17].....	16
Figure 2.6 Concepts studied under the 3AS project; (a) Active Wing Tip Concept ; (b) Roll Control Efficiency using Ailerons [22].	17
Figure 2.7 (a) EuRAM ; (b) Wing Tip Control Surfaces in EuRAM [22].....	17
Figure 2.8 All Movable Vertical Tail (AMVT) with Variable Stiffness Attachment [29]	18
Figure 2.9 Shell-joint and Tip-joint Configurations [31].....	19
Figure 2.10 (a) Smart Fin; (b) Angle of Attack generated by Piezoelectric Actuation [32].....	19
Figure 2.11 Rotating Rib Mechanism [24].....	20
Figure 2.12 Moving and Rotating Spars Concepts [34].....	21
Figure 2.13 Belt-Rib Configuration [38]	21
Figure 2.14 Options for Actuation Methods [39]	21
Figure 2.15 Phase change in SMA due to activation [40].....	22
Figure 2.16 The piezoelectric effect [41].....	23
Figure 2.17 Adaptive Wing Structure Concept [42].....	25
Figure 2.18 shape memory alloy actuators for a small UAV [48]	27
Figure 2.19 (a) Smart Wing and Torque Tube Arrangement; (b) SMA Flap [50]	28
Figure 2.20 Skin-flexcore Control Surface Structure [53].....	28
Figure 2.21 Stiffness Reduction using Aramid Flexcore [53].....	29
Figure 2.22 (a) Variable rear camber model; (b) Kinematics of the actuator [42].....	30
Figure 2.23 (a) Placement of the SMA in the leading-edge and aerofoil deflection; (b) Prototype of the wind tunnel model [55]	31
Figure 2.24 Original and Span extended [56]	31
Figure 2.25 (a) Pitch Control; (b) Roll Control [57].....	32

Figure 2.26 Flexible trailing-edge structure with the kinematic actuation mechanism [58]	33
Figure 2.27 (a) Structure of flap Track concept; (b) Deformation of Webs [58]	33
Figure 2.28 Deformed and un-deformed FE model of the smart LE device [59]	34
Figure 2.29 Modal Coupling	36
Figure 2.30 Aeroelastic Tailoring [61]	37
Figure 2.31 Pressure distribution over an aerofoil with two control surfaces and two-flap-to-chord ratios: 10 and 50% [77].....	41
Figure 2.32 (a) CL and (b) Cm comparisons of conventional and conformal surfaces [77].....	42
Figure 2.33 Conformal control surface shapes [77]	43
Figure 2.34 Control Effectiveness of (a) Rigid; and (b) Flexible Wing Models [64]	43
Figure 3.1 Difference between an isotropic and orthotropic plate.	46
Figure 3.2 Generally Orthotropic Lamina.	49
Figure 3.3 Idealisation of wing section [84].....	53
Figure 3.4 Idealisation of a panel [84]	54
Figure 3.5 Linear static analysis	56
Figure 3.6 Cross-sectional details of the wing box.....	57
Figure 3.7 A spanwise wing box segment modelled as a beam element.	58
Figure 3.8 Cantilever Beam with Arbitrary Spanwise Properties	59
Figure 3.9 An aerodynamic Doublet-Lattice Panel subdivided into boxes	71
Figure 3.10 Structural Damping Versus Viscous Damping	78
Figure 3.11 Control Reversal [61]	79
Figure 3.12 Control Effectiveness and Reversal Speed [84].....	79
Figure 3.13 Example of AERO-BEAM-SAW aircraft model.....	81
Figure 3.14 Notation diagram.....	82
Figure 3.15 Notation in Aircraft Axes in Eqn. (3.108).....	86
Figure 3.16(a) Source sheet (Source sheet is an infinite number of line sources)	87
Figure 3.17 Flow over the body of given shape [100].....	88
Figure 3.18 Notation [100].....	88
Figure 3.19 Wing Box Design Methodology	93

Figure 3.20 SAW Analysis Methodology	94
Figure 3.21 Aero-Structural coupling Methodology	96
Figure 4.1 (a) Aerofoil Geometric Parameters; (b) Definition of NACA 4-digit series Aerofoil [105].	99
Figure 4.2 Effect of Aerofoil thickness on the Pressure Distribution at $C_L = 0.48$ [106]	99
Figure 4.3 Camber effects on Aerofoil Pressure Distribution at (a) $C_L = 0.48$ and (b) $C_L = 1.43$ [106].	100
Figure 4.4 Pressure Distribution of an Aft Cambered Aerofoil, NACA 6712 [106]. ..	100
Figure 4.5 Comparison of Camber and Thickness Effect on C_{Lmax} [107]	101
Figure 4.6 Comparison of C_L by using the three different tools and test data	102
Figure 4.7 (a) Beam bending under pressure; (b) Flexible & (c) R-B TE bending angles	103
Figure 4.8 Flexible and Rigid TE Deflections of a Symmetric Aerofoil	104
Figure 4.9 C_L Comparison of Flexible and Rigid Trailing-edge at (a) $\delta_t = 5^\circ$; (b) $\delta_t = 10^\circ$; (c) $\delta_t = 15^\circ$	106
Figure 4.10 C_L Increase between R-B and Flexible TE deflections at $AOA = 0^\circ$	107
Figure 4.11 C_m Comparison of Flexible and Rigid Trailing-edge at $\delta_t = 15^\circ$	107
Figure 4.12 C_m Comparison of Flexible and Rigid Trailing-edge at $\delta_t = 15^\circ$	108
Figure 4.13 Comparison of Flexible and Rigid Trailing-edge at (a) $\delta_t = 5^\circ$; (b) $\delta_t = 10^\circ$; (c) $\delta_t = 15^\circ$	109
Figure 4.14 Leading and Trailing edge deflection effect on C_L	113
Figure 4.15 Leading and Trailing edge deflection effect on C_m	113
Figure 4.16 Eccentuator Mechanism [112]	114
Figure 4. 17 DARPA Eccentuator Concept [112]	114
Figure 4.18 Curved Beam Concept.....	115
Figure 4.19 Illustration of the relative motion of the discs and the TE skins	116
Figure 4.20 Track on Wing Surface.....	117
Figure 4.21 Twisted disc concept	117
Figure 4.22 Disc at a setting angle.....	118

Figure 4.23 Eccentric Tube Disc design	118
Figure 4.24 SAW Actuation mechanism	119
Figure 4.25 Model Dimensions (mm).....	120
Figure 4.26 Closed TE FE model and boundary conditions	121
Figure 4.27 Open TE FE model.....	121
Figure 4.28 TE displacement of Close TE Model (in mm).....	122
Figure 4.29 TE displacement of open TE Model (in mm)	122
Figure 4.30 Sliding TE design.....	123
Figure 4.31 Open TE design solutions.....	124
Figure 4.32 (a) SAW skin model, Spars, motor and curved tube; (b) Deformed SAW model.....	125
Figure 4.33 (a) Assembled SAW test model; (b) The TTAM mounted inside the SAW model.....	126
Figure 4.34 Servomotor Test Model Setup	127
Figure 4.35 (a) Torque tube test model setup; (b) Clamped torque tube model; (c) FE CTTAM model	128
Figure 4.36 Force Distribution	129
Figure 4.37 Bending Moment Comparison for Flexible and Rigid TE sections.....	131
Figure 5.1 DEMON V-n Diagram [125].....	136
Figure 5.2 SAW Planform.....	136
Figure 5.3 Bending moment and shear force diagrams at 4.2g load factor	137
Figure 5.4 (a) Wing box configuration (initial wing box; improved wing box); (b) Cross-sectional details of the wing box.	138
Figure 5.5 (a) Wing Box-2 FE model; (b) Applied Boundary conditions	140
Figure 5.6 Maximum Normal and Shear Stress results for Wing Box 1 and 2 (MPa) .	142
Figure 5.7 SAW (WB-2 Case 1) Deformation under maximum loading at 4.2g (in m)	142
Figure 5.8 Spanwise Stress (σ_1) Distribution on Wing Box at Limit Load due to Gust at 4.2g.....	143
Figure 5.9 Spanwise Stress (σ_2) Distribution on Wing Box at Limit Load due to Gust at 4.2g.....	143

Figure 5.10 Spanwise Stress (σ_{12}) Distribution on Wing Box at Limit Load due to Gust at 4.2g	143
Figure 5.11 Failure Index Results of the Baseline Wing Box-2 Design.....	145
Figure 5.12 Comparison of structural rigidities of the SAW box (WB-1) for the initial (I) and optimised (O) design. Note: EI-I = initial rigidity, EI-O = optimised rigidity.	148
Figure 5.13 Comparison of structural rigidities of the SAW box (WB-2) for the initial (I) and optimised (O) design. Note: EI-I = initial rigidity, EI-O = optimised rigidity.	149
Figure 5.14 Flutter Analysis using CALFUN	151
Figure 5.15 Flutter results for initial and optimised cases (1-2).....	153
Figure 5.16 Control effectiveness comparison of the initial (I) and Optimised (O) cases for WB -1.....	155
Figure 5.17 Control effectiveness comparison of the initial (I) and Optimised (O) cases for WB -2.....	156
Figure 5.18 Control Reversal Speed Summary	157
Figure 6.1 (a) SAW planform; (b) Geometrical model created in PATRAN	159
Figure 6.2 Wing Root Cross Section of the SAW FE model (dimensions in mm)	159
Figure 6.3 Wing Tip Cross Section of the SAW FE model (dimensions in mm)	160
Figure 6.4 Fibre Orientation system used in MSC NASTRAN/PATRAN.....	162
Figure 6.5 SAW Baseline Design with a closed TE	163
Figure 6.6 Open TE modelled in Model-2	164
Figure 6.7 RBE2 modelling.....	164
Figure 6.8 Curved beam model along with the discs modelled in FE	165
Figure 6.9 Maximum transverse deflections at the wing tip under the maximum load factor of 4.2g	167
Figure 6.10 Model 1- Carbon/Epoxy skin under 4.2g Aerodynamic load.....	168
Figure 6.11 Model 1- EGlass/Epoxy skin under 4.2g Aerodynamic load	169
Figure 6.12 Model 3- Carbon/Epoxy skin under 4.2g Aerodynamic load.....	170
Figure 6.13 Model 3- EGlass/Epoxy skin under 4.2g Aerodynamic load	171
Figure 6.14 E-Glass/Epoxy skin under 4.2g Aerodynamic load for (a) Baseline Model-1; (b) SAW Model-2	173
Figure 6.15 Deflected SAW due to TE Actuation	174

Figure 6.16 SAW Model-2 under TE actuation load for (a) Carbon/Epoxy; (b) E-Glass/Epoxy skin	174
Figure 6.17 Normal modes of SAW baseline Model-1 with Carbon/epoxy skin.....	176
Figure 6.18 Normal modes of SAW Model-3 with Carbon/epoxy skin	177
Figure 6.19 Normal modes of SAW Model-2 with Carbon/epoxy skin	178
Figure 6.20 Normal modes of SAW Model-2 with E-Glass/epoxy skin	179
Figure 6.21 Normal modes of SAW Model-2 with E-Glass/epoxy skin (without Rubber insert at the TE)	180
Figure 6.22 Velocity vs Damping (g) of Model 1-Carbon/Epoxy skin	185
Figure 6.23 Velocity vs Frequency (ω) of Model 1-Carbon/Epoxy skin.....	185
Figure 6.24 Velocity vs Damping (g) of Model 1-Optimised E-Glass/Epoxy skin	186
Figure 6.25 Velocity vs Frequency (ω) of Model 1-Optimised E-Glass/Epoxy skin...	186
Figure 6.26 Velocity vs Damping (g) of Model 2- Carbon/Epoxy skin	188
Figure 6.27 Velocity vs Frequency (ω) of Model 2-Carbon/Epoxy skin.....	188
Figure 6.28 Velocity vs Damping (g) of Model 2- Optimised E-Glass/Epoxy skin	189
Figure 6.29 Velocity vs Frequency (ω) of Model 2- Optimised E-Glass /Epoxy skin.	189
Figure 6.30 Velocity vs Damping (g) of Model 2- Optimised E-Glass/Epoxy skin (without TE Rubber)	191
Figure 6.31 Velocity vs Frequency (ω) of Model 2- Optimised E-Glass /Epoxy skin (without TE Rubber)	191
Figure 6.32 Velocity vs Damping (g) of Model 3- Carbon/Epoxy skin	194
Figure 6.33 Velocity vs Frequency (ω) of Model 3-Carbon/Epoxy skin.....	194
Figure 6.34 Velocity vs Damping (g) of Model 3- Optimised E-Glass/Epoxy skin	195
Figure 6.35 Velocity vs Frequency (ω) of Model 3- Optimised E-Glass /Epoxy skin.	195
Figure 6.36 Spring element to represent actuator stiffness	197
Figure 6.37 (a) Dynamic Response Loading location; (b) Input loading at 5 -20 Hz ..	197
Figure 6.38 Transient Response of (a) Model 2 – 5Hz; (b) Model 2 –10Hz	198
Figure 6.39 Transient Response of (a) Model 2 – 15Hz; (b) Model 2 –20Hz	199
Figure 6.40 Transient Response of (a) Model 2 – 25Hz; (b) Model 2 – 30Hz	200

List of Tables

Table 4.1 Ratios and deflections in option-1 and type-2 for equivalent TE angles.....	105
Table 4.2 Summary of LE and TE combinations considered.....	110
Table 4.3 Material Properties	120
Table 4.4 Displacement achieved under applied load.....	122
Table 4.5. Material properties of the torque tube and discs	126
Table 4.6 Comparison of force data for flexible and rigid configurations.....	130
Table 4.7 Bending moment data of flexible configuration	130
Table 4.8 Bending moment data of rigid configuration.....	131
Table 4.9 Total Power Requirement	132
Table 4.10 Smart and conventional actuator comparison [53].....	132
Table 4.11 Ultrasonic motor comparison [53]	133
Table 5.1 Geometric details of the wing structure.....	139
Table 5.2 Mechanical properties of Carbon-Epoxy and E-Glass-Epoxy.....	140
Table 5.3 Maximum direct and shear stresses for WB-2 Cases 1-2.....	144
Table 5.4 Optimised laminate layups, rigidity and flutter speed.....	154
Table 6.1 Aluminium and Rubber Material Properties [122]	163
Table 6.2 Stress Summary.....	172
Table 6.3 Fundamental Bending and Torsion Frequencies for the Carbon/Epoxy skin Case.....	181
Table 6.4 Fundamental Bending and Torsion Frequencies for the E-Glass/Epoxy skin Case.....	182
Table 6.5 Summary of Flutter Speeds.....	196

List of Abbreviations, Nomenclature and symbols

A_{ij}	components of the in-plane stiffness matrix (A)
A_e	cross sectional area of the closed-section beam
$A(s), B(s), C(s)$	reduced axial, coupling and shear stiffness of the closed-section beam
b	wing semi-chord
C_{ij}	stiffness coefficients of the closed-section beam
C_L	wing lift coefficient
$[D]$	generalised damping matrix of the structure
E_i	ply Young's modulus in the i – direction
EI, GJ, CK	bending, torsion and bending-torsion coupling rigidities
f_v	objective function
G_{ij}	ply shear modulus in the i - j plane
h	transverse displacement of the wing box beam
I_P	polar mass moment of inertia per unit length of the wing box beam
$[K_D(\omega)]$	frequency dependent generalised dynamic stiffness matrix
L, M_x, M_y	lift force, bending moment and torque applied to the wing box beam
m	mass per unit length of the wing box beam
$\{q\}$	generalised coordinates of the structure
$[QA]_R, [QA]_I$	real and imaginary parts of the generalised unsteady aerodynamic matrix
S	in-plane shear strength
V_d, V_f, V_R	divergence, flutter and reversal speed
X_α	distance between the mass and elastic axes of the wing box cross-section
X_b, X_c, Y_b, Y_c	ply tensile and compressive strength in longitudinal and transverse directions

α	wing angle of attack
δ_{LE}, δ_{TE}	leading and trailing edge control surface deflections
$\varepsilon_x, \varepsilon_y, \gamma_{xy}$	direct strain in the x and y -axis; shear strain in the x - y plane
θ	laminar fibre orientation
ν_{12}	ply Poisson's ratio in the 1-2 plane
ρ	density
$\sigma_x, \sigma_y, \tau_{xy}$	direct stress in the x and y -axis; shear stress in the x - y plane
ϕ	twist of the wing box beam
ω	frequency of the wing
ω_f	flutter frequency
AAW	Active Aeroelastic Wing
CTTAM	Curved Torque Tube Actuation Mechanism
FEM	Finite Element method
FE	Finite Element
FI	Failure Index
FLAVIIR	Flapless Air Vehicle Integrated Industrial Research
GBDM	Gradient Based Deterministic Method
LE	Leading Edge
SAW	Seamless Aeroelastic Wing
TE	Trailing Edge
TTAM	Torque Tube Actuation Mechanism
UAV	Unmanned Aerial Vehicle

1 Introduction

1.1 Background

The optimal use of structural materials in aircraft design has always been an objective of the designers. Achieving a minimum weight structure is one of the main aims. Reference [1] writes,

"Primary function of the aircraft structure is to transfer forces through space... The objective is to do this with minimum possible weight and minimum cost. . . the optimum structure is the one that does the best overall job of minimising the undesirable quantities (weight, air resistance, cost, service troubles, production time, etc.). "

Flexibility is generally associated with light weight structures so that aeroelastic problems were discovered and known from the earliest days of flight. The Wright Brothers in 1903 made favourable use of flexibility in the lateral control of their aircraft by wing warping. Among the other incidents of aeroelastic instabilities, S. P. Langley's failure to control his machine in its first flight over Potomac in the same year was due to Wing divergence, a static aeroelastic problem. In 1916, during World War I, elevator flutter of a British bomber was investigated by F. W. Lanchester and was solved by increasing the torsional rigidity of the elevators.

Although numerous other aeroelastic incidents followed in the pre-World War II period, problems in aeroelasticity did not attain the prominent role that they now play until the early stages of the war. This is because aircraft speeds were relatively low and their thickness to chord ratio was relatively high, thus giving the structural engineer the required design flexibility to obtain the required bending and torsional rigidities and thus producing rigid structures sufficient to prevent most aeroelastic phenomena.

Although many isolated aeroelastic incidences still occurred in that period (1916), they could generally be explained away and gave an ad-hoc solution. In particular, problems relating to flutter were prevented by isolating the motions in several freedoms, such as mass balancing of the lifting surfaces at the expense of an additional weight, and/or by

raising the lowest critical flutter speed safely beyond possible speeds of flight by increase of the relevant natural frequencies. The latter was usually effected by designing for increased stiffness with a less than proportional increase of weight or, preferably, without any increase of weight. Thus the two basic solutions for aeroelastic problems, increased stiffness and mass balance were already well established, and together with damping mechanisms, are still the basic elements that must be used in the vehicle structure to prevent aeroelastic instabilities.

For most designs developed between the two World Wars, flutter, which usually involved coupling between an almost pure bending and a pure torsional mode due to the unswept and more or less constant chord wing planform, would most often occur at a lower airspeed than divergence and as a result it was given more attention. This situation changed in the late 40's with the first approaches towards transonic flight as a result of the advent of jet engine and the introduction of improved light alloy structures. It was found that the best way to reduce the high transonic drag build-up was to sweep the wing relative to the airflow forward or backward. However, the divergence speed drops dramatically for even slight forward sweep angles due to the wash-in effect. The spanwise bending of a swept-forward wing induces an increase in the local streamwise angle of attack, resulting in an increase in aerodynamic loads. A swept back wing experiences an opposite or wash-out effect.

The objective of ever improved performance has led to thinner, lighter and more flexible wings which, coupled with moderately high aspect ratio and sweep, induced unintentional coupling between the various modes of structural deformation. These unintentional couplings, which proved to have adverse effects in design, have overlapped stability, response, and flutter [2-5]. Correspondingly this has narrowed the aeroelastic margins of required stiffness, so that aeroelastic instabilities have become more complex.

In the ten year period from 1947-1957 a survey by [6] indicated that more than 100 different aeroelastic incidents occurred in the United State alone, for civil and military aircraft. As a result, structural engineers were faced with requirements for stiffness,

which were now very severe so that their ability to meet such stiffness levels becomes increasingly marginal. This necessitated thinner and lighter wings, so designers turned to more complicated designs in order to control aeroelastic problems. The 'aero-isoclinic' wing proposed in 1951 by Professor Geoffrey T.R. Hill is an example of such practice. This wing was designed so that its incidence to the airflow remained constant along the span when the wing deformed. This was achieved, in part, by placing the torsion box well back in the wing. This showed that with careful design, bending-torsion coupling on a scale, which had not previously been experienced, could be successfully accommodated.

The introduction of composite material into the area of the aircraft design in the early 70s, has led to new airframe design concepts as well as the re-evaluation of older concepts. The main attraction in using composite material is the substantial weight saving that could be achieved because of their superior strength-to-weight and stiffness-to-weight ratios, compared with conventional materials of aircraft construction such as aluminium alloy. Weight savings of the order of 25% can generally be achieved using current composite instead of isotropic materials. The drawback of the composite structure as it is affected by the environment such as moisture and delamination in the laminate of the structure, which leads to a change in the static elastic and inertia stiffness of the structure especially the dynamic behaviour of the structure. Today almost every aerospace company is developing products made with fibre reinforced composite materials. The most common application of composites in fixed wing aircraft structures is the skin of wings, tail, and control surfaces.

The successful application of laminated composite materials in aircraft structures, coupled with their anisotropic property has generated a renewed interest in the field of aeroelasticity. Exploiting the directional properties of composite materials, and thereby creating aerodynamic loads through controlled deformation could control aeroelastic problems such as flutter and divergence, without excessive weight (i. e., mass balance, increase in bending and torsional rigidities by adding material, etc). The technology to design for a predetermined aeroelastic response of a lifting surface using composite materials has been named aeroelastic tailoring.

Aeroelastic performance benefit may be achieved through the passive technique of aeroelastic tailoring or active control techniques. Aeroelastic tailoring is defined as the employment of directional stiffness into aircraft structural design to control static or dynamic aeroelastic deformations, so that the aerodynamic and structural performances are achieved effectively [1].

Development of composite materials provided a new way for aeroelastic tailoring research. It was shown that the directional properties of composites could be used to create a coupling between bending and twist deformations, this coupling helped achieve shape control. Modern composite materials could be optimised by controlling the ply orientation so the required strength can be achieved. The ability to tailor the primary stiffness can reduce aircraft component weight and improve aeroelastic and aircraft performance. However, varying the composite ply orientations in order to produce twist may make the wings less stiff in bending and lead to higher static deflections and aeroelastic instability, therefore, the design of the active part of the structure should be considered within the overall context of aeroelastic design. As a result a design could be improved aerodynamically i.e. increase in lift and aeroelastically i.e. increased flutter speed. An example of successful innovation with advanced composites and integrated design was the development of the X-29 forward swept wing aircraft. Along with many, known advantages conferred or contributed by the use of structural composites, a series of challenges arises in consequence.

Some of these challenges derived from the complexities arising from anisotropic nature of composite materials themselves, and the structural couplings, which do not exist in the case of isotropic material structures such as light alloy materials. If one looks closer at the problem of flutter, only an increase in a wash-in deformation is required to increase the flutter speed, and vice versa is required for the divergence problem. Thus, the directional properties of laminated composite materials can be oriented to alter the static and dynamic characteristics of composite aircraft wings, leading to aeroelastic tailoring and thus to an optimum design. The introduction of composite materials can be regarded as a landmark in the history of aircraft design and the unusual static and

dynamic characteristics of these materials are expected to have a beneficial application in the field of aeroelasticity.

There are two ways in implementing aeroelastic control technology. One is through the use of conventional leading-edge and trailing-edge flaps and the other is concept of deformable aerofoil in which the control surface is seamlessly integrated into the wing structure. The disadvantage associated with the conventional control surfaces is the increase in induced drag due to flow separation at the gap between the wing and flap. Another drawback of using conventional flaps is the mechanical complexity associated with its actuation mechanism. As solution for these problems piezoelectric devices and shape memory alloys were introduced in the 90's.

Recent extensive use of Unmanned Aerial Vehicles (UAVs) has led to a need for improved endurance and range capabilities. UAVs are now capable of undertaking missions from a fraction of hour up to 40 hours. The issue is now that these aircraft have already been optimised for their current mission objectives and are limited by their storage capacity for fuel. An alternative to improve the power systems is to improve the fuel efficiency by adapting the geometry of the vehicle to the flight conditions. Again, morphing seems to be the appropriate solution, and is beginning to be applied in the UAV field.

1.2 Research Aims and Objectives

Active aeroelastic wing technology (AAWT) has been demonstrated and studied by many research programs. Active Aeroelastic Wing Technology (AAWT) is multidisciplinary and it integrates aerodynamics, active controls and structural aeroelastic behavior to maximise air vehicle performance. A different technology for achieving flapless flight of an Unmanned Air Vehicle (UAV) has been under development in the Flapless Air Vehicle Integrated Industrial Research (FLAVIIR) program. The FLAVIIR programme includes investigating a wide range of technologies (i.e. fluidic thrust vectoring system and fluidic circulation control devices [7]), integrating these technologies into an unmanned air vehicle that is then used to

demonstrate the technologies in a representative manner. The air vehicle chosen for this project was the DEMON demonstrator vehicle developed by Cranfield University [8]. One of the main aims for the DEMON under FLAVIIR was to demonstrate a full flight cycle from take-off to landing without the use of conventional flight control surfaces.

The primary aim of this study was to design a Seamless Aeroelastic Wing (SAW) structure applicable to a lightweight UAV such as DEMON. Therefore the current study focused on an optimal design of a SAW structure. Although similar to the AAWT and relevant to the FLAVIIR, the major difference from them is that a SAW will function as an integrated one piece lifting and control surface. It is designed to produce a desirable wing camber for control by deflecting a hinge-less flexible trailing edge (TE) part instead of a traditional control surface or unconventional coanda jet flow. The main advantages of the SAW concept include improvement of aerodynamic efficiency (high lift/drag ratio etc.), increase of operational flexibility, reduction of structural complexity, less concentrated hinge load and potential structure weight saving. In principle, this can be achieved in a mixture of passive design and active control approach. However the main challenge of the project was to design a feasible, simple and reliable SAW structure and actuation mechanism. The following challenge is how to optimise the design for further weight saving and improved performance under the design requirements.

In this current investigation, attention was firstly paid to the design of a SAW with a hinge-less flexible trailing part to replace the control surface. By adapting a curved torque beam design with a proposed innovative sliding trailing edge (TE), a certain structural warping is allowed for the SAW camber variation and TE deflection in a desirable shape and minimum control power demand. A bench-test model was built to demonstrate and prove this design concept works. For a lightweight and low speed UAV, wing load is usually relatively small even under large limited load factor. For this current UAV model of a large sweptback wing, significant structural weight saving was mainly constrained by aeroelastic stability and carbon/epoxy laminate manufacture rather than the usual structural strength criteria. Therefore further attention was focused on optimising the SAW structure for a minimum weight and maximum aeroelastic

stability. Initially, effort was therefore made to optimise the primary wing box structure for minimum weight under the strength criterion. The reduced weight wing box stiffness and aeroelastic stability and control effectiveness can be improved by applying the aeroelastic tailoring. In terms of aeroelastic tailoring, some previous work in this field has demonstrated that the divergence speed of a forward swept wing can be increased by optimising the laminate layup. The elastic or stiffness coupling due to an unsymmetrical laminate layups could also have significant effect on the aeroelastic behaviour of a composite wing. Therefore investigations were made in order to optimise the laminate layup of a composite wing structure for desirable aeroelastic behaviours. Due to the flexibility and large sweptback angle of the current SAW, flutter and control effectiveness will be the main design constraint and bending-torsion stiffness coupling will be a key design factor in aeroelastic tailoring.

Previous research has shown that a gradient-based deterministic method (GBDM) based on a continuous and finite gradient of objective function at each step efficient than a genetic algorithm (GA) method based on a stochastic procedure. In this study therefore, the GBDM is employed for the SAW structure optimisation to achieve a lightweight, adequate strength and aeroelastic stability design.

Based on the design features and an optimised wing box design, the investigation was then focused on the study of the dynamic and aeroservoelastic behaviour of the SAW by using FEM where the flexible actuation part was integrated to the FE model. An experimental model was built to test the design features and obtain the stiffness of the actuation system. The key parameters were identified from vibration test data of the system components. They were used to update the FE model and analyse the dynamic response of the SAW.

1.3 Structure of Thesis

In this chapter the main objectives of the study are defined and the importance of the work is emphasised. The procedure and the layout of the research that is necessary to

achieve the main aim behind the research is presented. The results and the research effort are organised as follows:

Chapter two covers the material in the area of static and dynamic aeroelastic phenomenon, along with the application of state of the art design and analysis of morphing wing concepts. The first section focuses on the introduction to aeroelastic instability problems associated with flexible structures, due to the close interaction of aerodynamic loads and structural deformations. Various AAW concepts which allow smooth deformations in aerofoil chamber are presented next. A number of studies have been carried out to investigate the active aeroelastic concepts, for example the Active Aeroelastic Wing program, the 3AS (Active Aeroelastic Aircraft Structures) program. Methods of wing morphing include camber change, wing twist, wing sweep change and wing span change. Varying the camber to achieve a desired lift can eliminate the need for conventional control surfaces. In order to replace the conventional control surfaces, the wing should be flexible enough to change shape to enhance aerodynamic performance, and at the same time have the correct stiffness to overcome aerodynamic loads. The next section presents the work carried out in the field of aeroelastic tailoring to improve the aeroelastic beneficial effect on flexible wing structures. Finally the benefits and challenges faced by potential use of adaptable/morphing structures are reviewed.

Chapter three initially deals with the micromechanical properties of composites, which is very important in the design analysis along with the stiffness modelling of composite box beams. Firstly, the basic laminate constitutive equations are presented and a summary of relevant literature in the stiffness modelling of thin-walled structure is outlined. These cover both beams, and thin-walled box beams. Explicit expressions for the bending, torsional and bending-torsion rigidities are provided. It also contains a brief summary about the solutions and the capability provided in the finite element package MSC/NASTRAN. These are listed as follows:

- Linear Static analysis (Sol 101)
- Normal mode analysis (Sol 103)
- Aerodynamic modelling methods used

- Interpolation Techniques
- Flutter Analysis (Sol 145)
- Direct Transient Response Analysis (Sol 109)

The preceding sections of chapter three looks at the modelling of the aero-structural coupling to evaluate the static aeroelastic instability (control reversal) phenomena related to SAW and the optimisation technique used for the passive aeroelastic tailoring carried out on the SAW design. Finally the methodology adapted in the SAW design and analysis using the theory and procedures presented in this chapter has been presented.

Chapter four lists the work carried out to identify a favourable aerodynamic shape by initially carrying out a 2D aerodynamic study to evaluate the aerodynamic beneficial effect of a seamless aeroelastic wing. Sections 4.1 - 4.3 summarises the tool selection from a number of available tools and its adaptation in the 2D aerodynamic study. The proposed SAW actuation mechanism along with initial actuation force/power requirements is presented in section 4.4 and 4.5 respectively.

Chapter five focused on an optimal design of a wing box structure for the SAW. One of the main challenges was to optimise the design for further weight saving and improved performance under the design requirements. For a lightweight and low speed UAV, wing load is usually relatively small even under large limited load factor. For this current UAV model of a large sweptback wing, significant structural weight saving is mainly constrained by aeroelastic stability and carbon/epoxy laminate manufacture rather than the usual strength criteria. Therefore further attention was focused on optimising the SAW structure for a minimum weight and maximum aeroelastic stability. Analytical methods were used for structural stress, vibration and aeroelastic analyses. The MSC/NASTRAN package based on the finite element method (FEM) was also used for structural analysis and comparison. Secondly, attention was focused on aeroelastic tailoring of the basic composite wing box model to achieve the maximum flutter speed under the strength criterion.

Chapter six presents the results from the linear static, normal mode, aeroelastic and dynamic analyses carried out for the SAW. The wing box structure with the optimised lay-up was integrated with the SAW actuation mechanism for detailed analysis. The analysis was carried out using the finite element code MSC/NASTRAN.

Chapter seven summarises the main findings of the research work on composite seamless aeroelastic wing structure, integrated with the proposed trailing edge actuation mechanism.

2 Literature Review

This chapter covers the material in the area of static and dynamic aeroelastic phenomenon, along with the application of state of the art design and analysis of morphing wing concepts. The first section focuses on the introduction to aeroelastic instability problems associated with flexible structures, due to the close interaction of aerodynamic loads, structural deformations and inertia loads (section 2.1). Various AAW concepts which allow smooth deformations in aerofoil chamber are presented in section 2.2. Section 2.3 presents the work carried out by researches to improve the aeroelastic beneficial effect on flexible wing structures. Finally the benefits and challenges faced by potential use of adaptable/morphing structures are reviewed in section 2.4.

2.1 Aeroelastic Phenomena

Aeroelasticity is mainly the concern of the interaction of flexible structures with the surrounding airflow. It is defined as the mutual interaction of aerodynamic (A), elastic (E) and inertial (I) forces, as demonstrated by the classic Collar's Aeroelastic Triangle shown in Figure 2.1. As an aircraft moves through the air, loads act on the structure and causes deformations of the flexible structure. These deformations will change the geometry of the structure which leads to a change in the flow and aerodynamic loads, resulting in a loop of loads and deformations. In most cases the aerodynamic loads and the internal elastic loads in the structure will converge to equilibrium. However, there are cases when the loop becomes unstable, causing increasing deformations leading to structural failure of the aircraft.

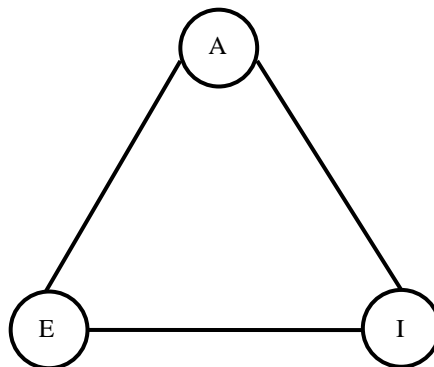


Figure 2.1 Collar's Aeroelastic Triangle [9]

Aeroelastic phenomena fall into two major categories;

- a. *Static* – involves interactions between aerodynamic and elastic forces, such as control surface efficiency at high airspeeds. As a control surface such as an aileron is deflected, the lift is increased. At the same time, due to the lift produced in the trailing edge region the wing experiences a nose down pitching moment. This pitching moment twists the whole wing, reducing the wing angle of attack and causing negative lift. Depending on the wing stiffness and geometry, there is a certain airspeed called the reversal speed, where the positive lift of the control surface deflection is compensated by negative lift due to wing twist, making any control input on the control surface ineffective.

- b. *Dynamic* – involves interactions between inertial, aerodynamic and elastic forces, such as flutter. Flutter occurs when the unsteady aerodynamics cause forces that tend to increase the total energy involved in the motion of the structure and the surrounding airflow. It can also be described as a fluid-structure interaction with negative damping, leading to oscillations with a magnitude increasing with time. All aircraft structures will suffer from flutter at some airspeed. The main challenge for engineers is to tailor the structures to ensure the flutter speed does not lie within the flight envelope for a given aircraft. Other forms of aeroelastic phenomenon are dynamic response and vibration. If the aircraft flutter speed is not within at least $1.15V_{\text{dive}}$ then the damping of the fluid-structure interaction may be very low, causing the structure to be very sensitive to gusts, landing, sudden control motions, moving shock waves, or other dynamic loads.

Present aircraft structures tend to be flexible to some extent due to weight restrictions. Aeroelasticity is therefore a main concern in aircraft design. Most importantly as mentioned before, the aircraft must not suffer from aeroelastic instabilities within the flight envelope. A number of analyses are required for certain flight conditions and might result in critical configurations that may lead to instabilities in a certain velocity or altitude range. Possible solutions for such results are either to avoid operation in this region of the flight envelope, or to modify the aircraft structure.

2.2 AAW Concepts

Aeroelasticity was often seen as a problem in the past that had to be eliminated when designing an aircraft. Recent research however has been focused on Active Aeroelastic Wing (AAW) technology, which integrates aerodynamics, active controls and structural aeroelastic behavior to maximise air vehicle performance. Many active aeroelastic concepts aim primarily at reducing structural weight, and deal with the flexibility increase by means of active control. This concept of wing flexibility would allow the use of high aspect ratio, thin, swept wings that could be deformed into aeroelastic shapes for optimum performance aerodynamically and aeroelastically.

There is a growing interest across the globe in the development of active aeroelastic structures to make use of the aeroelastic effect in a beneficial manner. For example, Wright brothers used wing warping, to control the Wright B flyer. As the aircraft speed increased, wings had to be stiffer to overcome aeroelastic instabilities such as divergence and flutter. Hence, wing warping could not be implemented further due to the power requirement, which could not be met by the actuators. As a result more efficient forms of shape control systems such as ailerons, flaps, trim tabs emerged. Another way of changing the shape of the aerofoil profile is the concept of variable camber. This is achieved by having trailing-edge flaps. Several research programs have been carried out to achieve innovative shape control concepts in the past two decades. However, most of the concepts have never been implemented in an air vehicle due to weight increase associated with actuation systems, and lack of efficient structures to deform the structure. One of the most innovative concepts emerged is the Active Aeroelastic Wing (AAW) technology [10], which uses both leading-edge and trailing-edge control surfaces to induce wing twist in order to increase the aerodynamic performance of the air vehicle. A number of examples of some of the AAW concepts immersed in recent years are presented in the following.

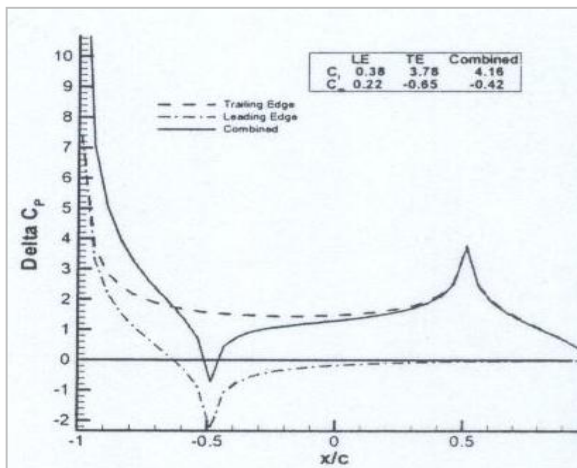


Figure 2.2 Change in Aerofoil section Pressure Distribution due to control Surface Deflection [10]

The primary goal of having variable camber, flexible camber, morphing wing, etc. is to change the wing camber to achieve a better performance aerodynamically and structurally than the conventional methods. It is also shown that changing the camber in a flexible manner results in a smooth

pressure distribution over the wing surface. Figure 2.2 shows the effect of the conventional trailing-edge and leading-edge control surfaces on the pressure distribution [10]. In designing a wing structure with variable camber features some considerations has to be kept in mind. It has to be capable of deforming regularly under flight loads, then remain rigid under further applications of load and be stiff enough to bear these loads without failure.

pressure distribution over the wing surface. Figure 2.2 shows the effect of

One of the first analyses for a variable camber wing was carried out in the 1920s [11]. It introduces a flexible camber configuration supported on two beams; a wire system has been set up to withstand the loading on the wing (see Figure 2.3). However, this wing design was used to analyse biplane or triplane wing configurations instead of designing a single variable camber wing for an air vehicle.

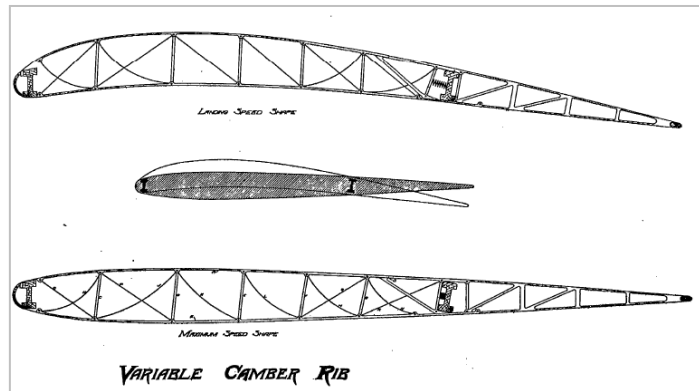


Figure 2.3 Variable Camber Wing [11]

Over the years a number of morphing aerofoils or seamless and gapless high lift devices have been developed. Figure 2.4 shows some of the patents from 1916, 1928, 1962 and 1980 [12-15].

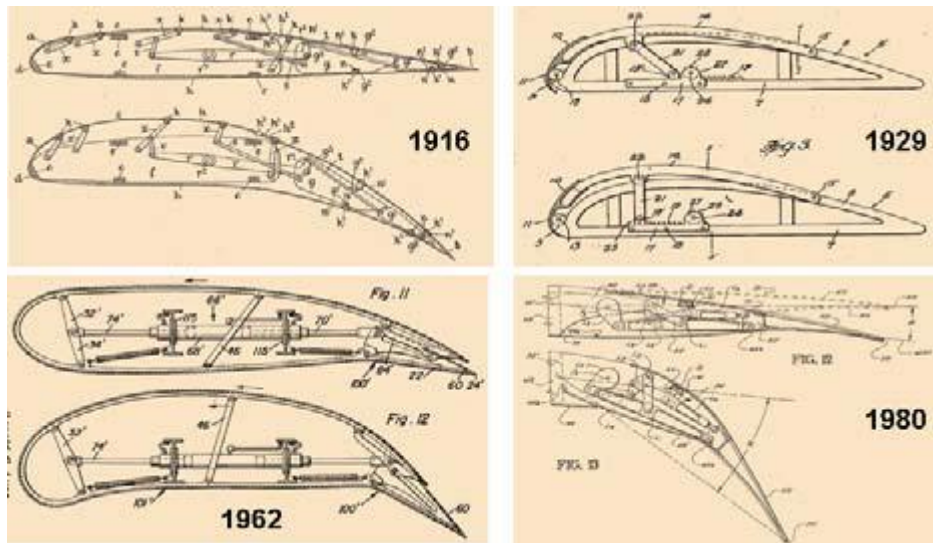


Figure 2.4 Morphing Aerofoil Patents [12-15]

Majority of these mechanisms deal with 2D complex mechanisms and kinematics assuming they are applicable to fully elastic skins, which are able to follow any motion of the mechanism for a desired shape change. Disregarding the skins, the concepts are complex and heavy mechanisms even though they are capable of bearing the aerodynamic loads and can provide the desired shapes accurately.

2.2.1 Active Aeroelastic Wing (AAW)

In the US, the Active Aeroelastic Wing (AAW) research project was initiated to demonstrate, in full scale, key AAW parameters and to measure the aerodynamic, structural and flight control characteristics associated with AAW [16]. The program used a modified F/A-18 aircraft to validate the overall aircraft performance using a lighter, more flexible wing. In order to avoid control surface reversal due to wing twist created by trailing-edge deflections, leading-edge control surfaces has been used. Even though it is a well known fact that trailing-edge control surfaces are effective in increasing lift, due to this change in lift the wing tends to twist and at high airspeeds effectiveness of trailing-edge control surface is reduced. Hence, studies carried out in the AAW project have shown that the effectiveness of the trailing-edge control surface in generating roll moment reduces at high airspeeds [10, 16]. However, the effectiveness of leading-edge control surface in generating roll moment increases with increasing airspeed. This design with both leading-edge and trailing-edge control

surfaces shows an improvement in rolling moment and the control surface deflection could be optimised to perform certain manoeuvres.

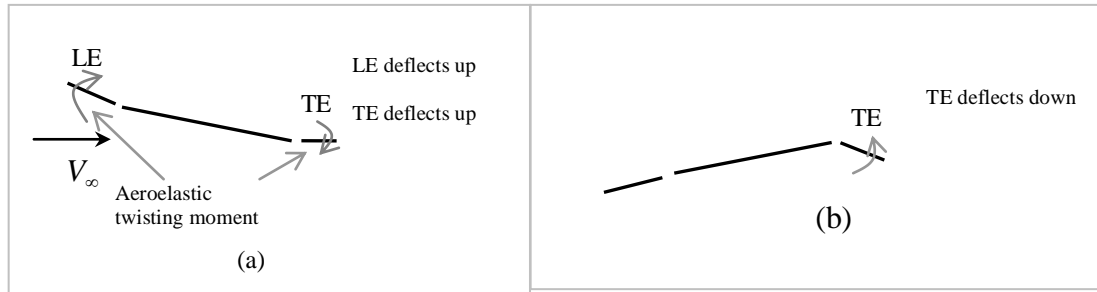


Figure 2.5 (a) AAW Technology; (b) Conventional Control Surface [17]

By carrying out a trim and structural optimisation it has been demonstrated that the structural weight can be reduced by 24% compared to the conventional control case [17, 18]. The structural optimisation has been carried out for the sizing of structural elements to minimise weight, considering stress and aeroelastic constraints and trim optimisation has been carried out to select the control surface deflection angles to trim the aircraft to a specified manoeuvre [17]. AAW flight research was carried out in two phases, where fifty and thirty four flights were conducted during the first phase and second phase respectively. The program showed that it was possible to exploit aeroelastic effect to improve a chosen aircraft performance parameter, which in this case was roll performance [19-20].

2.2.2 Active Aeroelastic Aircraft Structures (3AS)

A similar research project has been initiated in Europe, where the Active Aeroelastic Wing Structures (3AS) [21-25] project focuses on different concepts for improving aircraft performance by exploiting active aeroelasticity. Different concepts have been proposed under this project in the areas of active wing tips, aerodynamic control surfaces, active all-movable vertical tail concepts and more recently the rotating rib concept [21, 22] (see Figure 2.6).

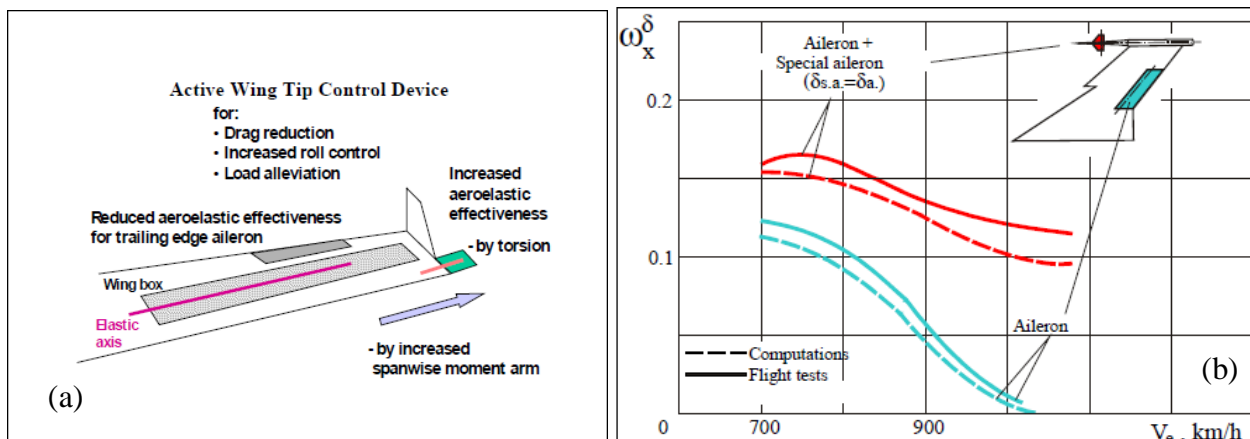


Figure 2.6 Concepts studied under the 3AS project; (a) Active Wing Tip Concept ; (b) Roll Control Efficiency using Ailerons [22].

The concepts were demonstrated in laboratory or by wind tunnel tests using mainly the European Research Aeroelastic Wing Tunnel Model (EuRAM) at the TsAGI Institute for Aeroelasticity in Moscow [26, 27]. In this model, similar to the AAW project, a wing tip control surface has been attached to the wing to increase roll efficiency compared to a conventional leading edge flap at high airspeeds. This is shown in Figure 2.7. Other studies have been performed to show the positive effect of the wing tip device on gust load alleviation [28].

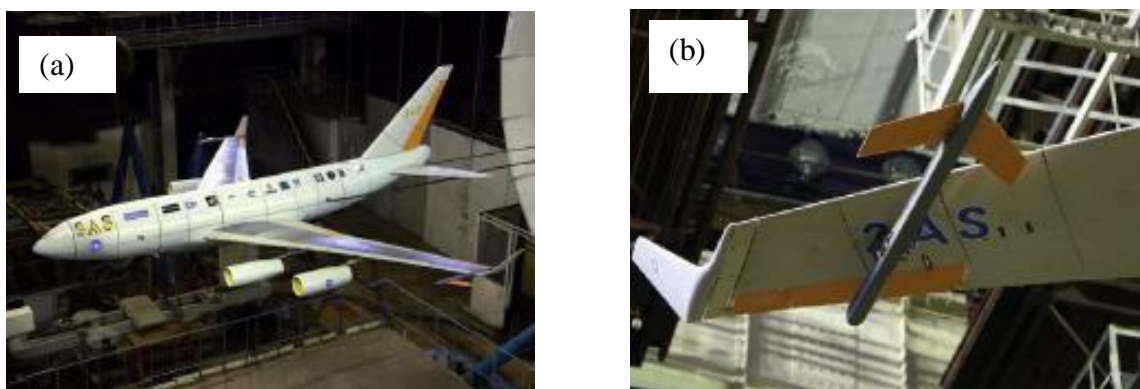


Figure 2.7 (a) EuRAM ; (b) Wing Tip Control Surfaces in EuRAM [22]



Figure 2.8 All Movable Vertical Tail (AMVT) with Variable Stiffness Attachment [29]

position could be adjusted, compared to the conventional fin where multiple attachments are being used [29]. A study has been carried out to investigate the effect of moving the attachment and the stiffness of the attachment. It has been found by experiments that by placing the attachment at a downstream position of the AMVT, the elastic deformation actually increases the efficiency of the tail if the attachment stiffness is reduced sufficiently. However, reducing the torsional stiffness of the attachment will tend to create aeroelastic instabilities, such as flutter or divergence. A trade off between the gains in aeroelastic efficiency and aeroelastic stability have to be considered in the design. The only way to achieve an optimal attachment stiffness and attachment position is through the use of an attachment with varying torsional stiffness. This has been achieved by the use of pneumatic cylinders whose stiffness can be varied by change in compressed air supply [30].

Another concept implemented in the EuRAM model was an all movable vertical tail studied at Manchester University, UK. The main objective was to reduced weight compared to a fixed tail with rudder. Similar to the wing trailing edge control surfaces, light fins tend to lose efficiency at high airspeeds. The fin is attached via a single attachment point whose

The following concepts discussed below are similar projects carried out for flexible/smart Fins. One of the first adaptive fins studied at Auburn University, USA uses a single bimorph actuator to drive an aerodynamic shell in pitch. Within the shell, a stiff main spar is pivoted to act as a rotational axis [31]. Two types of flexspar fins have been studied. The first configuration, known as a shell-joint flexspar, the base of the bimorph bender is rigidly joined to the main spar, while the tip is joined to the shell in a chordwise direction. This configuration is recommended for high-stiff low deflection applications. The second configuration, known as a tip-joint flexspar, uses a bimorph

bender element mounted at the base and has a connection to the tip of the shell [31], see Figure 2.9. After a series of experimental studies the results show that the fin reached $\pm 11^\circ$ in pitch using the flexspar control surface of 4-inch span and 3.33-inch chord.

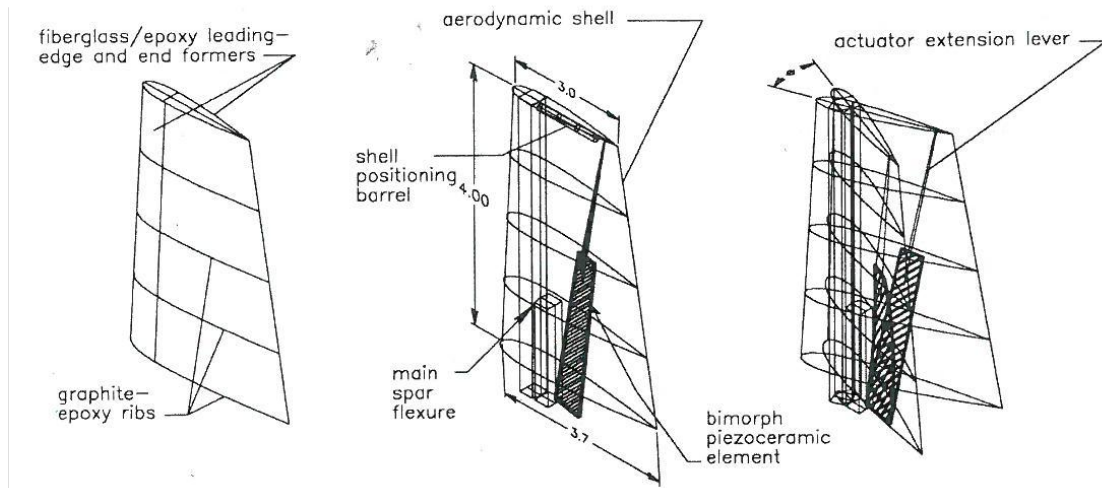


Figure 2.9 Shell-joint and Tip-joint Configurations [31]

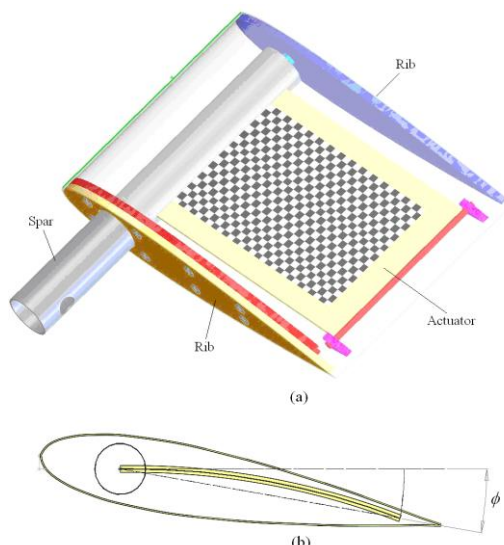


Figure 2.10 (a) Smart Fin; (b) Angle of Attack generated by Piezoelectric Actuation [32]

in compression [32], see Figure 2.10.

This design studied by University of Delaware, Newark, uses piezoelectric material to activate the fin. The piezoelectric material used in is Macro Fibre Composites (MFC) [32]. The design includes a hollow circular steel shaft used as the spar located approximately at the quarter chord of the fin. The actuator (rectangular plate) is cantilevered to the spar. MFC patches have been bonded to the composite plate. An angle of attack is achieved by activating one MFC patch in tension and the adjoining MFC patch

Another concept that emerged at a later stage of the 3AS project was the rotating rib concept [23, 24]. The main concept was a modification of the original idea presented by H. P. Monner from DLR [33]. The traditional connection between the skin and the ribs,

based on rivets of the trailing-edge of the aerofoil has been substituted by a separate number of linear slides which would allow the skin to move smoothly over the rib contour, see Figure 2.11. The rib is rotated by means of an actuator. A wing section model with four rotating ribs has been built to study the achievable camber angle and the torque requested on the ribs to produce the assigned shape with and without aerodynamic load. Figure 2.11 shows the rotating rib mechanism and its application to a wing model.

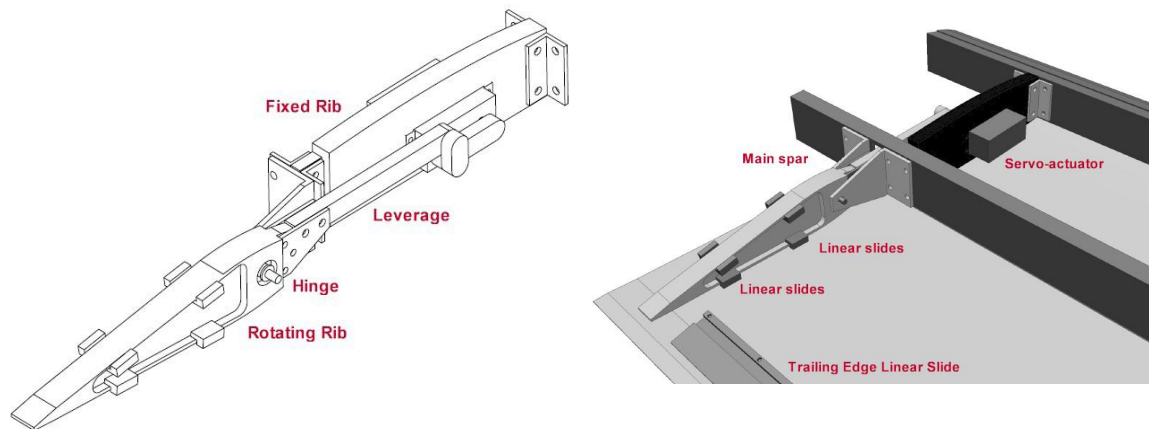


Figure 2.11 Rotating Rib Mechanism [24]

A further concept that was developed under the 3AS project was the smart spars by University of Manchester, UK. The proposed concepts are shown in Figure 2.12. The first concept, the torsional stiffness and the position of the local shear centre have been changed by moving part or the entire length of the spar [34]. In the second concept, the stiffness of the spars is altered by rotating the spars. It is expected that since the aerodynamic lifting area remains the same, the amount of twist along each part of the wing can be changed by these proposed methods. A prototype of this concept has been tested in order to examine the behaviour under static loading. The wind tunnel tests have shown that the static aeroelastic twist can be controlled through movement and rotation of the spars [34, 35]. In the next stage, the concepts have been modelled using MSC/NASTRAN to predict the effect of these moving/rotating spars on normal modes, static aeroelastic deflections, dynamic aeroelastic behaviour and aerodynamic lift. The results have shown that the concepts can be used to control static wing displacements to achieve aerodynamic objectives [36, 37]. However, further work is needed to determine

the aerodynamic gains against the extra weight and power penalties associated with such an approach on full-scale aircraft.

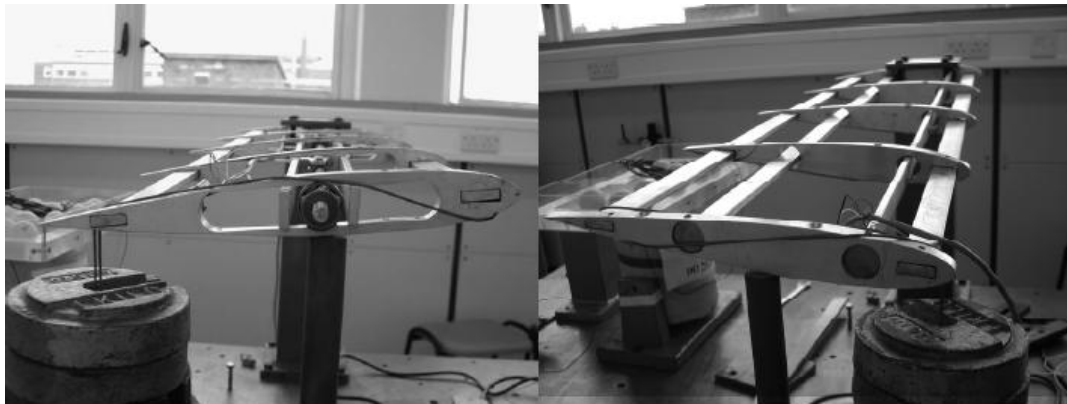


Figure 2.12 Moving and Rotating Spars Concepts [34]

2.2.3 Belt-Rib Concept

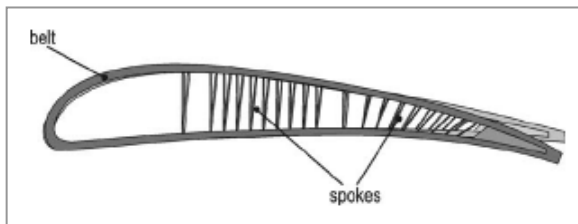


Figure 2.13 Belt-Rib Configuration [38]

The German Aerospace Centre (DLR) has carried out some research on the belt-rib concept for variable camber aerofoil [38]. This concept implements a design for light shape adaptable structures. The belt-rib concept adopts a rib structure which replaces the conventional rib structure. The ribs consist in closed shell form reinforced by in-plane stiffeners, which are connected to the belt by hinges [38], see Figure 2.13.

The German Aerospace Centre (DLR) has carried out some research on the belt-rib concept for variable camber aerofoil [38]. This concept implements a design for light shape adaptable structures. The belt-rib concept adopts a

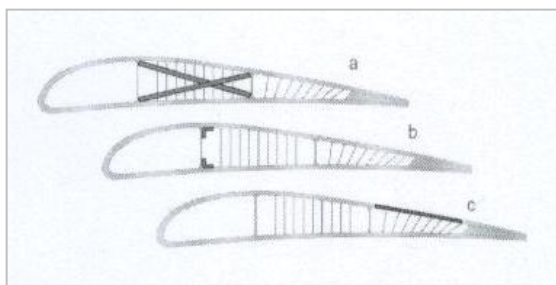


Figure 2.14 Options for Actuation Methods [39]

A number of options for activation methods have been introduced [39], the different types of activation methods that could be adopted are shown in Figure 2.14. In (a) Shape Memory Wires used to deflect the trailing-edge, in (b) the angle of the spokes changed using rotary actuators or

using active hinges, to produce a bending moment to change the angle, in (c) active material to be used in the belt to obtain the desired change of camber [39].

2.2.4 Smart Structures

The most common actuation materials are smart materials. Smart materials respond to temperature, moisture, or electric and magnetic fields. It can be used directly to make smart systems or structures or embedded in structures whose inherent properties can be changed to meet performance needs. Smart structures have the capability to sense, measure, process and diagnose at critical location any changes in selected variables, such as temperature, pressure, and to command appropriate action to preserve structural integrity and continue to perform the intended functions. The most common smart materials are;

Shape memory alloys (SMA), which have the property by which the metal ‘remembers’ its original size or shape and reverts to it at a characteristic transformation temperature. Shape memory alloys (SMA) change phase at certain critical temperatures and therefore they display different stress-strain characteristics in different temperature

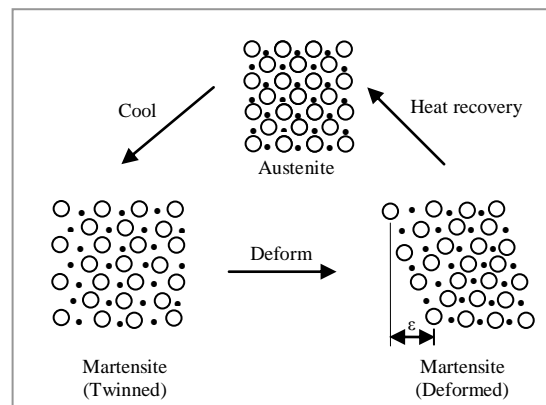


Figure 2.15 Phase change in SMA due to activation [40]

ranges. Shape memory alloys have a low temperature phase and high temperature phase and its unique properties arise from a change in its phase. The phase change is between two solid phases and involves rearrangement of atoms within a lattice (see Figure 2.15). The internal structure is different at different temperatures. The low temperature phase is known as martensite and the high temperature phase is called austenite [40]. Magnetic Shape Memory Alloys (MSMAs), also known as Ferromagnetic Shape Memory Alloys (FSMAs) are new actuator materials. These materials exhibit both ferromagnetism i.e. change shape when a magnetic field is applied and shape memory effect due to the presence of an austenitic-martensitic phase transformation that occurs

during cooling. Another type of SMA is the thermal SMAs, which has the ability to undergo plastic deformation at a low temperature, but recover when heated to a higher temperature.

Piezoelectric (PZT) materials, which have the property to experience a dimensional change when an electrical voltage is applied to them and generate electricity when pressure is applied (Figure 2.16). Piezoelectric materials undergo deformation (strain, ε) when an electric field is applied across, and conversely produce voltage when strain is applied, and thus can be used both as actuator and sensors [40]. When manufactured, a piezoelectric material has electric dipoles arranged in random directions. If an electric field is applied externally, the dipoles respond and produce a change in dimension of the PZT. The dipoles are permanently aligned with one another through a process called poling, in order to obtain a macroscopic response [40]. Some types of piezoelectric materials are polycrystalline piezoelectric and Single Crystal Piezoelectric (SCP) materials [41]. However, polycrystalline piezoelectric materials are limited in the amount of strain they produce when applied to an electric field, whereas SCPs produce higher strains up to 10 times the strain of polycrystalline material [41].

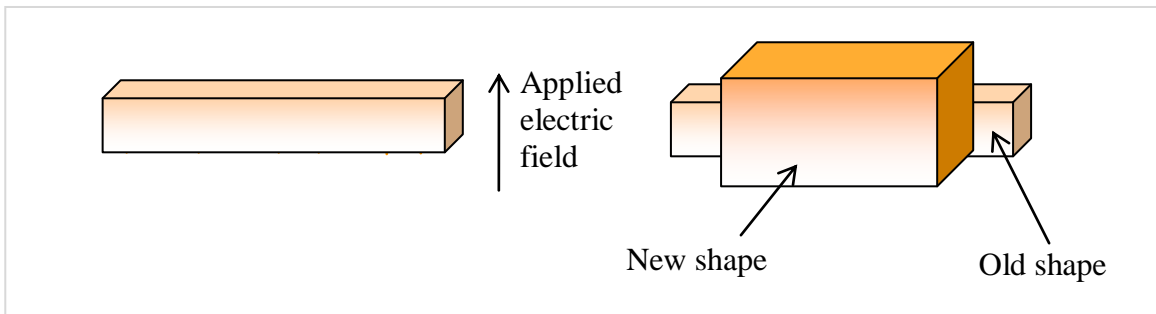


Figure 2.16 The piezoelectric effect [41]

Comparison of Actuator Materials with Conventional Actuators

The most commonly used actuators are pneumatic and hydraulic actuators, which use air cylinders that are moved by compressed air and a fluid respectively. The force available from the actuator is determined by the diameter of the cylinder [41]. Disadvantages of a pneumatic actuator are; it requires separate air lines for each cylinder and the internal forces acting on the piston are high [41]. As a result the lifetime of it is limited. Unlike the pneumatic actuators, the life time of the hydraulic

system is higher due to the fewer problems with the pistons. The main disadvantages of these systems are the risk of fluid leakage in a hydraulic actuator and the considerable weight factor for both actuators if high forces are required.

The main advantage of PZT application over other actuation mechanisms is that it is in solid state with no moving parts and requires less maintenance. Another type of actuation material discussed in the previous section is thermally activated shape memory alloys. The main advantages of thermal SMA actuation is that it can support large stresses (up to several hundred MPa) [41] during the actuation cycle. However, the main disadvantage is that the energy required to activate the shape memory effect is significantly higher than the other smart actuators, due to the heat losses which results in a low efficiency of the actuator system.

Electrorheological (ER) and Magnetorheological (MR) fluids are liquid systems that contain highly polarised particles that re-orientate in the direction of the applied electric or magnetic field respectively. The applied electric or magnetic field changed the mechanical properties of the fluid. When a field is not present ER and MR fluids act as normal oils. They will not flow until the shear stress exceeds a certain value called the Yield Stress. The yield stress depends on the applied field. However, this mechanism is limited as the use of actuators and could be used in controlling damping systems by varying the stiffness of the damper by changing the applied field [41].

Considering all these actuator materials discussed, it can be seen that MSMAs and SCPs are capable of doing better than the other smart actuation materials. However, they are still behind conventional actuators such as pneumatics and hydraulics. But the conventional actuators have a number of limitations that could be overcome by the use of smart actuation materials, such as [41]:

- Complexity of parts and the high number of moving parts which can lead to reliability problems related to friction and wear.
- System weight can be reduced by replacing the conventional actuators by smart actuators, which would result in an increase in payload, increase in range and reduction in fuel etc.

- Response time can be improved using smart actuators at high frequency operations.

The rest of the section will mainly focus on some of the key wing adaptation concepts that use smart actuation in order to change shape.

Adaptive wing – the adaptive wing concept has been adapted to achieve a shock free transonic flow for minimum cruise drag at changing freestream conditions. It incorporates active trusses in the wing rib structure as illustrated in Figure 2.17. The diagonal elements are smart linear actuators that expand and contract to deform the aerofoil.

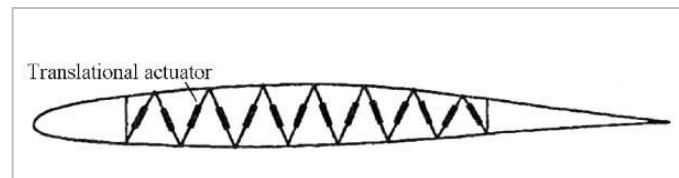


Figure 2.17 Adaptive Wing Structure Concept [42]

The adaptive wing concept represented the adaptation of an aerofoil upper surface between $0.05c$ and $0.95c$. This design has resulted in an aerofoil drag reduction of up to 36% compared to the baseline configuration designed at $M_\infty = 0.78$ [42]. Smart linear actuators has been used in the test model, where for the required change in geometry, of a Gulfstream III-type aircraft, 150 to 200 smart actuators have been required per wing [42]. Without weight penalty the adaptive wing would save up to 11% fuel. However, when the actuator and structural weight penalty is incorporated, the fuel savings drop to less than 1%.

Design concepts of this sort that make use of large number of actuators and complicated control algorithms are undesirable since realisation and maintenance penalties would cancel out the aerodynamic benefits. Especially, since more simpler and less complex approaches are available leading to similar aerodynamic performance improvements. Also such a system would need a significant power supply for its operation.

In a number of other applications, active material elements have been used to achieve a smooth continuous deformation to achieve aerodynamic performance gains over the conventional actuation concepts. Apart from the aerodynamics, the main focus of these studies has been to estimate the degree of twist required to maximise flutter and vibration reduction benefits. One interesting application of this is within the helicopter blades. One particular design included a composite blade structure embedded with diagonally oriented PZT wafers [43]. Electrical actuation of the PZT wafers induces a maximum tip twist of 1.1° . Other similar applications involved having active fibre composites for rotor blades. An active fibre composite is a laminated structure of fibreglass plies and PZT-fibre plies. In addition servo-flap concepts have been investigated as an alternative approach to achieving induced-strain rotor blade actuation [43].

NASA Langley Research Centre has been involved in numerous programs to investigate the flutter suppression and gust loads alleviation ability of fixed wings by piezoelectric actuators. One good example is the Piezoelectric Aeroelastic Response Tailoring Investigation (PARTI). A wing model of composite plate with 36 piezoelectric wafers surface bonded to each side of the plate has been tested in a wind tunnel test to successfully demonstrate flutter suppression and gust load alleviation [43]. Another concept investigated was using piezoelectric control to alleviate vertical tail buffeting under the ACROBAT (Actively Controlled Response of Buffet Affected Tails) [43, 44]. A full-scale computational investigation has been conducted to control tail buffeting responses of F/A-18 aircraft. The PZT actuators have been placed over both inboard and outboard surfaces of the vertical tail to alleviate the tail buffeting in the first bending and torsion modes. The PZT actuators were more effective in reducing structural responses in the first torsion mode (82%) than those in the first bending mode (22%) [44]. Several other researchers have made use of strain actuated devices along with two way shape memory effect for shape control and achieve similar benefits [45-47].

A recent study carried out by Icardi and Ferrero [48] have presented a preliminary design study to validate the feasibility of an adaptive wing powered by shape memory alloy actuators for a small UAV (see Figure 2.18). The wing consisting of a sandwich

box structure has a flexible skin and ribs made of CFRP. Torsion tubes and finger type truss links are used for wing camber control. The actuation proposed in this design consists of an external tube which hosts a counter rotating concentric tube. The external and internal tubes are being used for the wing downward and upward motions respectively. The concentric tubes are connected to the flexible ribs through an electro-mechanical clutch and a piezoelectric motor. The actuation is achieved by heating a tube and making free the other through the clutch. It has also been claimed that this actuation method could allow for any desired wing shape. The results presented shows that the aerodynamic benefit compared to a conventional flap mechanism has been realised. Preliminary studies carried out using FE analysis shows that a mean deflection of 21° has been achieved at the trailing edge with an actuation torque of 227 Nm. The initial finding looks promising in terms of power requirement and torque required. These are not been compared to a conventional mechanism requirements. Also the SMA torsion tube used has to be heated and this could be one of the downside to the whole actuation mechanism in terms of the total power required to carry out all these functions.

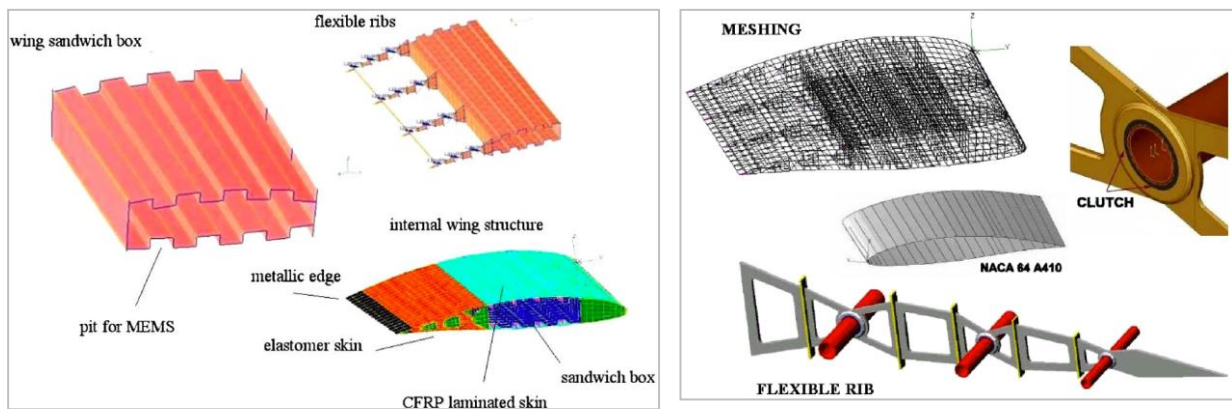


Figure 2.18 shape memory alloy actuators for a small UAV [48]

The main question here to be answered is, can such a system, demonstrated in small scale wind tunnel tests, be realized in a full scale aircraft? Power requirements for actuation for a full scale model will be significant. This indicates that the torque requirements for wing twist will be high. This is well beyond the capabilities of current actuators. A potential solution is then to avoid using smart actuation mechanisms in a purely power supplying manner, but rather use them to alter the aerodynamic forces which will alter the wing shape to optimise performance.

2.2.5 DARPA Smart Wing

The smart wing program initiated within the Defence Advanced Research Projects Agency (DARPA) in the USA. The primary goal of this project was to show the feasibility of using smart material based actuator concepts to construct a hingeless, gapless control surfaces in adaptive wing structures to improve both aerodynamic and aeroelastic performance characteristics of military aircraft. The wing design studied under the smart wing program looks at hingeless, smoothly contoured trailing edge control surfaces for variable camber and variable wing twist with the use of smart materials.

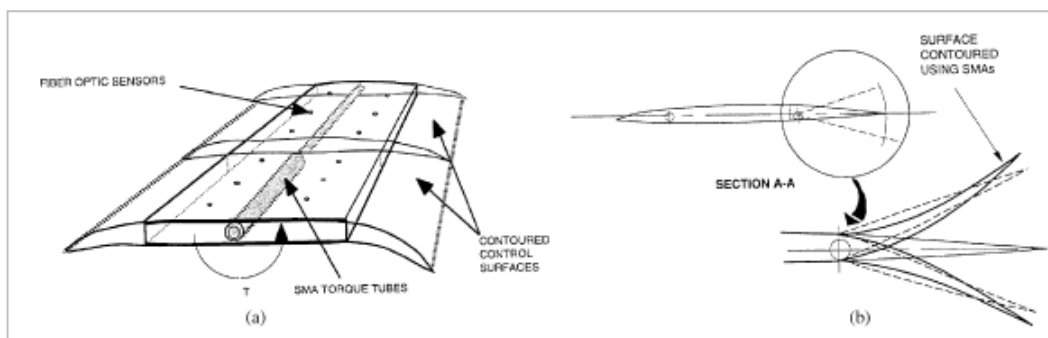


Figure 2.19 (a) Smart Wing and Torque Tube Arrangement; (b) SMA Flap [50]

Within the Smart Wing project, several configurations using shape memory alloys were tested. Phase 1 of the project modified a 16% scale model of an F/A-18 aircraft wing, which could be activated with a torque tube setting [49, 50]. Figure 2.19 shows the torque tube setup with two SMA actuators. This required less torque from each of the tubes, but provided only 1.25° deflection. At a later stage managed to demonstrate over 5° of span wise wing twist and aerodynamic benefits of 8 – 12% in lift and rolling moment due to improvements in the torque loading path in the structure and the use of a new SMA actuator [51, 52].

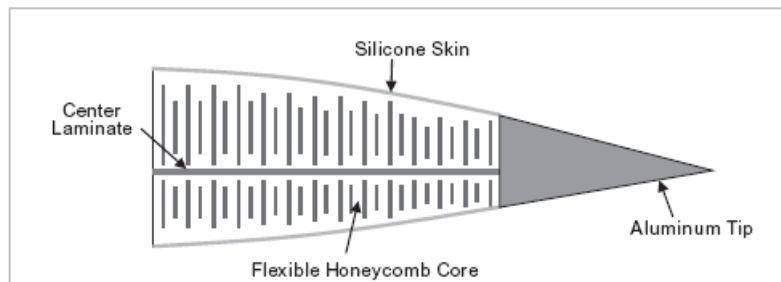


Figure 2.20 Skin-flexcore Control Surface Structure [53]

The main objective in phase 2 of the program was to demonstrate high-rate actuation of hingeless, spanwise and chordwise deformable control surface using smart materials. As part of the program a flexible control surface was designed. The flexible skin-flexcore concept is composed of elastometric (silicone) outer skin, flexible honeycomb and a fibreglass laminate in the centre [53], see Figure 2.20. The main objective of this particular design has been to reduce the overall stiffness which would result in a reduction of actuation power. This resulted in the use of an aramid core replacing the aluminium core, because it was shown that there was a 48% reduction in actuation force. There was also a 71% reduction in stiffness over the aluminium flexcore as shown in Figure 2.21.

The final trailing-edge concept refinement consists of eccentruators, high power piezoelectric ultrasonic motors and sandwich-based flexible structure. This smart trailing-edge control surface was deployed up to approximately 20° in less than 0.33s for various trailing-edge shapes [53].

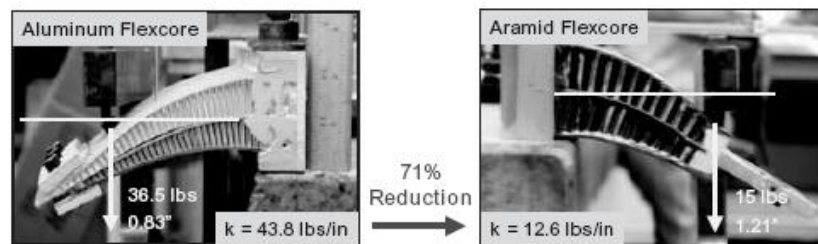


Figure 2.21 Stiffness Reduction using Aramid Flexcore [53]

2.2.6 Other AAW Concepts

Various concepts of realizing an adaptive wing have been investigated by several organisations incorporating actuation mechanism into the wing design. Some of the key designs that have been developed are discussed below.

Finger Concept

Another design concept is having the so called ‘finger’ concept at the flexible trailing edge, Figure 2.22 (a). Here the flexible part of the flaps is achieved by combining separate plate like elements with joints as indicated by the kinematics shown in Figure

2.22 (b). Each rib is individually actuated for spanwise camber variation, at a single point [42]. The rotation of the driven element is transferred from element to element, thereby providing the desired trailing edge deflected shape. The skin has been allowed to glide on the flexible ribs. This concept has been tested in a structural demonstrator.

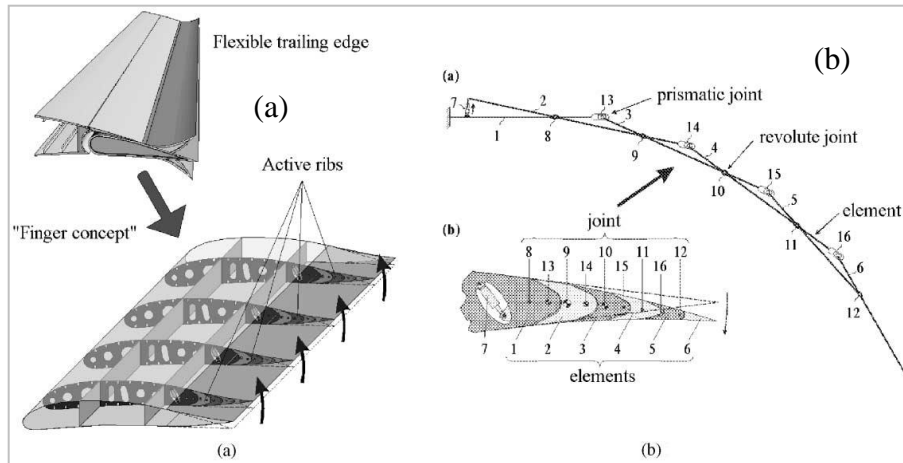


Figure 2.22 (a) Variable rear camber model; (b) Kinematics of the actuator [42]

Reconfigurable Aerofoil

This reconfigurable aerofoil design has been tested by the Aerospace Engineering Department of the Texas A&M University [54, 55]. A NACA 0012 aerofoil has been chosen to be tested under subsonic speed. The first setup consisted of a steel skin with 0.254mm thickness. The SMA wire used in the experiment was a two way wire of diameter 0.5mm, which would allow the structure to be driven back to the original position by itself. These SMA wire actuators can be attached to points on the inside of the airfoil, and can be activated to alter the shape of the airfoil. Figure 2.23 (a) and (b) show the deflection of the aerofoil when the SMA wires are activated and the experimental set up respectively. The SMA wire is linked to the aerofoil using a separate rope, such that the spanwise displacement of the SMA wire is transferred to the aerofoil [55].

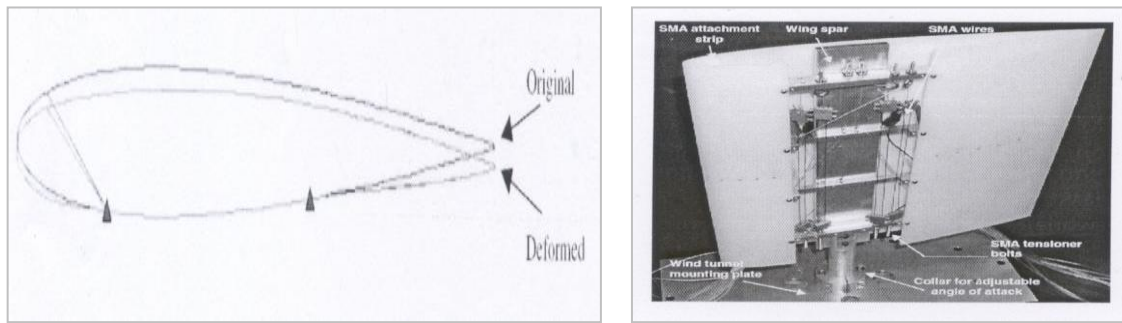


Figure 2.23 (a) Placement of the SMA in the leading-edge and aerofoil deflection; (b) Prototype of the wind tunnel model [55]

The steel skin used at the initial stage had a low deflection rate at the trailing-edge. The skin had been then replaced by ABS skin with a thickness of 2.54mm. With the use of the ABS skin a deflection of 6mm was achieved whilst the use of steel only produced a displacement of 3mm. The wind tunnel tests showed an increase in C_L by 6.2%, 4.5% and 5.5% at 0° , 5° and 10° angles of attack respectively [55].

Morphing Wing Concepts

The morphing concept used in this particular method is to change the wing span of a long-range cruise missile. Figure 2.24 shows the original wing, with no extension, and the fully extended wing. The full extension represents a 50% increase in wing span compared to the original wing [56]. The structure of this variable-span morphing wing is made up of two wings: one is the main wing box and the other is a moving wing box used to vary the wing span [56].

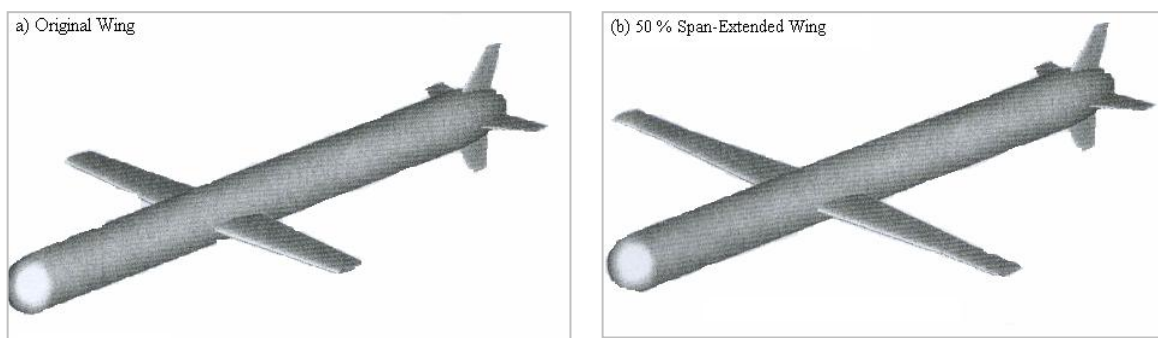


Figure 2.24 Original and Span extended [56]

Another similar type of concept applied to a low speed UAV has been investigated by the University of Bristol. In this design adaptive winglets are being used as control

effectors. Pitch control has been achieved through a dynamic static margin by changing the aerodynamic centre relative to the centre of gravity due to the movements of the winglets. By moving the adaptive winglets differentially, the air vehicle could experience roll, due to one wing producing more lift than the other with the deflected winglets.



Figure 2.25 (a) Pitch Control; (b) Roll Control [57]

This design can be an alternative to conventional control surfaces such as ailerons, elevators and rudders. However, this could be used for only basic manoeuvres, i.e. trimmed level turn can only be achieved for specific turn radius. The proposed morphing wing design consists of laminated composite materials that could undergo elastic coupling which would induce twist when the wing bends [57]. Studies have been carried out to assess the modification of the ply fibre orientation to achieve wing twist [57].

Morphing Concepts applied to commercial Aircraft

A small number of adaptive concepts applicable to transport aircraft are available in the literature and are presented below. A critical limitation in realizing these adaptive structures is the high wing loading requirement of transport aircraft. Also majority of the available 2D mechanisms are too complex. Due to the high weight penalties associated with these mechanisms and their incompatibility with light aircraft design, morphing is not realized in commercial airlines up to now.

One concept evaluated for a trailing edge mechanism was an adaptive flap structure developed by Daimler-Benz within the Adaptive wing guidance concept [58]. The basic idea behind this concept is a simple passive trailing-edge structure with an external kinematic actuation mechanism. The actuators are integrated to the flap support system,

instead of locating within the flap [58]. In this system the flap is mounted on a beam, which is linked to the flap track by a carriage at the front end and a rear flap link at the rear end [58]. Figure 2.25 shows the flap structure with the flexible trailing-edge.

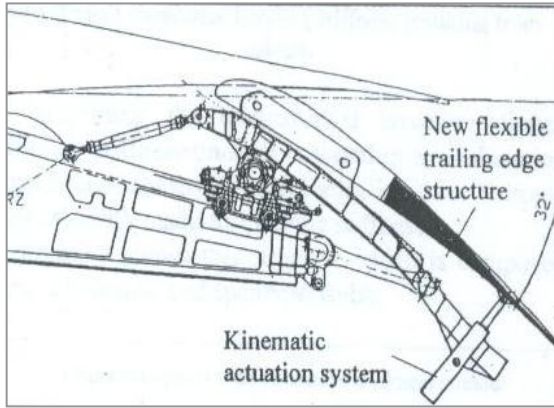


Figure 2.26 Flexible trailing-edge structure with the kinematic actuation mechanism [58]

The forward part of the flap is made to be stiff and is mounted so that it has fixed rotational degree of freedom. The flexible trailing-edge is then connected to the actuator. The rear trailing-edge of this design is a sandwich structure. Figure 2.27 (b) shows the rear section of the trailing-edge in detail. The flexible trailing-edge is then attached to the stiff flap nose structure by extending the upper skin panel. However, the lower skin panel of the flexible trailing-edge is not attached to the nose to allow for deflection of the trailing-edge [58] (see Figure 2.27 (a)).

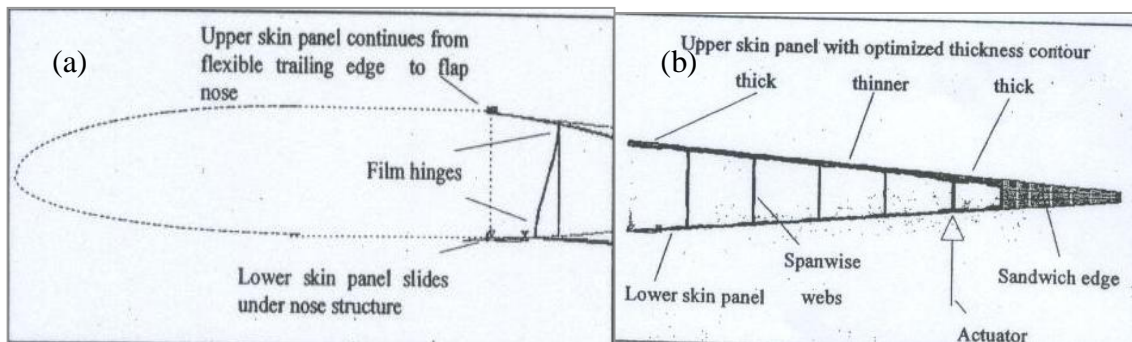


Figure 2.27 (a) Structure of flap Track concept; (b) Deformation of Webs [58]

This design looks promising in achieving a desired trailing edge flap deflection. However, it uses a complicated and rather heavy flap actuator mechanism, which does not differ from a conventional flap actuator mechanism. The idea of the lower skin panel not being attached to the flap nose structure could be investigated to look at the advantages it has in achieving a smooth deformation of the trailing edge.

The second concept looked at is a smart leading edge concept developed as an alternative to the droop nose device used for the A380. This work has been carried out under the European and national projects SADE (Smart High Lift Devices for Next Generation Wings) and SmartLED (Smart Leading Edge Device) [59].

The proposed concept based on a patent of the Dornier Company has been investigated numerically to simulate the overall system including the skin, substructure and kinematics, as can be seen in Figure 2.28. The results have been used to provide proof of the feasibility of the concept and the need for materials with improved strength for this type of application.

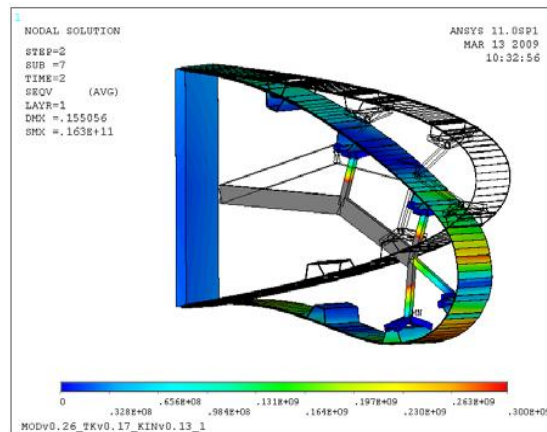


Figure 2.28 Deformed and un-deformed FE model of the smart LE device [59]

2.3 Concluding Remarks on AAW Concepts

Variable camber concepts are well known for their potential advantages; however in most cases the practical implementation difficulties limit the application of the concept for prototypes. The rotating rib concept, even though the results obtained for the rib torque and deflection looks attractive, it can only achieve a camber angle of ± 5 deg.s at a very slow actuation velocity. The linear slides integrated in the ribs and along the trailing edge of this particular design allow smooth deformation of the upper and lower skin.

Considering the piezoelectric trailing edge concept and the smart fin concept, the overall displacement achieved using these configurations in an aerofoil trailing-edge are much small. If a larger displacement is required then the piezoelectric material with larger deflection has to be used. The all moveable vertical tail, uses a change in stiffness in order to achieve a deformation, and this differs from the current research of this project which looks at achieving a flexible trailing edge.

The adaptive flexspar concept, belt rib concept and the concept developed during phase two of the smart wing program can be developed further in order to be integrated to an air vehicle. However, the conformal control surfaces studied during phase one of the smart wing program only generated 1.25° deflection. Similar results are achieved by the reconfigurable aerofoil, where the trailing edge deflections achieved using different materials for the aerofoil skin was a maximum of 6mm. The study carried out during the smart wing phase I stage has been used to validate the seamless control surface technology rather than the power supply and airframe integration. During phase II wind tunnel tests, it has been demonstrated that spanwise deflection of the control surfaces could be accomplished at significant rates.

The AAW project can be considered as the most innovative active aeroelastic wing concepts being employed with the use of both trailing and leading edge control surfaces to benefit from the aeroelastic effect. It uses conventional control surfaces instead of seamless control surfaces. A majority of the concepts discussed in section 2.2 of this report have never been implemented in an air vehicle due to weight increase associated with actuation systems, and lack of efficient structures to deform the structure.

2.4 Aeroelastic Tailoring

Due to its history, aeroelasticity was an effect that was eliminated by adding mass or stiffening a structure. However, in the 1960's an effort was made to include aeroelasticity into the design process. Aeroelasticity is defined as the interaction between aerodynamic forces and elastic forces, and the influence of this interaction on airplane design. Aeroelastic phenomena arise when structural deformations induce additional aerodynamic forces. These additional aerodynamic forces may produce additional structural deformations which induce still greater aerodynamic forces.

These interactions have the potential for instability of the structure that will result in a catastrophic failure, such as from the onset of flutter. Flutter begins from stiffness and frequency changes due to aerodynamic deformation dependent forces and moments. The onset of flutter is seen when modal coupling occurs between the natural torsional and bending modes. This can be seen in Figure 2.29. Elastic deformation of wings due to flight loads can have a profound influence on the performance, handling qualities, flight stability, structural load distribution, and control effectiveness/reversal phenomena.

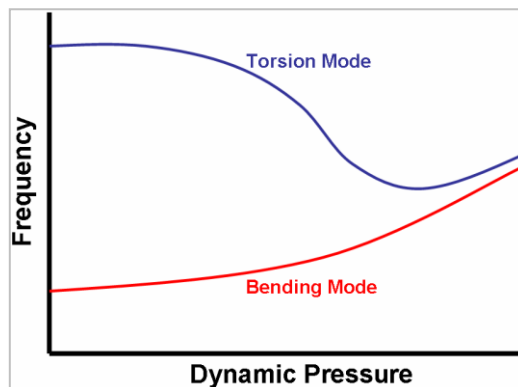


Figure 2.29 Modal Coupling

Composite materials are capable of coupling of the bending and torsional deformations depending on the orientation of the laminate skin. The skin laminate could be oriented in certain directions in order to benefit or adversely affect the deformation. This is commonly known as aeroelastic tailoring. Aeroelastic tailoring is defined as the employment of directional stiffness into aircraft structural design to control static or

dynamic aeroelastic deformations, so that the aerodynamic and structural performances are achieved effectively [60, 61]. Modern day tailoring is achieved by the use of advanced composite materials. The very first ideas for tailored advanced composite structures originated at Fort Worth Division of General Dynamics Corporation [62]. Aeroelastic performance benefit may be achieved through the passive technique of aeroelastic tailoring or active control techniques.

3.2.5 Passive -Aeroelastic Tailoring

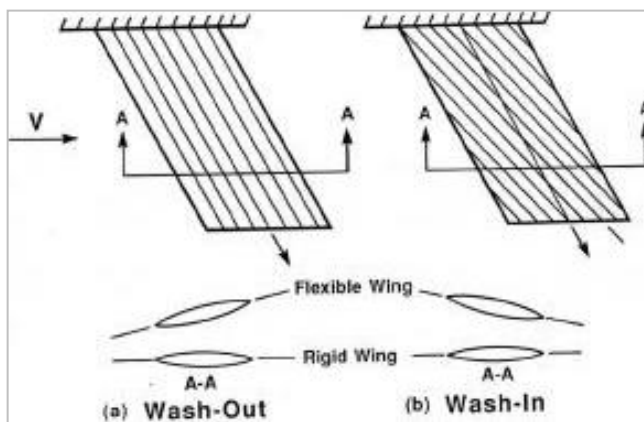


Figure 2.30 Aeroelastic Tailoring [61]

Development of composite materials provided a new way for aeroelastic tailoring research. It was shown that the directional properties of composites could be used to create a coupling between bending and twist deformations depending on the orientation of the laminate skin, this coupling helped achieve shape control [61]. Modern

composite materials could be optimised by controlling the ply orientation so the required strength can be achieved [61]. In section A-A of Figure 2.30 (a) the primary stiffness of the wing is oriented along the wing swept axis. As a wing is subjected to air loads, it induces wing bending most of the time, which in turn creates a nose down twist with respect to the freestream. This is known as “wash-out”. Wash-out characteristics include manoeuvre drag reduction, manoeuvre load relief, and divergence prevention. Laminates orientated as indicated in the A-A section of Figure 2.30 (b) will introduce coupling between bending and torsion so that the wing almost twist in the nose up direction, which creates a “wash-in” effect. Wash-in characteristics include control effectiveness and flutter prevention. The wash-out condition reduces the air load as a result of wing nose down bending, while in wash-in condition part of the air load is added back because the nose up twist accompanies the wing bending. The effect of torsional flexibility on the unswept lifting surface is to significantly change the

spanwise aerodynamic load distribution. Since this elastic torsional rotation will generally increase as the distance from the root (i.e., out along the span), the resultant aerodynamic load distribution will also increase.

The ability to tailor the primary stiffness can reduce aircraft component weight and improve aeroelastic and aircraft performance. However, varying the active composite ply orientations in order to produce twist may make the wings less stiff in bending and lead to higher static deflections and aeroelastic instability, therefore, the design of the active part of the structure should be considered within the overall context of aeroelastic design [62]. As a result a design could be improved aerodynamically i.e. increase in lift and aeroelastically i.e. increased flutter speed. An example of successful innovation with advanced composites and integrated design was the development of the X-29 forward swept wing aircraft [63].

3.2.5 Active - Aeroelastic Control

Rolling maneuvers for an aircraft are conventionally performed by deflecting the trailing edge control surfaces of the wings anti-symmetrically, this will thereby increase lift on one wing while decreasing lift on the other. Flexible wings will see a reduction in roll rate compared to a conventional wing due to the chordwise moment caused by the aerodynamic forces generated by the deflected control surface. As speed increases, a point is reached where roll reversal occurs. In the past, this phenomenon is dealt by increasing the structural stiffness of the wing to avoid roll reversal in the operational flight envelope of the aircraft. Hence traditionally, structural flexibility has been seen as undesirable as it can reduce control effectiveness.

AAW program was one of the first endeavors to address this issue by employing multiple leading and trailing edge control surfaces to twist the wing. Under this program the aeroelastic behavior of the wing has been carried out by examining the effectiveness of the control surfaces at various stiffnesses. The results show that the trailing edge control effectiveness decreased as the dynamic pressure was increased. Furthermore, the trailing edge effectiveness was decreased with reduction in wing torsional stiffness, and

resulted in reduced reversal speed as the wing became more flexible [64]. By contrast, the leading edge stiffness was increased with dynamic pressure increase and torsional stiffness decrease. The results also show that the leading edge effectiveness stays positive unlike the trailing edge effectiveness for a wide range of dynamic pressures. This shows that at the reversal point, the trailing edge alone will not be able to generate the desired roll rate. A number of other studies have been utilising design optimisation methodologies and adaptive changes in torsional stiffness to allow both pre- and post-reversal operation of active aeroelastic wings [65- 68]. They also have shown the benefit of using both leading and trailing edge control surfaces to maximise the roll performance of an aircraft. A leading edge upward control surface deflection will generate an aerodynamic moment on the wing that counteracts the adverse effect of the aerodynamic moment generated by the trailing edge control surface deflection used to increase lift [69]. Platanitis and Strganac [70, 71] have also experimentally validated the concept of using leading edge control to suppress and possibly eliminate control surface reversal.

2.5 AAW Benefits and Challenges

Active Aeroelastic wing technology is a novel way of providing powerful rolling forces for high performance aircraft. AAW technology is more effective with thin, flexible wings and allows the designers more freedom to exploit thin, efficient, higher aspect ratio wing planforms. Potential benefits of applying AAW technology to future air vehicles include substantially increased control power from conventional control surfaces by maintaining their effectiveness, reduced aerodynamic drag through optimum control surface deflections, and reduced structural weight due to reduced stiffness and hinge moment requirements [72]. Other benefits include reduced wing and control surface deflections. These benefits are achieved with an addition of hardware complexity due to integrated actuation mechanisms within the wing structure to deform the wing.

The use of camber morphing on a UAV could lead to significant performance benefits for control and flight efficiency. Additional benefits can be identified as eliminating

control surfaces and gaps associated with these, and their auxiliary equipment. The interest in adaptive structure has led to development of a number of innovative designs over the years, presented so far in this chapter. Through the use of such technology, an UAV will have the capability to perform missions with multiple flight regimes with increased performance, improved efficiency and effectiveness [73]. However, no matter how one chooses to achieve adaptive structures, there are several common engineering challenges. The main challenge out of all is to develop an actuation mechanism which is feasible and more importantly less complex with a high power density. Among the other challenges the key ones are identified as having flexible skins and control law development [74].

2.5.1 Benefits

The main aim of this section is to examine the benefits of using adaptive wing technology. Adaptive technology is hoped to be used to change size and shape of aircraft wings or structures during flight to enable the flight vehicle to change its base performance or characteristics. The primary goal of using such technology is to create a more efficient and more compliant aircraft by changing the size and shape of the aircraft wings to achieve the optimum design for each segment of the vehicle's mission. Conventional aircraft wings are designed as a compromise to suit all mission segments but cannot achieve an optimum configuration for any individual segment. In other words, most aircraft today are optimised for a specific flight condition, i.e., cruise for long range flight for commercial aircraft or high speed short range flight for fighter aircraft. Conventional hinged high lift devices are used during slow flight especially during take-off and landing. Although the current high-lift systems perform well, there is always a need to improve efficiency. Apart from the improved aerodynamic performance, reduction in drag and noise can be achieved by eliminating gaps of these conventional control surfaces [75]. A further reduction in high-lift system complexity could reduce mass and cost. Wlezien [76] states that half the mass and cost of a transport aircraft wing are due to the complexity of the high-lift system which could potentially be replaced by lighter and simpler morphing systems.

As described by Kudva [50] and Bartley-Cho [53], not only aerodynamic performance but also aeroelastic and control of a morphing aircraft can be improved. This results in an enlarged flight envelope and increased manoeuvrability.

To summarise, the University of Bristol morphing wing project [57] states that reasons for applying morphing technologies can be divided into four categories: “1. improve aircraft performance to expand its flight envelope; 2. replace conventional control surfaces for flight control to improve performance and stealth; 3. reduce drag to improve range and; 4. reduce vibration or control flutter” to improve comfort, safety and reduce fatigue.

Aerodynamic Performance

This design concept was studied under the DARPA smart wing phase one program; it uses smart material to design a control surface applicable for morphing aircraft. Smart materials have been integrated into a scaled fighter aircraft wing (a 16% scale model of an F-18 aircraft) to study the impact on the aerodynamic performance [77]. The model consists of SMA torque tubes to actively twist the wing and SMA wires to smoothly deform trailing-edge control surfaces, which are known as conformal control surfaces.

Two flap-to-chord ratios of, 50% and 10%, have been selected for the two-dimensional analysis for an aerofoil with conventional or conformal trailing edge control surface. However, it should be noted that the 0.5c flap is not viable in real life even though used here as an illustrative numerical study. As can be seen from Figure 2.31, the pressure distribution of the conformal control surface does not have the peak at the hinge line compared to the conventional control surface. It also shows that forward of the hinge line the pressure distribution is higher for the conformal control surface.

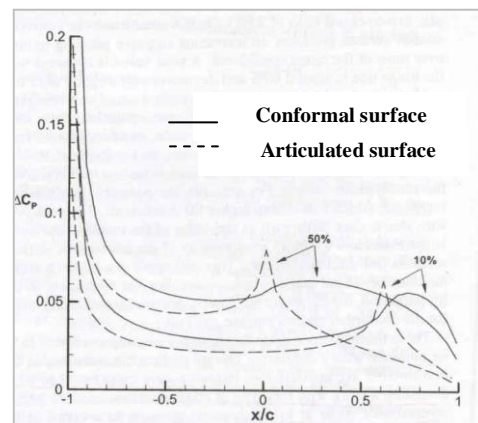


Figure 2.31 Pressure distribution over an aerofoil with two control surfaces and two-flap-to-chord ratios: 10 and 50% [77]

Another notable difference is that the conventional control surface shows a pressure spike due to

the sudden change in the direction of flow. However, for the conformal control surface, the pressure distribution reaches a peak behind the hinge line but does not have a pressure spike associated with it. The higher pressure distribution produced by the conformal control surface will induce a large nose down pitching moment about the elastic axis, which is typically about 30-40% aft of the leading edge. Figure 2.32 shows the aerodynamic coefficients as a function of flap-to-chord ratio, used to evaluate the aerodynamic performance resulting from these pressure distributions. As a result the increase in C_L is approximately 40% for the conformal control surface (see Figure 2.32 (a)). The maximum C_m for an aerofoil with a conventional control surface occurs when the flap-to-chord ratio is around 25%. On the other hand, the conformal control surface produces an increasing negative pitching moment (see Figure 2.32 (b)).

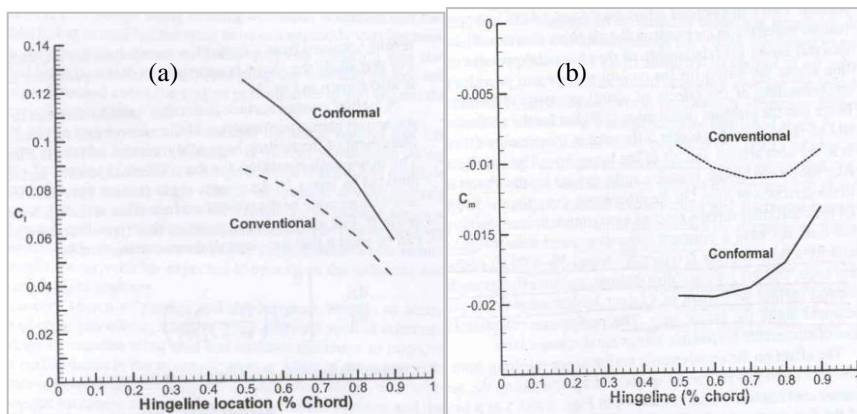


Figure 2.32 (a) C_L and (b) C_m comparisons of conventional and conformal surfaces [77]

The pressure distribution for higher order deflection shapes of the conformal control surface are shown in Figure 2.33 (b). As can be seen from Figure 2.33 (b), the higher order deformation of the control surface results in an increase in the pressure distribution, which leads to a higher C_L and shift the peak pressure point further aft.

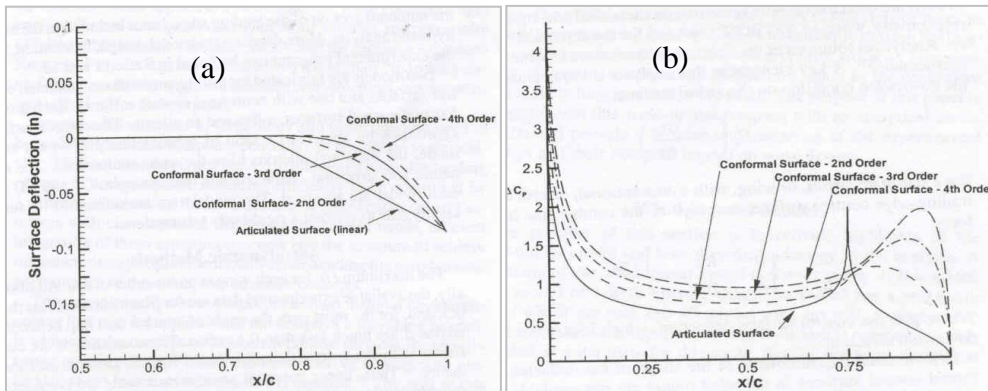


Figure 2.33 Conformal control surface shapes [77]

Roll Performance

Many researchers have investigated the effect of multiple control surfaces on roll performance and shown the benefits of having flexible leading- and trailing-edge control surfaces [64, 78-80]. Anderson, Forster, Kolonay and Eastep [64] carried out a study to investigate the use of multiple control surfaces effect on the roll performance of an aircraft. Analytical models of a rectangular wing and a fighter aircraft have been used as an example for steady aeroelastic and antisymmetric trim analyses. A control surface effectiveness study has been carried out for rigid and flexible wing models with both leading and trailing edge control surfaces (see Figure 2.34).

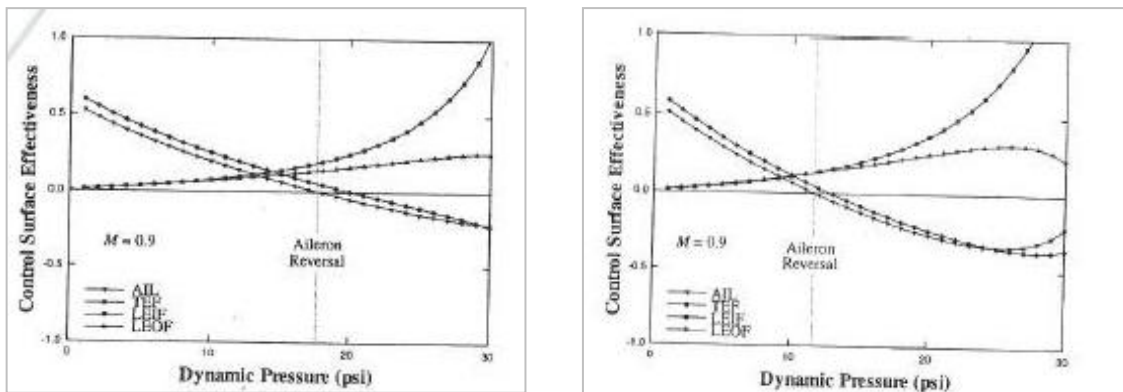


Figure 2.34 Control Effectiveness of (a) Rigid; and (b) Flexible Wing Models [64]

It can be seen from Figure 2.34 (a) that the trailing-edge flap and inboard leading-edge control surfaces had higher effectiveness than the outboard control surfaces. This is because the inboard surfaces had a much larger surface area compared to the outboard

surfaces. It is also evident that with increasing speed there was an increase in effectiveness of the leading-edge control surfaces and a decrease in effectiveness of the trailing-edge. Figure 2.34 (b) shows a similar plot generated for a reduced stiffness model with 50% wing torsional and bending stiffness of the original wing model. The trends are similar to those of the original wing model. However, the most noticeable difference is that at higher speeds the control effectiveness for the reduced stiffness wing model was higher than that of the original stiffness model. Similarly, for high speeds, the trailing-edge control surfaces had lower control effectiveness than the original stiffness model.

It has also been shown that the capability to achieve trim for the reduced stiffness model with a single aileron was substantially diminished with increasing speed. However, the multiple control surfaces proved to be effective throughout the entire flight speeds. Large deflections were seen at reversal point. The most noticeable benefit of the reduced stiffness model was the resulting significantly small control surface deflections beyond reversal speed.

The results obtained demonstrate that an increase in lift can be obtained through a conformal control surface and increase in roll performance could be obtained as well.

2.5.2 Challenges

These new adaptive concepts will come with a penalty that must be analysed in terms of the total mission performance [81, 82]. The actuation mechanisms realised within the wing structure will carry additional weight and would demand more from additional actuators to physically deform the wing. However, the main question which must be determined in terms of the overall design is that will the improved aerodynamics created by an adaptive concept offset the penalties associated with the additional weight and energy consumption yield a more optimum design?

3 Theoretical Background

This chapter initially deals with the micromechanical properties of composites, which is very important in the design analysis. The successful prediction of dynamic characteristics of a structure like an aircraft wing depends on adequate knowledge of the static structural properties such as bending, torsional and bending-torsion coupling stiffnesses. The material properties of isotropic materials, such as Young's modulus and shear modulus, are independent of the cross-section of the structure and the loading conditions and thus the rigidity properties depend on the geometrical properties of the cross section. In the case of composite materials, the material and, in consequence the rigidity properties vary with the fibre orientation, the stacking of the plies, the geometrical properties of the cross-section, and loading conditions. Thus, an alternative and as it turns out, more complicated theoretical analysis is required to predict the rigidity properties of a composite structure.

The wing structural analysis was then carried out by replacing the actual structure with an idealised approximated model. At the preliminary stage, the design process of the structure can be carried out using simple models. However, at some stage of the design, an accurate estimate of component loads and stresses is needed and in this case the idealised structure must be a close representation of the actual structure. At this stage, simplified models and methods become inadequate as they cannot cope with the necessary degrees of complexity. The finite element method was then used to analyse complex continuous structures.

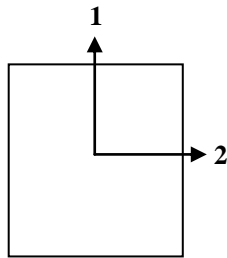
In the finite element method, matrix method of analysis is applied to determine forces and displacements of the continuous structures idealised by a number of elements interconnected at the nodes. Commercially available software has made this analysis method more accessible. The subsequent sections present the approach used by the finite element software package MSC/NASTRAN to carry out linear static and dynamic analyses.

3.1 Hooke's Law for Anisotropic Materials

3.1.1 Normal Stress and Strain

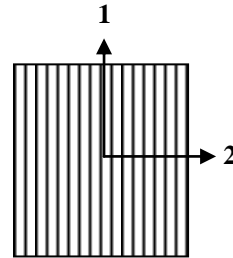
Normal stress is defined as the force per unit area acting perpendicular to the surface of the area. The corresponding strain is defined as the elongation per unit length of material in the direction of the applied force. For isotropic materials the stress-strain relationship is independent of the direction of force, thus only one elastic modulus is used to describe the stress-strain relationship for a uniaxially applied force. For an anisotropic material, at least two elastic moduli are needed to describe the stress-strain behaviour of the material.

Isotropic Plate



Stiffness in 1-direction = stiffness in 2-direction = stiffness in any direction

Orthotropic Plate



Stiffness in 1-direction \gg stiffness in 2-direction \neq stiffness in any direction

Figure 3.1 Difference between an isotropic and orthotropic plate.

Regardless of direction of the applied load, the stiffness of an isotropic material can be described by one elastic modulus, E , of the material. The stiffness of the orthotropic material must be described by two values, one along the longitudinal direction of the fibres, and one transverse to the direction of fibres, commonly referred to as E_1 and E_2 respectively. Thus, indices are added to the stress, strain and modulus values to describe the direction of the applied force. For an isotropic material, the stress-strain relationship is given as:

$$\sigma = E\varepsilon \quad (3.1)$$

For the orthotropic system, the direction must be specified, such as:

$$\sigma_1 = E_1\varepsilon_1 \text{ or } \sigma_2 = E_2\varepsilon_2 \quad (3.2)$$

3.1.2 Stress and Strain for Specially Orthotropic Plates

If the applied load acts either parallel or perpendicular to the fibres, then the plate is considered to be specially orthotropic. In general, plates will experience stresses in more than one direction within the plane. This stress is referred to as plane stress. In addition Poisson's ratio becomes more important. Poisson's ratio is the ratio of strain perpendicular to a given loading direction and the strain parallel to this given loading direction.

$$\begin{aligned} \text{Poisson's ratio (for loading along fibres)} &= \nu_{12} = \frac{\varepsilon_2}{\varepsilon_1} \text{ or} \\ \text{(for loading perpendicular to the fibres)} &= \nu_{21} = \frac{\varepsilon_1}{\varepsilon_2} \end{aligned} \quad (3.3)$$

Hence strain due to an applied force can be defined as:

$$\varepsilon_1 = \frac{\sigma_1}{E_1} - \nu_{21}\varepsilon_2 \text{ and } \varepsilon_2 = \frac{\sigma_2}{E_2} - \nu_{12}\varepsilon_1 \quad (3.4)$$

This includes the contraction of Poisson's effect due to another force perpendicular to the applied force. Eq. (3.4) can be redefined using Eq. (2) as:

$$\varepsilon_1 = \frac{\sigma_1}{E_1} - \nu_{21} \frac{\sigma_2}{E_2} \text{ and } \varepsilon_2 = \frac{\sigma_2}{E_2} - \nu_{12} \frac{\sigma_1}{E_1} \quad (3.5)$$

Similarly, if shear forces are present, shear stress and shear strain can be expressed using the shear modulus, G .

$$\tau_{12} = \gamma_{12}G_{12} \quad (3.6)$$

Where τ_{12} is the shear stress (the 1 and 2 indices indicates shear in 1-2 plane), and γ_{12} is the shear strain.

The relationship between the moduli and Poisson's ratio is defined as:

$$\nu_{21}E_1 = \nu_{12}E_2 \quad (3.7)$$

Eq. (3.5) and (3.6) can now be combined and written in matrix form as:

$$\begin{bmatrix} \varepsilon_1 \\ \varepsilon_2 \\ \gamma_{12} \end{bmatrix} = \begin{bmatrix} S_{11} & S_{12} & 0 \\ S_{12} & S_{22} & 0 \\ 0 & 0 & S_{66} \end{bmatrix} \begin{bmatrix} \sigma_1 \\ \sigma_2 \\ \tau_{12} \end{bmatrix} \quad (3.8)$$

where,

$$\begin{aligned}
S_{11} &= 1/E_1 & S_{22} &= 1/E_2 \\
S_{12} &= -\nu_{12}/E_1 = -\nu_{21}/E_2 & S_{66} &= 1/G_{12}
\end{aligned}
\tag{3.9}$$

The 3x3 matrix in Eq. (3.8) is commonly called the compliance matrix. The 3,3 position has subscripts 6,6 from a detailed treatment of arriving at a constitutive equation for an orthotropic material from an anisotropic one.

The compliance matrix can be inverted to get the stress as a function of strain. This inverted matrix is commonly known as the reduced stiffness matrix and is denoted by $[Q]$.

$$\begin{bmatrix} \sigma_1 \\ \sigma_2 \\ \tau_{12} \end{bmatrix} = \begin{bmatrix} Q_{11} & Q_{12} & 0 \\ Q_{12} & Q_{22} & 0 \\ 0 & 0 & Q_{66} \end{bmatrix} \begin{bmatrix} \varepsilon_1 \\ \varepsilon_2 \\ \gamma_{12} \end{bmatrix}
\tag{3.10}$$

where,

$$\begin{aligned}
Q_{11} &= \frac{E_1}{1 - \nu_{12}\nu_{21}} & Q_{11} &= \frac{E_2}{1 - \nu_{12}\nu_{21}} \\
Q_{12} &= \frac{\nu_{12}E_2}{1 - \nu_{12}\nu_{21}} = \frac{\nu_{21}E_1}{1 - \nu_{12}\nu_{21}} & Q_{66} &= G_{12}
\end{aligned}
\tag{3.11}$$

3.1.3 ***Stress and Strain for Generally Orthotropic Plates***

Now suppose that the unidirectional lamina in Figure 3.1 is loaded at some angle other than 0° or 90° . The lamina is now referred to as generally orthotropic. In this case the loading direction does not coincide with the principal material directions. The stresses and strains must now be transformed into coordinates that do coincide with the principal material directions. This can be accomplished using the free-body diagram in Figure 3.2

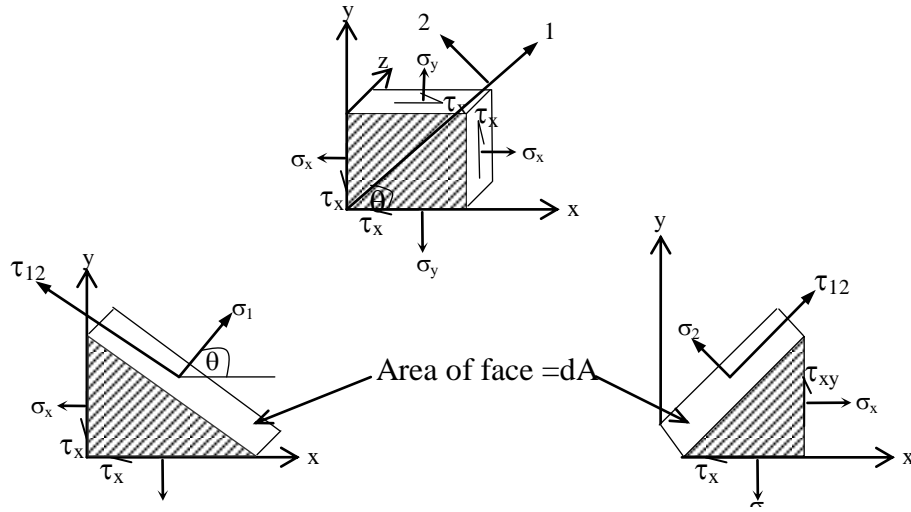


Figure 3.2 Generally Orthotropic Lamina.

$$\begin{bmatrix} \sigma_1 \\ \sigma_2 \\ \tau_{12} \end{bmatrix} = \begin{bmatrix} \cos^2 \theta & \sin^2 \theta & 2 \sin \theta \cos \theta \\ \sin^2 \theta & \cos^2 \theta & -2 \sin \theta \cos \theta \\ -\sin \theta \cos \theta & \sin \theta \cos \theta & (\cos^2 \theta - \sin^2 \theta) \end{bmatrix} \begin{bmatrix} \sigma_x \\ \sigma_y \\ \tau_{xy} \end{bmatrix} \quad (3.12)$$

The 3x3 matrix in Eq. (3.12) is commonly known as the transformation matrix and is denoted by $[T]$. the same matrix can be used to transform strains. In order to transform from 1-2 coordinate system to the x-y coordinate system, the inverse of $[T]$ is used and this is given as:

$$[T]^{-1} = \begin{bmatrix} \cos^2 \theta & \sin^2 \theta & -2 \sin \theta \cos \theta \\ \sin^2 \theta & \cos^2 \theta & 2 \sin \theta \cos \theta \\ \sin \theta \cos \theta & -\sin \theta \cos \theta & (\cos^2 \theta - \sin^2 \theta) \end{bmatrix} \quad (3.13)$$

Thus:

$$\begin{bmatrix} \sigma_1 \\ \sigma_2 \\ \tau_{12} \end{bmatrix} = [T] \begin{bmatrix} \sigma_x \\ \sigma_y \\ \tau_{xy} \end{bmatrix} \quad \text{and} \quad \begin{bmatrix} \sigma_x \\ \sigma_y \\ \tau_{xy} \end{bmatrix} = [T]^{-1} \begin{bmatrix} \sigma_1 \\ \sigma_2 \\ \tau_{12} \end{bmatrix} \quad (3.14)$$

Similarly for strain:

$$\begin{bmatrix} \epsilon_1 \\ \epsilon_2 \\ \epsilon_{12} \end{bmatrix} = [T] \begin{bmatrix} \epsilon_x \\ \epsilon_y \\ \epsilon_{xy} \end{bmatrix} \quad \text{and} \quad \begin{bmatrix} \epsilon_x \\ \epsilon_y \\ \epsilon_{xy} \end{bmatrix} = [T]^{-1} \begin{bmatrix} \epsilon_1 \\ \epsilon_2 \\ \epsilon_{12} \end{bmatrix} \quad (3.15)$$

Substituting Eq. (3.10) into the second part of Eq. (3.14):

$$\begin{bmatrix} \sigma_x \\ \sigma_y \\ \tau_{xy} \end{bmatrix} = [T]^{-1} [Q] \begin{bmatrix} \varepsilon_1 \\ \varepsilon_2 \\ \gamma_{12} \end{bmatrix} = [T]^{-1} [Q] \begin{bmatrix} 1 & 0 & 0 \\ 0 & 1 & 0 \\ 0 & 0 & 2 \end{bmatrix} \begin{bmatrix} \varepsilon_1 \\ \varepsilon_2 \\ \varepsilon_{12} \end{bmatrix} \quad (3.16)$$

Now substituting the first part of Eq. (3.15) into Eq. (3.16) gives:

$$\begin{bmatrix} \sigma_x \\ \sigma_y \\ \tau_{xy} \end{bmatrix} = [T]^{-1} [Q] \begin{bmatrix} 1 & 0 & 0 \\ 0 & 1 & 0 \\ 0 & 0 & 2 \end{bmatrix} [T] \begin{bmatrix} \varepsilon_x \\ \varepsilon_y \\ \varepsilon_{xy} \end{bmatrix} \quad (3.17)$$

Which gives rise to a new matrix called the lamina stiffness matrix, commonly denoted as $[\bar{Q}]$ and is defined as:

$$[\bar{Q}] = [T]^{-1} [Q] \begin{bmatrix} 1 & 0 & 0 \\ 0 & 1 & 0 \\ 0 & 0 & 2 \end{bmatrix} [T] \quad (3.18)$$

Letting $m = \cos \theta$ and $n = \sin \theta$, the components of matrix $[\bar{Q}]$ are:

$$\begin{aligned} \bar{Q}_{11} &= Q_{11}m^4 + 2(Q_{12} + 2Q_{66})m^2n^2 + Q_{22}n^4 \\ \bar{Q}_{12} &= (Q_{11} + Q_{22} - 4Q_{66})m^2n^2 + Q_{12}(m^4 + n^4) \\ \bar{Q}_{22} &= Q_{11}n^4 + 2(Q_{12} + 2Q_{66})m^2n^2 + Q_{22}m^4 \\ \bar{Q}_{16} &= (Q_{11} - Q_{12} - 2Q_{66})m^3n + (Q_{12} - Q_{22} + 2Q_{66})mn^3 \\ \bar{Q}_{26} &= (Q_{11} - Q_{12} - 2Q_{66})n^3m + (Q_{12} - Q_{22} + 2Q_{66})nm^3 \\ \bar{Q}_{66} &= (Q_{11} + Q_{22} - 2Q_{12} - 2Q_{66})m^2n^2 + Q_{66}(m^4 + n^4) \end{aligned} \quad (3.19)$$

If θ is any angle other than zero, there will be nonzero $[\bar{Q}_{16}]$ and $[\bar{Q}_{26}]$ terms.

Substituting this into Eq. (3.17) gives:

$$\begin{bmatrix} \sigma_x \\ \sigma_y \\ \tau_{xy} \end{bmatrix} = \begin{bmatrix} \bar{Q}_{11} & \bar{Q}_{12} & 2\bar{Q}_{16} \\ \bar{Q}_{12} & \bar{Q}_{22} & 2\bar{Q}_{26} \\ \bar{Q}_{16} & \bar{Q}_{26} & 2\bar{Q}_{66} \end{bmatrix} \begin{bmatrix} \varepsilon_x \\ \varepsilon_y \\ \varepsilon_{xy} \end{bmatrix}, \quad \begin{bmatrix} \sigma_x \\ \sigma_y \\ \tau_{xy} \end{bmatrix} = \begin{bmatrix} \bar{Q}_{11} & \bar{Q}_{12} & \bar{Q}_{16} \\ \bar{Q}_{12} & \bar{Q}_{22} & \bar{Q}_{26} \\ \bar{Q}_{16} & \bar{Q}_{26} & \bar{Q}_{66} \end{bmatrix} \begin{bmatrix} \varepsilon_x \\ \varepsilon_y \\ \gamma_{xy} \end{bmatrix} \quad (3.20)$$

It can be seen that a shear strain will produce normal stresses, and normal strains will contribute to a shear stress. This is referred to as extension-shear coupling and will take place in a lamina that is loaded at an angle to the fibres (other than 0° and 90°). There will be coupling if the $[\bar{Q}_{16}]$ and/or $[\bar{Q}_{26}]$ terms in the lamina stiffness matrix are nonzero.

From the derivation presented in Appendix H, the following constitutive relation for the laminate can be defined:

$$\begin{bmatrix} N_x \\ N_y \\ N_{xy} \\ M_x \\ M_y \\ M_{xy} \end{bmatrix} = \begin{bmatrix} A_{11} & A_{12} & A_{16} & B_{11} & B_{12} & B_{16} \\ A_{12} & A_{22} & A_{26} & B_{12} & B_{22} & B_{26} \\ A_{16} & A_{26} & A_{66} & B_{16} & B_{26} & B_{66} \\ B_{11} & B_{12} & B_{16} & D_{11} & D_{12} & D_{16} \\ B_{12} & B_{22} & B_{26} & D_{12} & D_{22} & D_{26} \\ B_{16} & B_{26} & B_{66} & D_{16} & D_{26} & D_{66} \end{bmatrix} \begin{bmatrix} \varepsilon_X^0 \\ \varepsilon_Y^0 \\ \gamma_{XY}^0 \\ K_X \\ K_Y \\ K_{XY} \end{bmatrix} \quad (3.21)$$

Where $[A]$, $[B]$ and $[D]$ matrices are the laminate stiffness matrix and are defined in terms of the ply stiffness as:

$$A_{ij} = \sum_{k=1}^n [\bar{Q}_{ij}]_k (h_k - h_{k-1}) \quad (3.22)$$

$$B_{ij} = \frac{1}{2} \sum_{k=1}^n [\bar{Q}_{ij}]_k (h_k^2 - h_{k-1}^2) \quad (3.23)$$

$$D_{ij} = \frac{1}{3} \sum_{k=1}^n [\bar{Q}_{ij}]_k (h_k^3 - h_{k-1}^3) \quad (3.24)$$

Written in contracted form, Eq. (3.21) becomes:

$$\begin{bmatrix} N \\ M \end{bmatrix} = \begin{bmatrix} A & B \\ B & D \end{bmatrix} \begin{bmatrix} \varepsilon^0 \\ K \end{bmatrix} \quad (3.25)$$

The [A] matrix is the extensional stiffness matrix relating the in-plane stress resultants to the mid-surface strains and the [D] matrix is the flexural stiffness matrix relating the stress couples to the curvatures. Since the [B] matrix relates stress couples to mid-surface strains and stress resultants to curvatures, it is called the bending-stretching coupling matrix. A laminated structure can have bending-stretching coupling even if the lamina are isotropic. Only for symmetric laminates, where the geometric midplane is also the neutral plane of the plate, the [B] matrix will have all elements equal to zero. However, if the laminate is unsymmetric, then the geometric midplane will not be the neutral plane of the plate. In this case the [B] matrix will have some nonzero elements.

3.2 In-Plane modulus for the Laminate

For a given stacking sequence of lamina whose material properties are known, it is possible to determine the in-plane bending constants of the laminate from the [A] matrix for symmetric laminates, and the [A], [B] and [D] matrices for unsymmetric laminates. In order to evaluate the x -direction modulus, the value of the x -direction stress to the x -direction strain must be calculated. In Equation form:

$$E_x = \frac{\sigma_x}{\varepsilon_x} = \frac{N_x / h}{\varepsilon_x} \quad (3.26)$$

Where h is the thickness of the laminate and N_x can be obtained using Eq. (3.43). Hence the modulus in x -direction for symmetric and unsymmetric laminates can be obtained using the [A] matrix and the [A], [B] and [D] matrices respectively.

The theory presented in sections 3.1 and 3.2 are the basics behind both in-house and finite element tools that have been used in this study to evaluate stresses of the wing box structure. For stress analysis, an in-house developed program TWBox based on the thin-walled structure stress analysis method presented was employed. Additional structural components such as stringers were included in the wing structure model. The resulting stress distribution over the wing at root section was used to evaluate the local

force acting on the skin laminate at the critical region. Based on the force, the detail stress and failure index in each ply of the skin laminate were calculated based on the composite laminate theory [83]. In addition, MSC PATRAN/NASTRAN code was also employed to evaluate the stresses in the structure under the aerodynamic loads. Detail structural components such as stringers and ribs were also included in the SAW FE model.

3.3 Stress Analysis of Stiffened Thin-Walled Beams Using the TWbox Program

The structures considered so far consisted of simple plates, however in aircraft structures most panels are reinforced by stiffeners. In order to simplify the analysis of these structures, it can be assumed that the shear loads are carried by the skins only; while the direct stresses are mainly carried by the stringers. Since the stress is constant across the stringer cross section it is possible to replace them with a concentrated area known as booms located along the mid line of the skin [84]. Figure 3.3 shows how a typical wing structure can be idealised for analysis simplification.

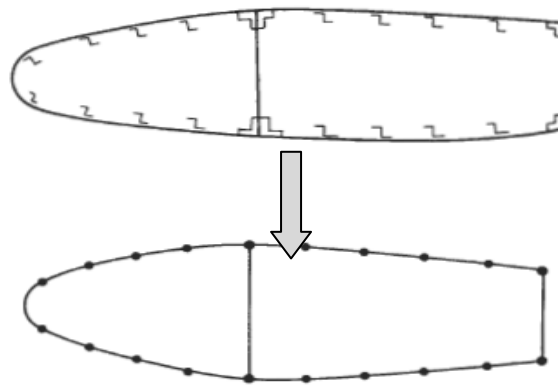


Figure 3.3 Idealisation of wing section [84]

The direct stress carrying capability of the skin can be taken into account by increasing the area of each boom by an area equivalent of the direct stress carrying capacity of the adjacent skin panels. Figure 3.4 (a) shows the actual stress distribution in an arbitrary panel while Figure 3.4 (b) shows how this distribution would be idealised when considering a structure made of panels and booms.

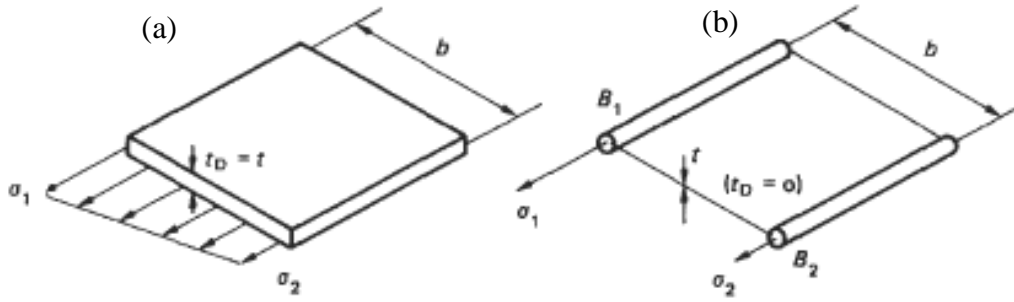


Figure 3.4 Idealisation of a panel [84]

In Figure 3.4 (a) the direct stress carrying thickness t_D is equal to the actual thickness t while in Figure 3.4 (b) $t_D = 0$. In the actual panel the direct stress distribution in the actual panel varies linearly from an unknown value σ_1 to an unknown value σ_2 . In the idealised panel this distribution is lost, however the direct stress in both panels must be the same. By equating the moments due to the direct stresses it is possible to obtain expressions for the boom areas B_1 and B_2 . Thus, taking moments about the right-hand edge of each panel:

$$\sigma_2 t_D \frac{b^2}{2} + \frac{1}{2} (\sigma_1 - \sigma_2) t_D b \frac{2}{3} b = \sigma_1 B_1 b \quad (3.27)$$

Hence

$$B_1 = \frac{t_D b}{6} \left(2 + \frac{\sigma_2}{\sigma_1} \right) \quad (3.28)$$

Similarly

$$B_2 = \frac{t_D b}{6} \left(2 + \frac{\sigma_1}{\sigma_2} \right) \quad (3.29)$$

In Eq. (3.28) and (3.29) the ratio of σ_1 and σ_2 , if unknown can be frequently assumed. The direct stress distribution in Figure 3.4 (a) is caused by a combination of axial load and bending moment. For axial load only $\sigma_1/\sigma_2 = 1$ and $B_1 = B_2 = t_D b/2$; for a pure bending moment $\sigma_1/\sigma_2 = -1$ and $B_1 = B_2 = t_D b/6$. Thus, different idealisations of the same structure are required for different loading conditions.

This skin and boom idealisation was employed to develop the TWbox program [85] which calculates the shear and direct stresses of stiffened composite single and double cell thin-walled beams. This program also allows analysing both constant cross section and tapered beams. The inputs required by the program are

- Number of booms
- Booms xy coordinate at the two ends of the beam
- Booms area
- Equivalent elastic modulus of the laminated composite
- In plane forces and torque applied

Using these data the program calculates the beam bending stiffness, the direct stress in the booms, the cross section basic shear flow and the shear stress in each section of the panels. This program is a useful tool when setting the initial sizes of a composite wing, in particular to assess whether the strength of the stiffened skin is enough to support the applied aerodynamic loadings.

3.4 Finite Element Approach used in MSC NASTRAN/PATRAN

The linear static approach implemented in MSC NASTRAN/PATRAN is illustrated in Figure 3.5.

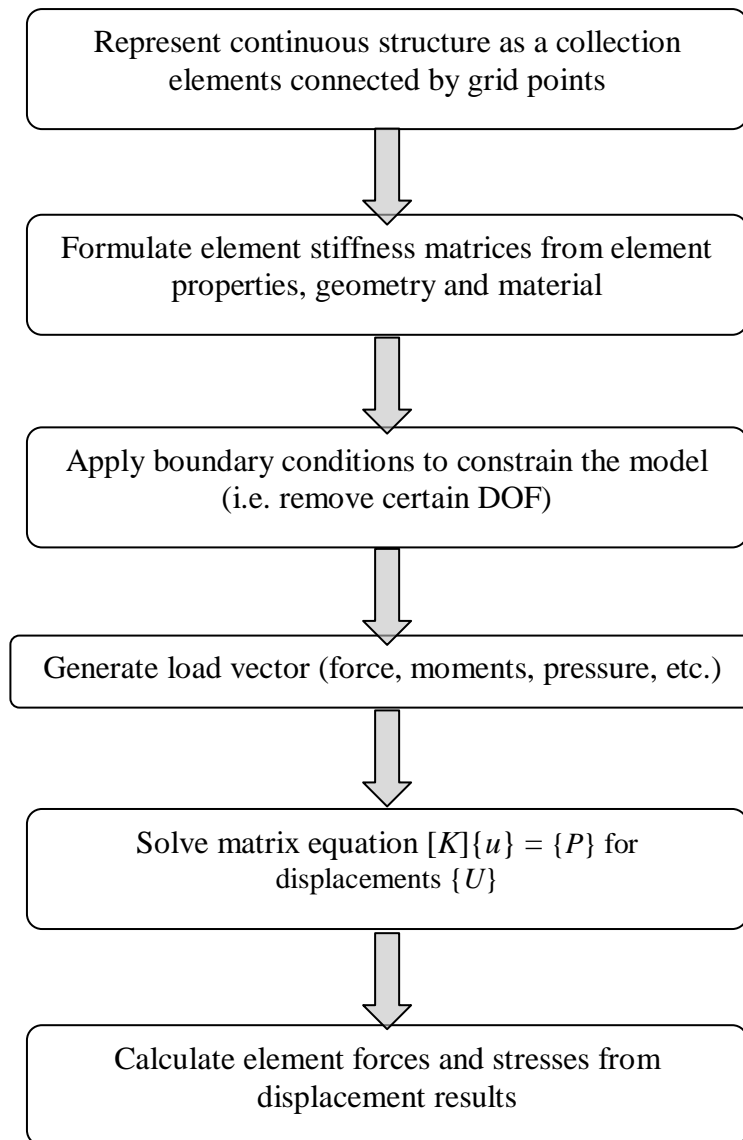


Figure 3.5 Linear static analysis

3.5 Anisotropic Thin-Walled Closed Section Beam Stiffness

The stiffness of a structure can be defined as the resistance to the displacement as an unbalanced system of forces and moments are applied to the structure. It mainly depends on the material properties and geometry of the structure. Therefore, a desired amount of

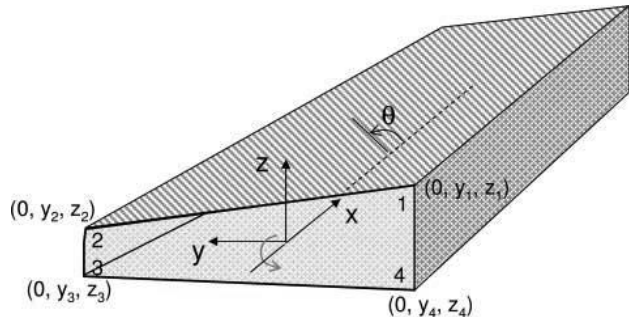


Figure 3.6 Cross-sectional details of the wing box.

stiffness can be achieved by selecting a range of materials and varying the geometrical parameters such as size and shape of the cross-section. In composite materials the fibre orientation and the stacking sequence paves way to a wider number of possibilities in achieving a particular stiffness. For thin-walled beams, bending stiffness EI , torsional stiffness GJ , extensional stiffness EA , and warping stiffness EF are often considered. In composite materials, the bend-twist coupling stiffness K for symmetric laminates and extension twist coupling K_{pa} for anti-symmetric laminates are added as additional stiffness. The accurate determination of the above stiffness will have a greater influence on determination of the dynamic behaviour of the wing structure.

In this investigation, a full-scale sweep back rectangular wing model is created for a small UAV. The wing structure is made of the front and rear spars, ribs and stringer reinforced skins. Based on the SAW design concept (from Chapter 4), most of the load on the flexible TE section is transferred to the rear spar through the curved beam. Since the wing box enclosed by the spars is the main load carrier, the modelling and analysis is focused on the wing box structure. In the structural model, the wing box was divided into a number of spanwise segments and each of them was modelled as a uniform thin-walled single-cell box beam as illustrated in Figure 3.6, and the whole wing structure was modelled as an assembly of those box beams.

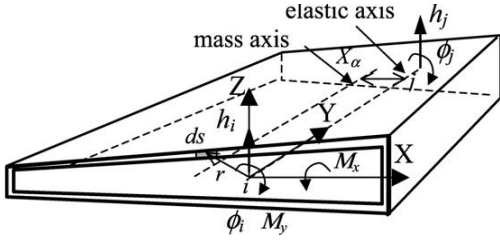


Figure 3.7 A spanwise wing box segment modelled as a beam element.

Based on the analytical method by Armanios and Badir [86, 87], a relationship between the bending moment M_x , torque M_y and the transverse and twist deflections at the end of an anisotropic thin-walled closed-section beam, as shown in Figure 3.7 are expressed below.

$$M_y = C_{22}\phi' + C_{23}h'' \quad \text{and} \quad M_x = C_{23}\phi' + C_{33}h'' \quad (3.30)$$

The stiffness coefficients C_{ij} of each segment can be calculated based on its geometry and material properties and integration along its cross sectional circumference,

$$C_{22} = \frac{A_e^2}{\oint (1/C(s)) ds} ; \quad C_{23} = -A_e \frac{\oint (B(s)/C(s)) z ds}{\oint (1/C(s)) ds}$$

$$C_{33} = \oint \left(A(s) - \frac{B(s)^2}{C(s)} \right) z^2 ds + \frac{\left[\oint (B(s)/C(s)) z ds \right]^2}{\oint (1/C(s)) ds} \quad (3.31)$$

where A_e is the enclosed area of the cross section; parameters $A(s)$, $B(s)$ and $C(s)$ are given below.

$$A(s) = A_{11} - \frac{(A_{12})^2}{A_{22}} ; \quad B(s) = 2 \left(A_{16} - \frac{A_{12}A_{26}}{A_{22}} \right) ; \quad C(s) = 4 \left[A_{66} - \frac{(A_{26})^2}{A_{22}} \right] \quad (3.32)$$

In the above equations, A_{ij} are the coefficients of stiffness matrix $[A]$ of the composite skin and spar webs of the closed-section beam derived in section 3.2.2. According to the force-deflection relationships in Eq. (3.30) and stiffness definition, the stiffness coefficients C_{33} , C_{22} and C_{23} actually represent the bending, torsion and bending-torsion coupling rigidities of the wing box beam, which are usually, expressed by symbols EI , GJ and K respectively. Contribution of the six stringers to the wing box bending stiffness is also included in the model.

3.6 Free Vibration analysis

3.6.1 Dynamic Stiffness Method

The dynamic stiffness matrix method [88, 89] was subsequently used for the vibration analysis and flutter analysis. In this method, the equations of motion for each of the thin-walled box beams were represented as follows, where the bending-torsion stiffness coupling was included but the transverse shear deformation and warping effect were neglected.

$$EI \cdot h'''' + CK \cdot \phi''' + m \cdot \ddot{h} - m \cdot X_\alpha \cdot \ddot{\phi} = 0 \quad (3.33)$$

$$GJ \cdot \phi'' + CK \cdot h''' + m \cdot X_\alpha \cdot \ddot{h} - I_p \cdot \ddot{\phi} = 0 \quad (3.34)$$

where $h'''' = \partial^4 h / \partial y^4$, $\ddot{h} = \partial^2 h / \partial t^2$, $\phi''' = \partial^3 h / \partial y^3$ and $\ddot{\phi} = \partial^2 h / \partial t^2$. By solving the differential equations, an exact solution for the transverse displacement $h(y)$ and twist $\phi(y)$ can be obtained. A dynamic stiffness matrix for a box beam can be subsequently created by relating the displacements to the bending moment and torque at both ends of the beam. A dynamic stiffness matrix for the whole wing box structure is obtained by assembling all the wing box beam stiffness matrices along the wing span direction.

3.6.2 Evaluation of Natural Modes and Frequencies

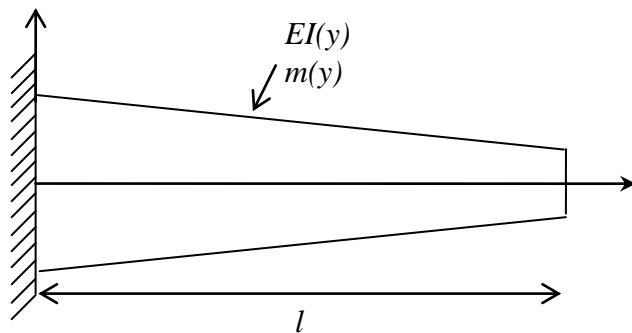


Figure 3.8 Cantilever Beam with Arbitrary Spanwise Properties

The deformation of a continuous structure under dynamic loads can be expressed in terms of natural modes and frequencies of vibration. Except in some cases, these cannot be determined exactly, instead approximate methods have been used for their computation. An

actual aircraft structure is continuous system with an infinite number of degrees of freedom. This means there are infinite number of natural modes and frequencies. The

approximation methods can give approximations only to a relatively small number of lower modes and their associated frequencies. These methods are divided into three groups, according to the manner which the problem is formulated: energy methods, integral equation methods, and differential equation methods. The Rayleigh-Ritz method [90] which is an energy method has been used to derive the expressions for natural modes and frequencies.

The natural modes and frequencies are derived from Lagrange's equation which is expressed in terms of the kinetic, T and strain, U energies as:

$$\frac{d}{dt} \left(\frac{\partial T}{\partial \dot{q}_r} \right) - \frac{\partial T}{\partial q_r} + \frac{\partial U}{\partial q_r} = Q_r \quad (3.35)$$

Lagrange's equation in this form can be used as a substitute for the more fundamental principle of virtual work as a means of writing the differential equations of equilibrium of a system whose configuration can be expressed in terms of generalised coordinates.

Since there are no external forces applied to the beam except at fixed constraints where they do no work, and since the beam is considered to be perfectly elastic, Eq. (3.35) can be further simplified by putting $\partial T / \partial q_r = Q_r = 0$:

$$\frac{d}{dt} \left(\frac{\partial T}{\partial \dot{q}_r} \right) + \frac{\partial U}{\partial q_r} = 0 \quad (3.36)$$

Lagrange's equation is applied by approximating the deformation of the structure in such a way that it can be described in terms of a finite number of generalised coordinates q_1, \dots, q_n . Considering the case of a restrained cantilever beam with varying cross section, as shown by Figure 3.8, the deflection curve of the neutral axis can be expressed as:

$$w(y, t) = \sum_{i=1}^n \phi_i(y) q_i(t) \quad (3.37)$$

The functions $\phi_i(y)$ are assumed displacement functions that satisfy the geometrical boundary conditions $\phi_i(0) = \phi_i'(0) = 0$, and they are selected so that a good approximation to each of the required natural modes can be obtained by superposition. The quantities

$q_i(t)$ are the generalised coordinates representing the contribution of each of the assumed functions.

Neglecting rotary inertia effects, the kinetic energy of the slender beam is given by:

$$T = \frac{1}{2} \int_0^l m(y) \dot{w}^2(y, t) dy \quad (3.38)$$

The dot indicates indicate differentiations with respect to time.

Neglecting shear deformation, the strain energy of a slender beam can be expressed in terms of the bending stiffness, as follows:

$$U = \frac{1}{2} \int_0^l EI(y) (w''(y, t))^2 dy \quad (3.39)$$

The primes indicate differentiations with respect to y .

The first term of the simplified Lagrange's Eq. (3.36) can be obtained by differentiating under the integral of Eq. (3.38).

$$\frac{\partial T}{\partial \dot{q}_r} = \int_0^l m(y) \dot{w}(y, t) \frac{\partial \dot{w}(y, t)}{\partial \dot{q}_r} dy$$

Substituting Eq. (3.37) we obtain:

$$\frac{\partial T}{\partial \dot{q}_r} = \int_0^l m(y) \left[\sum_{i=1}^n \phi_i(y) \dot{q}_i \right] \phi_r(y) dy$$

Further simplification gives:

$$\begin{aligned} \frac{\partial T}{\partial \dot{q}_r} &= \sum_{i=1}^n \dot{q}_i \int_0^l m(y) \phi_r(y) \phi_i(y) dy \\ &= \sum_{i=1}^n m_{ri} \dot{q}_i \end{aligned}$$

in which

$$m_{ri} = \int_0^l m(y) \phi_r(y) \phi_i(y) dy \quad (3.40)$$

is the generalised mass. Differentiating with respect to time we obtain the first term in the Lagrange equation:

$$\frac{d}{dt} \left(\frac{\partial T}{\partial \dot{q}_r} \right) = \sum_{i=1}^n m_{ri} \ddot{q}_i \quad (3.41)$$

The second term is obtained by differentiating under the integral in Eq. (3.39):

$$\frac{\partial U}{\partial q_r} = \int_0^l EI(y) w''(y, t) \frac{\partial w''(y, t)}{\partial q_r} dy$$

Substituting Eq. (3.37) followed by further simplification leads to the equation:

$$\frac{\partial U}{\partial q_r} = \sum_{i=1}^n q_i \int_0^l EI(y) \phi_r''(y) \phi_i''(y) dy$$

Here, the integral is defined as the generalised stiffness,

$$k_{ri} = \int_0^l EI(y) \phi_r''(y) \phi_i''(y) dy \quad (3.42)$$

Thus the second term is obtained as:

$$\frac{\partial U}{\partial q_r} = \sum_{i=1}^n k_{ri} q_i \quad (3.43)$$

Substituting Eqs. (3.42) and (3.43) into Lagrange's Eq. (3.36), the total differential equation of free vibrations can be obtained as:

$$\sum_{i=1}^n m_{ri} \ddot{q}_i + \sum_{i=1}^n k_{ri} q_i = 0 \quad (3.44)$$

In this problem however we are only concerned about the natural vibrations, in which case the q vary harmonically in time with the same angular frequency ω . Thus,

$$q_i = \bar{q}_i \sin(\omega t + \psi) \quad (3.45)$$

where \bar{q}_i is the amplitude of the displacement, ω is the frequency, and ψ is the phase angle. In this case Eq. (3.44) takes the form:

$$\sum_{j=1}^n (k_{ri} - m_{ri} \omega^2) \bar{q}_i = 0 \quad (3.46)$$

Since r may have any value from 1 to n , it is clear that n equations of Eq. (3.46) exist. Hence the set of equations can be given in matrix form as:

$$\omega^2 [m] \{q\} = [k] \{q\} \quad (3.47)$$

Solution of Eq. (3.47) yields a set of approximations to the natural frequencies $\omega_1, \omega_2, \dots, \omega_n$. It also yield a set of eigenvectors $\{q^1\}, \{q^2\}, \dots, \{q^n\}$, which when substituted into Eq. (3.36) give a set of approximations to the natural modes. Thus the r th natural mode is approximated by:

$$\phi_r(y) = \sum_{i=1}^n \phi_i(y) q_i^{(r)} \quad (3.48)$$

The characteristic equations given by Eq. (3.46) can be put into a form suitable for numerical calculation, using matrix notation. If the beam is divided into n spanwise stations, the mass and stiffness terms given by Eqs. (3.40) and (3.42), respectively, can be written in the following matrix forms:

$$[m_{ri}] = [\phi][m][\bar{W}][\phi]^T; [k_{ri}] = [\phi''][EI][\bar{W}][\phi'']^T \quad (3.49)$$

Where

$$[\phi] = \begin{bmatrix} \phi_1(y_1) & \cdots & \phi_1(y_n) \\ \vdots & & \vdots \\ \phi_n(y_1) & \cdots & \phi_n(y_n) \end{bmatrix}; [\phi]^T = \text{Transpose of } [\phi]; [\phi''] = \begin{bmatrix} \phi_1''(y_1) & \cdots & \phi_1''(y_n) \\ \vdots & & \vdots \\ \phi_n''(y_1) & \cdots & \phi_n''(y_n) \end{bmatrix};$$

$$[m] = \begin{bmatrix} m(y_1) & & & \\ & m(y_2) & & \\ & & \ddots & \\ & & & m(y_n) \end{bmatrix}; [EI] = \begin{bmatrix} EI(y_1) & & & \\ & EI(y_2) & & \\ & & \ddots & \\ & & & EI(y_n) \end{bmatrix}$$

$[\bar{W}]$ is the matrix of the weighting numbers corresponding to the n spanwise stations.

However, in the analysis carried out the mass matrix $[m]$ and the stiffness matrix $[k]$ have been obtained using the Finite Element Method (FEM). Also the matrices $[m]$, $[EI]$ and $[\bar{W}]$ are diagonal matrices. The mass and stiffness matrices are reduced to

diagonal form to give the generalised mass and stiffness matrices. This is done by using the normal modes obtained from the finite element analysis.

If $[\phi]$ is the modal matrix i.e. the matrix formed by the selected normal mode shapes so that each column of $[\phi]$ represents a normal mode shape ϕ_i , then the generalised mass and stiffness matrices are respectively, obtained by post multiplying the mass and stiffness matrices by the modal matrix $[\phi]$, and pre-multiplying the resultant matrix by the transpose of the modal matrix i.e. $[\phi]^T$. In matrix notation

$$[M] = [\phi]^T [m] [\phi] \quad (3.50)$$

$$[K] = [\phi]^T [k] [\phi] \quad (3.51)$$

where $[M]$ and $[K]$ are the generalised mass and stiffness matrices respectively. If the number of modes chosen in analysis is n , the order of $[M]$ and $[K]$ will each be $n \times n$ which will be used later on to evaluate the wing flutter.

3.6.3 *Finite Element Approach used in MSC NASTRAN/PATRAN*

The solution of the equation of motion for natural frequencies and mode shapes requires a special reduced form of the equation of motion. If there is no damping and no applied loading, the equation of motion in matrix form reduced to:

$$[M]\{\ddot{u}\} + [K]\{u\} = 0 \quad (3.52)$$

where $[M]$ is the mass matrix and $[K]$ is the stiffness matrix.

MSC/NASTRAN offers seven methods of real eigenvalue extraction in order to solve the wide variety of problems arising in finite element analysis applications. These methods are numerical approaches to solving for natural frequencies and mode shapes. In structural analysis, the representation of stiffness and mass in the Eigen-equation result in the physical representations of natural frequencies and mode shapes. Therefore, the Eigen-equation is written in terms of stiffness matrix and mass matrix. The equation of the normal mode analysis is of form:

$$[K - \omega_i^2 M]\{\phi_i\} = 0 \quad i = 1, 2, 3, \dots \quad (3.53)$$

where $\{\phi_i\}$ is the eigenvector or mode shape and ω is the natural frequency.

The methods of eigenvalue extraction belong to one or both of the following two groups [91]:

- a. Transformation methods
- b. Tracking methods

In the transformation method, the eigenvalue equation is first transformed into a special form from which eigenvalues are extracted, while in the tracking method, the eigenvalues are extracted one at a time using an iterative procedure [91]. Four of the real eigenvalue extraction methods available in MSC/NASTRAN are transformation methods. These methods are:

- a. Givens method
- b. Householder method
- c. Modified Givens method
- d. Modified Householder method

Two of the real eigenvalue extraction methods available in MSC/NASTRAN are classified as tracking methods. These methods are:

- a. Inverse power method
- b. Sturm modified inverse power method

The last and the recommended eigenvalue extraction method MSC/NASTRAN uses is the Lanczos method. The Lanczos method combines the best characteristics of both the tracking and transformation methods. This is an efficient method, and does not miss roots and computes accurate eigenvalues and eigenvectors. It is the recommended method for most medium-to large sized problems [91]. The solution number 103 can be used in the executive control section in the input data file for conducting a normal mode analysis. The set identification number specified by the METHOD case control command refers to the set identification number of an EIGR or EIGRL entry in the bulk data section of the input data file. The EIGR entry is used to select the modal extraction parameters for the Givens; Householder, Modified Givens, Modified Householder,

Inverse power, and Sturm modified inverse power methods. The EIGRL entry is used to select the modal extraction parameters for the Lanczos method. The detailed information about the theory and the algorithms behind each method can be found in [92].

3.7 Aeroelastic Analysis

3.7.1 Evaluation of Generalised Aerodynamic Matrix

The generalised aerodynamic matrix is formed by applying the principle of virtual work. The aerodynamic strip theory based on Theodorsen expressions for unsteady lift and moment [90, 93, 94] and the normal modes obtained from the finite element method are used when applying the principle of virtual work the displacements considered are the vertical deflection (bending) $h(y)$, and the pitching rotation (torsion) $\alpha(y)$, of the elastic axis of the wing at a spanwise distance y from the root. Thus the displacement components of the i th mode ϕ_i are respectively, $h_i(y)$ and $\alpha_i(y)$. If $q_i(t)$ ($i = 1, \dots, n$) are the generalised coordinates, $h(y)$ and $\alpha(y)$ can be expressed as

$$h(y) = \sum_{i=1}^n h_i(y) q_i(t) \quad (3.54)$$

$$\alpha(y) = \sum_{i=1}^n \alpha_i(y) q_i(t) \quad (3.55)$$

Eqs. (3.54) and (3.55) can be written in matrix form as:

$$\begin{bmatrix} h(y) \\ \alpha(y) \end{bmatrix} = \begin{bmatrix} h_1(y) & h_2(y) & \cdots & h_n(y) \\ \alpha_1(y) & \alpha_2(y) & \cdots & \alpha_n(y) \end{bmatrix} \begin{bmatrix} q_1 \\ \vdots \\ q_n \end{bmatrix} \quad (3.56)$$

If the unsteady lift and moment at a spanwise distance y from the root are $L(y)$ and $M(y)$ respectively, the virtual work done (δw) by the aerodynamic force is given by

$$\delta w = \sum_{i=1}^n \delta q_i \int_0^s \{L(y) h_i(y) + M(y) \alpha_i(y)\} dy \quad (3.57)$$

Where s is the semi-span (i.e. length) of the wing and n is the number of normal modes considered in the analysis. Eq. (3.57) can be written in matrix form as:

$$\begin{bmatrix} \frac{\delta w_1}{\delta q_1} \\ \frac{\delta w_2}{\delta q_2} \\ \vdots \\ \frac{\delta w_n}{\delta q_n} \end{bmatrix} = \int_0^s \begin{bmatrix} h_1 & \alpha_1 \\ h_2 & \alpha_2 \\ \vdots & \vdots \\ h_n & \alpha_n \end{bmatrix} \begin{bmatrix} L(y) \\ M(y) \end{bmatrix} \quad (3.58)$$

The unsteady lift $L(y)$ and moment $M(y)$ in two dimensional flow is given by Theodorsen [90, 93, 94] can be expressed as:

$$\begin{bmatrix} L(y) \\ M(y) \end{bmatrix} = \begin{bmatrix} A_{11} & A_{12} \\ A_{21} & A_{22} \end{bmatrix} \begin{bmatrix} h(y) \\ \alpha(y) \end{bmatrix} \quad (3.59)$$

Where

$$\begin{aligned} A_{11} &= -\pi\rho U^2 \{-k^2 + 2C(k)ik\} \\ A_{12} &= -\pi\rho U^2 b \left\{ (a_h k^2 + ik) + 2C(k) \{1 + ik(0.5 - a_h)\} \right\} \\ A_{21} &= -\pi\rho U^2 b \left\{ 2C(k)ik(0.5 + a_h) - k^2 a_h \right\} \\ A_{22} &= \pi\rho U^2 b^2 \left\{ 2(0.5 + a_h)C(k) \{1 + ik(0.5 - a_h)\} + k^2/8 + k^2 a_h^2 + (a_h - 0.5)ik \right\} \end{aligned} \quad (3.60)$$

In Eq. (3.60) U , b , ρ , k , $C(k)$ and a_h are in the usual notation: airspeed, semi-chord, density of air, reduced frequency parameter, Theodorsen function and elastic axis location from mid-chord, respectively.

Substituting Eq. (3.59) into Eq. (3.58) and using Eq. (3.56) gives:

$$\begin{bmatrix} \frac{\delta w_1}{\delta q_1} \\ \frac{\delta w_2}{\delta q_2} \\ \vdots \\ \frac{\delta w_n}{\delta q_n} \end{bmatrix} = \int_0^s \begin{bmatrix} h_1 & \alpha_1 \\ h_2 & \alpha_2 \\ \vdots & \vdots \\ h_n & \alpha_n \end{bmatrix} \begin{bmatrix} A_{11} & A_{12} \\ A_{21} & A_{22} \end{bmatrix} \begin{bmatrix} h_1 & h_2 & \cdots & h_n \\ \alpha_1 & \alpha_2 & \cdots & \alpha_n \end{bmatrix} \begin{bmatrix} q_1 \\ q_2 \\ \vdots \\ q_n \end{bmatrix} dy = \begin{bmatrix} QF_{11} & QF_{12} & \cdots & QF_{1n} \\ QF_{21} & QF_{22} & \cdots & QF_{2n} \\ \vdots & \cdots & \cdots & \vdots \\ QF_{n1} & QF_{n2} & \cdots & QF_{nn} \end{bmatrix} \quad (3.61)$$

where $[QF]$ is the generalised aerodynamic matrix with

$$QF_{ij} = \int_0^s (A_{11} h_i h_j + A_{12} h_j \alpha_i + A_{21} h_i \alpha_j + A_{22} \alpha_i \alpha_j) \quad (3.62)$$

The generalised aerodynamic matrix $[QF]$ is usually a complex matrix with each element having a real part and an imaginary part. This is as a consequence of the terms $A_{11}, A_{12} \dots$ etc. in Eq. (3.62) being complex (see Eq. (3.60)). In contrast, the generalised mass and stiffness matrices are both real and diagonal matrices.

3.7.2 **Formation and Solution of the Flutter Determinant**

The flutter determinant is the determinant formed from the flutter matrix, and the flutter matrix is formed by algebraically summing the generalised mass, stiffness, and aerodynamic matrices. Thus for a system without structural damping (structural damping has generally a small effect on the oscillatory motion and is not considered here) the flutter matrix $[QA]$ can be formed as

$$[QA]\{q\} = [-\omega^2[M] + [K] - [QF]]\{q\} \quad (3.63)$$

where ω is the circular frequency in rad/s of the oscillatory harmonic motion.

For the flutter condition to occur, the determinant of the complex flutter matrix must be zero so that from Eq. (3.63)

$$|-\omega^2[M] + [K] - [QF]| = 0 \quad (3.64)$$

The solution of the above flutter determinant is a complex eigenvalue problem because the determinant is primarily a complex function of two unknown variables, the airspeed (U) and the frequency (ω). The method used in the optimisation program selects the airspeed and evaluates the real and imaginary parts of the flutter determinant for a range of frequencies. The process is repeated for a range of airspeeds until both the real and imaginary part of the flutter determinant (and hence the whole flutter determinant) vanish completely.

3.7.3 **Application to the SAW**

By employing the normal mode method, the flutter equation for the SAW can be written in generalised coordinates as:

$$\left[[K_D(\omega)] - \frac{1}{2} \rho V^2 [QA]_R + i\omega[D] + i \frac{1}{2} \rho V^2 [QA]_I \right] \{q\} = 0 \quad (3.65)$$

The unsteady aerodynamic forces were calculated by using the classical Therdorsen theory [93, 95] and the strip method using incompressible airflow. For static aeroelastic analysis, the aerodynamic coefficients for each of the wing sections with deflected TE are calculated by employing the panel method [95]. By the assembly of the spanwise beam models and 2D aerodynamic forces, the static aeroelastic equation of the SAW can be established and written in matrix form as:

$$[K]\{d\} = \{AF(d, \delta_{TE}, \delta_{LE})\} \quad (3.66)$$

Where, (\mathbf{K}) is the stiffness matrix of the whole wing, vector $\{d\}$ contains the wing box beam transverse displacement h and twist ϕ ; $\{AF(d, \delta_{TE}, \delta_{LE})\}$ is the vector of aerodynamic lifting force and pitching moment acting on the wing, which depends upon $\{d\}$ especially the twist angle, and the flexible TE and LE section deflections δ . For the highly flexible and large sweep angle SAW, a geometrically nonlinear and large bending-torsion coupled deformation is expected. Eq. (3.66) is expressed in the following form and solved in an iterative procedure:

$$[K]\{d_{j+1}\} = \{AF(d_j, \delta_{TE}, \delta_{LE})\} \quad (3.67)$$

3.7.4 **Finite Element Approach used in MSC NASTRAN/PATRAN**

Aerodynamic influence coefficients

In MSC/NASTRAN, there are six aerodynamic theories used to create the aerodynamic finite elements and hence the aerodynamic influence coefficients. There are three matrix equations that summarize the relationships required to define a set of aerodynamic influence coefficients. These are the basic relationships between the lifting pressure and the dimensionless vertical or normal velocity induced by the inclination of the surface to the airstream; i. e., the downwash (or normal wash),

$$\{w_j\} = [A_{jj}] \left\{ \frac{f_j}{q} \right\} \quad (3.68)$$

where $\{w_j\}$ is the downwash (dimensionless), $[A_{jj}]$ is the aerodynamic influence coefficient matrix, which is a function of Mach number and reduced frequency, f_j is the pressure on lifting element j and \bar{q} is the flight dynamic pressure.

The substantial differentiation matrix of the deflections to obtain downwash is;

$$\{w_j\} = [D_{jk}^1 + ikD_{jk}^2] \{u_k\} + \{w_j^g\} \quad (3.69)$$

where D_{jk}^1, D_{jk}^2 are the real and imaginary parts of the substantial differentiation matrix respectively (dimensionless), u_k is the displacements at aerodynamic grid points, and w_j^g represents the static aerodynamic downwash; which includes, primarily, the static incidence distribution that may arise from an initial angle of attack, camber or twist. Subscript k is the reduced frequency, $k = \omega b/V$, where ω is the angular frequency, b is a reference semichord, and V is the free-stream velocity.

And the integration of the pressure to obtain forces and moments;

$$\{P_k\} = [S_{kj}] \{f_j\} \quad (3.70)$$

where P_k represents the forces at aerodynamic grid points and S_{kj} is the integration matrix.

The three matrixes of Eq. (3.68)- (3.70) can be combined to give an aerodynamic influence coefficient matrix:

$$[Q_{kk}] = [S_{kj} [A_{jj}]^{-1} [D_{jk}^1 + ikD_{jk}^2]] \quad (3.71)$$

All aerodynamic methods within MSC/NASTRAN compute the S , D^1 , and D^2 matrices at user-specified Mach numbers and reduced frequencies. However in this analysis the Doublet-Lattice method was incorporated to compute the Q matrix, which computes the A matrix and then carries out a matrix decomposition and forward and backward substitution in order to obtain the Q matrix. The following section will present the theoretical aspects of the Doublet-Lattice method used for this analysis [96].

Doublet-Lattice Method (DLM)

In MSC/NASTRAN, there are six aerodynamic methods used in the modelling and calculations of the aerodynamic influence coefficients and the generalized aerodynamic forces. These methods are:

- a. Doublet-Lattice subsonic lifting surface theory (DLM)
- b. ZONA51 supersonic lifting surface theory
- c. Subsonic wing-body interference theory (DLM with slender bodies)
- d. Mach Box method
- e. Strip theory
- f. Piston theory

In this section, brief description of the DLM is described. The theoretical basis of the DLM is linearised aerodynamic potential theory. The undisturbed flow is uniform and is either steady or varying (gusting) harmonically. The entire lifting surface is assumed to lie nearly parallel to the flow. This method (DLM) is an extension of the steady Vortex-Lattice method to unsteady flow.

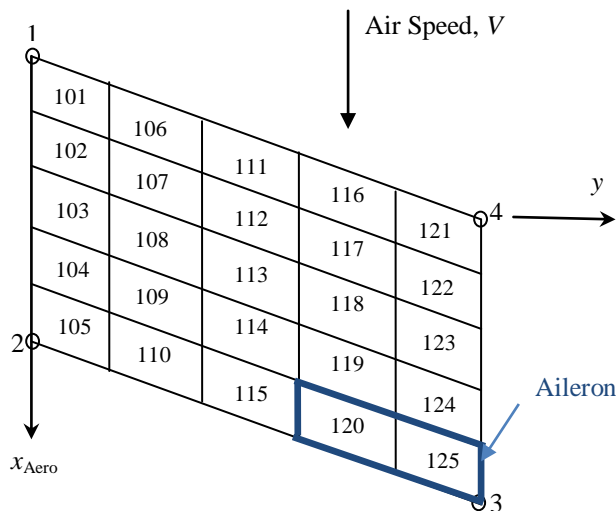


Figure 3.9 An aerodynamic Doublet-Lattice Panel subdivided into boxes

Each of the interfering surfaces (or panels) is divided into small trapezoidal lifting elements (boxes) such that the boxes are arranged in strips parallel to the free stream with surface edges, fold lines, and hinge lines lying on box boundaries as shown in Figure 3.9. The unknown lifting pressures are assumed to be concentrated uniformly across the one-quarter chord of each box.

There is one control point per box, centred spanwise on the three-quarter chord line of the box, and the surface normal downwash boundary condition is satisfied at each of these points. If a surface lies in (or nearly in) the wake of another surface, then its spanwise divisions should lie along the division of the upstream surface. The aspect ratio of the boxes should be approximate unity; less than three is acceptable in the subsonic case and no less than four boxes per chord should be used. The chord lengths of adjacent boxes in the streamwise direction should change gradually. Aerodynamic panels are assigned to interference groups. All panels within a group have aerodynamic interaction. The purpose of the groups is to reduce the computational effort for aerodynamic matrices when it is known that aerodynamic interference is important within the group but otherwise is negligible or to allow the analyst to investigate the effects of aerodynamic interference.

Interpolation methods

Structural and aerodynamic grids are connected by interpolation. This allows the independent selection of grid points of the structure and aerodynamic elements of the lifting surfaces/bodies in a manner best suited to the particular theory. The structural model for a wing may involve a one, two or three-dimensional array of grid points. The aerodynamic theory may be a lifting surface theory or a strip theory. A general interpolation method is available that will interconnect the various combinations. Any aerodynamic panel or body can be subdivided into sub-regions for interpolation, using separate function for each. The interpolation method is called splining. The theory involves the mathematical analysis of beams and plates. Three methods are available in MSC/NASTRAN [96, 97]:

- a. Linear splines, which are a generalisation of an infinite beam and allow torsional as well as bending degrees of freedom
- b. Surface splines, which are solutions for an infinite uniform plates
- c. An explicit user-defined interpolation

Several splines, including combinations of the three types, can be used in one model. The structural degrees of freedom have been chosen in MSC/NASTRAN as the independent degree of freedom; the aerodynamic degrees of freedom are dependent. A

matrix form that relates the dependent degrees of freedom to the independent ones. The structural degree of freedom may include any grid components. Two transformations are required: the interpolation from the structural deflections to the aerodynamic deflections and the structurally equivalent forces acting on the structural grid points. The derivation of elements of the interpolation matrix for the above methods is presented in [96, 97].

Flutter solution techniques

Flutter is the dynamic aeroelastic stability problem. It may be solved in any speed regime, by selecting the appropriate aerodynamic method. Three different flutter solutions techniques were provided in MSC/NASTRAN. These techniques are:

- a. The American K-method of Flutter Solution
- b. The American KE-method of Flutter Solution
- c. The British PK-method of Flutter Solution

The main advantages of the PK method was that the it produces results directly for a given values of velocity, where as the American methods require iteration to determine the reduced frequency of flutter and that the damping values obtained at subcritical flutter conditions appear to be more representative of the physical damping [96]. Therefore, the PK method was selected to calculate the flutter speed and frequency in this research. A brief description of the PK method is presented below, (for comprehensive details see [96]).

The fundamental equation for modal flutter analysis by the PK method is;

$$\left[M_{hh} P^2 + \left(B_{hh} - \frac{1}{4} \frac{\rho \bar{c} V Q_{hh}^I}{k} \right) P + \left(K_{hh} - \frac{1}{2} \rho V^2 Q_{hh}^R \right) \right] \{u_h\} = 0 \quad (3.72)$$

Where, M_{hh} - modal mass matrix; B_{hh} - modal damping matrix; K_{hh} - modal structural stiffness matrix; Q_{hh}^I - modal aerodynamic damping matrix, which is a function of reduced frequency and mach numbers; Q_{hh}^R - modal aerodynamic stiffness matrix, which is a function of reduced frequency and mach numbers; $P = \omega(\gamma \pm i)$ - ω, γ are the

circular frequency and the transient decay rate coefficient respectively; ρ - density of air; V - freestream velocity; \bar{c} - reference chord; k - reduced frequency and $\{u_h\}$ - modal amplitude vector.

The matrix terms in the equation above are all real. Q_{hh}^R and Q_{hh}^I are respectively the real and imaginary parts of Q_{hh} . An appropriate root finding algorithm is used, see ref. [96], by specifying the flight conditions of Mach number, density ratio on the outer loops and the velocities of interest on the inner loop. The output of the PK method will provide a summary of the variation of the induced frequency (k) and the velocities with damping and frequencies for each structural mode. The flutter point can be identified where there is instability in the structure, i.e. when the damping goes from being negative to positive.

3.7.5 *Dynamic Analysis*

The main purpose of a transient response analysis is to compute the behaviour of a structure subjected to time-varying excitation. The transient excitation is explicitly defined in the time domain. All of the forces applied to the structure are known at each instant in time. The important results obtained from a transient analysis are typically displacements, velocities, and accelerations of grid points, and forces and stresses in elements. Depending upon the structure and the nature of the loading, two different numerical methods can be used for a transient response analysis: direct and modal. The direct method performs a numerical integration on the complete coupled equations of motion. The modal method utilizes the mode shapes of the structure to reduce and uncouple the equations of motion (when modal or no damping is used); the solution is then obtained through the summation of the individual modal responses. The choice of the approach is problem dependent. In this analysis the direct transient response method has been adopted.

Several factors are important in computing accurate transient response. These factors include: the number of retained modes (for modal transient response), the integration time step, the time duration of the computed response, and damping.

Size of the Integration Time Step

The value of the integration time step, Δt , is important for the accurate integration of the equations of motion. Rough guidelines for the selection of are as follows [91]:

- ✦ Δt must be small enough to accurately capture the magnitude of the peak response, which means that at least ten time steps per cycle of the highest mode be used. For example, if the highest frequency of interest is 100 Hz, then Δt should be 0.001 second or smaller.
- ✦ Δt must be small enough to accurately represent the frequency content of the applied loading. If the applied loading has a frequency content of 1000 Hz, then must be 0.001 second or less (preferably much less in order to represent the applied loading with more than one point per cycle).

Duration of the Computed Response

The length of the time duration is important so that the lowest flexible (e.g., non-rigid body) mode oscillates through at least one cycle. For example, if the lowest flexible mode has a frequency of 0.2 Hz, then the time duration of the computed response should be at least 5.0second. A better guideline is to make the duration the longer of the following: twice the period of the lowest flexible mode or one period of the lowest flexible mode after the load has been removed or reached a constant value. The time duration is set on the TSTEP entry by multiplying (the integration time step) by the number of time steps (N).

Value of Damping

The proper selection of the damping value is relatively unimportant for analyses that are of very short duration, such as a crash impulse or a shock blast. The specification of the damping value is most important for long duration loadings (such as earthquakes) and is critical for loadings (such as sine dwells) that continually add energy into the system.

Verification of the Applied Load

The applied load can be verified by applying the load suddenly (over one or two time increments) and comparing the results to a static solution with the same spatial load distribution. The transient results should have a peak value of twice the static results. If

the transient results are not twice the static results, check the LSEQ and DAREA entries. Another way to verify the applied load is to inspect it visually via the X-Y plots.

Direct Transient Response Analysis

The structural response in a direct transient response analysis is computed by solving a set of coupled equations using direct numerical integration. The dynamic equation of motion in matrix form:

$$[M]\{\ddot{u}(t)\} + [B]\{\dot{u}(t)\} + [K]\{u(t)\} = \{P(t)\} \quad (3.73)$$

The fundamental structural response (displacement) is solved at discrete times, typically with a fixed integration time step Δt . The velocity and acceleration are expressed by using a central finite difference representation:

$$\begin{aligned} \{\dot{u}_n\} &= \frac{1}{2\Delta t} \{u_{n+1} - u_{n-1}\} \\ \{\ddot{u}_n\} &= \frac{1}{\Delta t^2} \{u_{n+1} - 2u_n + u_{n-1}\} \end{aligned} \quad (3.74)$$

And averaging the applied force over three adjacent time points, the equation of motion can be rewritten as:

$$\begin{aligned} &\left[\frac{M}{\Delta t^2}\right](u_{n+1} - 2u_n + u_{n-1}) + \left[\frac{B}{2\Delta t}\right](u_{n+1} - u_{n-1}) \\ &+ \left[\frac{K}{3}\right](u_{n+1} + u_n + u_{n-1}) = \frac{1}{3}(P_{n+1} + P_n + P_{n-1}) \end{aligned} \quad (3.75)$$

The equation of motion can be further simplified by collecting terms:

$$[A_1]\{u_{n+1}\} = [A_2] + [A_3]\{u_n\} + [A_4]\{u_{n-1}\} \quad (3.76)$$

Where:

$$\begin{aligned} [A_1] &= \left[\frac{M}{\Delta t^2} + \frac{B}{2\Delta t} + \frac{K}{3}\right]; [A_2] = \frac{1}{3}(P_{n+1} + P_n + P_{n-1}); [A_3] = \left[\frac{2M}{\Delta t^2} - \frac{K}{3}\right]; \\ [A_4] &= \left[-\frac{M}{\Delta t^2} + \frac{B}{2\Delta t} - \frac{K}{3}\right] \end{aligned}$$

Matrix $[A_1]$ is known as the dynamic matrix, and $[A_2]$ is the applied force (averaged over three adjacent time points). In the method MSC/NASTRAN adopts, $\{P(t)\}$ is averaged over three time points and $[K]$ is modified such that the dynamic equation of motion is reduced to a static solution $[K]\{u\} = \{P_n\}$ if $[M]$ or $[B]$ does not exist.

The transient solution is obtained by decomposing $[A_1]$ and applying it to the right hand side of the above equation. In this form, the solution behaves as succession of static solutions with each time step performing a forward-backward substitution on the new load vector. The transient nature of the solution is carried out by modifying the applied force matrix $[A_2]$ with $[A_3]$ and $[A_4]$ terms. For simplification the $[M]$, $[B]$ and $[K]$ matrices are assumed to be constant throughout the analysis and do not change with time. If Δt remains constant throughout the analysis, the $[A_1]$ matrix will need to be decomposed only once. Each step in the analysis is then a forward-backward substitution of the new load vector. If Δt is changed, then $[A_1]$ must be re-decomposed.

Transient response analysis does not permit the use of complex coefficients. Therefore, structural damping is included by means of equivalent viscous damping. In order for this to take effect on the solution, a relation between structural damping and equivalent viscous damping must be defined. Viscous damping force is a damping force that is a function of a damping coefficient b and the velocity. It is the induced force represented in the equation of motion, Eq. (3.73), using the $[B]$ matrix and the velocity vector.

The structural damping force is a displacement dependant damping. It is a function of a damping coefficient G and a complex component of the structural stiffness matrix.

$$[M]\{\ddot{u}(t)\} + (1 + iG)[K]\{u(t)\} = \{P(t)\} \quad (3.77)$$

Assuming constant amplitude oscillatory response for an single degree of freedom system, the two damping forces are identical if:

$$Gk = b\omega; \text{ or } b = \frac{Gk}{\omega} \quad (3.78)$$

Where G is structural damping; b is equivalent viscous damping; k is reduced frequency and ω represents the frequency.

Therefore, if structural damping is to be modelled using equivalent viscous damping, then the Eq. (3.78) is only true for one frequency (see Figure 3.10)

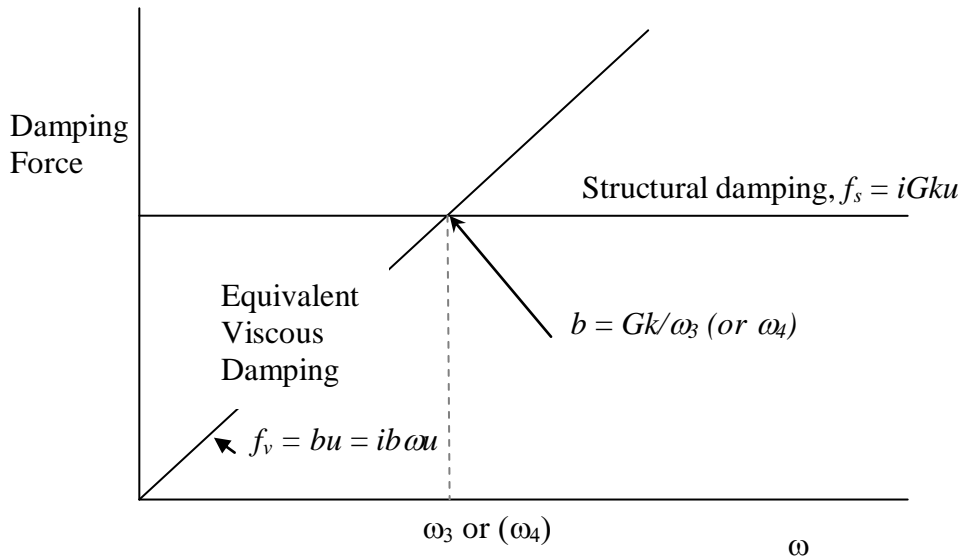


Figure 3.10 Structural Damping Versus Viscous Damping

An overall structural damping coefficient can be applied to the entire system stiffness matrix at the circular frequency at which damping is to be made equivalent. This parameter is defined as W_3 in the input deck and is used in conjunction with parameter G which is defined as the structural damping coefficient.

3.8 Control effectiveness

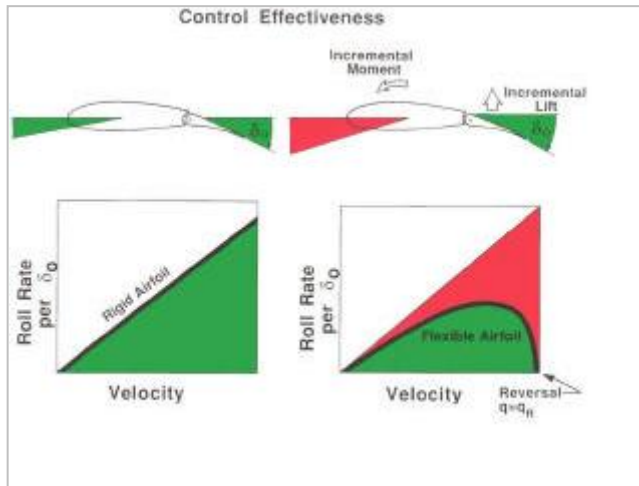


Figure 3.11 Control Reversal [61]

The flexibility of a wing adversely affects the effectiveness of the control surface. For example, the downward deflection of a control surface such as an aileron will cause a nose down pitching moment of the wing which consequently reduces the angle of attack (shown in red in the right hand picture of Figure 3.11). This nose down wing twist will cause a reduction in lift

produced by the control surface deflection. If the control surface was deflected to perform a roll manoeuvre, then the rolling moment will be reduced to a value less than that for a rigid wing.

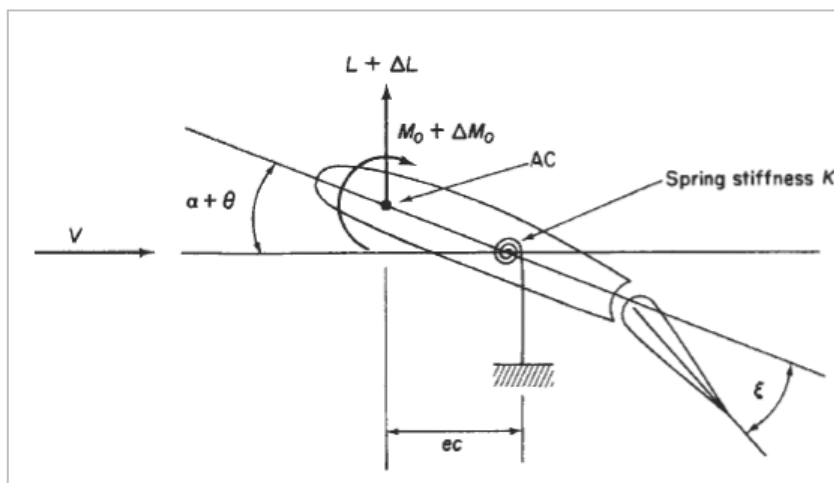


Figure 3.12 Control Effectiveness and Reversal Speed [84]

As illustrated in Figure 3.12 the case of a wing aileron combination in a two-dimensional flow has been investigated. An aileron deflection produces changes ΔL and ΔM , in the wing lift, L , and wing pitching moment M_0 .

As expressed in Eq. (3.79), a small increase ΔL is produced by a positive aileron (TE downward) rotation angle ξ and a positive (nose-up) wing twist angle θ due to elastic deformation of the wing.

$$\Delta L = \left(\frac{\partial C_L}{\partial \alpha} \theta + \frac{\partial C_L}{\partial \xi} \xi \right) \frac{1}{2} \rho V^2 S \quad (3.79)$$

For a 'rigid' wing with elastic twist ignored, the increase of lift due to ξ becomes

$$\Delta L_R = \frac{\partial C_L}{\partial \xi} \xi \frac{1}{2} \rho V^2 S \quad (3.80)$$

The ratio of ΔL against ΔL_R is defined as aileron effectiveness to assess the control effectiveness of a flexible wing.

$$\text{Aileron Effectiveness} = \Delta L / \Delta L_R \quad (3.81)$$

The wing static elastic twist is caused by two types of forces. One is due to the lift and wing bending-torsion coupling deformation. For a sweptback wing, the induced twist angle is normally negative (nose-down). Associated with the lift, an aerodynamic pitching moment M_0 about the wing elastic centre is produced. It is normally positive for a general case that the aerodynamic centre is forward of the elastic centre. Since the wing elastic restoring moment against the twist remains constant depending on the torsional stiffness of the wing structure [84], the twist angle will vary with the flight speed. When flight speed increases, an aileron rotation downward may produce a negative twist of the wing and consequently reduce the effective aileron incidence [84] and lift. In this case, the aileron effectiveness is reduced as the speed increases. When the speed exceeds a certain value, the aileron reversal speed, the aileron rotation produces zero rolling moment.

3.8.1 *Aerodynamic and Structural Integration*

A detailed study of the control effectiveness was later carried out using the program AERO-BEAM-SAW for the optimised cases 2.1 and 2.2 in section 4.2.4. This program is a combination of BEAM3D program and the UNSPM (unsteady panel method)

program to calculate the aerodynamic force, pitching moment and their interaction with structural deformation for the control effectiveness of the whole wing.

Structural Representation

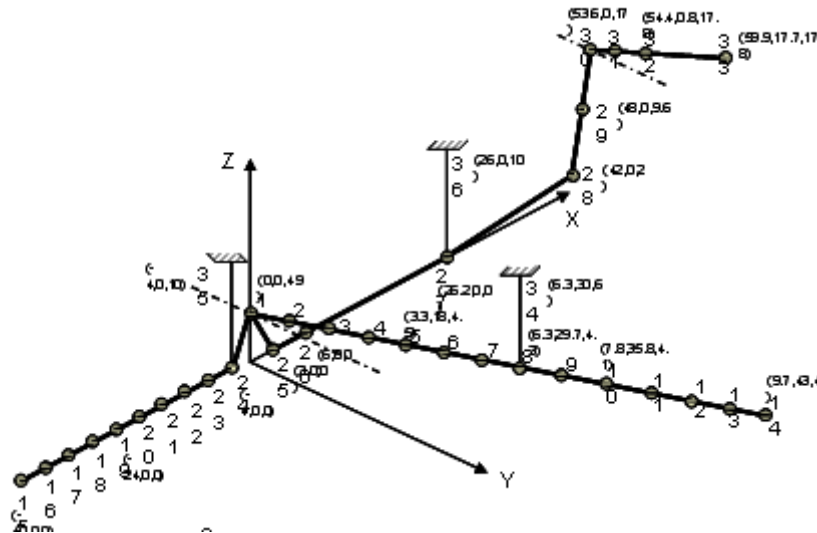


Figure 3.13 Example of AERO-BEAM-SAW aircraft model

As shown in Figure 3.13 a beam element may be defined between two nodes by specifying the stiffness properties at the nodes (i.e. at the two ends of the beam). The stiffness properties are assumed to vary linearly along the length of the beam. The beams are allowed bending and shear deformation in each of the two orthogonal planes, twisting and extension. For each beam element a (12x12) stiffness matrix is formed from the inverted flexibility matrix, and then added in to the stiffness matrix of the complete structure. Given the geometry and stiffness of a branch, considered as a beam with straight flexural axis, the program BEAM3D forms a flexibility matrix calculated by the engineer's theory of bending under the assumptions that:

- The beam is clamped at the root
- All sections of the beam have the same incidence, dihedral and sweep
- The flexural axis is straight
- The required nodes are joined to the beam by rigid arms
- Each node has up to six degrees of freedom

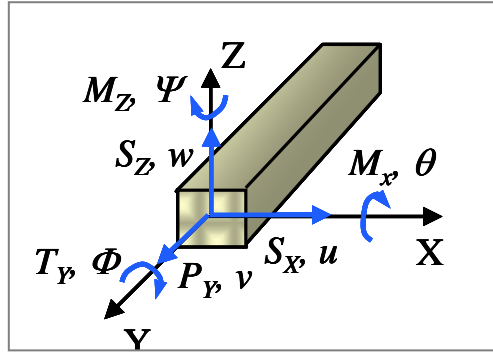


Figure 3.14 Notation diagram

The flexibility matrix $[F]$ (6x6) for a single beam element is given by

$$[F] = \begin{bmatrix} u/P & 0 & 0 & 0 & 0 & u/N \\ 0 & \omega/R & 0 & 0 & \omega/L & 0 \\ 0 & 0 & \phi/M & 0 & 0 & 0 \\ 0 & 0 & 0 & -v/-Q & 0 & 0 \\ 0 & \theta/R & 0 & 0 & \theta/L & 0 \\ \psi/P & 0 & 0 & 0 & 0 & \psi/N \end{bmatrix} = \begin{bmatrix} F_{11} & 0 & 0 & 0 & 0 & F_{61} \\ 0 & F_{22} & 0 & 0 & F_{52} & 0 \\ 0 & 0 & F_{33} & 0 & 0 & 0 \\ 0 & 0 & 0 & F_{44} & 0 & 0 \\ 0 & F_{52} & 0 & 0 & F_{55} & 0 \\ F_{61} & 0 & 0 & 0 & 0 & F_{66} \end{bmatrix}$$

Where

$$F_{11} = \int_0^l \frac{(l-\delta)^2}{EIZ} d\delta + \int_0^l \frac{1}{GAX} d\delta; \quad F_{22} = \int_0^l \frac{(l-\delta)^2}{EIX} d\delta + \int_0^l \frac{1}{GAZ} d\delta;$$

$$F_{33} = \int_0^l \frac{1}{GJ} d\delta; \quad F_{44} = \int_0^l \frac{1}{EA} d\delta; \quad F_{55} = \int_0^l \frac{1}{EIX} d\delta;$$

$$F_{66} = \int_0^l \frac{1}{EIZ} d\delta; \quad F_{52} = \int_0^l \frac{(l-\delta)}{EIX} d\delta; \quad F_{52} = -\int_0^l \frac{(l-\delta)}{EIZ} d\delta$$

l is the length of the beam, $EIX = E \times \bar{I}_{xx}$, $EIZ = E \times \bar{I}_{zz}$, $GAX = G \times A_{sx}$, $GAZ = G \times A_{sz}$.

The flexibility matrix is first formed, in beam axes, for a simple cantilever at nodes which lie on the beam. The sub-matrices of the flexible matrix are formed by integrating along the beam for unit loads and moments to find the resultant deflections and twist from Eqn. (3.82).

$$\begin{Bmatrix} u \\ w \\ \phi \\ v \\ \theta \\ \psi \end{Bmatrix} = [F] \begin{Bmatrix} P_x \\ R_z \\ M_y \\ Q_y \\ L_x \\ N_z \end{Bmatrix} \quad (3.82)$$

This flexibility matrix is then transformed to data axes (data axes – is a left handed set of axes which are parallel to the line of flight axes and are such that the y-axis is nearest to the beam) and to the required nodes.

For a beam element $[F]^{-1}$ (6x6) is given by

$$[F]^{-1} = \begin{bmatrix} F_{11}^{-1} & 0 & 0 & 0 & 0 & F_{61}^{-1} \\ 0 & F_{22}^{-1} & 0 & 0 & F_{52}^{-1} & 0 \\ 0 & 0 & F_{33}^{-1} & 0 & 0 & 0 \\ 0 & 0 & 0 & F_{44}^{-1} & 0 & 0 \\ 0 & F_{52}^{-1} & 0 & 0 & F_{55}^{-1} & 0 \\ F_{61}^{-1} & 0 & 0 & 0 & 0 & F_{66}^{-1} \end{bmatrix} \quad (3.83)$$

Where

$$\begin{aligned} F_{11}^{-1} &= \frac{F_{66}}{F_{11}F_{66} - F_{61}^2}; & F_{22}^{-1} &= \frac{F_{55}}{F_{22}F_{55} - F_{52}^2}; & F_{33}^{-1} &= \frac{1}{F_{33}}; \\ F_{44}^{-1} &= \frac{1}{F_{44}}; & F_{55}^{-1} &= \frac{F_{22}}{F_{22}F_{55} - F_{52}^2}; & F_{66}^{-1} &= \frac{F_{11}}{F_{11}F_{66} - F_{61}^2} \\ F_{52}^{-1} &= \frac{F_{52}}{F_{22}F_{55} - F_{52}^2}; & F_{61}^{-1} &= \frac{F_{61}}{F_{11}F_{66} - F_{61}^2} \end{aligned}$$

Using the inverted flexibility matrix, the stiffness matrix $[E]$ (12x12) for a beam element is given by

$$[E] = [C]^T [F]^{-1} [C] \quad (3.84)$$

$$\text{Where, } [C] = \begin{bmatrix} 1 & 0 & 0 & 0 & 0 & -l & -1 & 0 & 0 & 0 & 0 & 0 \\ 0 & 1 & 0 & 0 & l & 0 & 0 & -1 & 0 & 0 & 0 & 0 \\ 0 & 0 & 1 & 0 & 0 & 0 & 0 & 0 & -1 & 0 & 0 & 0 \\ 0 & 0 & 0 & 1 & 0 & 0 & 0 & 0 & 0 & -1 & 0 & 0 \\ 0 & 0 & 0 & 0 & 1 & 0 & 0 & 0 & 0 & 0 & -1 & 0 \\ 0 & 0 & 0 & 0 & 0 & 1 & 0 & 0 & 0 & 0 & 0 & -1 \end{bmatrix}, \text{ and } []^T \text{ indicates}$$

matrix transposition.

However, this stiffness matrix is in beam axes and requires to be transformed to the reference axes system. If we consider the stiffness matrix $[E]$ to be partitioned into 96x60 sub-matrices $[E_{AA}]$, $[E_{AB}]$, $[E_{BA}]$, $[E_{BB}]$, such that;

$$[E] = \begin{bmatrix} [E_{AA}] & [E_{AB}] \\ [E_{BA}] & [E_{BB}] \end{bmatrix} \quad (3.85)$$

Hence the stiffness matrix in the reference axes is given by

$$[E] = \begin{bmatrix} [T]^T & [E_{AA}] & [T] & [T]^T & [E_{AB}] & [T] \\ [T]^T & [E_{BA}] & [T] & [T]^T & [E_{BB}] & [T] \end{bmatrix} \quad (3.86)$$

Where $[E_{AA}]$, $[E_{AB}]$, $[E_{BA}]$, $[E_{BB}]$ are in beam axes and the transformation matrix $[T]$ (6x6) is given by

$$[T] = \begin{bmatrix} L_x & N_x & 0 & -M_x & 0 & 0 \\ L_z & N_z & 0 & 0 & 0 & 0 \\ 0 & 0 & M_y & 0 & L_y & N_y \\ -L_y & -N_y & 0 & M_y & 0 & 0 \\ 0 & 0 & M_x & 0 & L_x & N_x \\ 0 & 0 & M_z & 0 & L_z & N_z \end{bmatrix} \quad (3.87)$$

Here $L_x, L_y, L_z, M_x, M_y, M_z, N_x, N_y, N_z$ are $NS \times NS$ (NS -Number of stations at which the flexibility matrix is to be generated) diagonal sub-matrices with constant diagonal formed as by letting $t_1 = \tan(\text{Sweep} - \text{Angle})$; $t_2 = \tan(\text{Dihedral} - \text{Angle})$;

$t_3 = \tan(\text{Incident})$ and $a_1 = (1 + t_1^2 + t_2^2)^{1/2}$; $a_2 = (1 + t_1^2 + (1 + t_1^2)t_3^2 + 2t_1t_2t_3)^{1/2}$.

$$[L_x]_{ii} = (1 + t_1^2 + t_1t_2t_3)/a_1a_2; \quad [L_y]_{ii} = t_1/a_1; \quad [L_z]_{ii} = t_3/a_2;$$

$$[M_x]_{ii} = (t_2t_3 - t_1)/a_1a_2; \quad [M_y]_{ii} = 1/a_1; \quad [M_z]_{ii} = -(t_1t_3 + t_2)/a_2;$$

$$[N_x]_{ii} = -(t_3 + t_1 t_2 + t_1^2 t_3)/a_1 a_2; \quad [N_y]_{ii} = t_2/a_1; \quad [N_z]_{ii} = 1/a_2$$

The stiffness matrix now in the reference axes has to be transformed to the aircraft axes.

This is given by:

$$[E] = \begin{bmatrix} [S]^T & [T]^T & [E_{AA}] & [T] & [S] & [S]^T & [T]^T & [E_{AB}] & [T] & [S] \\ [S]^T & [T]^T & [E_{BA}] & [T] & [S] & [S]^T & [T]^T & [E_{BB}] & [T] & [S] \end{bmatrix} \quad (3.88)$$

Where the transformation matrix $[S]$ is given by: $[S] = [I]$ (i.e. a 6 x 6 unit matrix) for

$ICY = 0$

$$[S] = \begin{bmatrix} -1 & 0 & 0 & 0 & 0 & 0 \\ 0 & 1 & 0 & 0 & 0 & 0 \\ 0 & 0 & -1 & 0 & 0 & 0 \\ 0 & 0 & 0 & -1 & 0 & 0 \\ 0 & 0 & 0 & 0 & -1 & 0 \\ 0 & 0 & 0 & 0 & 0 & 1 \end{bmatrix} \quad \text{for } ICY = -2;$$

$$[S] = \begin{bmatrix} 0 & -1 & 0 & 0 & 0 & 0 \\ 0 & 0 & 0 & -1 & 0 & 0 \\ 0 & 0 & 0 & 0 & -1 & 0 \\ 0 & 0 & 0 & 0 & 0 & 0 \\ 1 & 0 & 0 & 0 & 0 & -1 \\ 0 & 0 & 1 & 0 & 0 & 0 \end{bmatrix} \quad \text{for } ICY = -1$$

$$[S] = \begin{bmatrix} 0 & 1 & 0 & 0 & 0 & 0 \\ 0 & 0 & 0 & -1 & 0 & 0 \\ 0 & 0 & 0 & 0 & 1 & 0 \\ 0 & 0 & 0 & 0 & 0 & 0 \\ -1 & 0 & 0 & 0 & 0 & 1 \\ 0 & 0 & 1 & 0 & 0 & 0 \end{bmatrix} \quad \text{for } ICY = 1$$

$$[S] = \begin{bmatrix} 1 & 1 & 0 & 0 & 0 & 0 \\ 0 & 0 & 0 & 1 & 0 & 0 \\ 0 & 0 & 0 & 0 & 0 & 1 \\ 0 & -1 & 0 & 0 & 0 & 0 \\ 0 & 0 & 0 & 0 & 1 & 0 \\ 0 & 0 & -1 & 0 & 0 & 0 \end{bmatrix} \quad \text{for } ICY = 2$$

Hence the complete stiffness matrix is then obtained by summing (for each element) the contributions to the element from each of the sub-system stiffness matrices (either from beam element or input inverted flexibility matrices) and deleting rows and columns corresponding to freedoms which are to be fixed.

Then the (6x6) mass matrix $[M_I]$ for station I is formed as

$$[M_I] = \begin{bmatrix} M & 0 & MZ & 0 & 0 & -MY \\ 0 & M & -MX & 0 & MY & 0 \\ MZ & -MX & I_{YY} & 0 & -I_{XY} & -I_{YZ} \\ 0 & 0 & 0 & M & MZ & -MX \\ 0 & MY & -I_{XY} & MZ & I_{XX} & -I_{XZ} \\ -MY & 0 & -I_{YZ} & -MX & -I_{XZ} & I_{ZZ} \end{bmatrix} \quad (3.89)$$

Where $MX = m \cdot (x_2 - x_1)$; $MY = m \cdot (y_2 - y_1)$; $MZ = m \cdot (z_2 - z_1)$;

$$I_{XX} = m \cdot [(y_2 - y_1)^2 + (z_2 - z_1)^2]; \quad I_{YY} = m \cdot [(x_2 - x_1)^2 + (z_2 - z_1)^2];$$

$$I_{ZZ} = m \cdot [(x_2 - x_1)^2 + (y_2 - y_1)^2]; \quad I_{XY} = m \cdot (x_2 - x_1)(y_2 - y_1);$$

$I_{YZ} = m \cdot (y_2 - y_1)(z_2 - z_1)$; $I_{XZ} = m \cdot (x_2 - x_1)(z_2 - z_1)$ are obtained using the coordinates and the mass per unit length of the station as shown in Figure 3.15 .

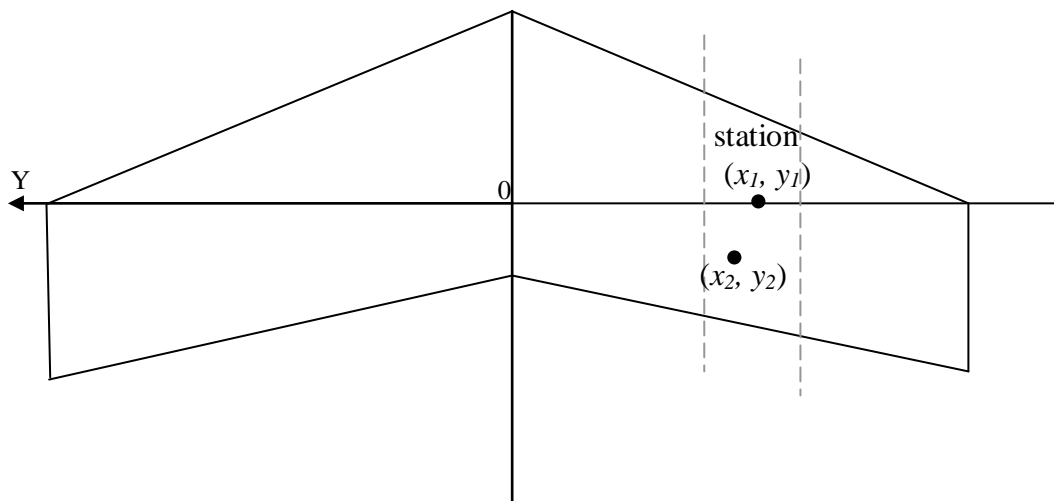


Figure 3.15 Notation in Aircraft Axes in Eqn. (3.108)

Having formed the total system mass matrix $[M]$ and stiffness matrix $[E]$ the following equation is solved.

$$[E]\{v_k\} = \lambda_k [M]\{v_k\} \quad (3.90)$$

Where $\{v_k\}$ and λ_k are the roots and eigenvectors respectively.

2D Aerodynamic Representation – Panel Method

Although thin aerofoil theory does give fairly good results for lift and pitching moment coefficients, it ignores the effect of lift and pitching moment on the thickness distribution. Furthermore, it gives good results of the pressure distribution away from the stagnation points. Therefore, for a more accurate prediction of pressure, lift, moment and drag coefficients the panel method could be used. The original panel method developed by Hess and Smith [97, 98] is a combination of sources and vortices. More recent development of the panel method is a combination of sources and doublets oriented normal to the surface [99]. If the source strength is specified, the doublet strength will be the only unknown and it is related to the velocity potential on the surface. The surface velocity can then be calculated by differentiating the doublet strength [99].

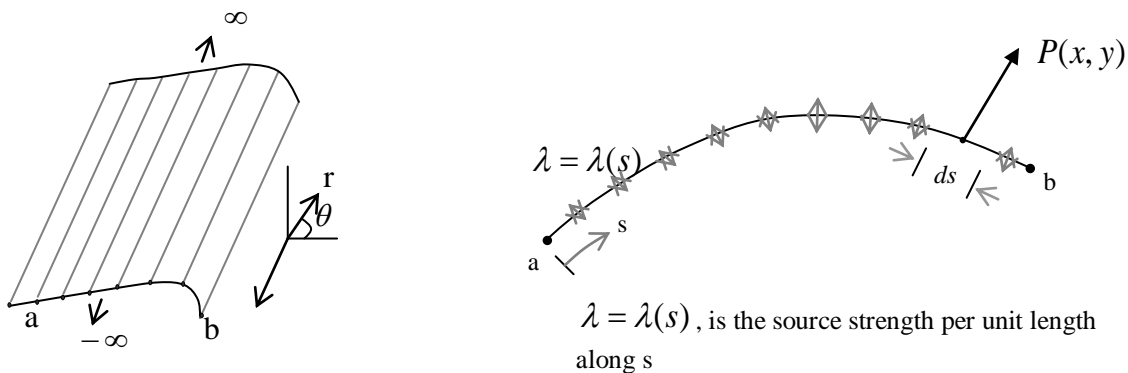


Figure 3.16(a) Source sheet (Source sheet is an infinite number of line sources)

The strength of a single line source Λ is the volume flow rate per unit depth that is per unit length in the z direction. The strength of a source sheet $\lambda(s)$, is the volume flow rate per unit depth (in the z -axis) and per unit length (in s direction). Therefore the

strength of the portion ds is λds . This small section of the source sheet of strength λds induces a small potential $d\phi$ at point P .

$$d\phi = \frac{\lambda ds}{2\pi} \ln r \quad (3.91)$$

The complete velocity potential at point P , induced by the entire source sheet from a to b is obtained by integrating Eqn. (3.91)

$$\phi(x, y) = \int_a^b \frac{\lambda ds}{2\pi} \ln r \quad (3.92)$$

Consider an arbitrary shape in a flow with freestream velocity V_∞ . If the surface of the body is assumed as a source sheet, where $\lambda(s)$ varies in a way that the combined effect of the uniform flow and the source sheet makes the surface a streamline of the flow. The problem will be to find the appropriate $\lambda(s)$.

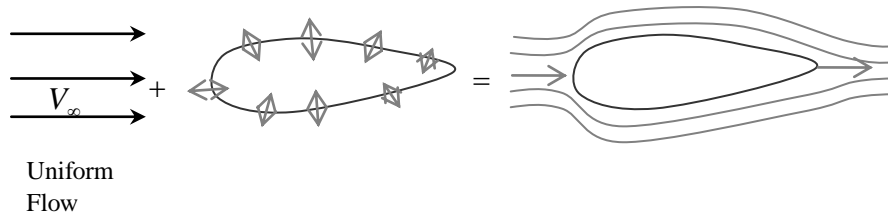


Figure 3.17 Flow over the body of given shape [100]

The source sheet is approximated by a series of straight panels, and λ per unit length is constant over a given panel. However, vary from one panel to the next, i.e. if there are n panels, the source panel strengths per unit length are $\lambda_1, \lambda_2, \dots, \lambda_j, \dots, \lambda_n$. These panel strengths are the unknowns and the main aim of the panel method is to solve for λ_j , where $j = 1$ to n , such that the body surface becomes a streamline of the flow [100].

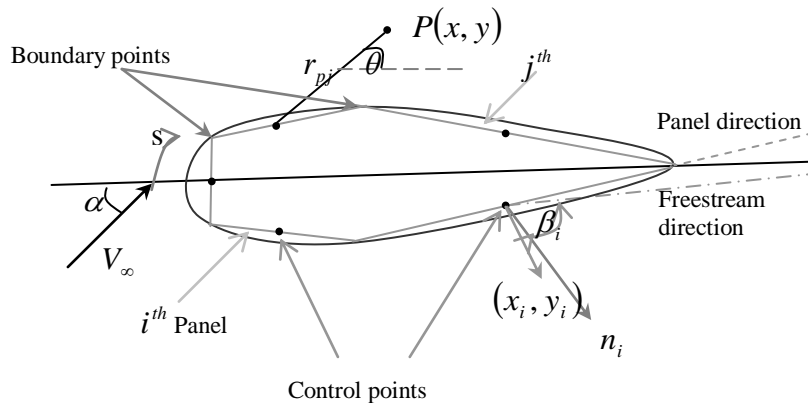


Figure 3.18 Notation [100]

Boundary conditions are imposed by defining the mid point of each panel as a control point and by determining λ_j , such that the normal component of the flow velocity is zero at each control point [100].

The velocity potential induced at point P due to the j^{th} panel $\Delta\phi_j$ is,

$$\Delta\phi_j = \frac{\lambda_j}{2\pi} \int \ln r_{pj} ds_j \quad (3.93)$$

Eqn. (3.91) summed over all the panels;

$$\phi(P) = \sum_{j=1}^n \Delta\phi_j = \sum_{j=1}^n \frac{\lambda_j}{2\pi} \int \ln r_{pj} ds_j \quad (3.94)$$

where $r_{pj} = \sqrt{(x - x_j)^2 + (y - y_j)^2}$

Hence

$$\phi(x_i, y_i) = \sum_{j=1}^n \frac{\lambda_j}{2\pi} \int \ln r_{ij} ds_j \quad (3.95)$$

$$\text{and } r_{ij} = \sqrt{(x_i - x_j)^2 + (y_i - y_j)^2} \quad (3.96)$$

V_∞ normal to the i^{th} panel is,

$$V_{\infty,n} = V_\infty \cdot n_i = V_\infty \cos \beta_i \quad (3.97)$$

(n_i is the unit vector normal to the i^{th} panel)

The normal component of the velocity induced at (x_i, y_i) by the source panels is obtained from Eqn. (3.95)

$$V_n = \frac{\partial}{\partial n_i} [\phi(x_i, y_i)] \quad (3.98)$$

Hence Eqn. (3.98) combined with Eqn.(3.95) becomes;

$$V_n = \frac{\lambda_i}{2} + \sum_{\substack{j=1 \\ (j \neq i)}}^n \frac{\lambda_j}{2\pi} \int \frac{\partial}{\partial n_i} \ln r_{ij} ds_j \quad (3.99)$$

However, the boundary conditions state that

$$V_{\infty,n} + V_n = 0 \quad (3.100)$$

Substituting Eqn. (3.97) and Eqn. (3.99) into Eqn. (3.100) gives,

$$\frac{\lambda_i}{2} + \sum_{\substack{j=1 \\ (j \neq i)}}^n \frac{\lambda_j}{2\pi} \int_j \frac{\partial}{\partial n_i} \ln r_{ij} ds_j + V_\infty \cos \beta_i = 0 \quad (3.101)$$

Eqn. (3.101) is a linear algebraic equation with n unknowns $\lambda_1, \lambda_2, \dots, \lambda_n$. It represents the flow boundary conditions evaluated at the control point of the i^{th} panel. Once λ_i ($i = 1$ to n) are obtained the velocity tangent to the surface at each control point can be calculated using,

$$V_{\infty, s} = V_\infty \sin \beta_i \quad (3.102)$$

As before the tangential velocity V_s at the control point of the i^{th} panel induced by all the panels is obtained by differentiating Eqn. (3.95) with respect to s ,

$$V_s = \frac{\partial \phi}{\partial s} \frac{\lambda_i}{2} = \sum_{j=1}^n \frac{\lambda_j}{2\pi} \int_j \frac{\partial}{\partial s} \ln r_{ij} ds_j \quad (3.103)$$

The total surface velocity at the i^{th} control point, V_i is the sum of the contribution from the freestream (Eqn. 3.102) and from the source panels (Eqn. 3.103)

$$V_i = V_{\infty, s} + V_s = V_\infty \sin \beta_i + \sum_{j=1}^n \frac{\lambda_j}{2\pi} \int_j \frac{\partial}{\partial s} \ln r_{ij} ds_j \quad (3.104)$$

Hence the pressure coefficient of the i^{th} control point is obtained as

$$C_{p,i} = 1 - \left(\frac{V_i}{V_\infty} \right)^2 \quad (3.105)$$

3.9 Gradient Based Design Optimisation

An optimiser can be used in order to choose input values for the quantities that prescribe the design. An optimum design is expected because it is assumed that these input values are chosen in such a way that the design will satisfy all limitations and restrictions placed on it and will result in the best design possible in some cases. The main approach of the optimiser is to find an acceptable design in the presence of restrictions of the input variables. These are commonly known as design variables, which are defined as numerical quantities for which values are to be chosen in producing a design [101].

A design is simply a set of values for the design variables. Some designs are useful to the design problem and others are not. If the design meets all the requirements placed on it, it will be categorised as an acceptable design. The design restrictions that must be satisfied in order to produce an acceptable design are called constraints. There are two types of constraints in engineering problems: side constraints and behaviour constraints [101]. A constraint that restricts the range of design variables for reasons other than direct consideration of performance is known as side constraints. A constraint that derives from those performance or behaviour requirements that are explicitly considered are known as behaviour constraints.

Of all acceptable designs, some are categorised as better than others. In this case there is a need for a measure to verify the quality of the better designs compared to the less desirable ones. This quality can be expressed as a function of the design variables. This function which the design is optimised is known as the objective function. This is commonly designated as $F(D)$, to emphasize its dependability on the design variables, D .

In the optimisation process, the GBDM is employed for the SAW aeroelastic tailoring. Effort is primarily focused on achieving a maximum flutter speed by tailoring the fibre orientations of the skin and spar web laminates. Since the wing weight will not be affected by fibre orientation, an unconstrained optimisation problem was therefore formulated and expressed as follows:

$$\text{Minimise } f_v(x) = \left[1 - \frac{V_f(x) - V_f(\theta_0)}{V_f(\theta_0)} \right]^2 \quad (3.106)$$

$$x \in \{A|(\theta_1, \theta_2, \dots, \theta_n)\}, \theta_n \in [-90, 90]$$

where $f_v(x)$ is the objective function, the $V_f(x)$ wing flutter speed, x a vector containing the fibre orientations $(\theta_1, \theta_2, \dots, \theta_n)$ set as design variables with a lower and upper bounds of $\pm 90^\circ$, θ_0 represents a set of specified fibre orientations in the initial laminate layup of the skin and spar webs. It is expected that the optimiser will minimise the objective function, $f_v(x)$ in order to maximise the flutter speed.

The solution of this optimisation problem is separated into three basic levels [101]:

- 1) Strategy (mathematical modelling of the problem) – which is used to convert a constrained optimisation problem into a sequence of unconstrained problems.
- 2) Optimise (find the direction) – convert a minimising function $f_v(x)$ into a sequence of one-D search problems and provide search direction. In the current method adopted the Davidon-Fletcher-Powell (DFP) variable metric method [102] was used as the optimiser.
- 3) One-D search – finding the minimum of the function $f_v(x)$ under the current direction by implementing the Golden Section method [101] based on polynomial interpolation.

3.10 Methodology

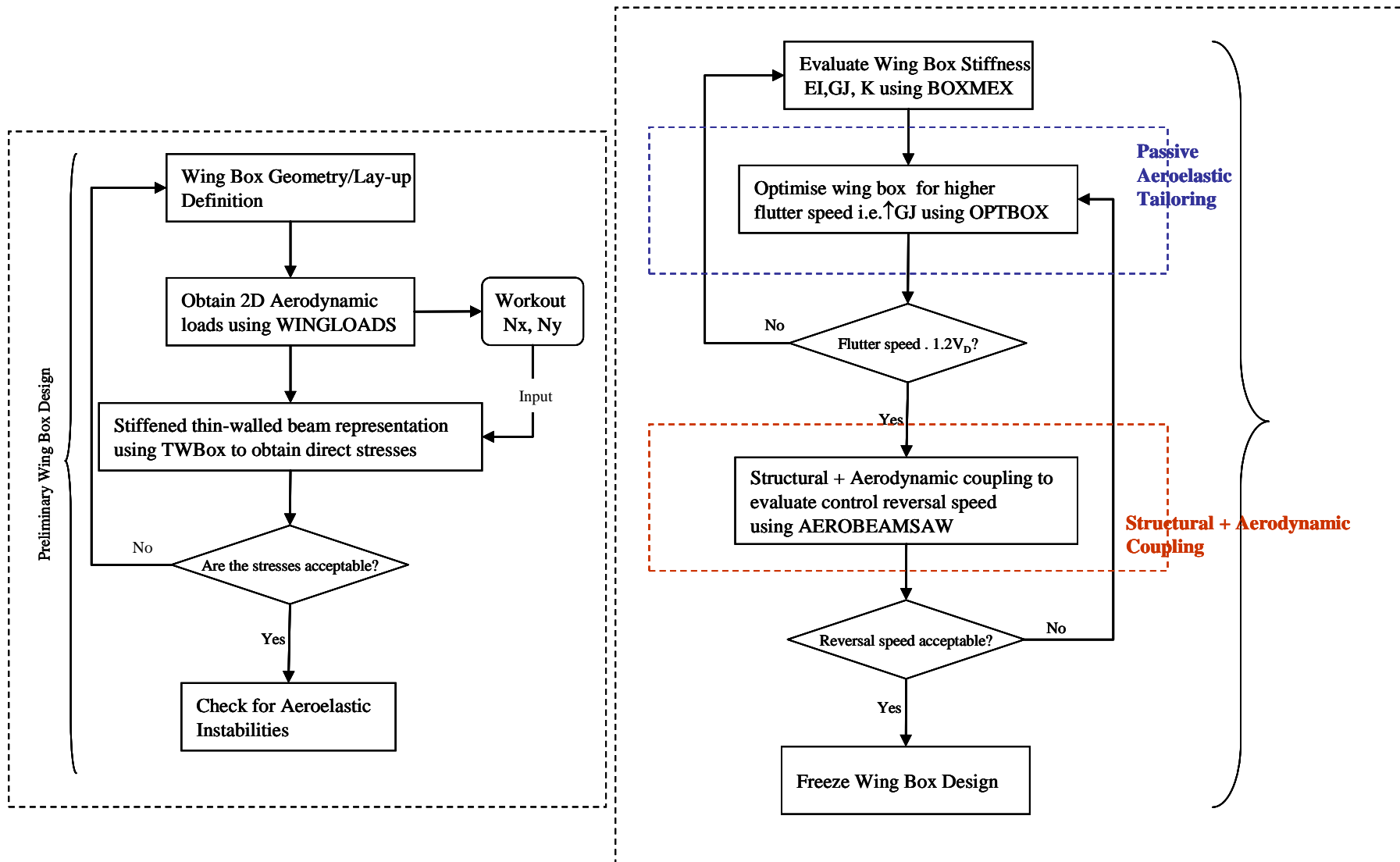


Figure 3.19 Wing Box Design Methodology

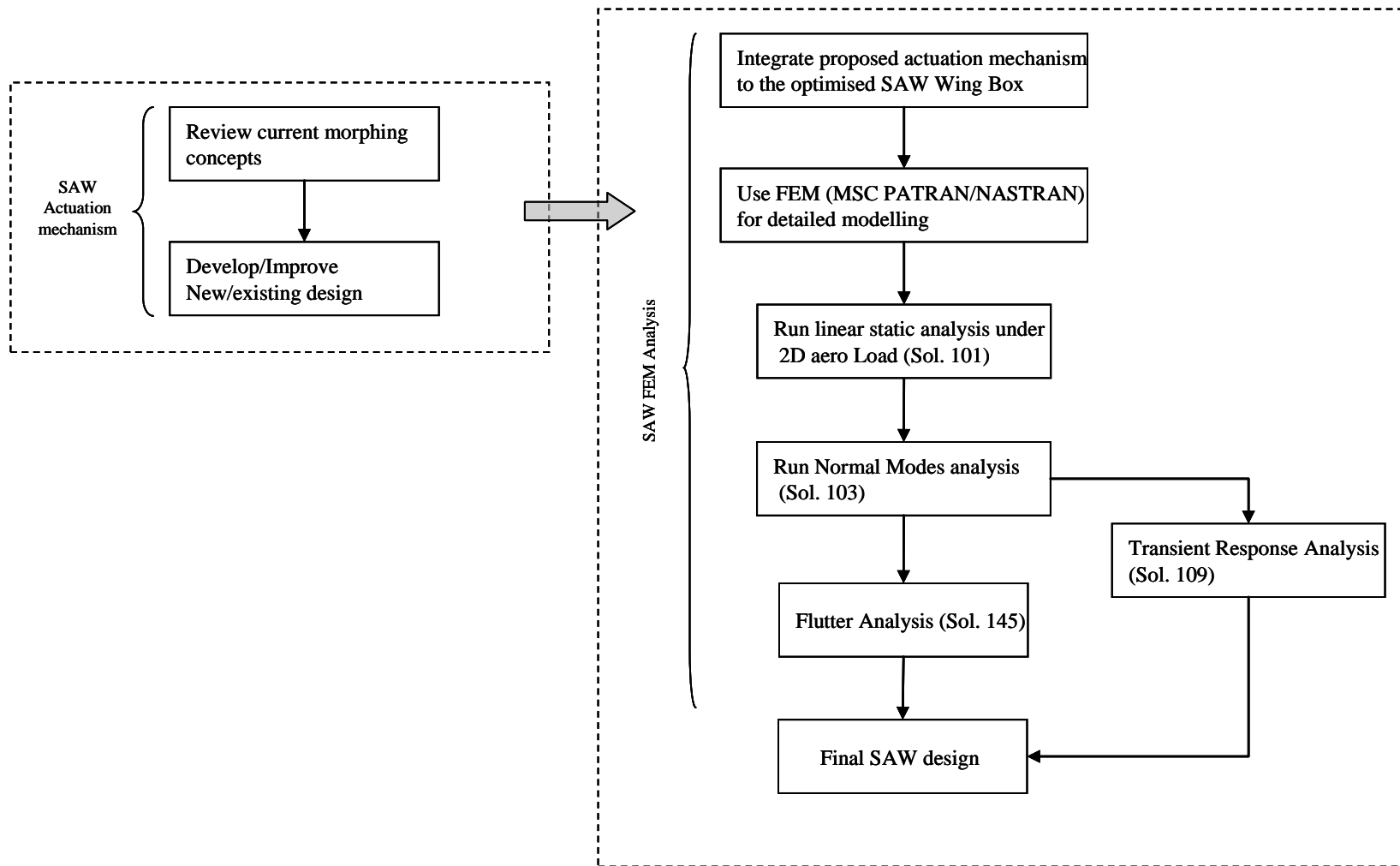


Figure 3.20 SAW Analysis Methodology

Figure 3.19 and Figure 3.20 illustrates the methodology followed in this research using the theoretical material presented in this chapter, in order to design and analyse the SAW design integrated with the proposed actuation mechanism.

Aero-Structural Coupling

Subjected to aerodynamic forces acting on the wing, the aeroelastic equations for each of the beam sections can be represented as;

$$EI_i \frac{\partial^4 h}{\partial y^4} + CK_i \frac{\partial^3 \phi}{\partial y^3} = \bar{q} S_i C_{Li}(\phi, \delta_{TE}, \delta_{LE}) \quad (3.107)$$

$$GJ_i \frac{\partial^2 \phi}{\partial y^2} + CK_i \frac{\partial^3 h}{\partial y^3} = \bar{q} S_i C_{mi}(\phi, \delta_{TE}, \delta_{LE}) + \bar{q} S_i C_{Li} \quad (3.108)$$

where h and ϕ are transverse displacement and twist angle at the end of the i th beam; EI , GJ and CK are the bending, torsion and bending-torsion coupling stiffness of the i th beam; $\bar{q} = \frac{1}{2} \rho V^2$ is the dynamic pressure of air density, ρ , and speed V ; S_i is the section surface area; C_{Li} and C_{mi} represent the aerodynamic lift and pitching moment coefficient of the section, which depends on the aerofoil shape, the section twist angle ϕ , the TE and LE control surface deflection angle δ_{TE} and δ_{LE} ; e_i is the distance between the reference point of C_{mi} and the wing box elastic centre along the beam.

The aerodynamic coefficients for each of the wing sections with deflected LE and TE surfaces are calculated by employing the panel method. By assembly of the spanwise beam models and 2D aerodynamic forces, the static aeroelastic equation of the wing can be established and written in matrix form:

$$[K]\{d\} = \{AF(d, \delta_{TE}, \delta_{LE})\} \quad (3.109)$$

where $[K]$ is the stiffness matrix of the whole wing; $\{d\}$ is the wing deformation vector in terms of the beam sections' h and ϕ ; $\{AF(d, \delta_{TE}, \delta_{LE})\}$ is the aerodynamic force vector including the lifting force and pitching moment acting on the wing, which are dependent on $\{d\}$ especially the twist angle, and the LE and TE control surface deflections.

For a highly flexible wing of large sweepback angle, a geometrically nonlinear and bending-torsion coupled large deformation is expected. To solve the equation in an iterative procedure, Eq. (3.109) is expressed in the following form:

$$[K]\{d_{j+1}\} = \{AF(d_j, \delta_{TE}, \delta_{LE})\} \quad (3.110)$$

Starting from an initial wing shape $\{d_0\}$ and a control surface input, an initial $\{AF(d_0, \delta_{TE}, \delta_{LE})\}$ can be calculated. Under the aerodynamic load, the wing elastic deformation $\{d_1\}$ can be calculated from Eq. (3.110). It will then feedback to calculate $\{AF(d_1, \delta_{TE}, \delta_{LE})\}$ and subsequently the next step $\{d_2\}$. This aeroelastic calculation continues until the maximum difference $\{\Delta d\} = \{d_j\} - \{d_{j+1}\}$ converges to a specified small value. Once this condition is satisfied, Eq. (3.109) is solved for the final solution of $\{d\}$ and $\{AF\}$. A diverge iteration result indicates an unstable system under the specified control case.

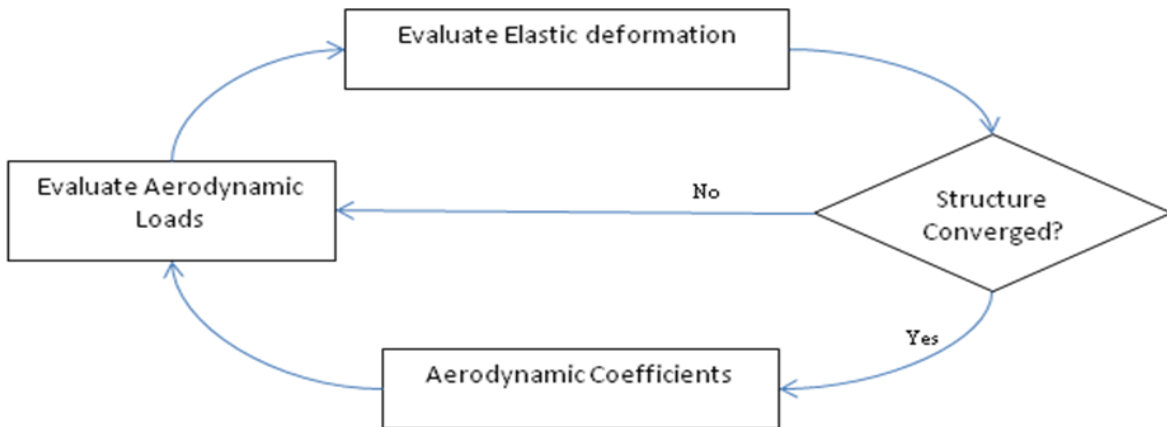


Figure 3.21 Aero-Structural coupling Methodology

4 SAW Actuation Mechanism

In order to identify a favourable aerodynamic shape, initially a 2D aerodynamic study was carried out to evaluate the aerodynamic beneficial effect of a seamless aeroelastic wing. Sections 4.1 - 4.3 summarises the tool selection from a number of available tools and its adaptation in the 2D aerodynamic study. The proposed SAW actuation mechanism along with initial actuation force/power requirements is presented in section 4.4 and 4.5 respectively.

4.1 Aerodynamic Tools

Aerodynamic analysis was carried out for a NACA aerofoil (NACA 0009) using three different types of aerodynamic tools based on panel method: ESDUpac A9931, JavaFoil and USPM (Unsteady Panel Method).

4.1.1 ESDUpac A9931

This program calculates the maximum lift coefficient, the lift coefficient at zero angle of attack and the lift curve of the aerofoil section with high-lift devices deployed at low speeds [103]. The method incorporated is only for free-stream Mach numbers up to $M = 0.25$. In order to carry out the aerodynamic calculation the program reads the required data from a single input file. In the entry of the basic aerofoil geometry the user can specify whether the aerofoil section is 'conventional' or 'modern' type. A modern aerofoil section is classified as a section with a small trailing edge base thickness, large rear camber and has a higher lift coefficient than a 'conventional' section. Calculations can be made at a number of Mach number and Reynolds number pairs. The user is given the option to select from a number of different types of run. In the analysis option number one was selected as the type of run; which calculates C_{LmB} and C_{Lm} . The program also gives the option of selecting different types of high-lift devices. In the analysis the type of trailing-edge flap was considered to be a plain flap with no leading-edge devices.

4.1.2 JavaFoil

The program uses two methods; potential flow analysis and boundary layer analysis, in order to calculate the maximum lift coefficient. Since JavaFoil does not model flow separation, the results could be inaccurate for an analysis beyond stall [104].

4.1.3 Unsteady Panel Method - USPM

The program USPM has been developed to predict the forces on a single aerofoil undergoing pitch and plunge motions based on the assumption of inviscid flow [105]. It consists of two FORTRAN programs, one (DWW) which deals with flat plates, while the other (UPM) is able to predict forces on thick aerofoils. The program DWW uses the method of quasi-steady circulation for a flat plate [105]. UPM in the other hand uses the unsteady panel method.

The input file for USPM consists of 121 points (i.e. x and y) of the aerofoil geometry starting from the trailing-edge along the top surface to the leading-edge and from the leading-edge along the bottom surface to the trailing-edge, the required angle of attack along with the chordwise pitching moment location.

4.1.4 Tool Selection

- a. ESDU A9931 has the advantage of performance efficiency and availability of the source code if needed to combine with a different tool. However, it is not capable of C_p calculations for chordwise loading distribution.
- b. JavaFoil has the advantage of taking stall into account. However, it is limited by the lack of C_p data and source code for integrating the program into our design code.
- c. USPM has the disadvantage of performance efficiency and stall prediction. However, has the advantage of calculating C_L , C_m and C_p for a given aerofoil section.

Having considered these three types of aerodynamic tools, the most appropriate program to perform the rest of the analysis at this stage was chosen to be USPM.

4.2 2-D Aerodynamics

An initial study of the aerofoil camber on aerodynamic performance was carried out using available test data. The result are summarised in the next section.

4.2.1 Camber Effect

The essential aerofoil geometric parameters used in the analysis are shown in Figure 4.1 (a) and the definition of the NACA 4-digit aerofoil series notation is shown in Figure 4.1 (b). The mean line between the upper and lower surfaces is the mean camber line. The amount of this curvature is called camber and is expressed in terms of the maximum mean line coordinate as a percent of chord. The primary purpose of having camber is to increase the aerofoil maximum lift coefficient.

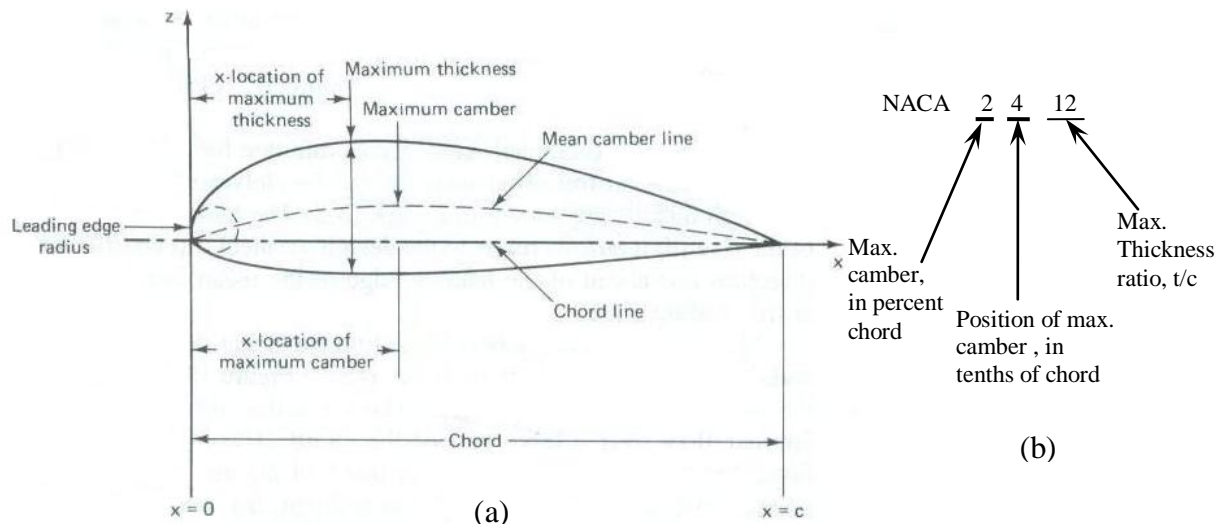


Figure 4.1 (a) Aerofoil Geometric Parameters; (b) Definition of NACA 4-digit series Aerofoil [105].

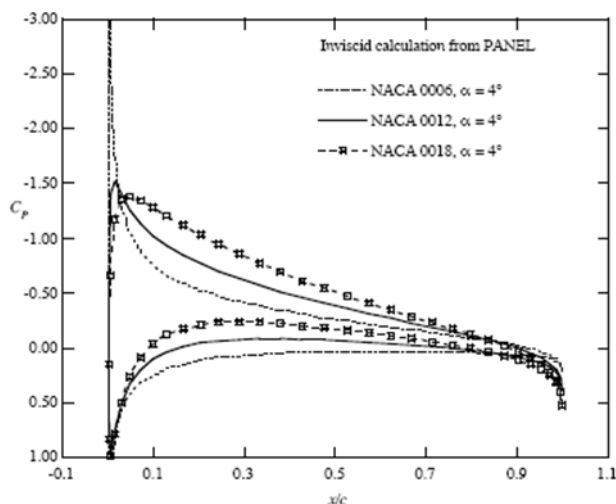


Figure 4.2 Effect of Aerofoil thickness on the Pressure Distribution at $C_L = 0.48$ [106]

The effect of thickness on the pressure distribution is shown in Figure 4.2 at $C_L = 0.48$. As can be seen from the C_p graph, the thinnest aerofoil has a dramatic expansion due to the stagnation point being below the leading-edge point that has a very small radius of curvature. The thicker

airfoil has a milder expansion due to its large leading-edge radius.

The pressure distributions on the cambered airfoil for two different angles of attack at the same lift coefficient are shown in Figure 4.3. It can be seen that the lift coefficient is obtained by a 4% cambered airfoil at 0° angle of attack, whilst the uncambered airfoil would achieve the same lift coefficient at 4° angle of attack. However, as the lift coefficient increases, the angle of attack effect overcomes the camber effect, and the pressure distributions start to look very similar [106].

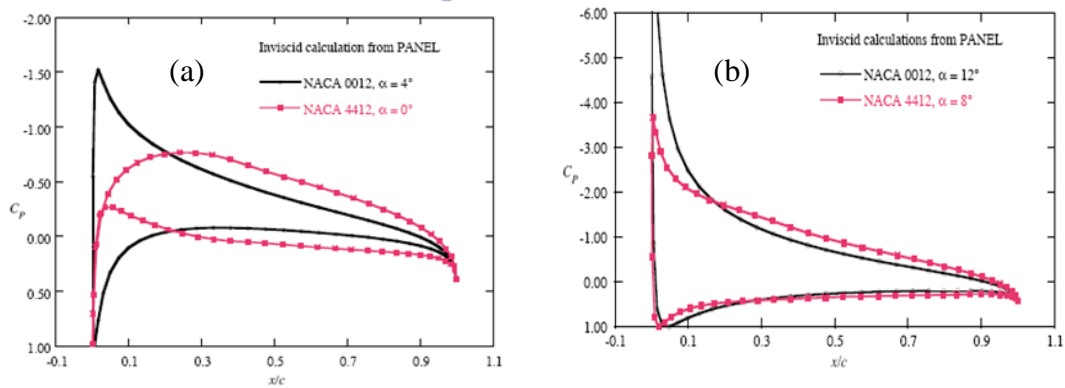


Figure 4.3 Camber effects on Airfoil Pressure Distribution at (a) $C_L=0.48$ and (b) $C_L=1.43$ [106]

Finally, the effect of extreme aft camber has been shown in Figure 4.4. The pressure distribution of an airfoil with aft camber shows that the zero lift pitching moment is high and the upper surface shows a rapid pressure recovery [106].

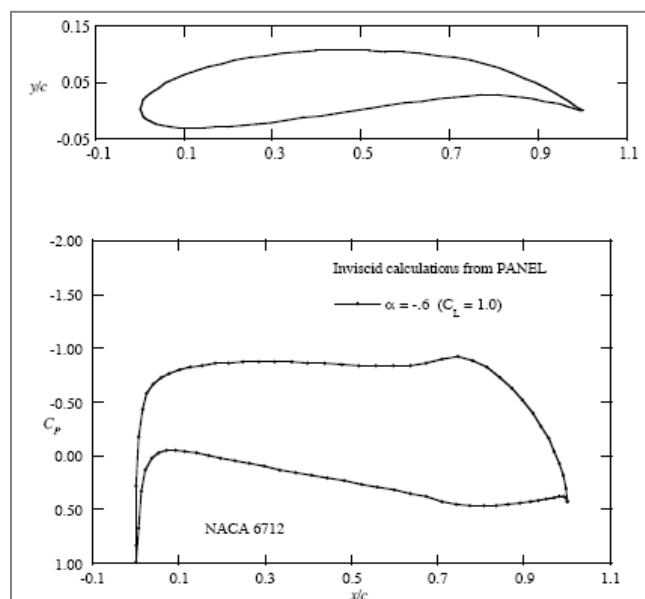


Figure 4.4 Pressure Distribution of an Aft Cambered Airfoil, NACA 6712 [106]

In the following section the effect of maximum thickness, camber and camber position variations are investigated using available test data for cambered NACA 4-digit aerofoils ranging from 6% to 21% thick in 3% increments, 2% to 6% camber in 2% increments and 0.2c to 0.7c camber location in 0.1c increments respectively [107].

A comparison of available test data for NACA 2306 to 6306 in 2% increments in camber is presented in Figure 4.5. As can be seen from this figure, $C_{L_{max}}$ increases with increasing camber for the three different thicknesses.

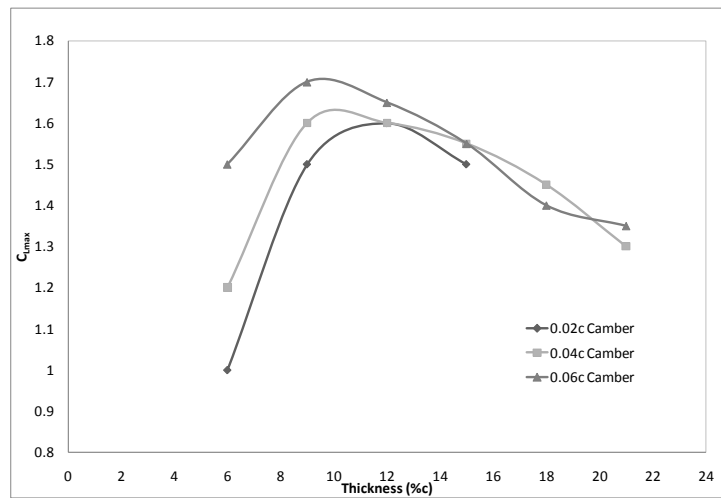


Figure 4.5 Comparison of Camber and Thickness Effect on $C_{L_{max}}$ [107]

Aerofoil thickness variation has two main performance effects. A drag penalty and a reduction in lift curve slope due to increased thickness [108]. The behaviour of lift is significantly different, with increasing thickness [108]. As can be seen from the above figure, $C_{L_{max}}$ peaks at 9%c thickness for all three camber ratios, i.e. 2% to 6% and then shows a linear decrease for increasing aerofoil maximum thickness. From 6% to 9% thickness there is a 50% increase in $C_{L_{max}}$. It can also be seen that the thinner the aerofoil, the effect of camber on $C_{L_{max}}$ is much greater, i.e. at 6% thickness; $C_{L_{max}}$ increase for different camber ratios is much higher relative to the rest of the thicknesses.

Further analysis was carried out to investigate the possible benefits of varying the magnitude and distribution of camber. However, from the available test data it was evident that the position of camber has no significant effect on the maximum lift coefficient. However, there is a slight increase in $C_{L_{max}}$ when the camber position is moved towards the trailing-edge.

4.3 Two Dimensional Aerodynamic Analysis

A comparison of C_L obtained using the three aerodynamic tools (ESDU, JavaFoil and USPM) with available test data for the aerofoil NACA 0009 is presented in section 4.3.1. The primary aim was to illustrate how the flexibility of the aerofoil affects the aerodynamic characteristics, i.e. C_L . The calculations were carried out using the USPM program.

4.3.1 Validation of Aerodynamic Tools

A comparison of the lift curves for NACA 0009 from the aerodynamic tools and test data are presented in Figure 4.6. The results were obtained for Reynolds number 9E06.

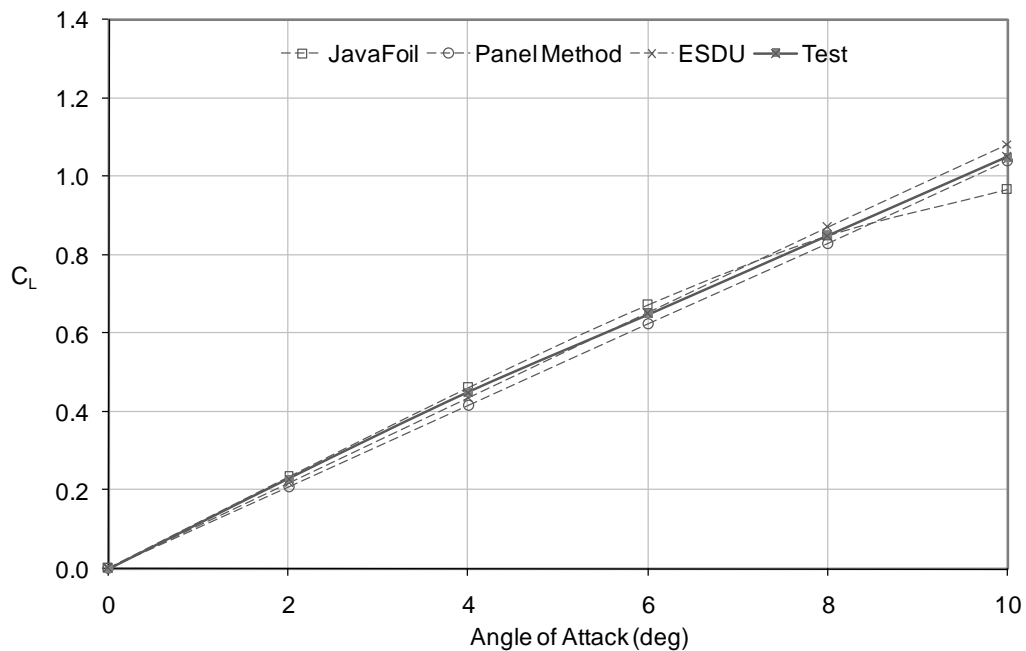


Figure 4.6 Comparison of C_L by using the three different tools and test data

As can be seen all four curves exhibit a linear lift range. The C_L curves obtained using the different aerodynamic tools agree very well with the available test data. Lift coefficients calculated by the aerodynamic tools has an inaccuracy of approximately 3% compared to available test data for NACA 0009.

4.3.2 Effect of Trailing-edge Deflection

In the following section the aerodynamic effect of the trailing-edge deflection has been studied. Initially preparation of data and how the trailing-edge has been deflected for the equivalent trailing-edge flap angle are being discussed.

Assumption of a Trailing-edge Deflection

In order to carry out the aerodynamic analysis, three different types of trailing-edge (TE) deflections have been considered:

- 1) Flexible TE with bending angle due to pressure;
- 2) Flexible TE with bending angle proportional to chordwise length;
- 3) Rigid body TE of constant rotating angle.

The type-1 deflection assumes that the rear part of an aerofoil deforms like a cantilever beam under tapered distributed pressure as shown in Figure 4.7 (a). The flexible rear part starting from 50% chord is divided into six sections as shown in Figure 4.7 (b).

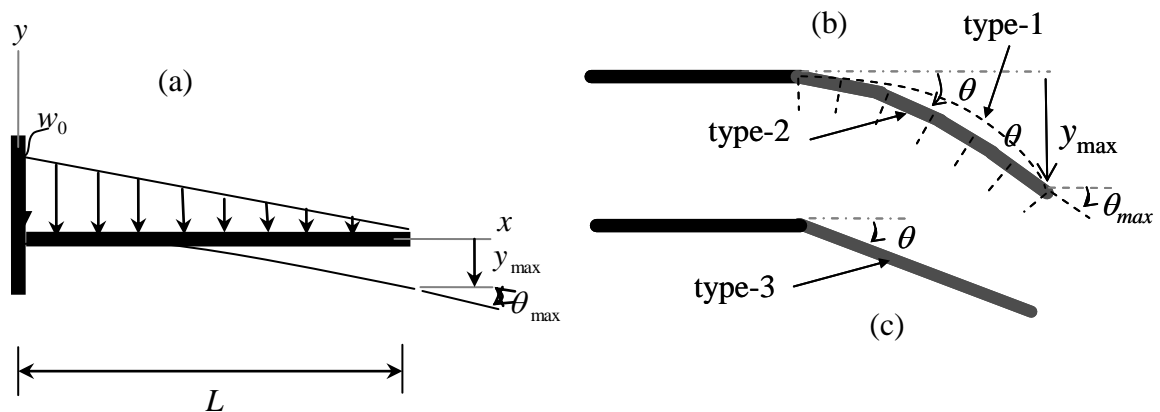


Figure 4.7 (a) Beam bending under pressure; (b) Flexible & (c) R-B TE bending angles

The y – coordinate along the deflected beam neutral axis in x -direction at the six different chordwise locations is calculated using Eqs. (4.1) – (4.3).

$$\theta_{\max} = \frac{w_0 L^3}{24EI} \quad ; \quad y_{\max} = \frac{w_0 L^4}{30EI} \quad (4.1)-(4.2)$$

Where $w_0 = \frac{24}{L^3} EI \theta_{\max}$; and y_{\max} can also be written in terms of θ_{\max} by substituting the expression for w_0 into Eqn. (4.2):

$$y_{\max} = \frac{24}{30} \theta_{\max} L \quad (4.3)$$

The type-2 deflection assumes that the flexible rear part of an aerofoil deforms with a bending angle in proportion to the distance L measured from the 50% starting point. The bending angle increases linearly towards the TE and is calculated based on a given constant Ratio: $\theta = \text{Ratio} \times x$, where $\text{Ratio} = w_0/EI$ is user specified. The associated deflection remains the same as Eqn. (4.3). Obviously for the same TE angle, the type-1 and type-2 will result in the same y_{\max} . However the type-1 deflection normally starts with smaller bending angle and gradually increases towards the TE, while the type-2 deflection is the opposite as illustrated in Figure 4.7 (b).

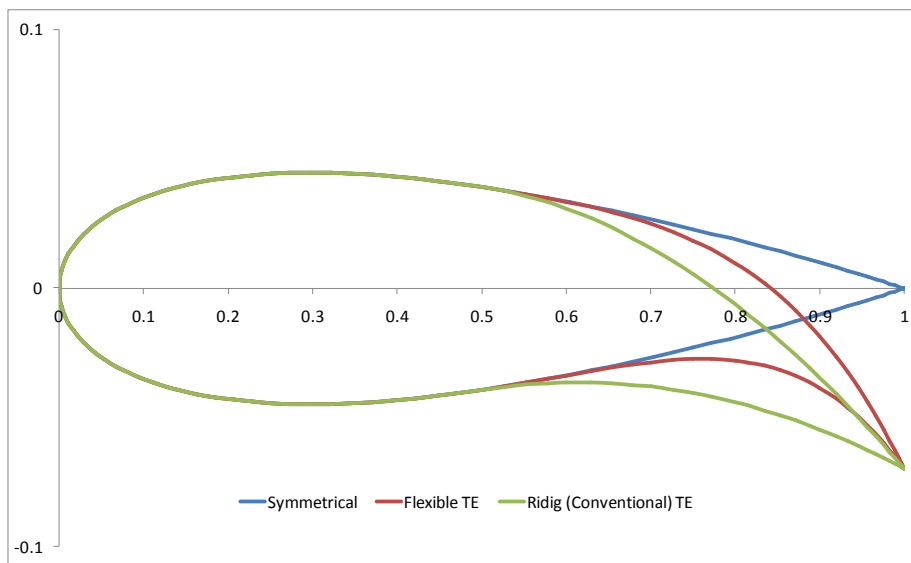


Figure 4.8 Flexible and Rigid TE Deflections of a Symmetric Aerofoil

The type-3 deflection assumes that the rear part of an aerofoil rotates like a rigid-body flap with a specified constant angle $\theta = \text{Ratio}$ and the deflection linearly increase $y_{\max} = 24 \times \theta \times L / 30$ along the chord as illustrated in Figure 4.7 (c). By setting the beam neutral axis coincide with the aerofoil central line, the y-coordinate along the upper and

lower surface of the deflected aerofoil at any chordwise x-coordinate can also obtained by calculation and interpolation.

Giving a R-B TE bending angle in type-3, an equivalent flexible TE bending angle for type-1 and type-2 can be obtained by trial and error using different input Ratio w_0/EI . It is noted that for the same TE angle θ_{max} , the TE deflection y_{max} from different types is normally different. Table 4.1 shows the input ratios w_0/EI and the resulting TE deflections from type-1 and type-2 models for the required TE angles. As can be seen from the table, the maximum deflection for a required TE bending angle of 5° is approximately 3.5% of the aerofoil chord, i.e. if the aerofoil chord is one, the flexible trailing-edge deflection is 0.035. A program named 'Aerodata' was written in FORTRAN to calculate θ , y_{max} and deformed aerofoil geometry for the three deflection types based on its original aerofoil (x, y) coordinates.

Table 4.1 Ratios and deflections in option-1 and type-2 for equivalent TE angles

θ_{max} (deg.)	Ratio w_0/EI	Ratio w_0/EI	y_{max} / c (%)
	(Type-1)	(Type-2)	(type-2)
5	-16.75	-0.1744	3.49
10	-33.50	-0.3489	6.98
15	-50.26	-0.5233	10.47
20	-66.99	-0.6978	13.96
25	-83.75	-0.8725	17.45
30	-100.48	-1.0467	20.93

Aerodynamics of an Aerofoil with Trailing-edge Deflection

The Figure 4.9(a) – (c) show the comparison of C_L between the rigid body (R-B) and the equivalent flexible trailing-edge flap deflections. Using the trial and error method, i.e. keeping the trailing edge deflection obtained by the rigid body configuration constant, the corresponding flexible trailing edge deflection was calculated using the tool Aerodata. Using the deflected aerofoil geometry for an R-B trailing-edge and the equivalent aerofoil geometry for the flexible trailing-edge the aerodynamic characteristics (C_L, C_m) were obtained using the aerodynamic tool USPM. The

comparison was made for a range of trailing edge flap deflections, i.e. $\delta_t = 5^\circ, 10^\circ$ and 15° .

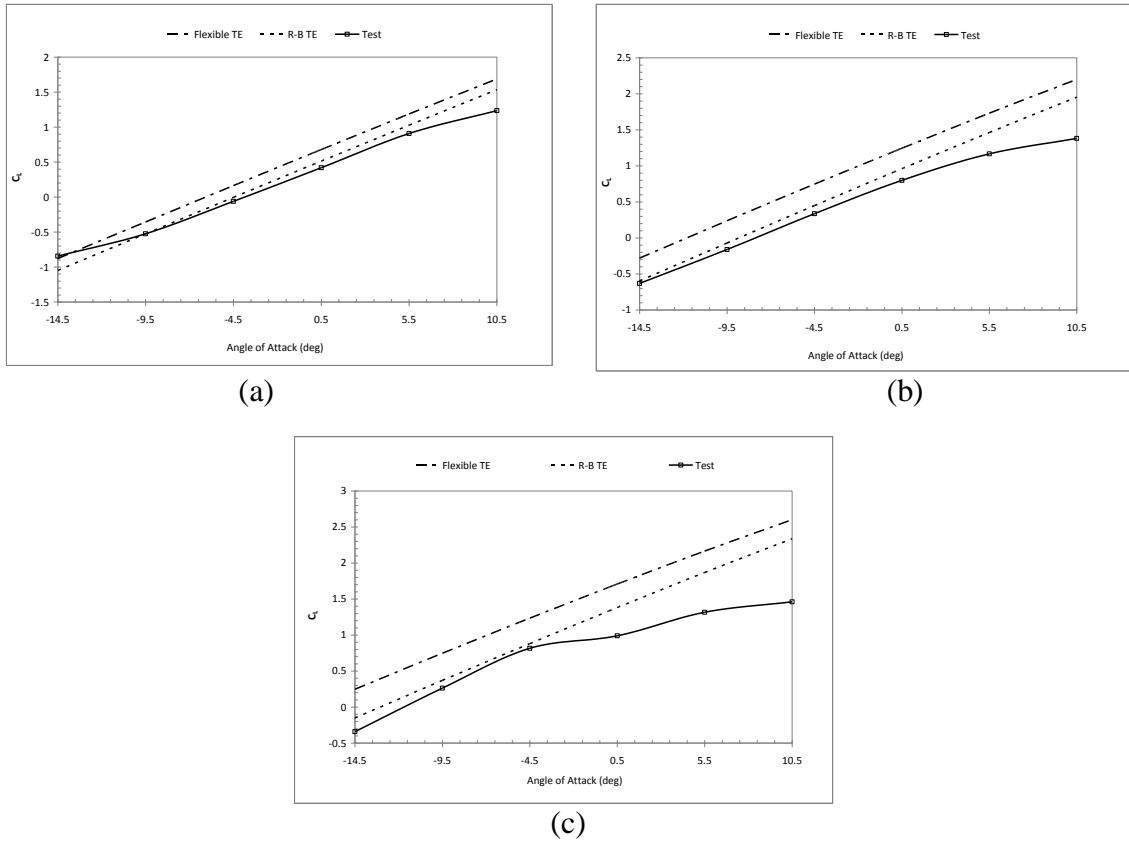


Figure 4.9 CL Comparison of Flexible and Rigid Trailing-edge at (a) $\delta_t = 5^\circ$; (b) $\delta_t = 10^\circ$; (c) $\delta_t = 15^\circ$

Figure 4.9(a) – (c) shows the comparison of C_L between the rigid body, flexible trailing-edge configurations and the available test data of NACA 0009 with a 0.5-chord flap. For the case where the trailing-edge is being considered to be rigid, i.e. the rear section of the aerofoil from 0.5-chord is being rotated down to the required flap angle, δ_t . The C_L results are very close to the test data up to around -4.5° for flap deflections of $\delta_t = 5^\circ, 10^\circ$, and 15° for the rigid body case. For the case where the trailing-edge undergoes flexible bending, i.e. the rear 0.5-chord of the aerofoil is being deflected to the equivalent flap angle. For this case, although the trailing-edge deflection at the tip is almost the same as the rigid configuration, the bending angle along the chord is actually smaller compared to the rigid body case. However, it can be seen from that C_L results

for a flexible TE configuration is higher than the rigid body case and the available test data for each flap angle.

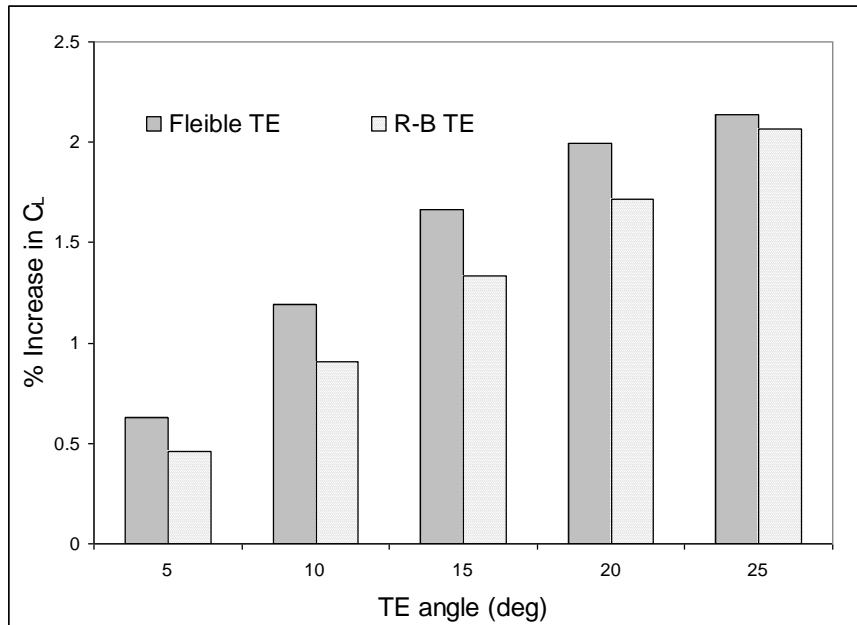


Figure 4.10 C_L Increase between R-B and Flexible TE deflections at $AOA=0^\circ$

At lower TE deflections, the effect of having a flexible TE as oppose to a rigid TE shows a significant increase in C_L i.e. approximately 10% increase. This aerodynamic beneficial effect due to the favourable TE shape will be incorporated in the proposed actuation mechanism later on in this thesis.

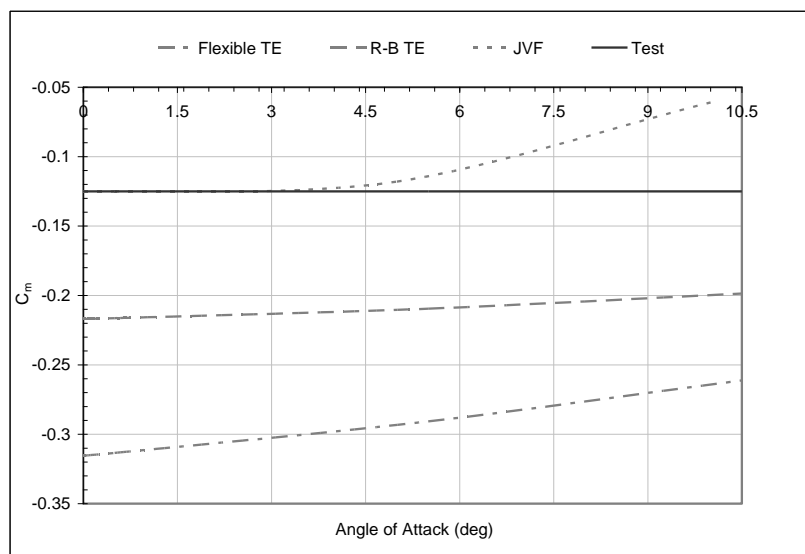


Figure 4.11 C_m Comparison of Flexible and Rigid Trailing-edge at $\delta_t = 15^\circ$

Figure 4.11 shows a comparison of C_m obtained for the two trailing-edge configurations (i.e. flexible and rigid), relative to Javafoil results and available C_m test data. The pitching moment for the rigid configuration is much closer to the test data and Javafoil, compared to the flexible configuration C_m results. However, the results obtained through the panel method was carried out assuming the elastic centre to be at the pressure centre, but the test data and the Javafoil results takes the elastic centre to be further back for a flap down configuration. This is why there is a difference between the test data and the panel method data presented.

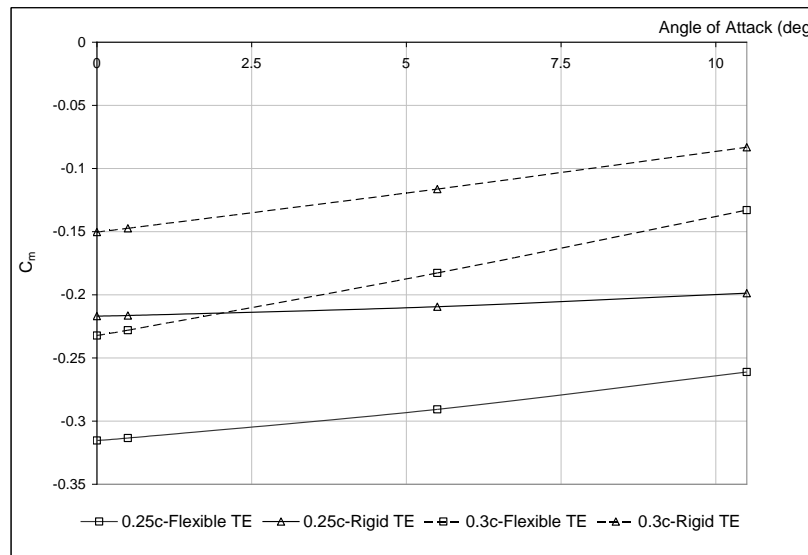


Figure 4.12 C_m Comparison of Flexible and Rigid Trailing-edge at $\delta_f = 15^\circ$

Figure 4.12 represents the C_m results about the pressure centre at 0.25c and elastic centre at 0.30c obtained for the NACA 0009 aerofoil with both trailing edge configurations. As can be seen the C_m results are less negative about the elastic centre located behind the pressure centre. Also it has been noted that the C_m for the flexible configuration is more negative compared to the rigid configuration, due to the higher lift being generated by the flexible configuration. However, if the elastic centre is moved further backwards, the C_m could be expected to be reduced further and be close to being more positive or else being less negative. This means that the induced nose down pitching moment as a result of the flexible TE will be reduced.

4.3.3 Pressure Distribution

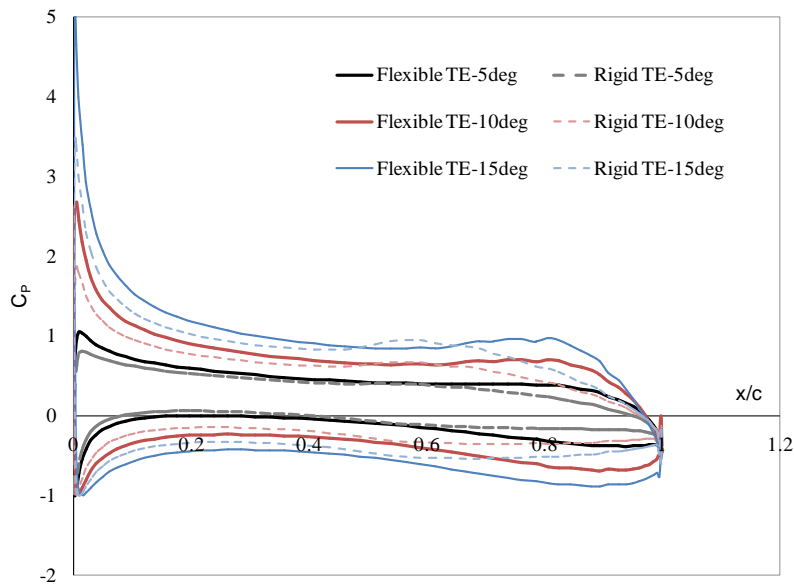


Figure 4.13 Comparison of Flexible and Rigid Trailing-edge at (a) $\delta_t = 5^\circ$; (b) $\delta_t = 10^\circ$; (c) $\delta_t = 15^\circ$

Figure 4.13 summarises pressure distributions for both flexible and rigid trailing edge configurations at AOA = 0° and at trailing edge angle (δ_t), 5° , 10° and 15° respectively. The pressure distribution for the flexible trailing edge deflection shapes shown, result in an increase in the pressure distribution compared to the rigid body trailing edge which leads to a higher C_L . The negative effect of the C_m on the aeroelastic phenomena are analysed in chapter five.





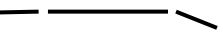



4.3.4 Leading and Trailing Edge combinations

As it was presented in section 4.3.2, it is evident that a flexible control surface results in a more negative pitching moment as oppose to a conventional flap mechanism. This negative pitching moment could result in a control reversal problem (see Chapter 5). The feasibility of suppression of control reversal using both leading- and trailing-edge control surfaces has been studied by many researchers [109-111]. By examining the lift effectiveness of the wing section for various deflection ratios of the leading-edge and trailing-edge surfaces, experiments and analytical methods have been used to

demonstrate control reversal behaviour and validate the concept of using leading-edge and trailing-edge control to suppress and possibly eliminate control surface reversal [111].

As a potential solution for the control reversal occurring in flexible wing structures, it was suggested to have both leading and trailing edge control surfaces to minimise this effect and increase the control effectiveness of flexible wing structures compared to conventional (rigid) wing structures. A 2-D aerodynamic analysis was carried out for a NACA 0009 symmetric aerofoil having both leading and trailing edge deflected. The leading edge was defined as 30% of the chord whilst the trailing edge was defined as 40% of the chord. Table 4.2 summarises the LE and TE combinations considered in this 2-D aerodynamic study.

Table 4.2 Summary of LE and TE combinations considered

Case	Description	
1	Both leading and trailing edges deflected up	
2	LE deflected up and TE not deflected	
3	LE deflected up and TE deflected down	
4	LE not deflected and TE deflected up	
5	LE not deflected and TE deflected down	
6	LE deflected down and TE deflected up	
7	LE deflected down and TE not deflected	
8	Both LE and TE are deflected down	

Case 1 – As the leading edge deflection remains the same and the positive trailing edge deflection is increased, the C_L decreases whilst the C_m increases and becomes more positive. For the case where the positive leading edge deflection is increased whilst the trailing edge is the same, C_L remains unchanged as can be seen from Figure A.1 (see

Appendix A) and C_m becomes more positive as before due to the positive leading edge deflection.

Case 2 – This shows the effect of the positive leading edge deflection on C_m . As before the results show that a more positive C_m can be achieved by a positive leading edge deflection. However, since the trailing edge remains at 0^0 deflection, the C_L obtained is the same for both cases (see Figure A.2 in Appendix A).

Case 3 – As the leading edge deflection remains the same and the negative trailing edge deflection is increased, the C_L increases whilst the C_m decreases. For the case where the positive leading edge deflection is increased whilst the trailing edge is the same, C_L remains unchanged as can be seen from Figure A.3 (see Appendix A) and C_m becomes more positive as before due to the positive leading edge deflection.

Case 4 – This case study shows that as the trailing edge is deflected up the C_L decreases for increasing positive trailing edge deflection. However, C_m becomes more positive with increasing positive trailing edge angle.

Case 5 – As can be seen from Figure A.5 (see Appendix A), the C_L increases with increasing trailing edge deflection down, however, C_m becomes more negative.

Case 6 – As the leading edge deflection remains the same and the positive trailing edge deflection is increased C_L decreases as expected due to the positive deflection of the trailing edge, however, the C_m increases. For the case where the negative leading edge deflection is increased whilst the trailing edge remains the same, C_L remains unchanged as can be seen from Figure A.6 (see Appendix A) and C_m becomes more negative.

Case 7 – This shows the effect of the negative leading edge deflection on C_m . The results show that C_m becomes more negative with increasing negative leading edge

deflection. However, since the trailing edge remains at 0^0 deflection the C_L obtained is the same for both cases (see Figure A.7 – Appendix A).

Case 8 – As the leading edge deflection remains the same and the trailing edge deflection is increased the C_L increases due to the negative trailing edge deflection, whilst the C_m decreases and becomes more negative as expected. For the case where the negative leading edge deflection is increased whilst the trailing edge remains the same, C_L remains unchanged as can be seen from Figure A.8 (see Appendix A) and C_m becomes more positive as before due to the positive leading edge deflection.

Figure 4.14 and Figure 4.15 show the effect of leading and trailing edge deflections on C_L and C_m respectively at $AOA = 0^0$. As can be seen from Figure 4.14, the most suitable control surface combination to achieve a higher C_L would be to deflect both leading and trailing edges down. However, Figure 4.15 shows that this combination will result in a significantly more negative C_m . From the study cases it was apparent that a positive leading edge deflection would result in a more positive C_m . Also a positive trailing edge deflection would have the same effect on C_m . Hence, the best possible solution would be to initially have a positive leading edge deflection and a negative trailing edge deflection until the required C_L is achieved, and before this higher C_L result in control reversal, the trailing edge control surface could be deflected up in order to counteract the more negative C_m caused due to the higher C_L . Therefore from the list of study cases, a combination of Cases 1 and 3 would be suitable in order to overcome the control reversal phenomenon.

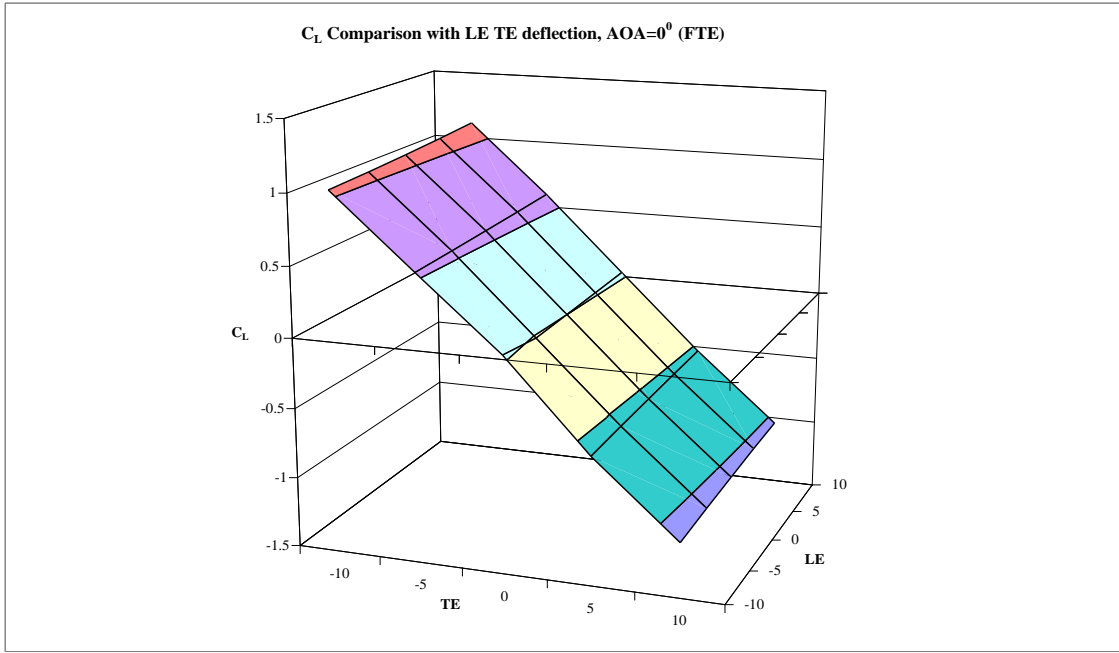


Figure 4.14 Leading and Trailing edge deflection effect on C_L

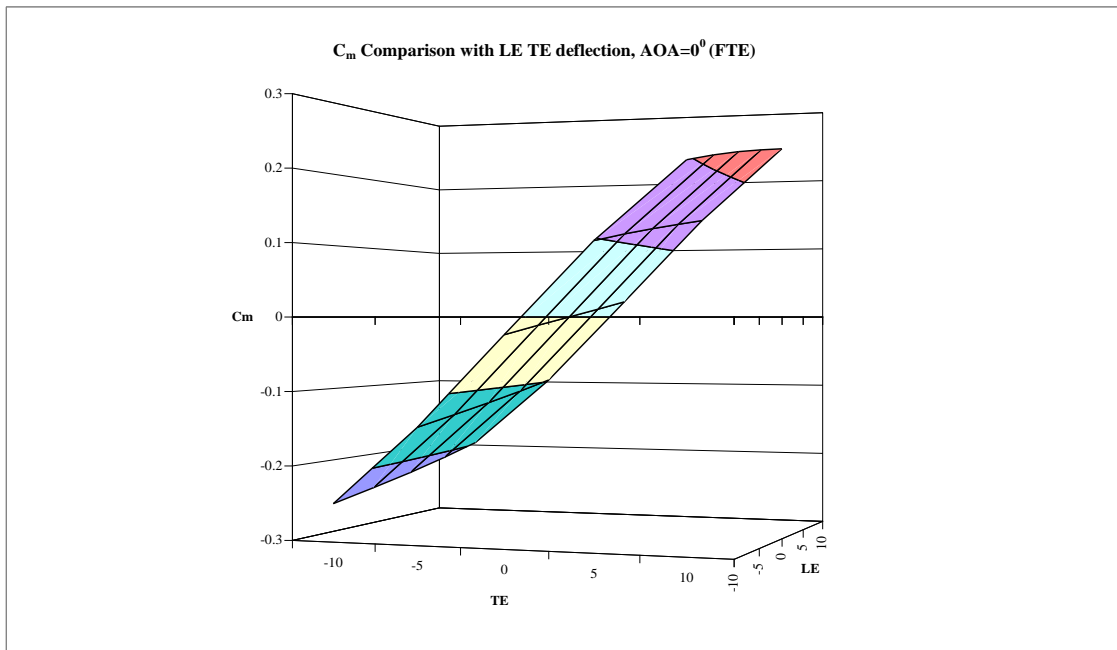


Figure 4.15 Leading and Trailing edge deflection effect on C_m

4.4 Actuation Mechanism

An eccentric beam design concept for deflecting a flexible wing control surface was initiated by the DARPA Smart Wing project [112, 113]. Eccentuation was a concept developed in 1970s for variable camber control surfaces. This concept proposes an eccentuator to convert a rotational input motion into a vertical and lateral displacement at the output end, Figure 4.16 [112 - 115]. The output end of

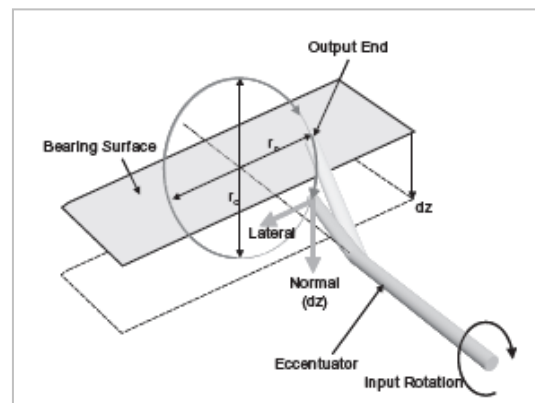


Figure 4.16 Eccentuator Mechanism [112]

the curved tube is connected to a bearing surface which is moved up or down depending on the direction of the input rotation. At 90° eccentuator rotation, the control surface is fully deployed, and zero actuation force is required because the entire external load is transferred into the substructure. One of the disadvantages in this design was the accompanying spanwise and chordwise lateral motion of the output end which results in a sliding motion on the bearing surface [112-114]. This was later eliminated by rotating the curved beam within a carrier cylinder [114, 115].

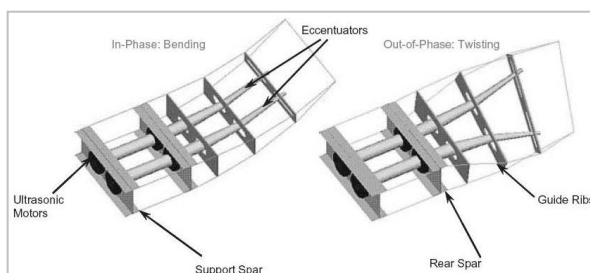


Figure 4.17 DARPA Eccentuator Concept [112]

successful, displaying numerous shape configurations with a maximum deflection of 20° at rates up to $80^\circ/\text{sec}$.

A demonstrator was manufactured by DARPA, which had a 2.8m Span, with a 2.5m chord length and weighed 273kg. The demonstrator was tested in a wind tunnel at Mach 0.8 with dynamic pressures of up to 14,400 Pa [112]. The demonstration was deemed to be

4.4.1 SAW Actuation Mechanism Design

The current actuation mechanism concept was based on the concept presented in the DARPA smart wing project. As this concept leads to a simple mechanism, it is adapted and improved in the current SAW actuation mechanism design. The common feature of the design is the eccentric curved beam, which converts an actuated rotation motion into a vertical displacement along the beam. The required TE chamber shape is determined by the tube curvature at all rotating angles, see Figure 4.18. The beam curvature has been defined as optimum shape achieved from section 4.3.2, in favour of the aerodynamic performance. Another important parameter is the length of the beam which should correspond to the percentage of the chord to be deflected. Finally, the most challenging design feature would be to link this rotating beam to the morphing wing skins.

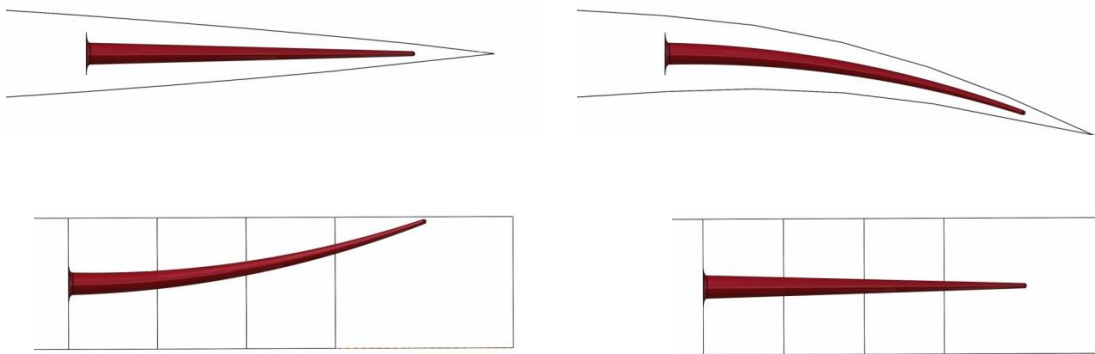


Figure 4.18 Curved Beam Concept

The wing deformation has to be equal to the defined beam curvature. This would require a solid link between the curved beam and the wing skins. Since the movement of the beam is rotational, the use of circular discs was considered as a solution. However a major issue is encountered from the relative movement between the discs and the morphing wing surfaces.

Any particular disc will be in contact with both the upper and lower skin stringers; however the skins will be travelling in opposite directions to each other as shape change is effected, see Figure 4.19. During the rotation, in addition to its vertical motion, any point on the disc circumference will also have a horizontal movement induced by the

increasing beam curvature. The motion of the discs along the stringers therefore requires careful consideration to reduce chordwise sliding friction to a minimum.

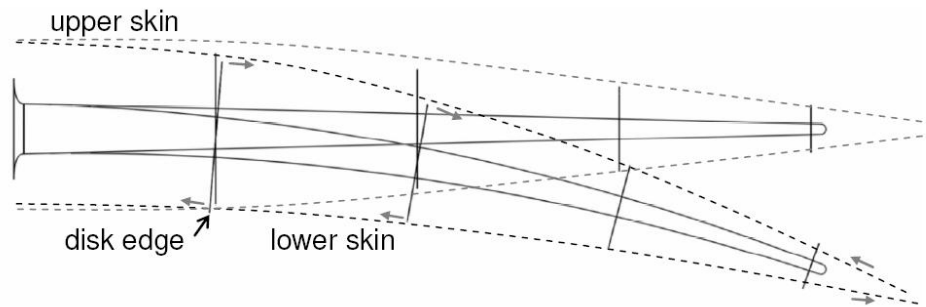


Figure 4.19 Illustration of the relative motion of the discs and the TE skins

Considering the wing skins, a fixed point on the surface has its two coordinates changing during the warping: vertically and horizontally (chordwise). For small angles of bending, this last motion can be approximated as the horizontal component of a circular arc. As a result and still in the case of a downward rotation, a fixed point on the upper wing surface W_{up} will move backward while one on the lower surface W_{lp} will move forward.

Hence placing the discs perpendicular to the curved beam axis would lead to a sliding effect between the discs attached to the curved beam and the wing skins. However for many reasons including the resulting wear damage on the materials, this is not acceptable and the following designs were proposed as potential solution to that issue.

At the initial stages, design solutions were expected to allow the horizontal relative motion of the parts by having a spherical track, which will allow the disc to slide on the wing surface. However this would mean that only a single point on the disc will be in contact with the track, restricting the relative rotational motion between the curved beam and the disc. A possible solution to this would be to add a pivot joint between the beam and disc which would consequently make the mechanism more complicated.

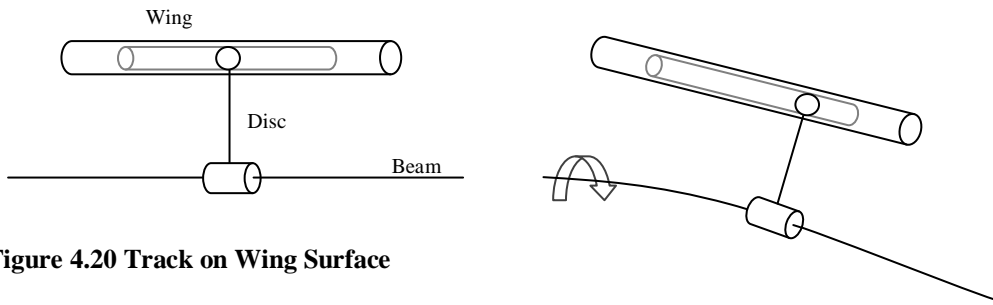


Figure 4.20 Track on Wing Surface

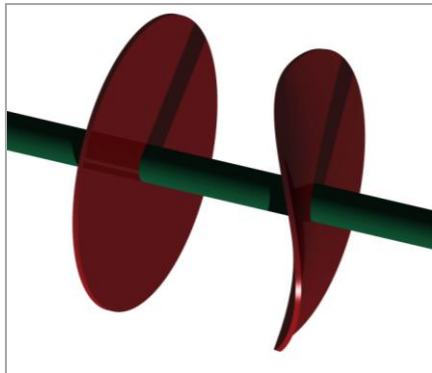


Figure 4.21 Twisted disc concept

Another design proposed was to have a twisted disc. By having the disc perpendicular to the beam curve, this design proposes to twist it so that at any given time, the outer most point on the disc should follow exactly the same path of the fixed point on the wing surface in the spanwise direction. Given that the beam only needs a $\pm 90^\circ$ rotation to achieve a maximum deflection of the TE, only half of the disc will required to be twisted. The main feature of this

design is to find out the correct shape for the twisted disc section. It could be determined by combining both the horizontal movement (chordwise) of the wing and the lateral motion (spanwise) of the disc during the beam rotation. The resulting 2D curve could then be used in order to obtain a 3D twisted disc. Although the determination of the twisted shape is not very complex the complexity of the shape will cause manufacturing constraint, hence would not be economically feasible.

Finally the proposed design for this challenging issue of chordwise sliding of the discs was based on the same concept as the previous solution but includes a notable simplification. Rather than twisting the disc, it is simply rotated along the vertical axis so that the movement of outermost point of the disc during rotation changes its direction (from backward to forward for example) to remain on the same line as the wing skin i.e stringers.

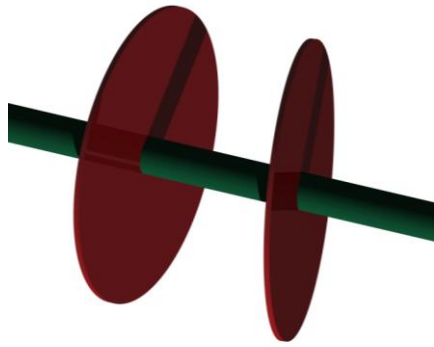


Figure 4.22 Disc at a setting angle

The disc remains planar but in a new plane which is set at a setting angle to the initial plane (normal to the beam curve) as shown in Figure 4.22. The setting angle of the plane can be adjusted in order to minimise the gap between the motion of the disc and the wing surface. However, if a twisted disc were to be used this relative movement can be accurately modelled to have no gap between the disc motion and the wing surface motion. In

exchange for this loss in accuracy, the manufacturing complexity is significantly reduced. The determination of the setting angle along the curved beam based on a symmetric aerofoil is presented in Appendix B.

This disc mechanism along with the curved beam is a key design improvement made in the current actuation mechanism. A number of these discs of different sizes could be mounted along the curved beam to form a torque tube actuation mechanism. Figure 4.23 illustrates the current curved beam and disc configuration used in the SAW to replace the original design.

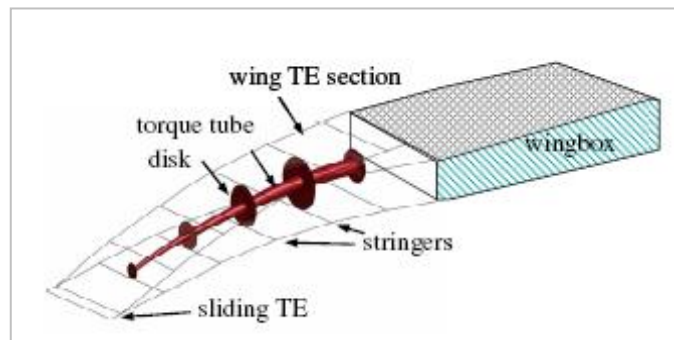


Figure 4.23 Eccentric Tube Disc design

In this SAW design as illustrated in Figure 4.23, the discs of different sizes are mounted along the beam with their edges in contact with the upper and lower skin stiffeners. The discs work as an active rib to support and maintain the TE chordwise shape and force it to deform as the beam is being rotated. The discs are mounted at different angles to the beam axis to keep the disk edges move in a straight track in the spanwise direction to minimise the chordwise sliding and friction between the disc edge and the stiffener.

These discs will allow the eccentuator to rotate with reduced contact friction, whilst still providing the necessary support to the wing skins.

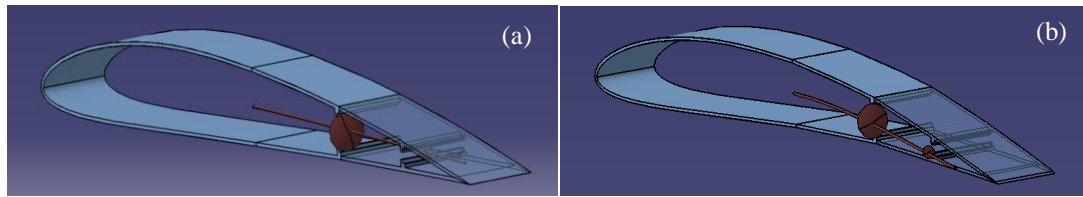


Figure 4.24 SAW Actuation mechanism

As the curved beam is rotated under the actuator operation, the actuator torque is distributed to the discs and converted to compressive forces acting on the stiffeners to bend the skin and deflect the TE section, Figure 4.24 (b). The bending moment produced by the skin elastic force and aerodynamic pressure can be calculated in order to work out the required actuation torque and power.

One advantage of the eccentuator concept is that the ‘hinge moment’ of the deflected surface is passed into the main wing box structure through the curved beam structure (i.e. the beam is a structural load bearing feature) rather than through the wing skins, which allows the skins at the TE sections to be less important from a structural standpoint and therefore more flexibility can be afforded to the skins.

Intention is to link two eccentuator together and to drive these from a single motor and actuator mechanism assembly. In this regard there are a number of possible motor and actuator configuration options. The drive could be provided from either a rotary motor or a linear motor. The mode of operation of these motors is very different and their capabilities are different also.

With a linear motor providing the required actuation and the eccentuator beams requiring some form of rotary drive input, there will need to be a motion conversion in order to allow the two systems to work effectively together. Using influences from other industries, such as the automotive industry, it is possible to see such rack and pin down based designs working well, such as Windscreen Wipers.

4.4.2 SAW Open TE Design

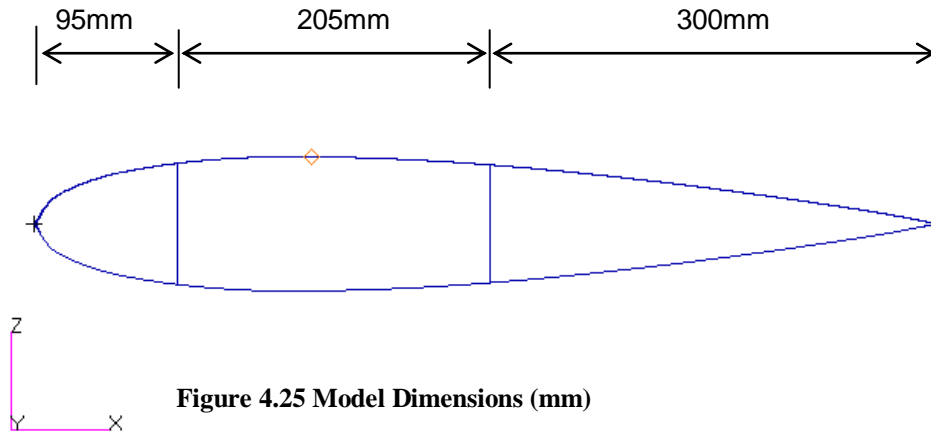


Figure 4.25 Model Dimensions (mm)

A finite element analysis was carried out in order to justify the design selection of the SAW, to have an open TE mechanism. The analysis was carried out for two simple wing models to calculate the translational magnitude of the displacement and the load requirement in order to deform the structure. Model 1 represents a closed TE design Model 2 represents the current design for the SAW concept, with an open TE design. The axis system for all the models is such that, the x axis lies along the chord, z axis is along the vertical plane of the model, and y axis is along the span of the wing models.

Table 4.3 Material Properties

Material	E_1 (GPa)	E_2 (GPa)	G_{12} (GPa)	ν_{12}	X_t (MPa)	X_c (MPa)	Y_t (MPa)	Y_c (MPa)	S (MPa)	ρ □ (Kg/m ³)
Carbon-Epoxy (Ply thickness 0.125mm)	135	9.5	4.9	0.3	1680	1100	61	244	90	1600

Closed TE Design

The closed TE design was modelled in MSC/NASTRAN in carbon/epoxy laminate of symmetric layup $[0/45/90/-45]_s$ with material properties given in Table 4.3. The dimensions of the 1mm thick 300 mm span design are shown in Figure 4.25.

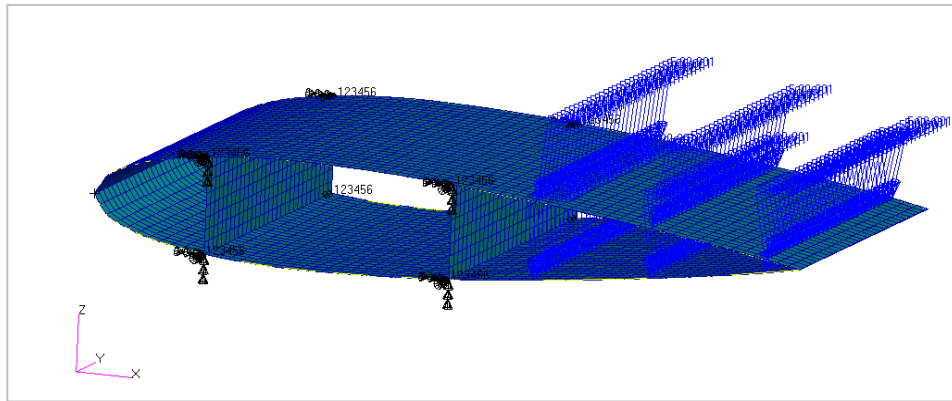


Figure 4.26 Closed TE FE model and boundary conditions

The finite element model generated by MSC/NASTRAN and the initial boundary conditions applied to the model are illustrated in Figure 4.26. The two spars were clamped for simplicity, where all six degrees of freedoms were fixed and distributed forces were applied along the top and bottom skins. This particular loading case was applied to achieve a TE displacement equivalent to 10^0 flap deflection.

Open TE Design

The same model was then used to analyse the open TE feature. The dimensions of the 1mm thick 300 mm span design remained the same as the closed TE model. The only difference was that this model had a gap of 4mm at the tip of the TE as can be seen from Figure 4.27. The finite element model generated by MSC/NASTRAN and the boundary conditions applied are shown in Figure 4.27. The boundary conditions applied are the same as the closed TE model, where the distributed forces were varied to achieve the equivalent TE deflection.

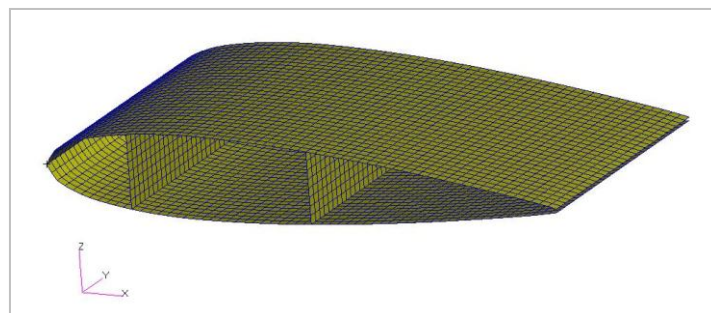


Figure 4.27 Open TE FE model

Loading / Displacement

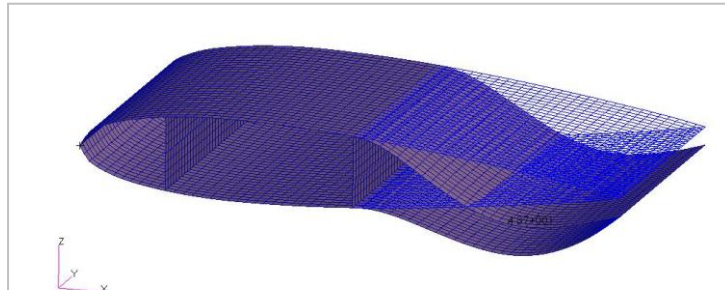


Figure 4.28 TE displacement of Close TE Model (in mm)

Figure 4.28 shows the deflection achieved for the closed TE model under the applied load. As it is presented in Table 4.4, the maximum deflection of the TE section under a 900 N distributed force is 49 mm approximately at 0.85c. A double curvature is seen as expected in this model instead of a smooth TE deflection, due to the TE being a closed design as a result buckling will occur in the top and bottom skins. Since the TE tip is fixed the bottom surface will not have the possibility to extend to allow smooth TE sliding with the upper surface, and this is when buckling occurs and a double curvature is seen in the model.

Table 4.4 Displacement achieved under applied load

Model	Displacement Achieved (mm)	Force (N)
Closed TE	48.7	900
Open TE	65	63

The open TE, on the other hand deflected with a maximum TE deflection of 65 mm at the tip, equivalent to 10^0 TE deflection angle, under a total distributed force of 63 N. Also an overlapping of the top surface with the bottom surface is present due to the open TE mechanism not being modelled in detail.

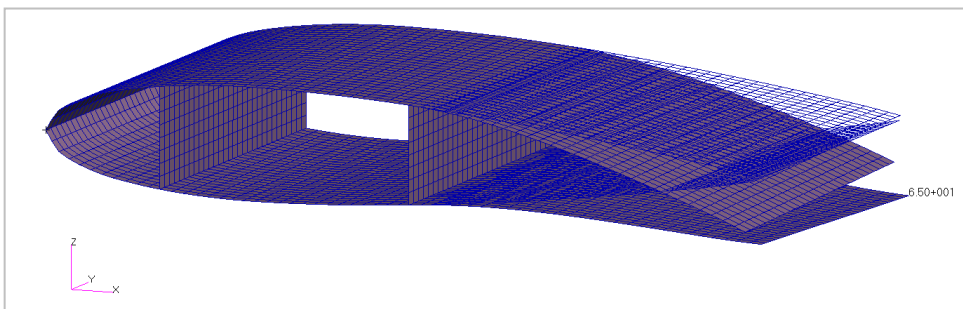


Figure 4.29 TE displacement of open TE Model (in mm)

The open TE design only required approximately 7% of the total force applied for the closed TE design in order to achieve the same deflection at the TE.

4.4.3 Open TE Design Solutions

During the camber change of a wing section there are certain choices which need to be made regarding the materials choice for the skins:

- a. The material skins can be selected to elastically deform (or stretch/compress) to allow for the required change in length as the skin undergo compression and tension.
- b. The skins do not exhibit strain, but are allowed to slide over one another, which introduce the concept of sliding skins.

As the shape of the wing changes from a positive camber (trailing edge down) to a negative camber (trailing edge up), the skins will maintain their original length, as will the mean camber line (defined by the curved beam). The relative motion of the upper skin to the curved beam and indeed the lower skin leads to a challenging issue. In order for the required motion to be achieved without buckling of the skins, the trailing edge will need to be open to enable the skins to be free to slide relative to each other for a certain warping when the trailing edge is being deflected.

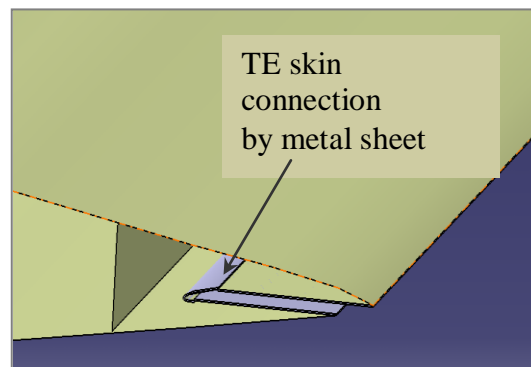


Figure 4.30 Sliding TE design

To produce the required SAW TE deflection with minimum actuation power, an open TE has been designed. As illustrated in Figure 4.30, two metallic sheets are bonded to the TE upper and lower skin and one of the lower sheet is folded to cover the upper one. This open-edge design allows the skins sliding relative to each other for a certain

warping when the TE is being deflected. However, this simple open TE solution will need further detailed modelling before it can be applied on to an aircraft wing structure.

Two design concepts have been proposed for the open TE section, as illustrated in Figure 4.31. The only difference is that, Figure 4.31 (a) has a closed wing box section as opposed to Figure 4.31 (b) having an open wing box structure. The elastic skins can be selected to elastically deform (or stretch/compress) to allow for the required change in length as the skin undergo compression and tension when the TE is being deformed. Also the honeycomb core will be capable of bearing the aerodynamic loads and provide the desired shapes accurately. The open wing box design would result in a smooth TE bending shape. However, this needs to be further analysed experimentally.

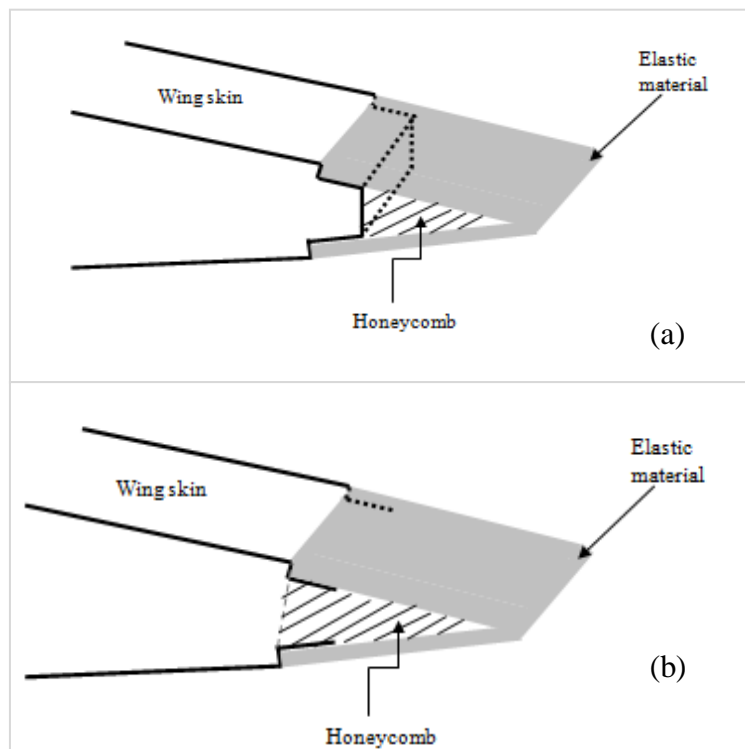


Figure 4.31 Open TE design solutions

Another design challenge will be the deflection of the skins between stringers and also between the eccentuator along the span due to the elimination of TE ribs. This indicates that the stringers need to be much stiffer and supported at much shorter spans. This indicates that the number of eccentuator required across the span may need to be much higher. An alternative is to design articulating ribs to support the stringers, which

can be spaced between the eccentuator. A simple solution will be to make the wing TE section a sandwich construction and to use flexible foam/honeycomb section to stiffen the wing between the skins and this will need to be assessed to establish how this would affect the actuation power requirement.

4.4.4 SAW Experimental Design

To demonstrate the SAW design concept of the flexible TE section with curved tube actuation mechanism and open TE, a scaled model was built as shown in Figure 4.32. It is a NACA0015 airfoil section 100mm long and 200mm in chord. The skin is made of four layers of glass fibre polyester prepreg in 0/90 layup. The spars and stiffeners were made of wood. The front spar was positioned at 20% chord and rear spar at 50% chord together with a mid spar at 40%. A servomotor mounted to the mid spar produces a torque of 37.3 Nm at 4.8 V. Two stiffeners were bonded to the skin above and below the motor to reinforce the motor mounting against the reaction torque in operation. Two pairs of stiffeners were placed at 60% and 90% chord after the rear spar to reinforce the skin. A curved torque tube was connected to the motor at one end and supported by the rear spar through a bearing. For this reduced scale model, the tube without the disks was in touch with the stiffeners directly in the flexible TE section. These stiffeners will keep in touch with the rotating tube to transfer the actuating force to the skin bending. The required TE chamber shape will be enforced by the tube curvature at all rotating angles. Figure 4.32 (a) and (b) presents the SAW experimental model before assembly and the SAW when deformed by the internal actuation mechanism in place respectively.

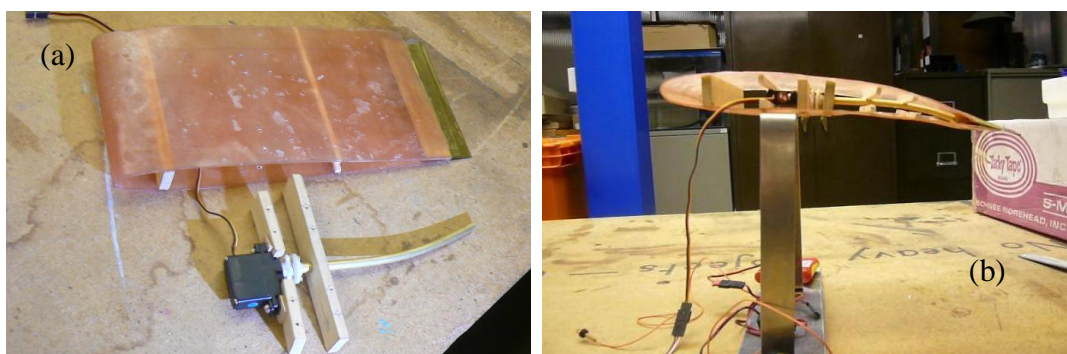


Figure 4.32 (a) SAW skin model, Spars, motor and curved tube; (b) Deformed SAW model

A second scaled model was built to carry out further testing of the SAW design concept integrated with the curved beam actuation mechanism and sliding TE. The main aim of this test was to work out the stiffness contribution from the actuator and actuation mechanism on the entire design. The skin made of glass/polyester composite is shown in Figure 4.33 (a). The wing model section is 600mm long and 300mm in chord. The skin was made of three layers of glass fibre polyester fabric in 0/90 layup. The front spar made of wood was positioned at 18% chord and the rear spar at 55% of chord from the leading edge. Two sets of curved torque tube actuation mechanism (CTTAM) was made and mounted to the spars through bearings as shown in Figure 4.33 (b). Two servomotors were mounted between the spars and connected to the curved torque tubes through gears. The tube has a diameter of 5.56mm with two discs mounted along it. The material properties of the tube and discs are listed in Table 4.5. Each motor can produce a maximum torque of 0.085Nm operated at 6V. The two Hi-tech RS4549 digital servo motors were mounted to drive each of the curved torque tubes independently. The actuation forces were delivered to the stringers and deflect the skin up or down to achieve the required shape.

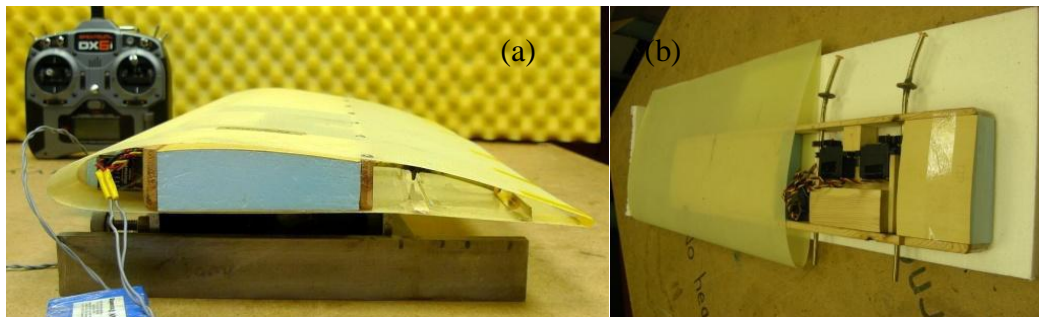


Figure 4.33 (a) Assembled SAW test model; (b) The TTAM mounted inside the SAW model

Table 4.5. Material properties of the torque tube and discs

	Elastic Modulus (GPa)	Poisson Ratio	Density (kg/m ³)
Brass Beam	85	0.33	7250
Copper Disc1	110	0.33	8600
Plastic Disc2	0.75	0.33	1100

As the CTTAM was integrated into the SAW as shown in Figure 4.33, it becomes part of the SAW structure, especially the flexible control surface in the rear part. The servomotor acts like a stiff torque spring and the curved torque tube connected to the motor works like an active rib to reinforce the seamless control surface and maintain its shape. The stiffness of this CTTAM system is an important parameter in the SAW structure model for static, dynamic response and aeroservoelastic analysis. However this key mechanical parameter is not available due to the lack of data from the servomotor manufacture. Experiment was therefore carried out based on the test model to identify the effective stiffness of the CTTAM, especially the servomotor.

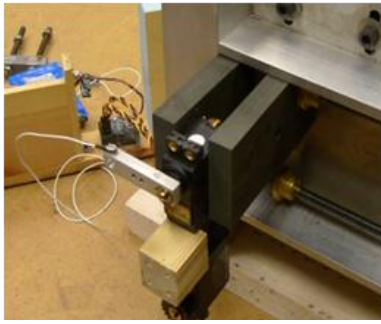


Figure 4.34 Servomotor Test Model Setup

First an actuator test model was built. The test model consisted of the servomotor, which was clamped to a rigid test rig and connected to a short aluminium alloy beam mounted to its axis as shown in Figure 4.34. The measured frequency of the model by performing a vibration test was $f=305\text{Hz}$. This frequency is identified as the torsional mode of the servomotor since the 1st bending mode frequency of the short beam alone clamped at one end was measured as 770Hz. The mass of the short beam was measured as 0.00644kg and the motor mass was 0.05kg. The mass centre distance between the two parts is measured as 0.00225m. Based on the formula $\omega = 305 \times 2\pi = \sqrt{k_m / I_p}$, where $I_p = 8.3 \times 10^{-6} \text{kgm}^2$ is the polar mass moment of inertia of the test model, the torsional stiffness of the motor is estimated as 30.3Nm/rad. When the electric power was supplied to the motor, the test model frequency increased as expected to $f=373 \text{ Hz}$ as a result of an added larger effective stiffness from the motor.

To ensure the high accuracy of the curved torque tube model in the assembled CTTAM system as shown in Figure 4.35(a), the curved torque tube was tested separately to be validated by a FE model. This second test model was setup by clamping the curved torque tube at the rear bearing support point with the CTT in the neutral position as shown in Figure 4.35 (b). The measured frequency for the coupled bending-torsion

mode of the curved torque tube was $f=387\text{Hz}$, which agrees very well with the FE result of $f=376\text{Hz}$.

Based on the validated torque tube FE model and the effective stiffness of the motor, the FE model of the assembled CTTAM was created as shown in Figure 4.35 (c). In the FE model, the torque tube was supported at the two bearing points by letting the rotational degree of freedom and fixing the rest of the degrees of freedom. The motor was represented by a torque spring and given the measured effective stiffness of 30Nm/rad . The FE results show that the motor model has little influence on the pure bending frequency $f=327\text{ Hz}$ of the system. However it has constrained the rotation freedom and made the frequency of torsion mode increased to 306 Hz , which agrees very well with the measured 312.5 Hz from the vibration test.

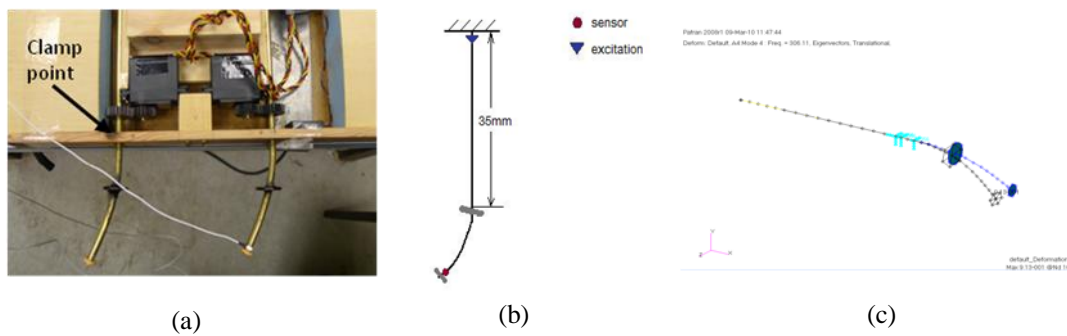


Figure 4.35 (a) Torque tube test model setup; (b) Clamped torque tube model; (c) FE CTTAM model

Although the FE model of this particular test model could not be used directly in the larger scale SAW model in the next section, the effective stiffness of the actuator was used to analyze its influence on the dynamic behaviour in chapter six.

4.5 SAW Actuation Force Requirement

Development of a seamless control surface concept is achieved through the relationship between actuators and induced deformation. In this case the seamless control surface is modelled as a clamped beam with distributed forces along the beam. The distributed forces are composed of two parts: aerodynamic loads and actuator loads. The actuator would apply vertical forces and moments, or a combination in order to deform the seamless control surface into a favourable shape. Hence, one aspect of designing a seamless control surface involves determining these forces, and more importantly how these forces are being produced and transmitted to the structure.

4.5.1 Actuation Force/Power Requirement

This section of the report analyses the actuation force and power requirements of the two TE configurations introduced in section 4.3.2. The TE is assumed to be a thin plate of aluminium alloy bending down to 15 degrees. The method of obtaining the values presented in Table 4.6, Table 4.7 and Table 4.8 are presented in Appendix D.

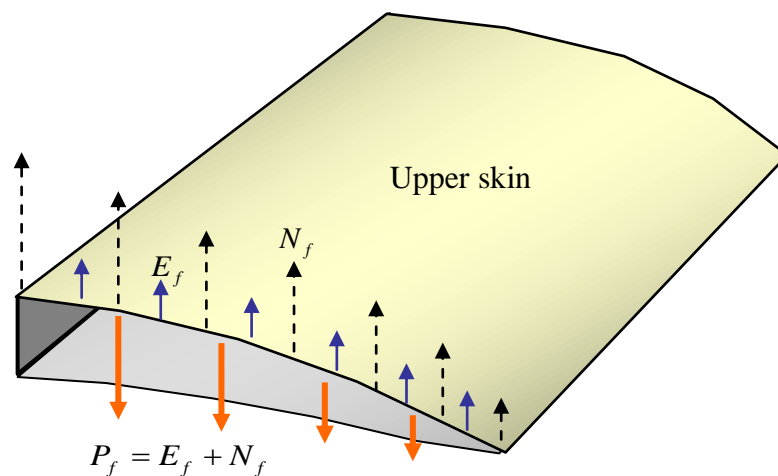


Figure 4.36 Force Distribution

The total actuation force required is worked out as two separate forces; force required to overcome the elastic effect of a 1mm thick unit span plate in bending (E_f) for each chordwise TE section and the normal force (N_f) generated as a result of the pressure distribution (see Figure 4.36). Table 7.1 summarises the results of these forces for both flexible and rigid TE configurations. However, the conventional rigid TE configuration

would not require an elastic force to achieve the desired deflection due its actuator mechanism with a hinge.

Table 4.6 Comparison of force data for flexible and rigid configurations

Chordwise TE Section (%c)	Flexible E_f (N)	Flexible N_f (N)	Rigid N_f (N)
0.9 - 1.0	1.26	58.32	28.94
0.8 - 0.9	7.54	125.73	68.07
0.7 - 0.8	12.57	120.62	79.97
0.6 - 0.7	17.59	120.92	101.56
0.5 - 0.6	22.62	139.47	140.49

As can be seen from Table 4.6, the overall actuation force requirement is higher for a flexible TE compared to a rigid TE configuration. This is because of the requirement of forces to deform the structure and the higher lift distribution of each TE section for the flexible configuration results in a higher normal force due to the redistribution of the pressure closer to the tip. Hence, a higher force more towards the tip for the flexible configuration compared to the rigid configuration.

Table 4.7 Bending moment data of flexible configuration

Chordwise Location (%c)	BM due to skin bending (Nm)	BM due to pressure (Nm)	Total BM (Nm)
0.9	0.06	2.92	2.98
0.8	0.38	15.04	15.41
0.7	0.63	39.47	40.10
0.6	0.88	75.99	76.86
0.5	1.13	125.52	126.65

The bending moments presented in Table 4.7 were calculated as the individual bending moment needed to deflect each chordwise section of the TE.

Table 4.8 Bending moment data of rigid configuration

Chordwise Location (%c)	BM due to pressure (Nm)	Total BM (Nm)
0.9	1.45	1.45
0.8	7.74	7.74
0.7	21.44	21.44
0.6	44.22	44.22
0.5	79.10	79.10

Table 4.7 and Table 4.8 summarise the bending moment (BM) created at each chordwise location due to the loads E_f and N_f . The bending moment created by each individual force i.e. E_f and N_f , and the total bending moment is higher for the flexible TE configuration compared to the rigid configuration. However, this is due to the force required to deform the TE section. The total bending moment at each chordwise locations are almost double for the flexible configuration than the rigid configuration at each location.

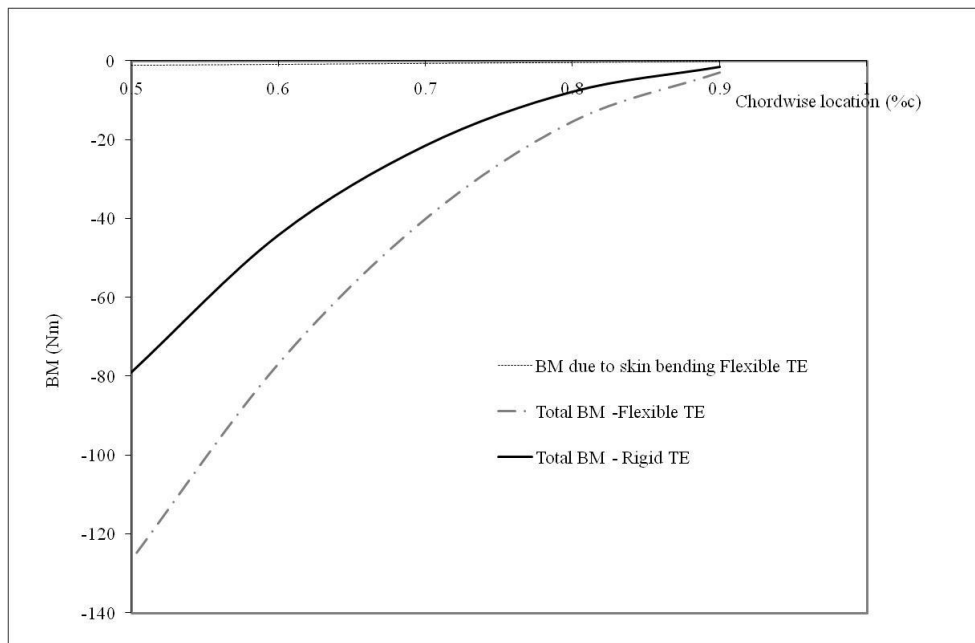


Figure 4.37 Bending Moment Comparison for Flexible and Rigid TE sections

The bending moment requirement for the flexible TE configuration is high due to the redistribution of the pressure compared to the rigid TE. This is summarised in Figure 4.37. The dashed line shows the bending moment due to the elastic force as a result of

skin bending. The elastic force only requires an additional bending moment of about 1.1% as opposed to a hinged rigid flap design.

Table 4.9 Total Power Requirement

Total Power (W) (Rigid TE)	3.77
Total Power (W) (Flexible TE)	7.96

The total power required for the flexible configuration is almost double the value for the conventional control surface. This is because there is an added requirement of the elastic bending of the structure to achieve the desired TE deflection for the flexible configuration.

4.5.2 Available Actuators

The recently completed DARPA smart wing program [53] evaluated a variety of new actuation concepts. Two types of actuators were studied; Shape memory alloys and a piezoelectric/ultrasonic motor. Table 4.10 compares the basic details of some of the available smart and conventional actuators of similar size and power output.

Table 4.10 Smart and conventional actuator comparison [53]

Actuator	Output Torque (in.-lbs)	Output Power (W)	Actuator Weight (kg)	Power Density (W/kg)
SPL-801 Ultrasonic motor	9.4	23.3	0.249	95
UCLA Mesoscale actuator	-	1.1-2.4	0.099	11-24
Penn St. bimorph resonant motor	1.3	3.8	N/A	N/A
Maxon DC motor (graphite brushes)	0.24	20	0.132	154
Maxon DC motor (brushless)	0.06	20	0.086	235
Maxon brushless DC motor with gearhead	10.6	29	0.186	154
Harmonic gear drive electric motor	28	20	0.739	27

The power density of the SPL-801 ultrasonic motor is higher than any current smart material based motor or actuator. This significant high power density is due to the high frequency operation of the piezoelectric element [53]. The SPL-801 ultrasonic motor has a number of advantages over conventional motors; higher torque density (torque per rpm), a built in braking/holding capability, quiet operation and quick response time due to low inertia [53].

Table 4.11 Ultrasonic motor comparison [53]

Model	USR-30	USR-45	USR-60	SPL-801
Rated torque (in.-lbs)	0.35	1.3	3.3	9.38
Rated Speed (rpm)	250	150	100	210
Power Output (W)	1.0	2.3	3.9	23.3
Weight (lbs)	0.07	0.15	0.39	0.54
Lifetime (h)	1000	1000	1000	100

The SPL-801 has six times the power output of the other ultrasonic motors of similar size, i.e. USR-60. However, the increased power output comes at a higher cost, lower life (100hrs for the SPL-801 compared to 1000hrs for the USR-60) and higher current requirements. But the design of piezoelectric ultrasonic motors is in its immature state, where optimisations and improvements could be made in order to maximise the power output.

5 Seamless Aeroelastic Wing box Design

As mentioned previously, the primary aim of this project is to design a Seamless Aeroelastic Wing (SAW) structure applicable to a lightweight UAV. Therefore this chapter is focused on an optimal design of a wing box structure for the SAW. One of the main challenges was to optimise the design for further weight saving and improved performance under the design requirements. For a lightweight and low speed UAV, wing load is usually relatively small even under large limited load factor. For this current UAV model of a large sweptback wing, significant structural weight saving is mainly constrained by aeroelastic stability and carbon/epoxy laminate manufacture rather than the usual strength criteria. Therefore further attention was focused on optimising the SAW structure for a minimum weight and maximum aeroelastic stability.

Composite materials are considered for the wing structure mainly because of their favourable high specific strength and stiffness. In addition, fibre reinforced composites offer great potential for a designer to optimise the fibre orientations and achieve desirable directional stiffness and aeroelastic behaviour of a wing structure with little weight penalty. In terms of aeroelastic tailoring, some previous work in this field has demonstrated that the divergence speed of a forward swept wing can be increased by optimising the laminate layup. The elastic or stiffness coupling due to an unsymmetrical laminate layup could also have significant effect on the aeroelastic behaviour of a composite wing. Therefore investigations have been made in order to optimise the laminate layup of a composite wing structure for desirable aeroelastic behaviours. Due to the flexibility and large sweptback angle of the current SAW, flutter and control effectiveness will be the main design constraint and bending-torsion stiffness coupling will be a key design factor in aeroelastic tailoring.

The gradient based deterministic method (GBDM) was employed for the SAW structure optimisation to achieve a lightweight, adequate strength and aeroelastic stability design. The investigation was conducted in two stages. Firstly, effort was made to design and model a composite wing box for a minimum weight structure option. An analytical

method was used for structural stress, vibration and aeroelastic analyses. The NASTRAN package based on the finite element method (FEM) was also used for structural analysis and comparison. Secondly, attention was focused on aeroelastic tailoring of the basic composite wing box model to achieve the maximum flutter speed under the strength criterion.

5.1 DEMON

The DEMON UAV was designed as a flying test bench for the integration of advanced sub-systems, primarily fluid based flapless controls and innovative control algorithms for guidance and navigation [118]. Figure 5.1 shows the layout of the DEMON UAV. Due to the essential demonstrative nature of the DEMON mission, the aircraft flight envelope is significantly limited, as it can be inferred from the V-n diagram presented in Figure 5.2. The DEMON maximum take-off weight has been fixed at 70 kg; this, together with the narrow bounds of the V-n diagram, implies that the aircraft structure is subjected to modest amounts of aerodynamic and inertial loadings.

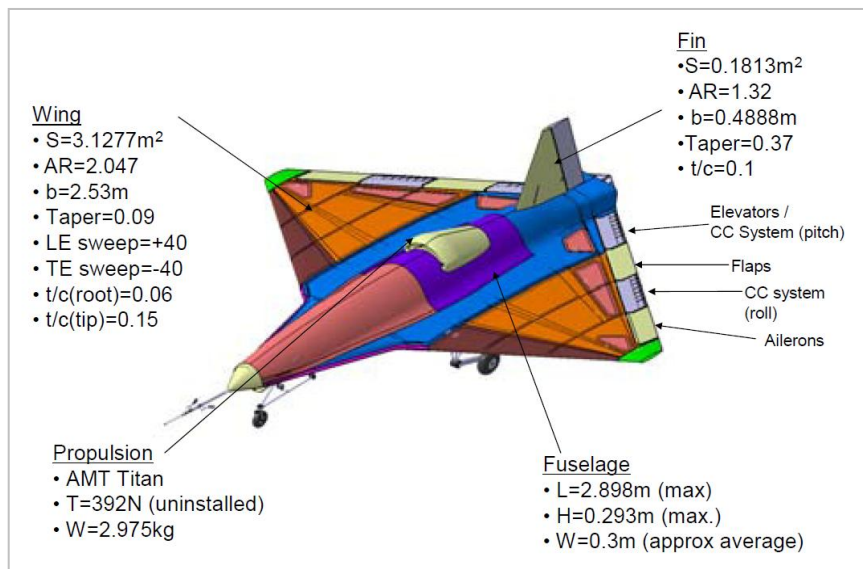


Figure 5.1 DEMON [8]

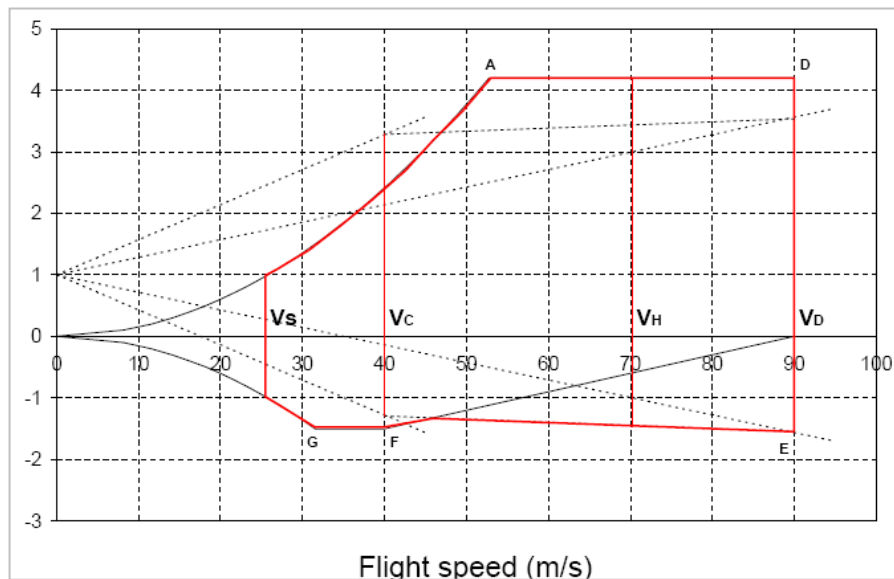


Figure 5.2 DEMON V-n Diagram [118]

5.2 Wing Loading condition

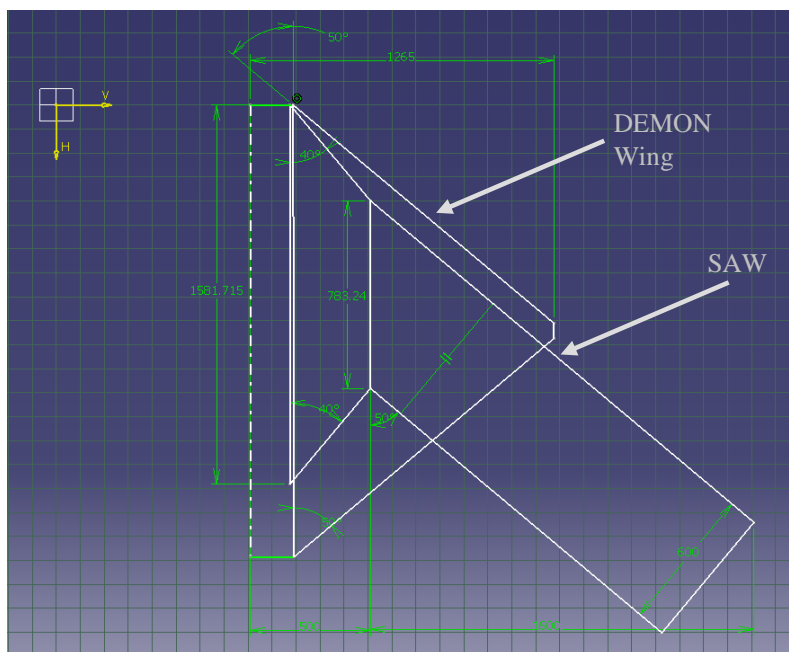


Figure 5.3 SAW Platform

A SAW as shown in Figure 5.3, which has a different planform from the DEMON wing but produces the required aerodynamic forces for the DEMON is designed and taken as an example. As stated above, the UAV has a maximum take-off mass of 70 kg. The cruise speed is 40 m/s

and dive speed 60 m/s. The design ultimate load factors are +4.2g and -1.5g respectively, which is mainly due to the gust load. This makes the wing structure experience a large load causing a concern in strength in the design. In addition, the large sweptback angle of 40 degree causes another concern in aeroelastic stability.

The stress analysis was carried out under the total shear force, torque and maximum bending moment. The shear force and bending moment diagrams of the base-line wing model at 4.2g is shown in Figure 5.4. The wing structure experience a total shear force of 995 N and maximum bending moment of 814 Nm at ultimate load 4.2g.

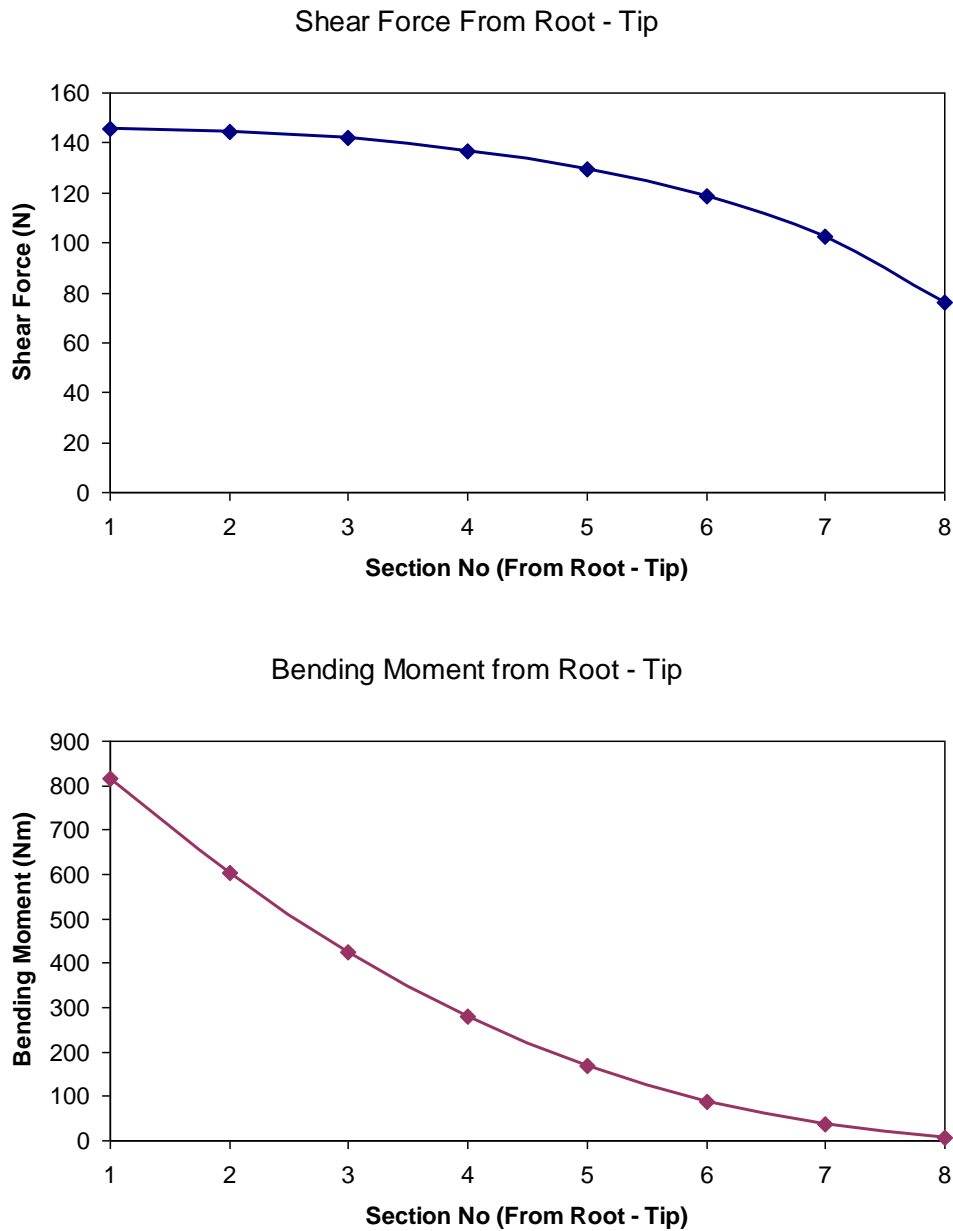


Figure 5.4 Bending moment and shear force diagrams at 4.2g load factor

5.3 SAW Structure Design

Figure 5.5 (a) and (b) and Table 5.1 show the planform and dimensions of the wing respectively. The wing structure comprises the centre wing box, the leading and trailing edge (LE & TE) sections. Because of the flexibility of Leading and Trailing edge sections, the central single-cell wing box is the main load carrying structure. The centre wing box is made of the front and rear spars and skins reinforced by six T-shape stringers, three on the upper and three on the lower skin.

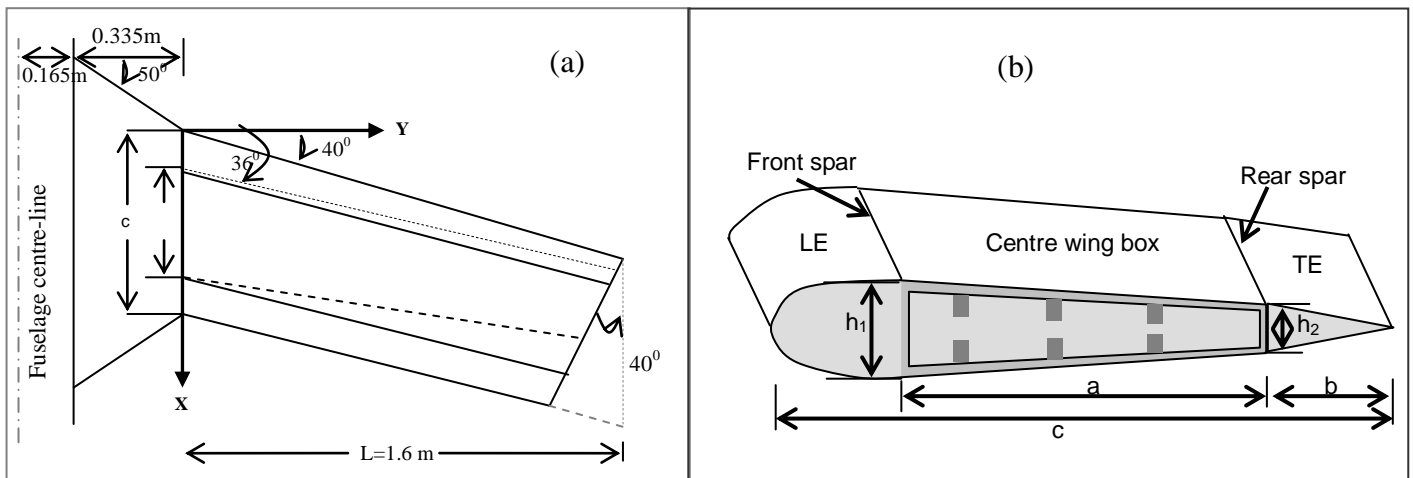


Figure 5.5 (a) Wing box configuration (— initial wing box; - - - - improved wing box); (b) Cross-sectional details of the wing box.

Two structural configurations were considered in the current design as shown in Figure 5.5 (a). The solid line shows the initial design Wing box-1 with the usual spar arrangement and the dotted line shows an alternative configuration Wing box-2 with the spars and stringers relocated to reduce the effective sweptback angle of the wing box elastic axis. The detailed geometry and dimensions of the wing root and tip sections are shown in Table 5.1 and Figure 5.5 (b) for the two types of wing box configurations. In the structural model, the wing box was clamped at the root section and was divided into eight spanwise single-cell box beam segments.

Table 5.1 Geometric details of the wing structure

<i>Section</i>		<i>a (m)</i>	<i>b (m)</i>	<i>c (m)</i>	<i>h₁ (m)</i>	<i>h₂ (m)</i>	<i>Aerofoil</i>
<i>Wing box 1</i>	<i>Root</i>	0.18	0.24	0.60	0.117	0.048	NACA 0015
	<i>Tip</i>	0.18	0.24	0.60	0.036	0.027	NACA 0006
<i>Wing box 2</i>	<i>Root</i>	0.27	0.18	0.60	0.116	0.072	NACA 0015
	<i>Tip</i>	0.27	0.30	0.60	0.021	0.032	NACA 0006

Baseline Design (Case 1) – This design was taken as a baseline example, in which the wing skin and spars are made of 8-ply carbon/epoxy laminate of symmetric layup $[0/45/90/-45]_s$ with skin thickness of 1 mm. The six stringers have the same material and thickness as the skin. The material properties are listed in Table 5.2.

Reduced Weight Design (Case 2) – An alternative design was made to reduce the SAW structure weight. In this case, the material and layup for the spars remain the same, but the skin and stringers are reduced to only two layers of uni-directional E-glass/epoxy. The change of material is mainly due to the constraint on the number of carbon/epoxy plies in a symmetric layup. Because the composite was cured at elevated temperature, unsymmetrical layup will cause thermal distortion. Since the E-glass/epoxy can be cured at room temperature, unsymmetrical layup will not cause this problem. This gives flexibility in material thickness. Three different E-glass/epoxy laminates were used, i.e. $[0/90]$ as Case 2.1, $[+45/-45]$ as Case 2.2 and $[+20/-20]$ as Case 2.3 were considered for the two wing box configurations. Material properties of the E-glass/epoxy used in the analysis are listed in Table 5.2. In both cases, the skin thickness has been reduced to 0.5 mm and the wing box structural weight reduced by approximately 30% comparing with the baseline design.

Table 5.2 Mechanical properties of Carbon-Epoxy and E-Glass-Epoxy

Material	E_1 (GPa)	E_2 (GPa)	G_{12} (GPa)	ν_{12}	X_t (MPa)	X_c (MPa)	Y_t (MPa)	Y_c (MPa)	S (MPa)	ρ (Kg/m ³)
Carbon-Epoxy (Ply thickness 0.125mm)	135	9.5	4.9	0.3	1680	1100	61	244	90	1600
E-Glass-Epoxy (Ply thickness 0.25mm)	40	8.0	4.0	0.25	1000	600	30	110	40	1900

5.3.1 Wing Box FE Model

To provide further details of the design, the improved wing box (WB-2) was also modelled by using MSC PATRAN/NASTRAN based on FE method. The same material properties, boundary and loading conditions as analytical approach were implemented in PATRAN. The skin and ribs were modelled using quadrilateral shell elements (QUAD4), as they were appropriate to model composite properties. The stringers were also created in shell elements and the offset command was used to separate the surfaces representing the skin and the stringers respectively.

Figure 5.6 (a) shows the improved WB-2 model created using MSC/PATRAN. Figure 5.6 (b) represents the boundary conditions applied to represent the aerodynamic loading at 4.2g.

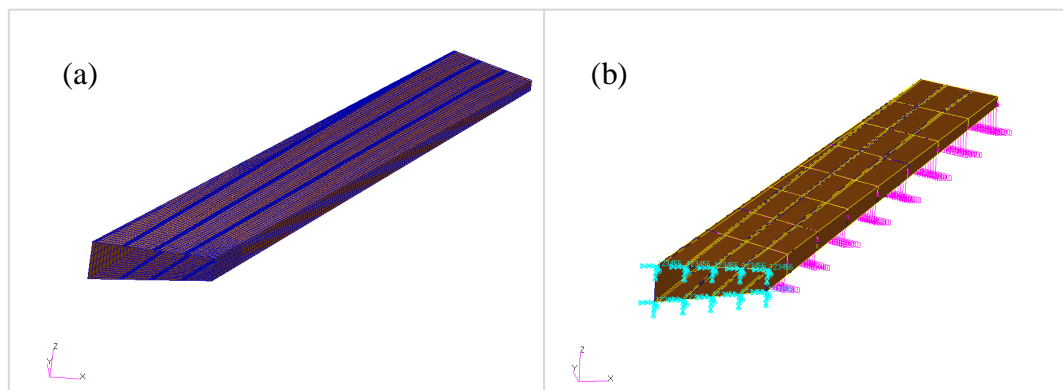


Figure 5.6 (a) Wing Box-2 FE model; (b) Applied Boundary conditions

5.3.2 Analytical Results

Firstly the thin-walled box method and laminate theory were used to calculate the average stress through the laminate thickness and then the stress and failure index (FI) of each ply. In the approximate method, the maximum normal stress is expected to occur on the skins close to the front spar and shear stress in the spar web at the clamped end respectively. The ultimate load factor of 4.2g was applied. This makes the wing structure experience a total shear force of 995 N and maximum bending moment of 814 Nm. For the two wing box models, the maximum normal and shear stresses in the skin and spar web laminate of the root section under the same loading at 4.2g are presented in Figure 5.7.

For the baseline (carbon/epoxy material) design Case 1, the maximum average normal stresses 21.2 MPa and 22.1 MPa for WB -1 and -2 respectively occurring in the lower skin indicate that the stress level is well below the safe limit. In order to conduct further detailed stress analysis of each laminate ply, the maximum average stresses of WB-1 and WB-2 were used to calculate the maximum force intensity 21.2 kN/m and 22.1 kN/m; and shear force intensity 3.24 kN/m and 3.73 kN/m respectively acting on the skin laminates. Under this loading, the maximum failure index (F.I.) in the skin laminate was calculated based on the classic laminate theory. The resulting Hoffman F.I. of 0.01 and 0.06 in the 90-deg ply for the WB-1 and WB-2 respectively indicates that the carbon/epoxy wing box is too conservative and obviously over designed in terms of the strength

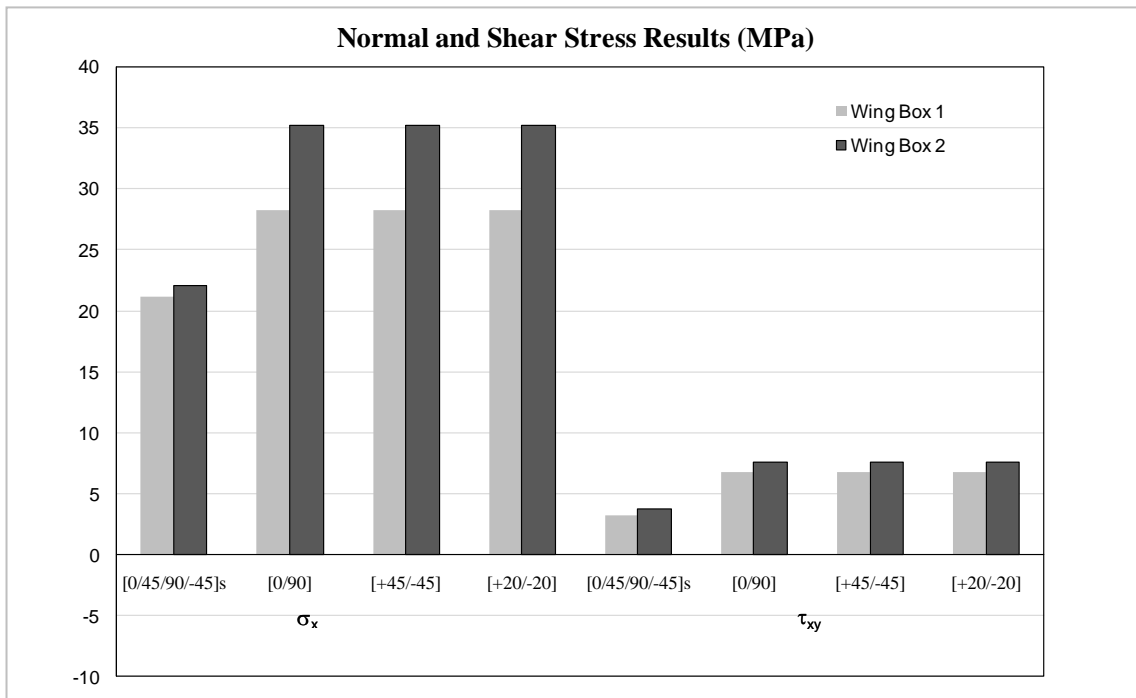


Figure 5.7 Maximum Normal and Shear Stress results for Wing Box 1 and 2 (MPa)

For the reduced weight design (glass/epoxy skins) Case 2, the maximum average normal stress located in the same region of the skin laminate at the root section as the baseline design is between 32 MPa – 35 MPa. The resulting maximum Hoffman F.I. of 0.02 in the skin laminate indicates that the wing box design still has plenty strength reserves and shows the potential for design optimisation and further structural weight reduction.

5.3.3 Finite Element Results

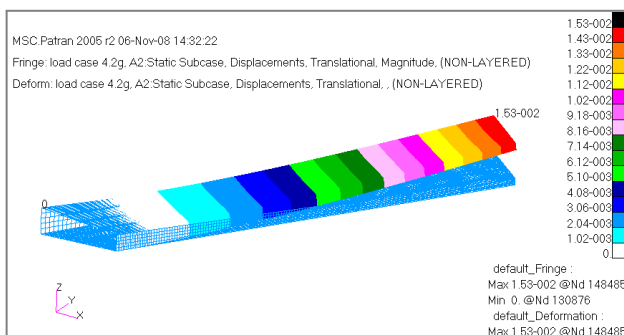


Figure 5.8 SAW (WB-2 Case 1) Deformation under maximum loading at 4.2g (in m)

MSC PATRAN/NASTRAN was used for more accurate and detailed stress analysis of the wing box FE model. As mentioned before, the baseline design case of wing box-2 configuration was modelled in FE for comparison with the analytical results. Analytical results were also

used to validate the FE model. Figure 5.8 shows the maximum transverse deflection of 15.3 mm at the wing tip under the maximum loading due to gust at 4.2g. The spanwise stress distribution around the wing box-2 root section under the maximum aerodynamic loading is shown in Figure 5.9 - Figure 5.11. From Figure 5.9 and Figure 5.10, a maximum of 59 MPa and 5.3 MPa can be seen for σ_1 and σ_2 respectively.

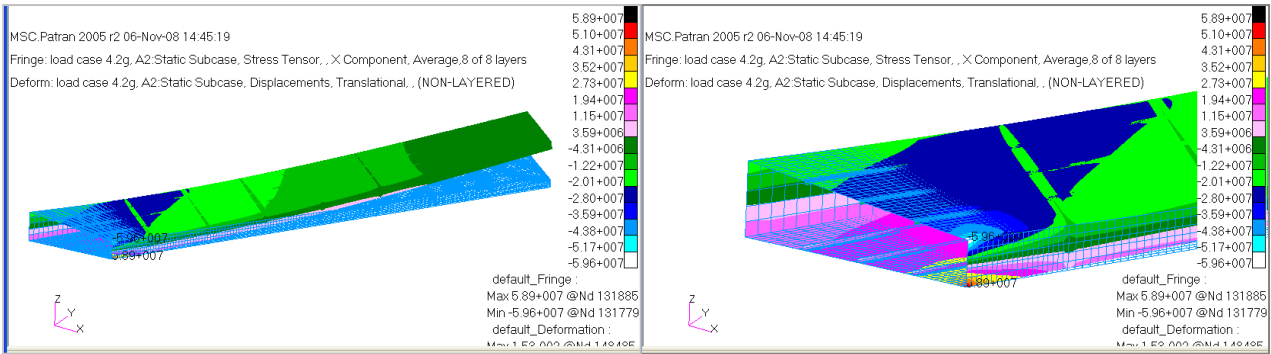


Figure 5.9 Spanwise Stress (σ_1) Distribution on Wing Box at Limit Load due to Gust at 4.2g.

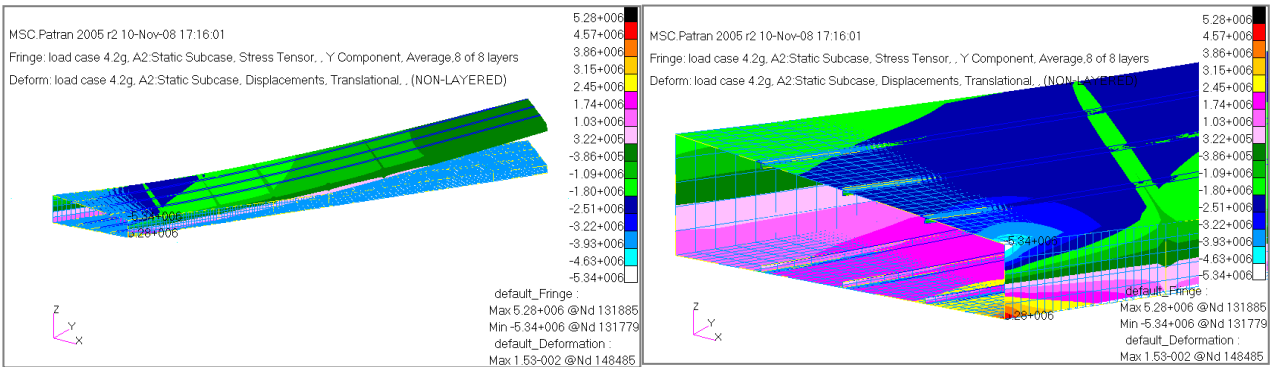


Figure 5.10 Spanwise Stress (σ_2) Distribution on Wing Box at Limit Load due to Gust at 4.2g.

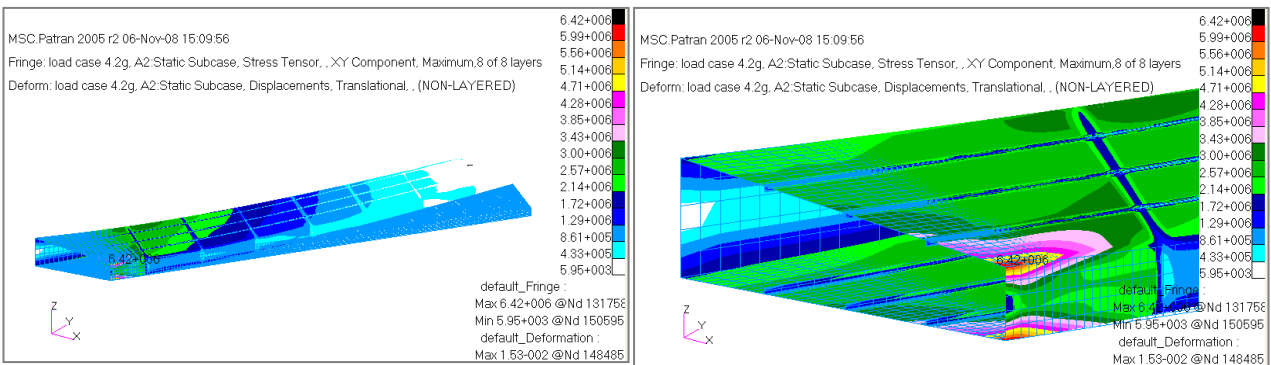


Figure 5.11 Spanwise Stress (σ_{12}) Distribution on Wing Box at Limit Load due to Gust at 4.2g.

The comparison between the results obtained from the FE model together with the results obtained by analytical methods are listed in Table 5.3. The comparison indicates that the FE and analytical stress results in the specified region agree very well. However two major differences are noted in the comparison. First, although the FE stress is distributed and more detailed the comparison with analytical result can only be made in the same region and ply rather than point to point. Secondly, the FE model also considered the structural coupling effect (swept angle) and the stress concentration effect. Therefore the stress on the skin near the spar and at the sharp corner of the FE model cannot be predicted by the analytical method.

Table 5.3 Maximum direct and shear stresses for WB-2 Cases 1-2

Design case	Case 1 (Analytical)	Case 2.1 - 2.2 (Analytical)	Case 1 (FEM)	Case 2.1 (FEM)	Case 2.2 (FEM)
Direct stress (MPa)	±22.1	35.3	19.4/-20.1	25	24
Shear stress (MPa)	3.73	7.60	1.72	2.31	1.88
Hoffman Failure Index	0.06	0.02	0.04	0.07	0.02

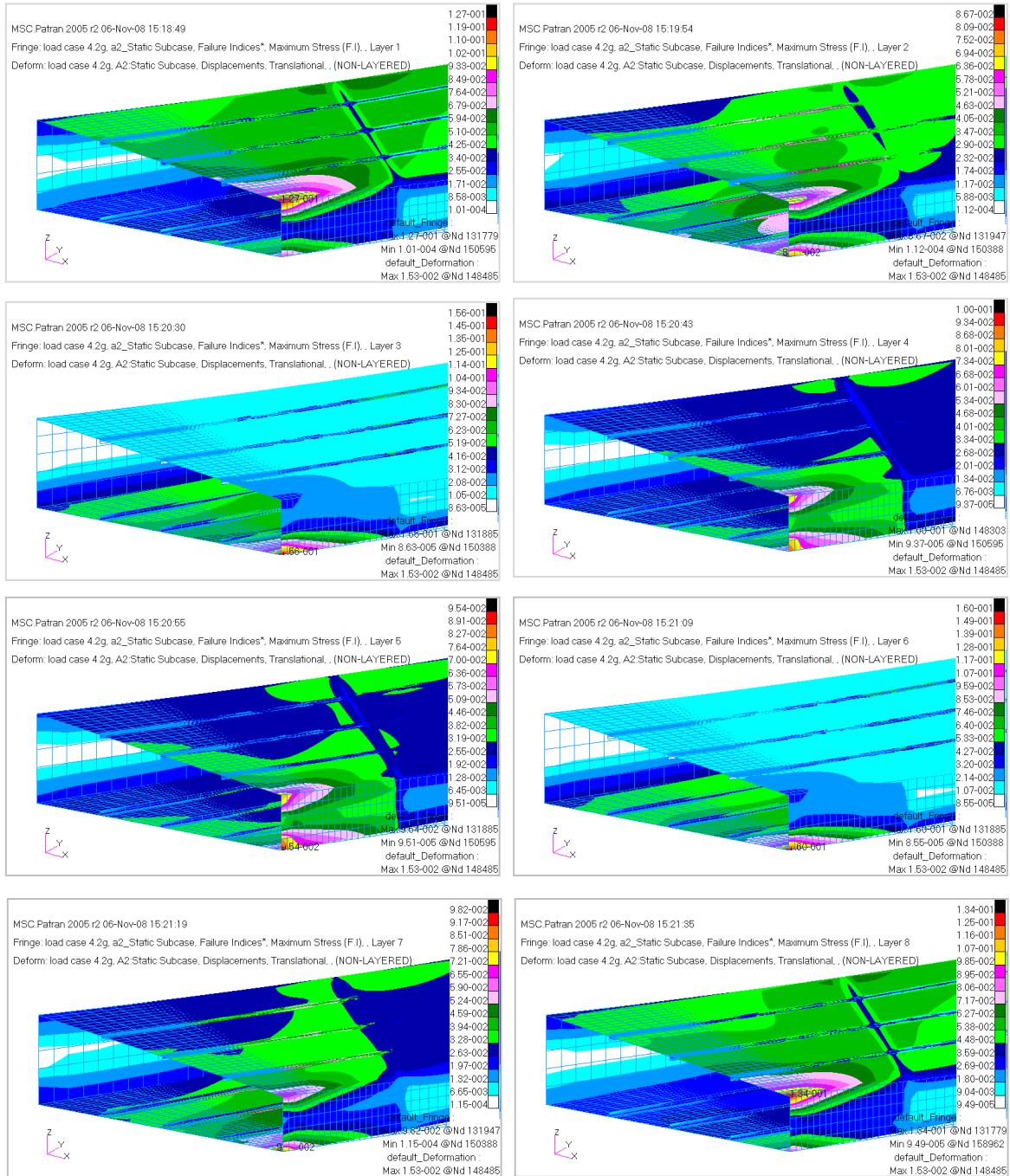


Figure 5.12 Failure Index Results of the Baseline Wing Box-2 Design

Since the reduced weight (glass/epoxy skins) wing box design cases are still very conservative in terms of strength, attention was subsequently paid to the stiffness and aeroelastic stability.

5.4 Aeroelastic Tailoring

Aeroelastic tailoring was carried out by optimising the SAW skin laminate layup to find an optimal combined bending and torsion stiffness for aeroelastic stability without increasing the weight and violating the strength criterion. Only the lightweight design Cases 2.1 ([0/90] skin), 2.2 ([±45] skin) and 2.3 ([±20] skin) were considered. In the model, each section of the eight spanwise segments of the wing model was divided into four laminate panels representing the upper and lower skins, and front and rear spar webs along the thin-walled box cross section circumference. It results in 20 pieces of laminate panels and 160 plies in the whole wing box. In the optimisation process, each of the fibre orientations of the 160 plies can be taken as an independent design variable, which results in the maximum number of 160 design variables. However the design variables can be reduced under specified conditions. Eight ply orientations were taken as design variables including two in the upper skin, two in lower skin and two in each of the spar web panels at the root section for all the design cases considered in this study. The laminates in the rest seven spanwise sections were kept the same as the optimised root section during the optimisation. This condition keeps the laminate layup uniform along the spanwise wing box for easy manufacture.

5.4.1 Wing Box Stiffness

Eight ply orientations were taken as design variables including two in the upper skin, two in lower skin, and two in each of the spar web panels at the root section. The laminates in the rest of the seven spanwise sections were kept the same as the optimized root section during the optimisation. This condition keeps the laminate layup uniform along the spanwise wing box for easy manufacture. A comparison between the initial rigidities and their optimised values of the wing box segments along the span is shown in Figure 5.13 and Figure 5.14. The tip section is marked as point 1 and the root section is marked as point 8.

The box section rigidities shown in Figure 5.13 indicates that the design case 2.1 [0/90] has a greater EI but lower GJ than that of case 2.2 [±45]. This was expected considering the layup difference. A similar trend can be seen for cases 2.1 and 2.2 for the improved

wing box design (WB-2). As can be seen from Figure 5.14, the design case 2.3 ([+20/-20] layup) has a greater EI than that of case 2.1 ([0/90] layup) and case 2.2 ([±45] layup). Case 2.2 resulted in a higher GJ than that of case 2.1 and case 2.3.

From the rigidity comparison presented, following observations are made. Firstly the rigidities remain reduced along the wing span as the wing box is tapered down in both cases. Secondly the optimised layups result in a greater GJ and smaller EI than the initial layups in the spanwise segments. Finally the bending-torsion coupling rigidity K produced from an optimised asymmetric layup plays a beneficial role in favour of the flutter speed. It is also noted that the aeroelastic tailoring is much more effective by optimising the skin and web layups around the wing box section circumference rather than along the spanwise section. The results shown in Figure 5.13, Figure 5.14 and Table 5.4 indicate that an optimum layup in favour of aeroelastic stability is normally associated with a great torsional stiffness combined with beneficial bending-torsion stiffness K .

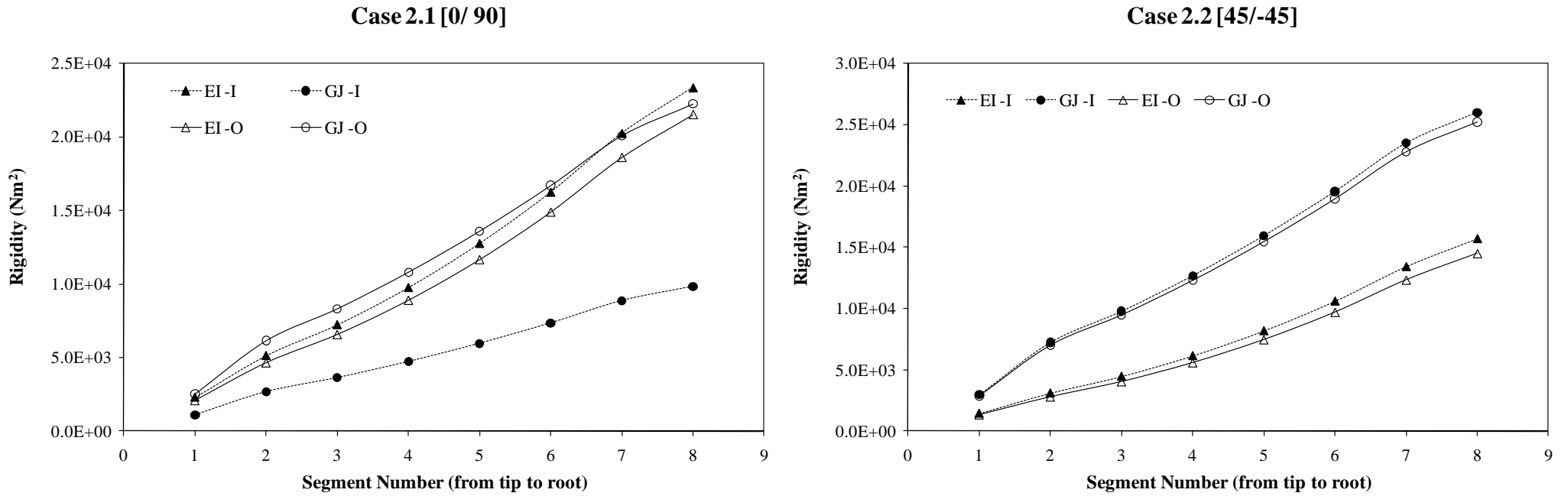
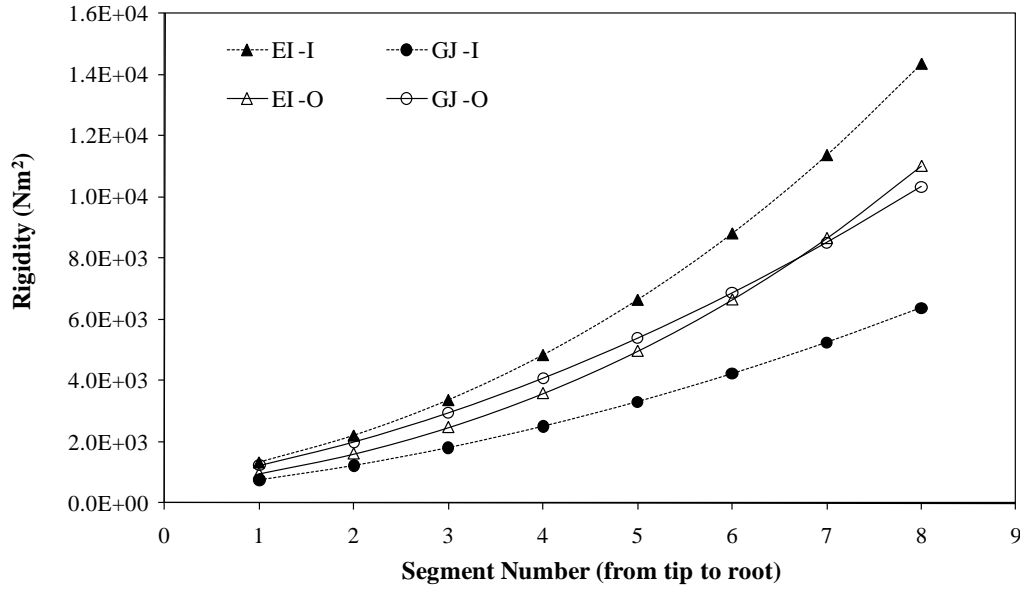
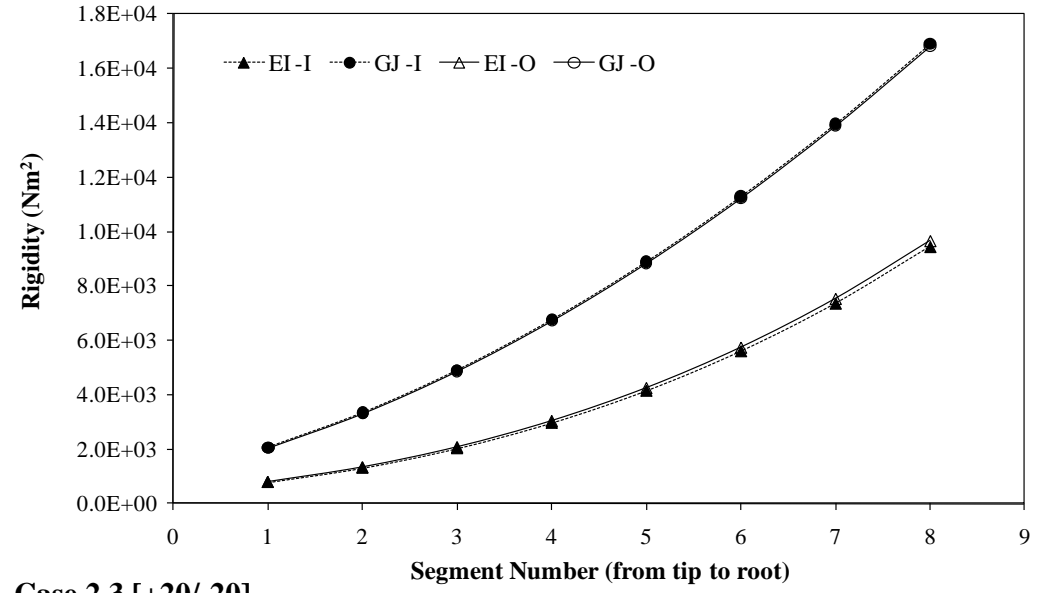


Figure 5.13 Comparison of structural rigidities of the SAW box (WB-1) for the initial (I) and optimised (O) design. Note: EI-I = initial rigidity, EI-O = optimised rigidity.

Case 2.1 [0/ 90]



Case 2.2 [45/-45]



Case 2.3 [+20/-20]

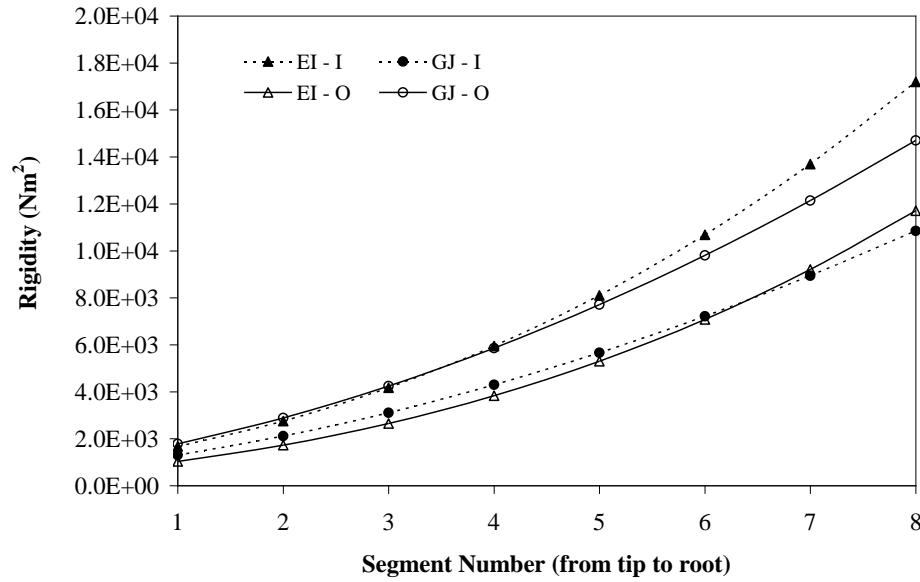


Figure 5.14 Comparison of structural rigidities of the SAW box (WB-2) for the initial (I) and optimised (O) design. Note: EI-I = initial rigidity, EI-O = optimised rigidity.

5.5 Wing Box Aeroelastic Analysis

5.5.1 Wing Box Flutter Analysis

CALFUN is a FORTRAN program which calculates the flutter speed of an unswept cantilever aircraft wing using finite element method and two dimensional unsteady aerodynamics. It uses the normal mode method and generalised coordinates to compute the flutter speed of an aircraft wing from its basic structural and aerodynamic data [119 - 121]. The method used relies on the fact that the mass, stiffness and aerodynamic properties of the aircraft wing can be expressed in terms of the generalised coordinates. Therefore, using the usual finite element method, the natural frequencies and normal modes of the aircraft wing is being calculated and then its generalised mass, stiffness and aerodynamic matrices are obtained respectively, as discussed in Chapter 3. The flutter matrix is then formed by algebraically summing the generalised mass, stiffness and aerodynamic matrices.

CALFUN can be used for complete flutter calculation or can be used to calculate natural frequencies and mode shapes only. In the structural idealisation of the wing, beam and lumped mass elements are being used in CALFUN to obtain the mass matrix and the stiffness matrix. It has four main subroutines namely [120]: (1) *MODES*, (2) *XEXM*, (3) *AIRMAT* and (4) *FLUTTER*. The subroutine *MODES* calculates the natural frequencies and mode shapes of the aircraft, *XEXM* computes the generalised stiffness and mass matrices from selected modes, *AIRMAT* forms the aerodynamic matrix in modal coordinates using strip theory and Theodorsen expressions for unsteady lift and moment and *FLUTTER* forms and solves the complex flutter determinant for flutter speed, flutter frequency and flutter mode. The procedure used in CALFUN is expressed in Figure 5.15.

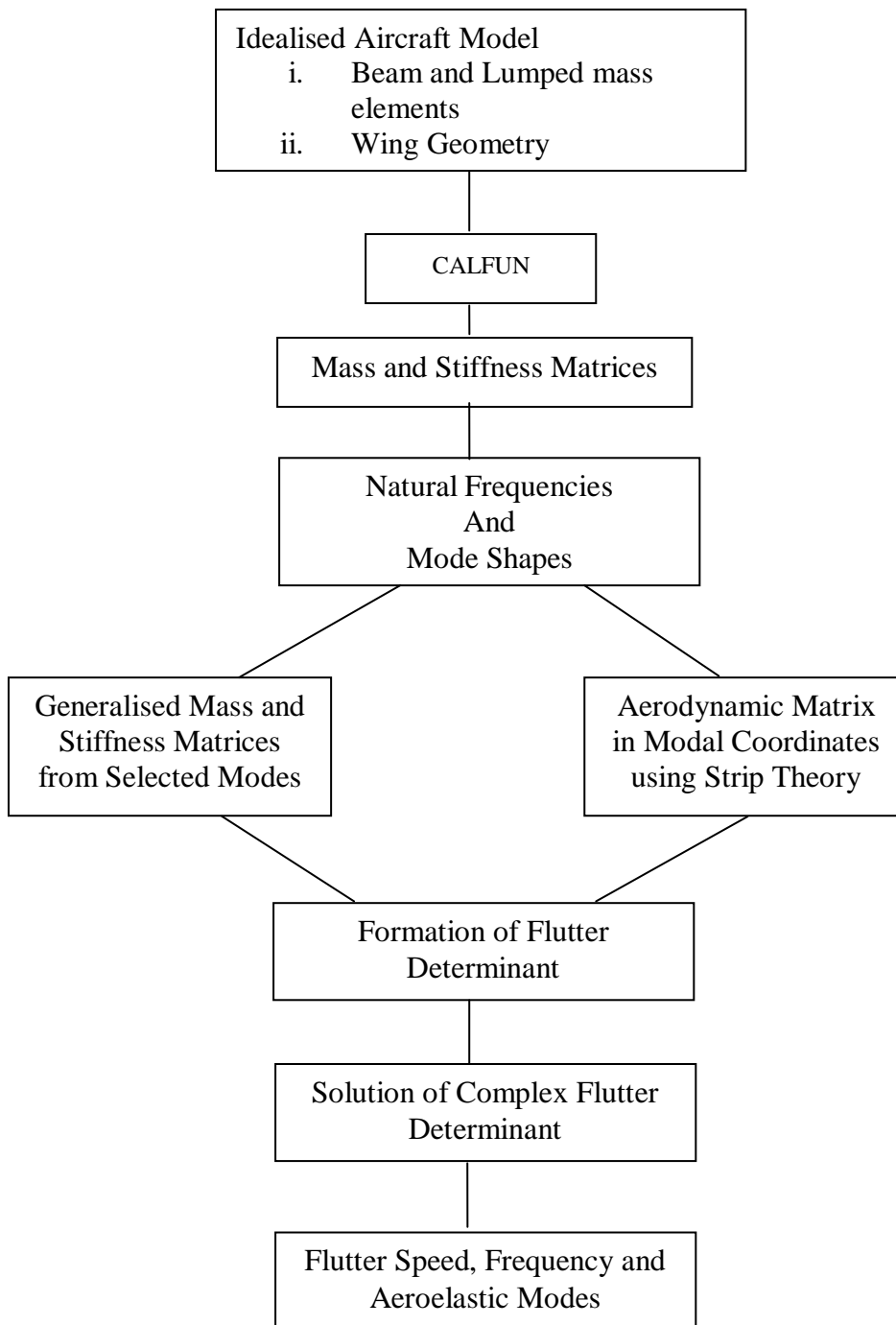


Figure 5.15 Flutter Analysis using CALFUN

The solution for flutter determinant is a complex eigenvalue problem because the determinant is primarily a complex function of two unknown variables, the airspeed and the frequency. The method used in CALFUN, is to select airspeed and evaluate the real and imaginary parts of the flutter determinant for a range of frequencies. This process is

repeated for a range of airspeeds until both the real and imaginary parts of the flutter determinant vanish completely. Flutter usually occurs at a frequency which lies between the fundamental bending and torsional frequencies. These two frequencies can be obtained from the modal analysis, hence, can be used as the lower and upper limit of the frequency range respectively. The increment could be chosen to be suitably.

The wing was divided into a number of beam elements (i.e. 8 elements) rigidly jointed together at the nodes. The elements and nodes were then numbered from tip to root. In the data file used for each design, there are 15 groups of input data which are described in more detailed in Appendix 5-B. The optimisation program uses CALFUN to calculate the flutter speeds of the optimised wing box designs. Table 5.4 shows the optimum laminate layup of the wing box at the root section.

Wing Box-1 Case 2.1 [0/90] – when carrying out the optimisation analysis for maximum flutter speed, eight ply orientations were taken as design variables including two in the upper skin, two in lower skin and two in each of the spar web panels at the root section. The laminates in the rest seven spanwise sections were kept the same as the optimised root section during the optimisation. In this case, the flutter speed for the initial skin layup [0/90] was 165 m/s. When the laminates were optimised, the flutter speed was increased up to 182 m/s as shown in Figure 5.16. This considerable increase is due to the significant increase in torsional stiffness for the optimised case

Wing Box-1 Case 2.2 [± 45] – As shown in Figure 5.16 the flutter speed of the initial layup [45/-45] was 235 m/s. When two layers were selected and optimised, a slightly higher flutter speed of 242 m/s was obtained. Summary of the optimised laminate layups at root section and the flutter results are in Table 5.4.

Wing Box-2 Case 2.1 [0/90] – Eight ply orientations were taken as design variables from the four panels at the root section. The laminates in the rest seven spanwise sections were kept the same as the optimised root section during the optimisation. This condition keeps the laminate layup uniform along the spanwise wing box for easy manufacture. When the laminates were optimised, the flutter speed V_f was increased

from its original 123 m/s up to 169.7 m/s. The reduced flutter speed is a result of the lower torsional stiffness of this case compared to the equivalent case of the WB-1.

Wing Box-2 Case 2.2 [± 45] – Similar to the previous cases, the eight plies (two for each of the four laminate panels) at the root section were taken as design variables. The layups of the eight spanwise sections were kept uniform in the optimisation. The flutter speed of the initial skin layup [± 45] was 318 m/s. Following the optimisation, a slightly higher value of 321 m/s was achieved. Details of the original and optimised design results are shown in Table 5.4.

Wing Box-2 Case 2.3 [± 20] - Started from this particular initial layup, the optimisation was carried out with the same design variables similar to the previous cases. The laminates in the rest of the seven spanwise sections were kept uniform as the optimised root section during the optimisation. The flutter speed for the optimised layup was increased from 162 to 189 m/s. The optimised laminate layups at the root section together with the flutter results are summarised in Table 5.4.

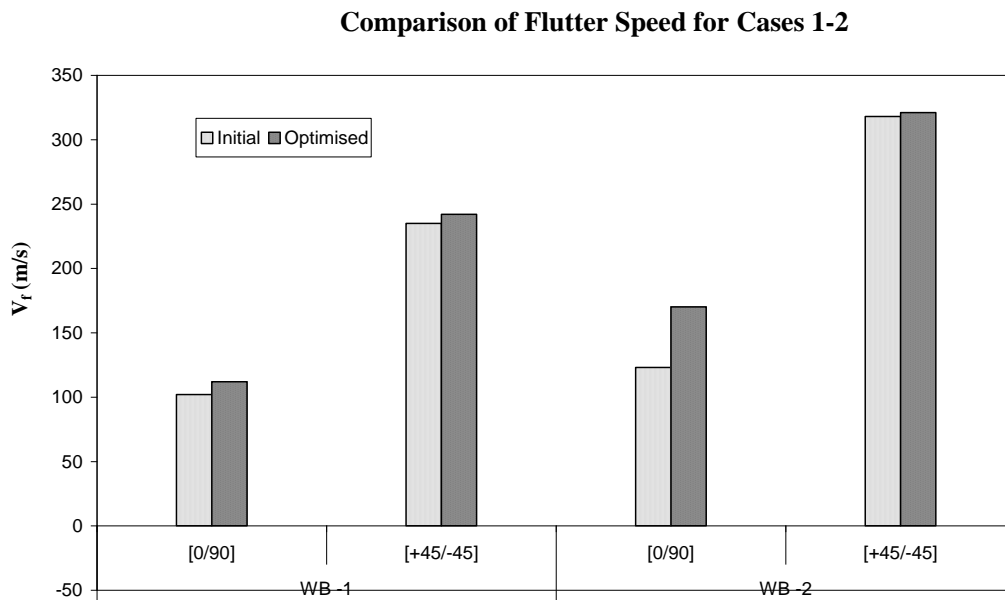


Figure 5.16 Flutter results for initial and optimised cases (1-2)

Table 5.4 Optimised laminate layups, rigidity and flutter speed

Cases	Panel	Wing Box -1			Wing Box - 2		
		Optimum layup (degree)	Rigidity ^a (kNm ²) and V_f (m/s)		Optimum layup (degree)	Rigidity ^a (kNm ²) and V_f (m/s)	
			Initial	Optimised		Initial	Optimised
Case 2.1 [0/90]	Upper skin	[-27.6/ 35.4]	EI=21.5 GJ = 9.8	21.5 22.3	[-25.4/ 84.0]	$EI = 14.4$ $GJ = 6.0$	11.02 10.34
	Lower skin	[-27.62./ 32.7]	K = 0.0	-2.1	[35.7/ 90]	$K = 0.0$	-3.61
	Front spar web	[-11/ 44.6/ 90/ -45/ -45/ 90/ 45/ 0]	$V_f = 165$	182	[16.1/41.2/90/-45/-45/90/45/0]	$V_f = 123$	169.7
	Rear spar web	[-5.5/ 44.7/ 90/ -45/ -45/ 90/ 45/ 0]			[7.9/43.0/90/-45/-45/ 90/45/0]	$\varpi_f = 72$	126.4rad/s
Case 2.2 [+45/-45]	Upper skin	[45.1/ -35.3]	EI=15.7 GJ =26	14.5 26	[45.9/ -42.8]	$EI = 9.45$ $GJ = 16.0$	9.61 16.84
	Lower skin	[30.8/ -45.4]	K = 0.0	-6.3	[41.1/ -45.9]	$K = 0.0$	-0.44
	Front spar web	[0.4/ 45/ 90/ -45/ -45/ 90/ 45/ 0]	$V_f = 235$	242	[0/45/ 90/-45/-45/90/45/0]	$V_f = 318$	331
	Rear spar web	[0.05/ 45/ 90/ -45/ -45/ 90/ 45/ 0]			[0/45/90/-45/-45/90/45/0]	$\varpi_f = 115$	118rad/s
Case 2.3 [+20/-20]	Upper skin				[30.7/ -36.8]	$EI = 17.2$ $GJ = 10.9$	11.70 14.70
	Lower skin				[27.8/ -51.4]	$K = 0.0$	-1.05
	Front spar web				[-6.5/44.9/ 90/-45/-45/90/45/0]	$V_f = 162.5$	189
	Rear spar web				[-9.6/44.9/90/-45/-45/90/45/0]	$\varpi_f = 91$	95.4rad/s

^a Optimum layups and the optimum rigidities are for the root section.

5.5.2 Control Effectiveness

A detailed study of the control effectiveness was carried out using the program AERO-BEAM-SAW for the design cases for both SAW box models considered. This program is a combination of BEAM3D program and UNSPM (unsteady panel method) program, which calculates the aerodynamic force, pitching moment and their interaction with structure deformation for the control effectiveness of the whole wing.

The control effectiveness of the whole wing takes into account the swept angle and elastic twist effect. The control effectiveness results over a flight speed range for case 1 and case 2 designs of the two wing box configurations were obtained using Eqs. (97) from Chapter 3. Figure 5.17 and Figure 5.18 show that the reversal speeds have been increased as a result of the aeroelastic tailoring.

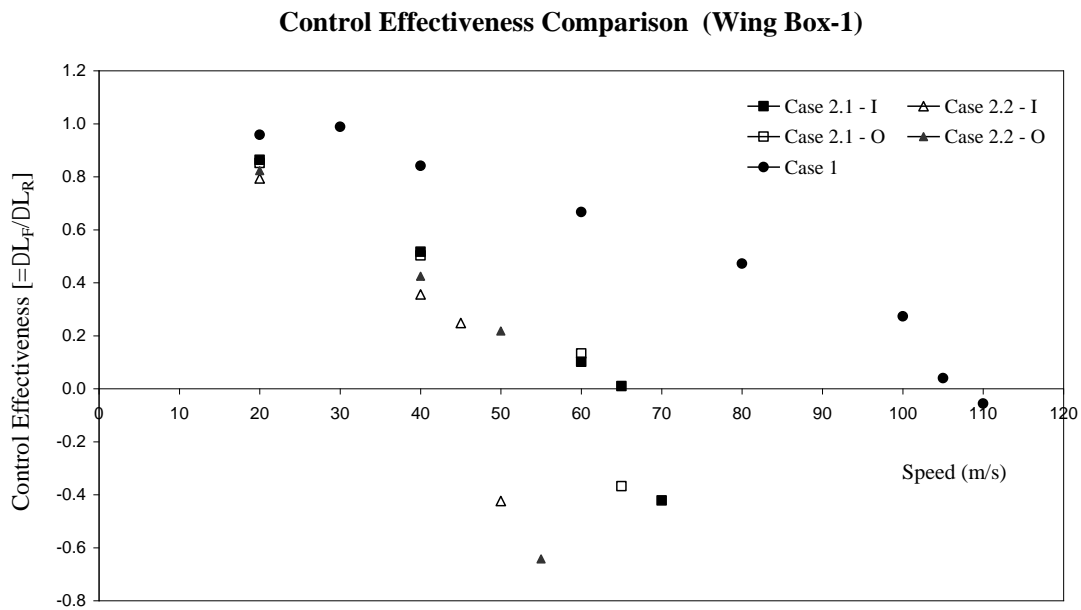


Figure 5.17 Control effectiveness comparison of the initial (I) and Optimised (O) cases for WB -1

Wing Box 1 – as can be seen from Figure 5.17, the control reversal speed obtained for case 1 [carbon/epoxy] was approximately 105 m/s. The control reversal speed obtained for case 2.1 [0/ 90] for both initial and optimised wing box are significantly low, i.e. 65 m/s. This is due to the flexibility of the wing box and a negative twist is being generated as a result. A similar analysis was then carried out for case 2.2 [+45/-45]. The reversal

speed has been further reduced to approximately 55 m/s. This is due to the lower bending stiffness of the wing box, even with a higher torsional stiffness compared to case 2.1. The significantly low reversal speed is a result of the bending stiffness being reduced in cases 2.1 and 2.2 compared to that of case 1.

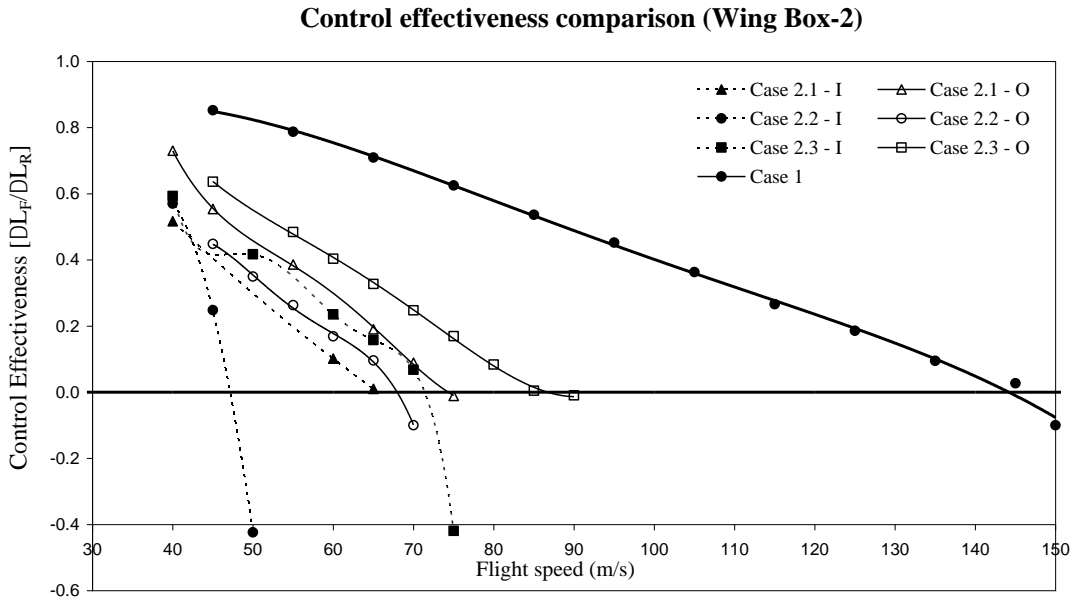


Figure 5.18 Control effectiveness comparison of the initial (I) and Optimised (O) cases for WB -2

Wing Box 2 - As shown in Figure 5.18, the control reversal speed V_R of the carbon/epoxy wing for the improved wing box was 145 m/s compared to the baseline design case 1 of the wing box-1 configuration. However, for the optimised design case 2.1 [0/ 90] V_R is significantly low at 75 m/s. For optimised case 2.2 [+45/-45], V_R is further reduced to 70 m/s. The reversal speed for optimised case 2.3 [+20/-20] remains higher compared to case 2.1 and 2.2 at 85 m/s.

Figure 5.19 summarises the reversal speed of all the design cases considered for the two wing box configurations. For all three cases 2.1, 2.2 & 2.3, the lower V_R is mainly due to the lower GJ compared to the case 1. Although the case 2.2 has a greater GJ compared to case 2.1, the V_R is even lower. This is mainly due to the lower EI in case 2.2 and the strong bending-torsion coupling of the flexible wing box. The reduced EI induced a nose down twist and resulted in a lower V_R . Therefore an optimal layup with both greater EI and GJ should be a better solution. Since the optimised case 2.3 met this

requirement, the resulting $V_R = 85$ m/s was indeed higher than the other two cases. Despite the $V_F = 189$ m/s of this solution being lower than case 2.2, it is higher compared to the first option of case 2.1 and gives adequate safety margin for aeroelastic stability.

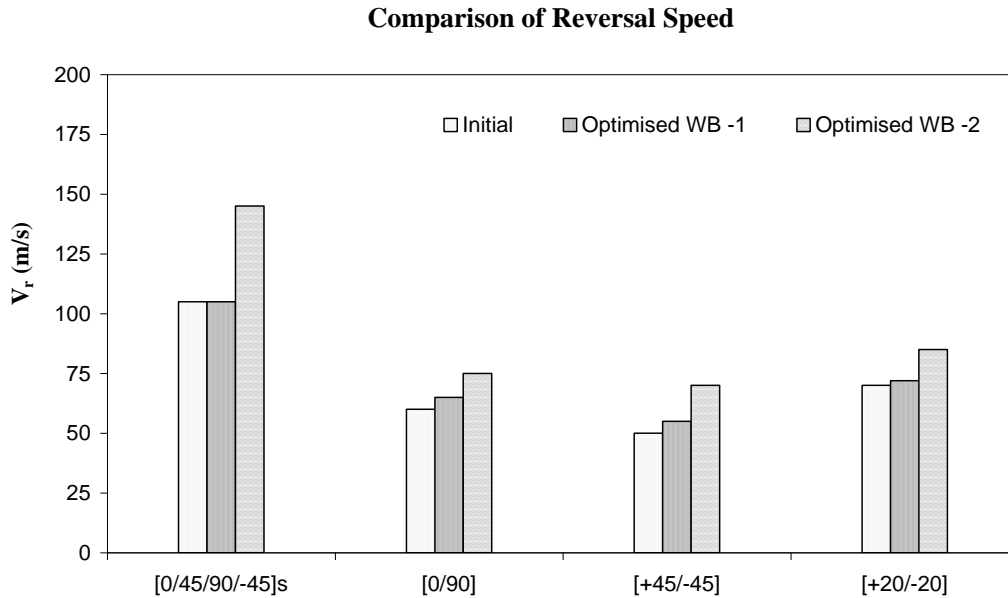


Figure 5.19 Control Reversal Speed Summary

5.6 Discussion of Results

Structurally the two wing box designs allows for a significant reduction of structural weight without compromising the strength. Because of the relatively low stress level at the 4.2g ultimate load factor, the structural strength has enough safety margin for even two layers of glass/epoxy skin laminate. However the reduced wing box stiffness leads to a significant reduction of aeroelastic stability in terms of flutter speed and control reversal speed. This was solved by performing an aeroelastic tailoring with optimum solutions. It was found that both the flutter and control reversal speeds are dominated by the torsion stiffness. It is also noted that the large sweep angle has negative aeroelastic effect on both flutter speed and control effectiveness due to the large negative bending-torsion coupling. Therefore the bending stiffness of the SAW of this particular wing planform also plays a significant role in the control effectiveness and was taken into consideration in the optimisation process.

6 SAW Structural and Dynamic Analysis

This chapter presents the results from the linear static, normal mode, aeroelastic and dynamic analyses carried out for the SAW. The wing box structure with the optimised Case 2.3 lay-up was integrated with the SAW actuation mechanism for detailed analysis. The analysis was carried out using the finite element code MSC/NASTRAN. The aerofoil sections of the wing root and tip sections remained the same as NACA 0015 and NACA 0006 respectively.

The finite element modelling of the composite wing box was conducted using MSC/PATRAN, the pre and postprocessor for MSC/NASTRAN. The material properties and laminate lay-ups of the composite wing were as presented in Table 5.2 and Table 5.4 respectively. The wing box was modelled to simulate the cantilevered boundary condition, which is closed to the physical fuselage-wing attachment. The linear static analysis was then carried out for the maximum aerodynamic loading due to gust at 4.2g. The natural frequencies and mode shapes (with zero structural damping) of the wing were calculated using the Lanczos method through solution number 103 available in MSC/NASTRAN.

Aerodynamic modelling of the wing as a first step towards the flutter analysis after the structural modelling was done applying the Doublet-Lattice Method (DLM) in the subsonic speed. The PK method was selected to solve the flutter equation of motion through the use of the flutter solution number 145. The flutter speed (velocity at which the damping is zero) was identified from the variations of the flight velocity against the total damping. Subsequently the flutter frequency (at flutter speed for particular mode) was identified from the variations of the flight velocity against frequency Figure (V-g plot and V-freq Plot).

Finally, transient-response analyses were carried out for a time-varying excitation due to the sudden change in aerodynamic load at 5^0 TE deflection. The distributed loads were applied along TE section varying at 5 - 20Hz. MSC/NASTRAN solution 109 was used to perform the transient response analysis.

6.1 SAW FE Model

The SAW finite element model comprises a centre wing box and the LE and TE sections. As presented in the previous chapter the centre wing box is made of the front and rear spars and skins reinforced by six T-shaped stringers, three on the upper and three on the lower skin. The Wing Box-2 configuration with the spars and stringers relocated to reduce the effective sweptback angle will be used for the rest of the analysis.

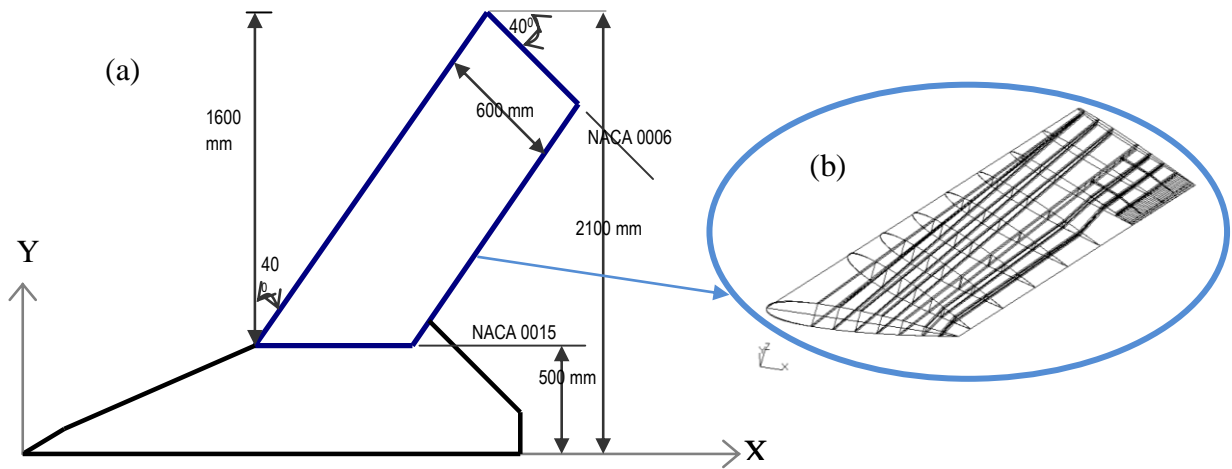


Figure 6.1 (a) SAW planform; (b) Geometrical model created in PATRAN

A description of the SAW composite wing box design was given in chapter 5. Figure 5.4 (a) and (b) of Chapter 5 illustrates the primary dimensions of the SAW wing box. The baseline aircraft wing planform and its basic dimensions are given in Figure 6.1 (a). The model created in MSC/PATRAN consisted of the proposed SAW actuation mechanism integrated to the whole wing model at the last two sections of the wing as shown in Figure 6.1 (b). The cross sectional dimensions at the root and tip of the whole wing are shown in Figure 6.2 and Figure 6.3.

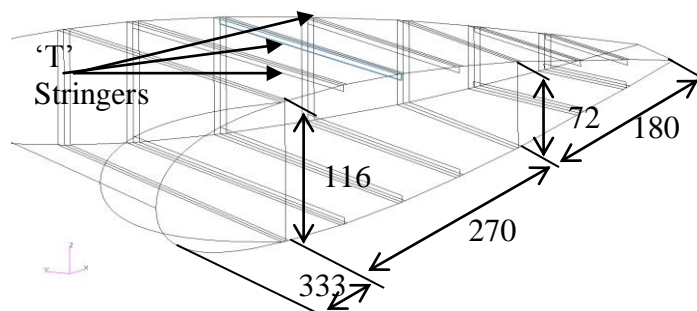


Figure 6.2 Wing Root Cross Section of the SAW FE model (dimensions in mm)

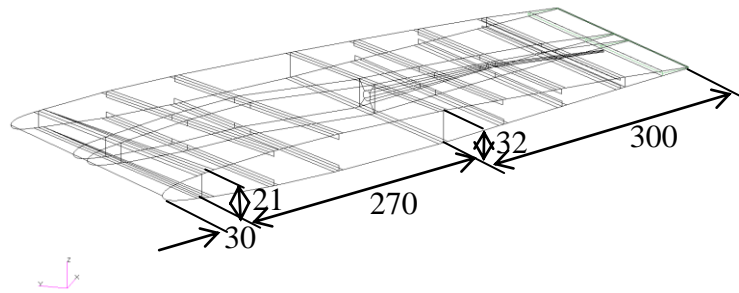


Figure 6.3 Wing Tip Cross Section of the SAW FE model (dimensions in mm)

6.1.1 Finite Element model development of SAW

The finite element model of the SAW was constructed from the upper and lower skins, front and rear spars webs, front and rear spars stiffeners (caps), ‘T’ shaped stringers and a total of nine ribs.

The finite element model of the SAW is shown in Figure 6.4. In the FE model, three types of elements were used in the modelling of the composite wing. The first element was CQUAD4 plate element, which was used to model the following components of the wing structure;

- upper and lower skin surfaces of the wing
- ‘T’ shaped stringers (with an offset)
- front and rear spar webs, flanges
- wing ribs

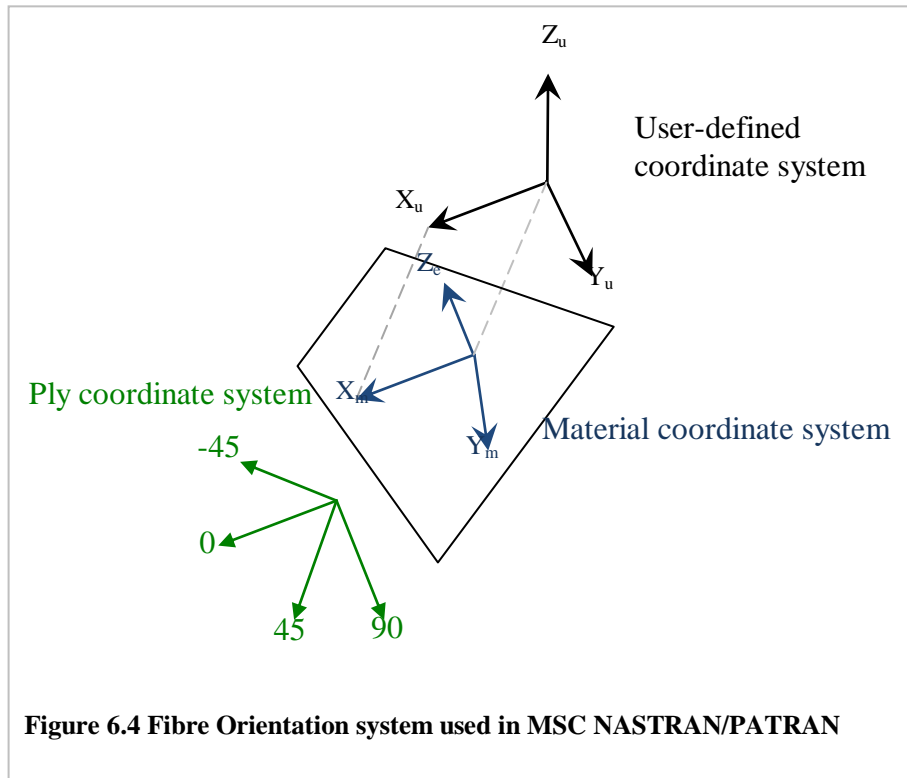
The CQUAD4 is a quadrilateral plate element and is represented by the fully coupled laminate equations, which are shown in equation [43] of Chapter 3. This is a four noded element and is the most commonly used and recommended by many who use FE tools to create numerical models of realistic structures. The CQUAD4 plate element represented the above structural components through the use of the PCOMP and MAT8 cards. For more details about the CQUAD4 and other types of elements, the reader shall refer to the MSC NASTRAN/PATRAN quick reference guides.

The second type of elements used in the modelling of the composite wing was the Triangular Plate Element (CTRIA3). This is a three node element, which is most commonly used for mesh transitions and filling in irregular boundaries. The element may exhibit excessive stiffness, particularly for membrane strain. Therefore whenever possible, CTRIA3s should not be used in regions of interest. Similarly, the CTRIA3s element was used through the use of the PCOMP and MAT8 cards.

The third element used was a solid element CHEXA8 (three dimensional element), which is usually used in modelling of thick plates and solids. CHEXA8s elements were used to represent the elastic material insert at the trailing-edge. This solid element has six sides with eight nodes; each node has only translation degrees of freedom. The solid elements were used through the use of the PSOLID and MAT 1 cards.

The wing model was simulating the fixed free boundary condition, representative of the wing-fuselage attachment on the actual aircraft. A number of rectangular coordinate systems were created using the CORD2R card. The first global rectangular coordinate system employed was such that the x -axis was in the chordwise direction (positive in the stream wise direction), the y -axis was along the span (positive outboard) and hence the z -axis was in the vertical direction (positive upwards). A number of other local coordinate systems were created to define the composite material coordinate system. The Cartesian coordinate system employed for the ribs was such that the X -axis was in the chordwise direction (positive in the stream wise direction), the Y -axis was along the span (positive outboard) and hence the Z -axis was in the vertical direction (positive upwards). The Cartesian coordinate system used to define the material orientation (longitudinal axis of the fibre) through the use of PCOMP card for the upper and lower skin and stringers such that the X -axis was in the spanwise direction (positive outboard), the Y -axis was in the vertical direction (positive upwards) and hence the Z -axis was in the chordwise direction (positive in the streamwise direction). The coordinate system used for the front and rear spar webs material longitudinal axis was the same as the coordinate system used for the wing skins. In MSC NASTRAN/PATRAN the material coordinate system is defined by a user defined coordinate system whose x -axis is projected onto the element to define the element's

material coordinate system's x -axis. This along with the z -axis of the element coordinate system defines the material coordinate system (see Figure 6.4). The positive y -axis of the material coordinate system was then found by the right hand rule for a positive fibre angle 0 as shown in Figure 6.4.



Four different types of material were used in the SAW finite element model. The material properties of carbon/epoxy and E-glass/epoxy were the same as listed in Table 5.2 in Chapter 5. The optimised laminate layup from Table 5.4 was used in creating the properties of the wing skins in the E-glass/epoxy model (Optimised Case 2.3). The front and rear spar web layups remained the same as the baseline model made up of carbon/epoxy. Unidirectional material was used for all the plies of the FE model. The elastic material used for the trailing-edge and the eccentric beams within the wing was modelled using isotropic material, which has material properties as listed in Table 6.1.

Table 6.1 Aluminium and Rubber Material Properties [122]

Material	E (MPa)	G (MPa)	ν	ρ (Kg/m ³)
Aluminium	72.9E3	27.3E3	0.33	2800
Rubber	7.5	2.8	0.339	1270

The ply thickness of the unidirectional material was 0.125 mm and 0.25 mm for the carbon/epoxy and E-glass/epoxy respectively. The generations of the structural materials for the composite components were done through the use of the MAT8 and PCOMP cards.

6.1.2 SAW Actuation Mechanism Creation

Three different wing models were created in PATRAN to determine the effect of incorporating an open trailing-edge with the eccentric beams. A baseline SAW design (Model 1) having a closed trailing-edge model was taken as a reference to compare with the models of a more flexible trailing-edge, see Figure 6.5. The TE section was integrated with the actuation mechanism adapting the same design concept proposed in Chapter 4.

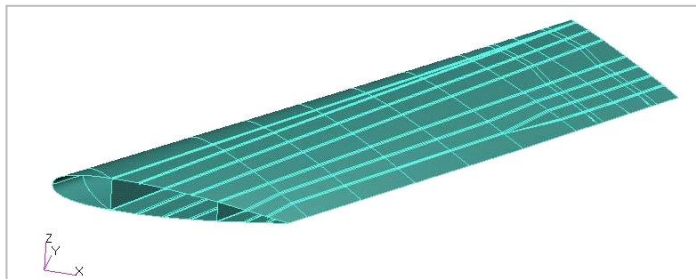


Figure 6.5 SAW Baseline Design with a closed TE

In Model -2 and -3, an open trailing-edge was modelled at the wing tip section of 0.4 m along the span for these two models. In the Model-2 as shown in Figure 6.6, a plastic material insert was used to connect the upper and lower skins along the TE. In Model-3 however, the upper and lower skins were connected along the TE with a 1mm gap for a more flexible warping control surface.

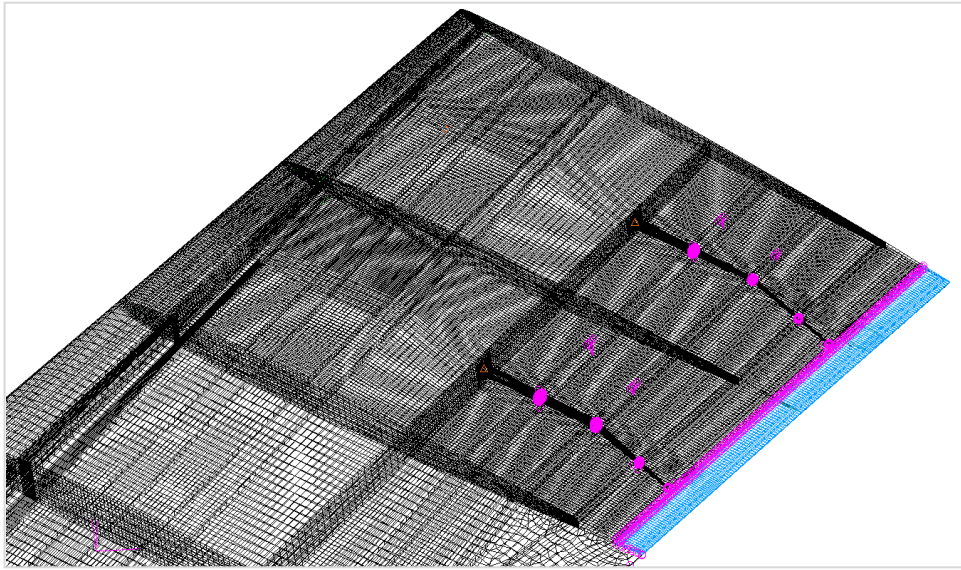


Figure 6.6 Open TE modelled in Model-2

The proposed eccentric beam actuation mechanism was built as part of the structure in all the models. The connection of the discs to the skin stiffeners were modelled using RBE2 elements in the FE models. RBE2 elements are multipoint constraints (MPCs) available within NASTRAN to model a rigid connection using one independent node and multiple dependent nodes. The RBE2 element uses the small deflection theory as shown in Figure 6.7. It uses a linear relationship between the independent and dependent nodes based on the displacement of the independent node. Other properties such as stiffness mass and loads at the dependent degree of freedoms are transferred to dependent degree of freedoms.

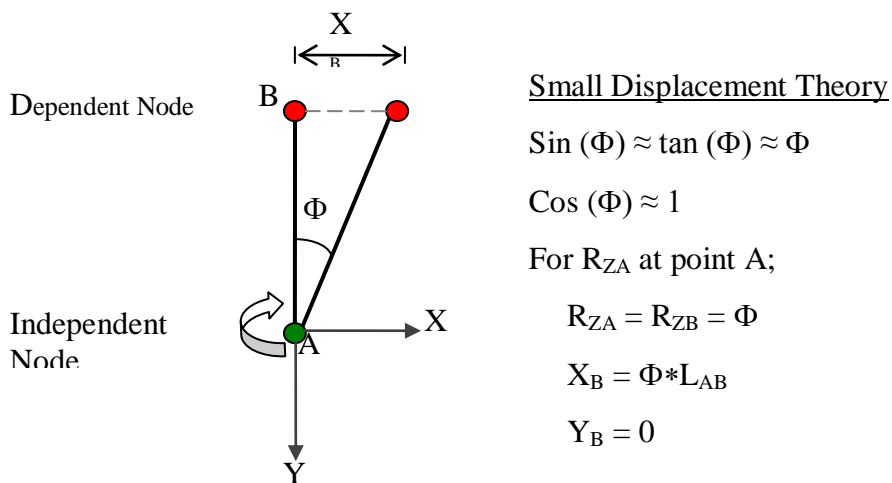


Figure 6.7 RBE2 modelling

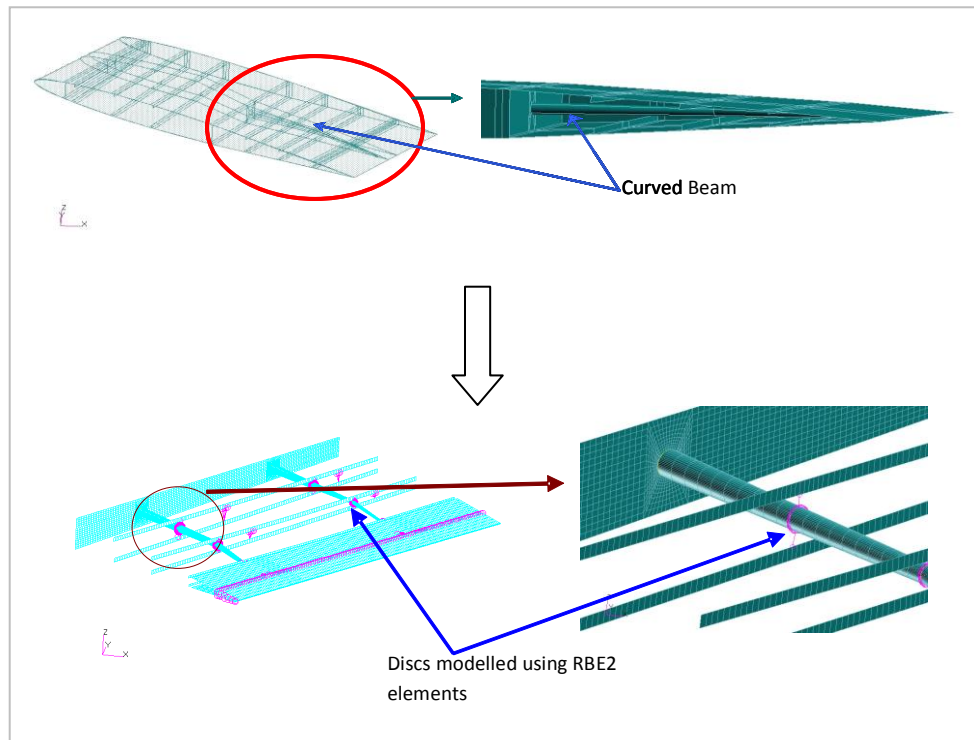


Figure 6.8 Curved beam model along with the discs modelled in FE

6.1.3 FE Model Cases

The same material properties were applied as presented in Chapter 5 for the SAW FE models. The baseline model, Carbon/Epoxy SAW model – In this design, the wing skin and spars are made of 8-ply carbon/epoxy laminate of symmetric layup $[0/45/90/-45]_s$ with skin thickness of 1 mm. The stringers have the same material and thickness as the skin. The material properties are listed in Table 5.3.

The reduced weight and optimised Glass/Epoxy SAW model - In this case, the carbon/epoxy material and layup remain the same for the front and rear spar webs. The skin and stringers were made up of E-glass/epoxy with the optimised lay up of $[30.7/-36.8]$ and $[27.8/-51.4]$ for the upper and lower skins respectively. Material properties of the E-glass/epoxy used in the model are listed in Table 5.3.

6.2 SAW Structural Analysis

6.2.1 Static Aerodynamic Loading Results

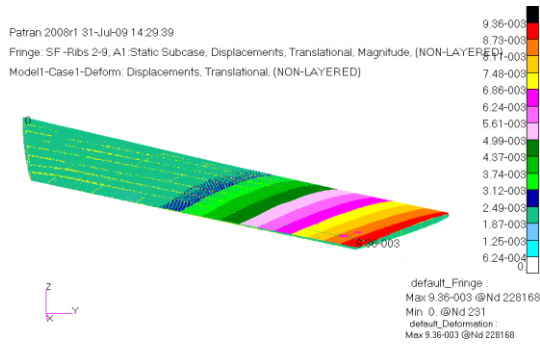
The maximum transverse deflections at the wing tip under the maximum load factor of 4.2g for these cases are summarized in Figure 6.9. The results indicate that the deflection of Case 2 is higher compared to that of Case 1 and this is mainly due to the skin being more flexible in Case 2. Comparing the three models indicate that the open TE wing results in a higher deflection compared to the closed TE wing. However, model 2 with the rubber shows that it is much stable under the applied loading compared to model 3. The change in leading edge deflection stays relatively small compared to the change in the TE deflection under the loading for the three different SAW models. The open TE in model 2 and 3 influences a relatively higher TE deformation compared to the baseline closed TE model.

SAW Model 1

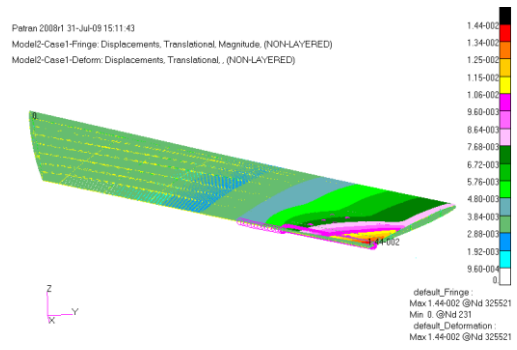
SAW Model 2

SAW Model 3

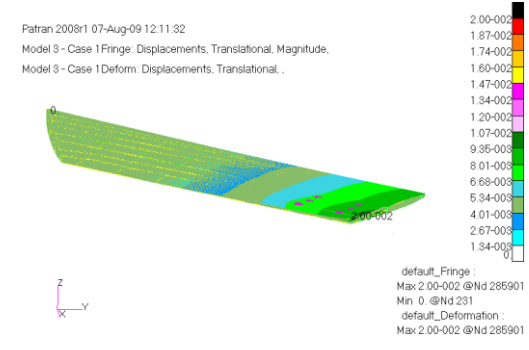
Carbon/Epoxy Skin



Z = 9.4 mm

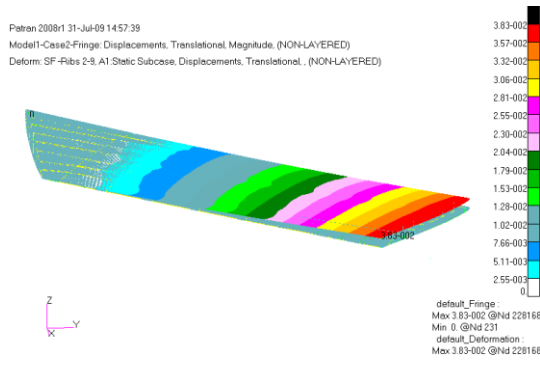


Z = 14.4 mm

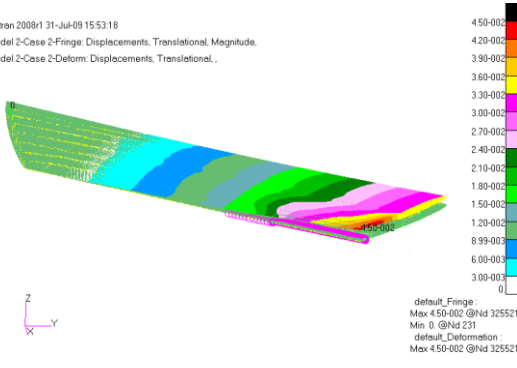


Z = 20 mm

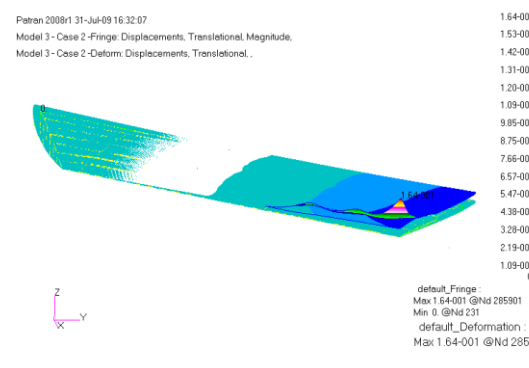
Glass/Epoxy Skin



Z = 38 mm



Z = 45 mm



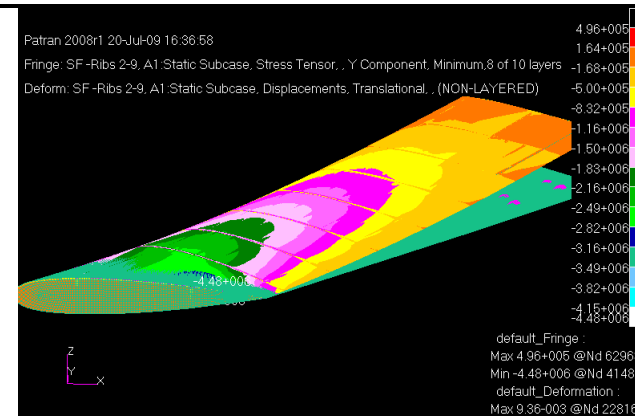
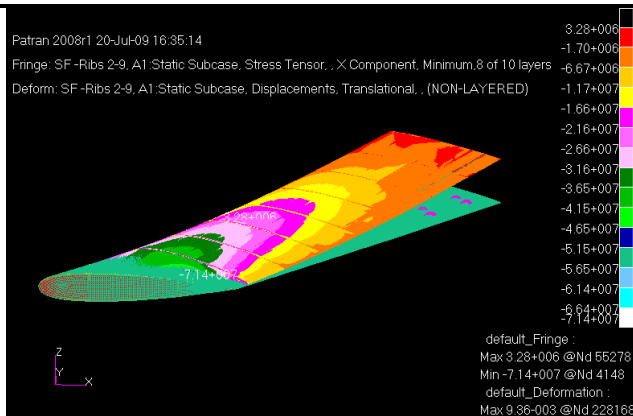
Z = 164 mm

Figure 6.9 Maximum transverse deflections at the wing tip under the maximum load factor of 4.2g

Fiber Direction (1)

Off- Fiber Direction (2)

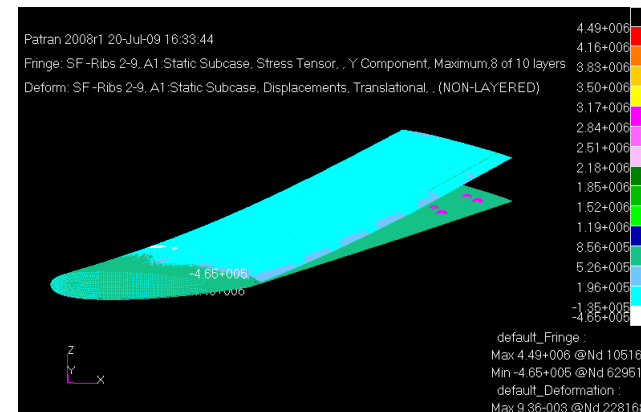
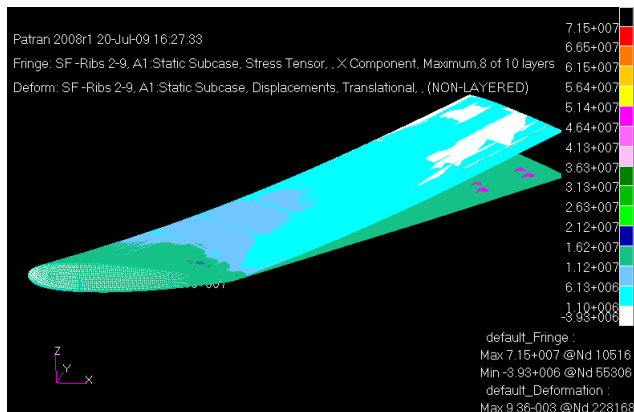
Compressive



Max = 3.28 MPa

Max = 0.496 MPa

Tensile



Max = 71.5 MPa

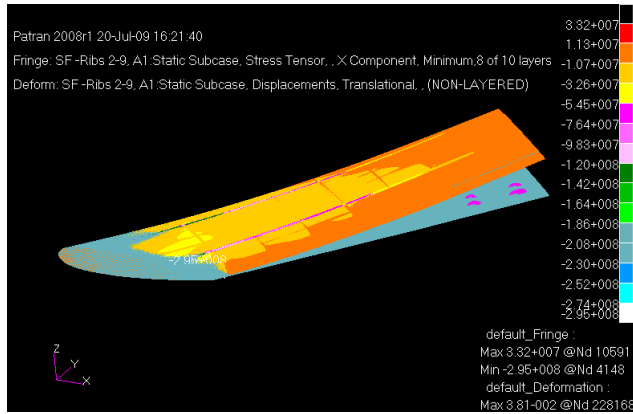
Max = 4.49 MPa

Figure 6.10 Model 1- Carbon/Epoxy skin under 4.2g Aerodynamic load

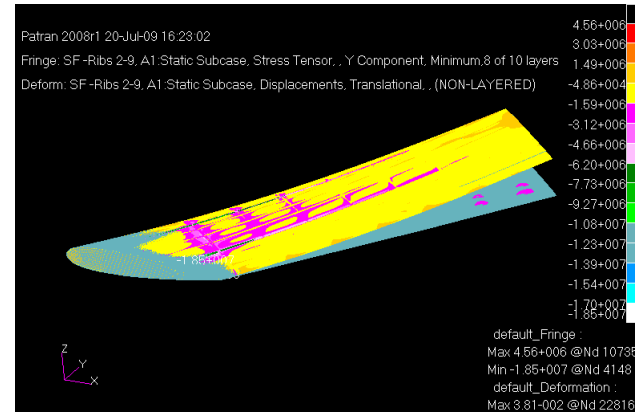
Fiber Direction (1)

Off- Fiber Direction (2)

Compressive

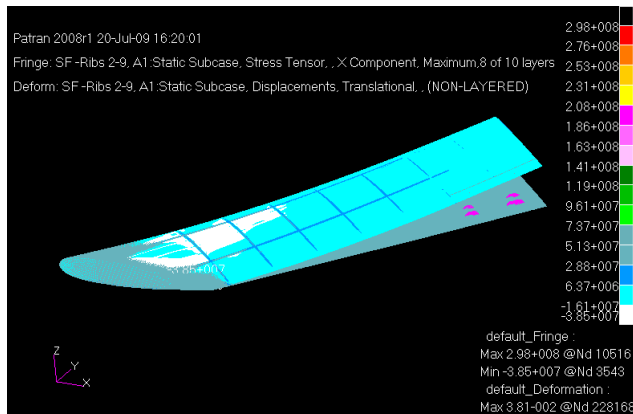


Max = 33.2 MPa

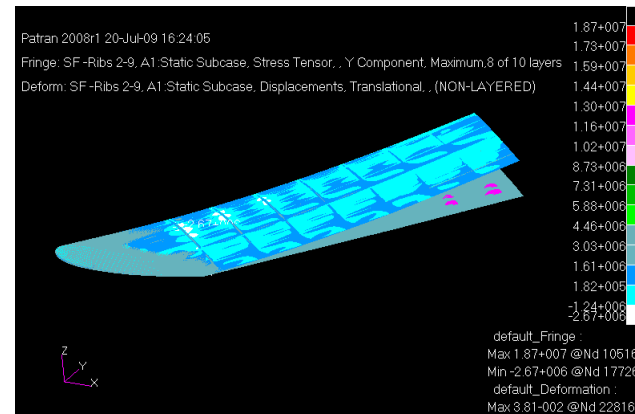


Max = 4.56 MPa

Tensile



Max = 298 MPa



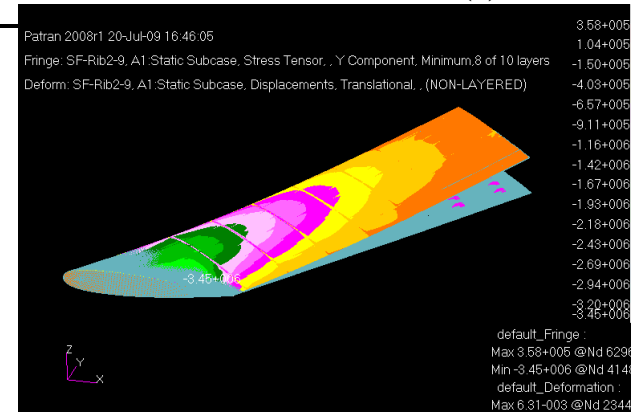
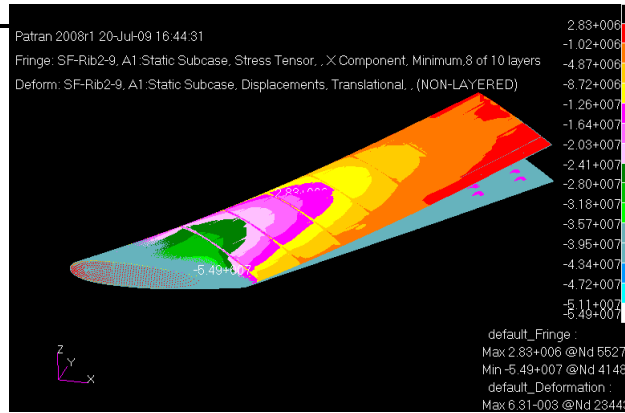
Max = 18.7 MPa

Figure 6.11 Model 1- EGlass/Epoxy skin under 4.2g Aerodynamic load

Fiber Direction (1)

Off- Fiber Direction (2)

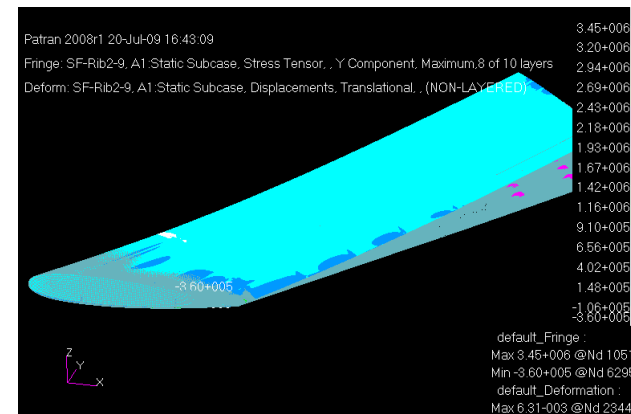
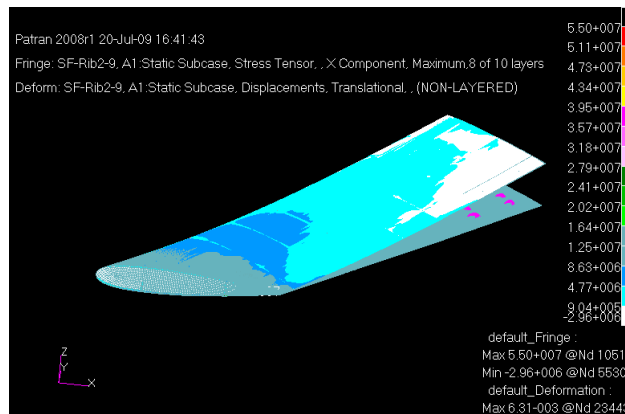
Compressive



Max = 2.83 MPa

Max = 0.358 MPa

Tensile



Max = 55 MPa

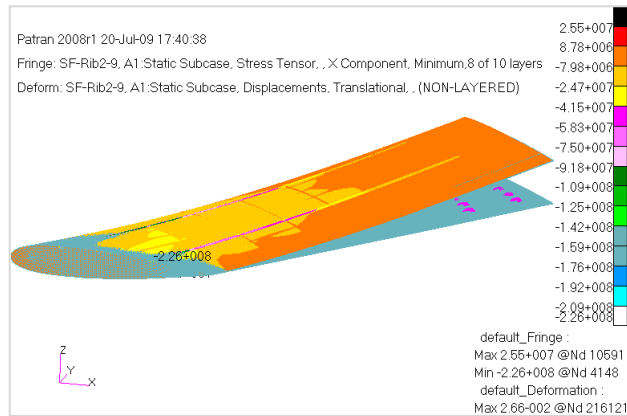
Max = 3.45 MPa

Figure 6.12 Model 3- Carbon/Epoxy skin under 4.2g Aerodynamic load

Fiber Direction (1)

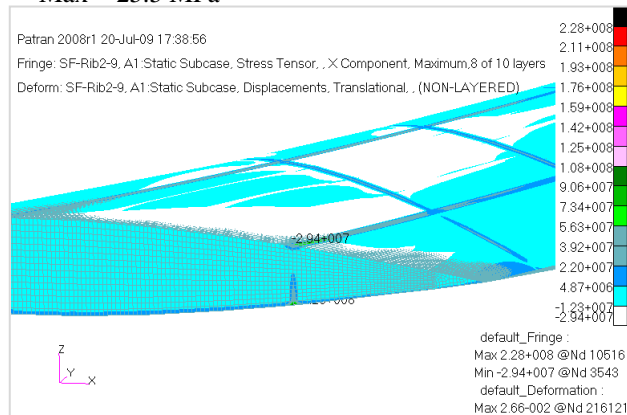
Off- Fiber Direction (2)

Compressive

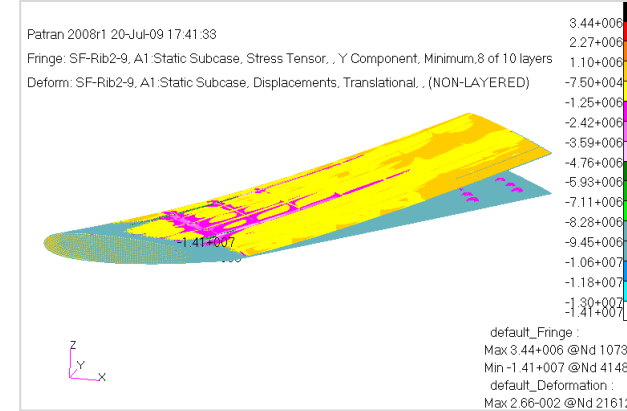


Max = 25.5 MPa

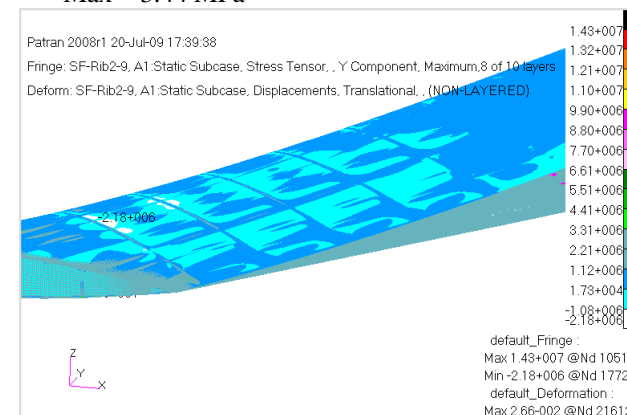
Tensile



Max = 228 MPa



Max = 3.44 MPa



Max = 14.3 MPa

Figure 6.13 Model 3- EGlass/Epoxy skin under 4.2g Aerodynamic load

The maximum stress for all three FE models occur at the root of the rear spar. These results are presented in Table 6.2. As expected the SAW with the E-Glass fibre skin resulted in a higher stress value compared to the carbon/epoxy skin model for the baseline and open TE SAW FE models. The most noticeable difference is that the open TE SAW design results in low stress values compared to the baseline design. This shows that the addition of an open TE changes the standard load path and results in a lower stress at the wing root.

Table 6.2 Stress Summary

		Fiber Direction (1)	Off-Fiber Direction (2)
		(MPa)	(MPa)
Model 1-	<i>Compressive</i>	3.28	0.50
Carbon/Epoxy	<i>Tensile</i>	71.5	4.49
Model 1- E-	<i>Compressive</i>	33.2	4.56
Glass/Epoxy	<i>Tensile</i>	298	18.7
Model 3-	<i>Compressive</i>	2.83	0.36
Carbon/Epoxy	<i>Tensile</i>	55	3.45
Model 3- E-	<i>Compressive</i>	25.5	3.44
Glass/Epoxy	<i>Tensile</i>	228	14.3

Figure 6.14 (a) and (b) summarises the TsaiWu failure indices for the baseline and the detailed SAW model-2 under the same aerodynamic loading respectively. The two models were considered as being the worst case with an E-Glass/epoxy skin. The baseline SAW model resulted in a 0.36 failure index whilst the open TE SAW model resulted in 0.29 failure index. These results further confirms that the open TE model shows lower stress levels compared to a conventional closed TE model. The comparison between the deflections and the stresses indicates that even the open TE design has enough strength under the maximum shear force loading.

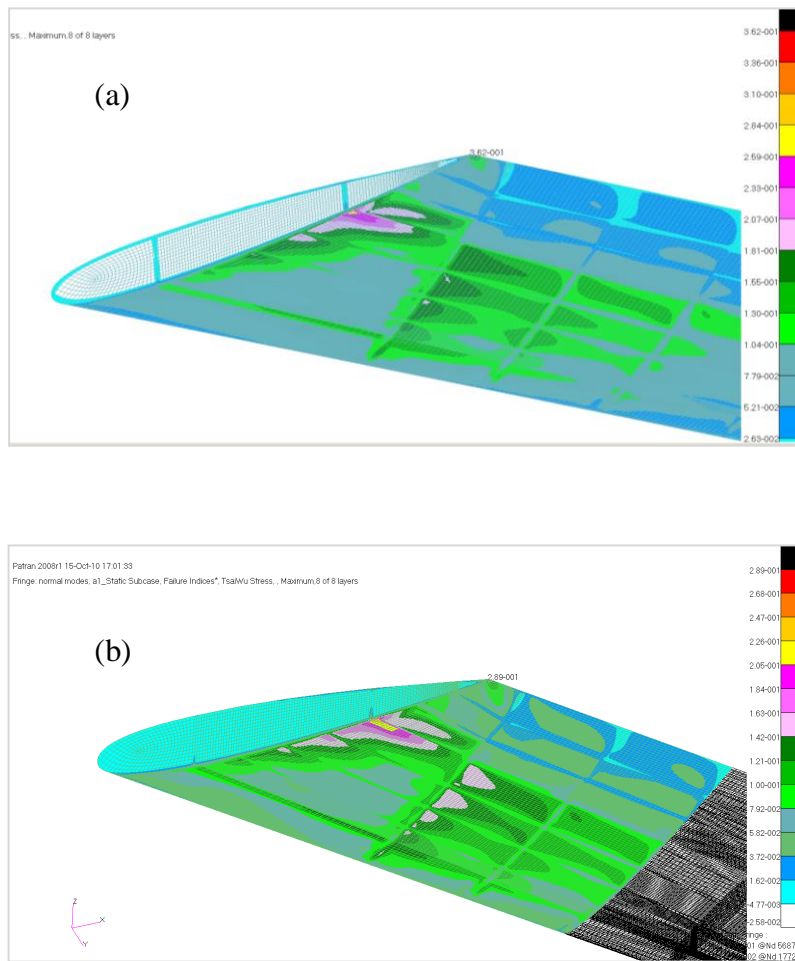


Figure 6.14 E-Glass/Epoxy skin under 4.2g Aerodynamic load for (a) Baseline Model-1; (b) SAW Model-2

6.2.2 Actuation Results

Figure 6.15 shows the deflected SAW due to TE actuation under the maximum actuation force required to deflect the TE equivalent to 10 degrees of conventional flap deflection. The open TE mechanism used in Model 2 allows smooth TE sliding between the upper and lower skins in order to achieve the required deflection. The total actuation force required to deflect the TE for the carbon fibre skin was 680N compared to 200N for the glass fibre skin.

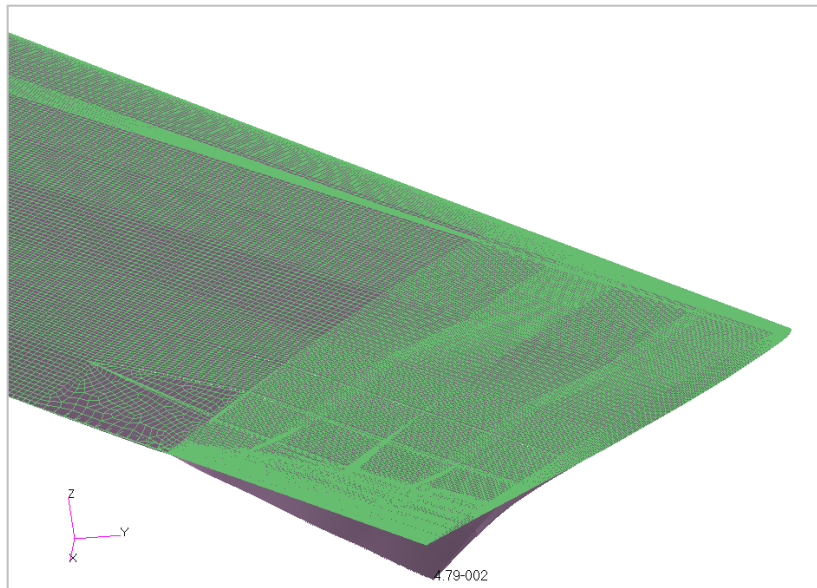


Figure 6.15 Deflected SAW due to TE Actuation

The figure below illustrates the TsaiWu failure index results of the SAW model-2 for the two types of skins considered in this study, under the maximum actuation force required to deflect the TE for an equivalent deflection of 10^0 conventional flap deflection. The maximum failure index for the carbon/epoxy model was 0.52, at the tip of the TE. Similarly the maximum failure index for the E-Glass/Epoxy skin model was 0.66 around the same region.

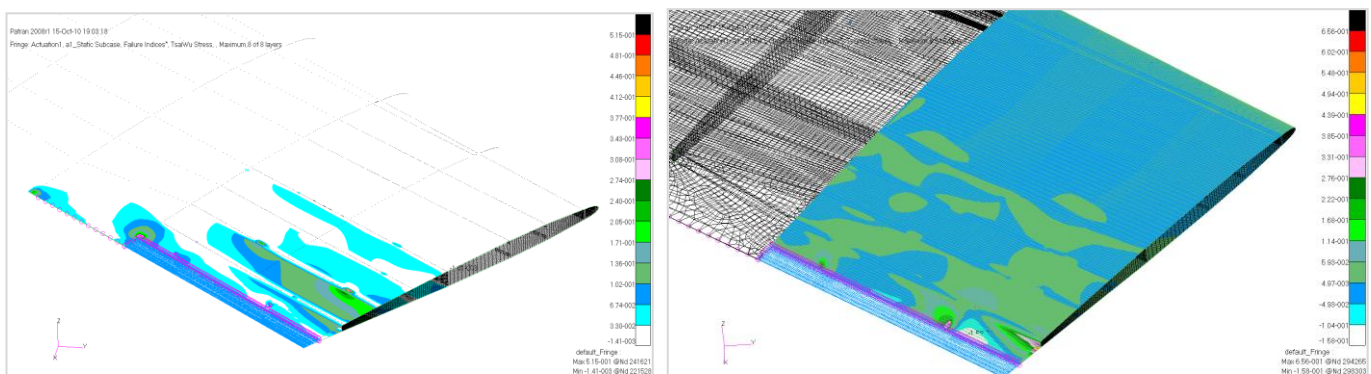
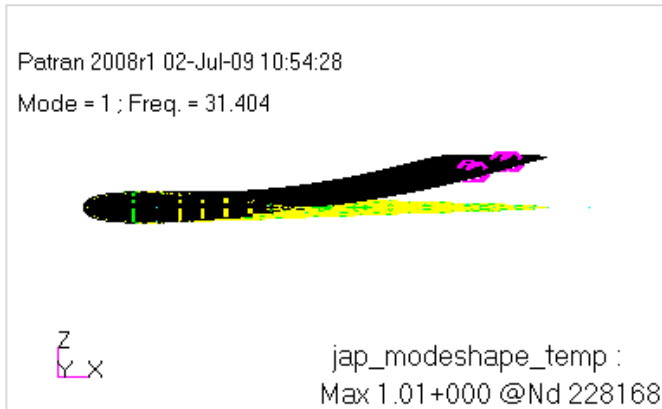


Figure 6.16 SAW Model-2 under TE actuation load for (a) Carbon/Epoxy; (b) E-Glass/Epoxy skin

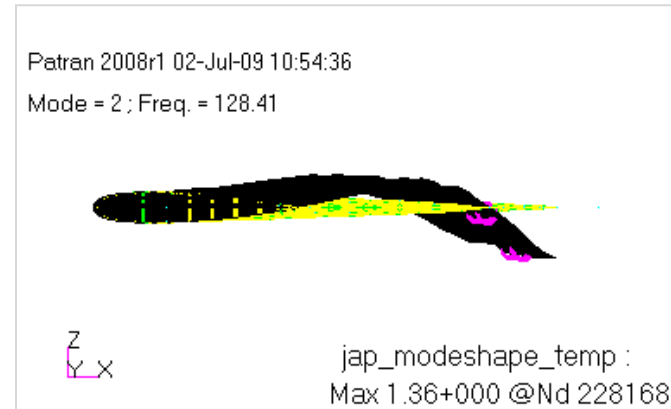
6.3 SAW Vibration Analysis

Normal mode analysis or real eigenvalue (undamped free vibrations) was conducted by using the Lanczos method, via MSC/NASTRAN, Sol 103, for the three SAW FE models using the material properties and the laminates layups presented in chapter 5. This method was used to determine the basic dynamic characteristics of the composite wing; natural frequency and mode shapes, for the three models. The natural frequencies and mode shapes were then used to guide the subsequent transient response analysis.

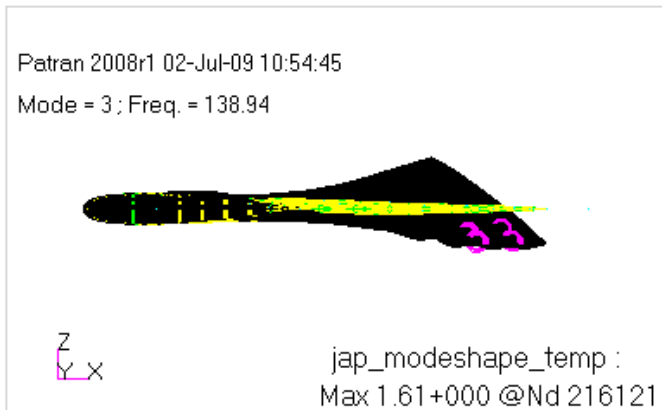
Normal mode analysis was carried out for model 1 and model 3 to look at the effect of the open TE. Figure 6.17 and Figure 6.18 summarises the mode shapes for design case with the Carbon/epoxy skin (Case 1) of model 1 and model 3. The first bending mode is around 30 Hz for both models and the second mode of model 3 is a local mode at the open TE region. A similar pattern of modes were obtained for the E-glass/epoxy skin (Case 2.3-optimised) for the two models, however, the first bending mode occurred at 19 Hz and the resulting frequencies of the modes were lower compared to the carbon/epoxy model. The subsequent figures summarise these results.



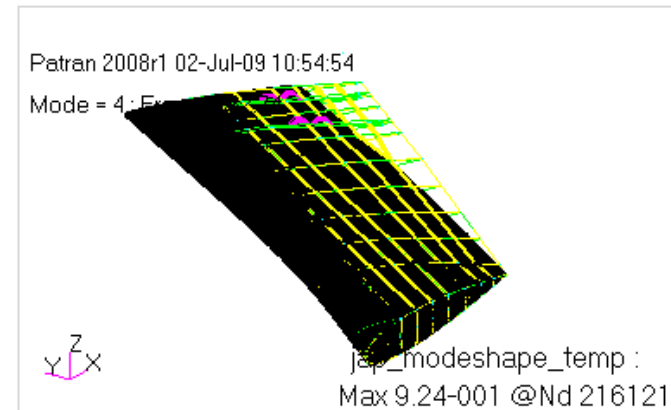
First Bending; 31 Hz



Second Bending; 128 Hz

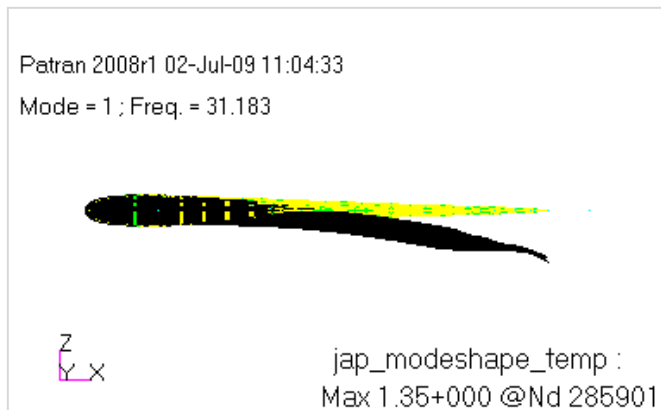


Torsional mode: 139 Hz

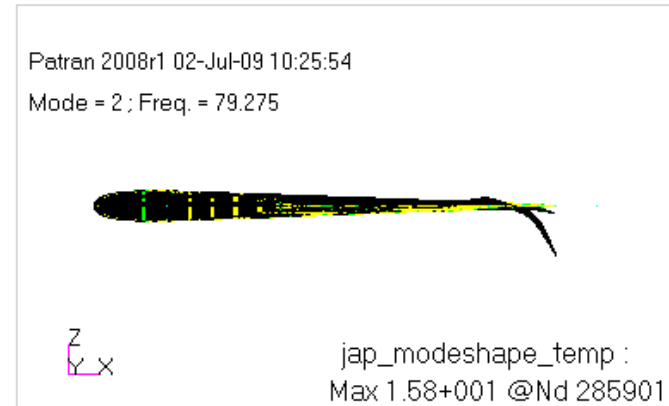


In-plane Bending: 163 Hz

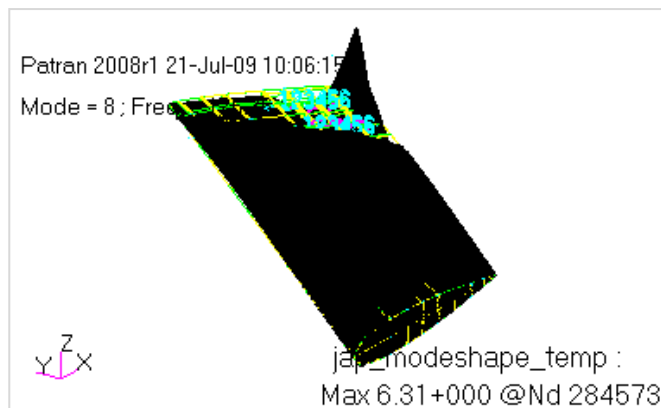
Figure 6.17 Normal modes of SAW baseline Model-1 with Carbon/epoxy skin



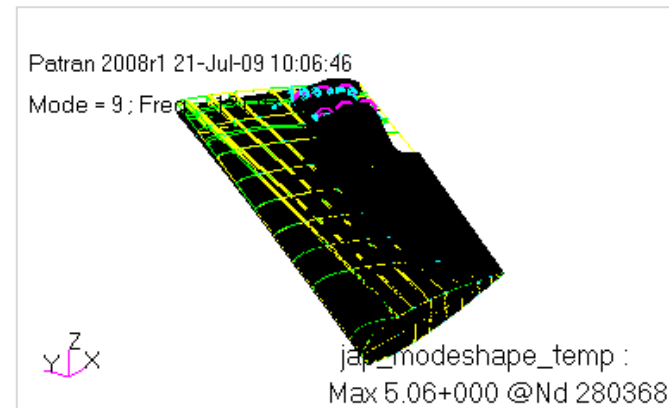
First Bending; 31.2 Hz



TE local bending mode; 79 Hz

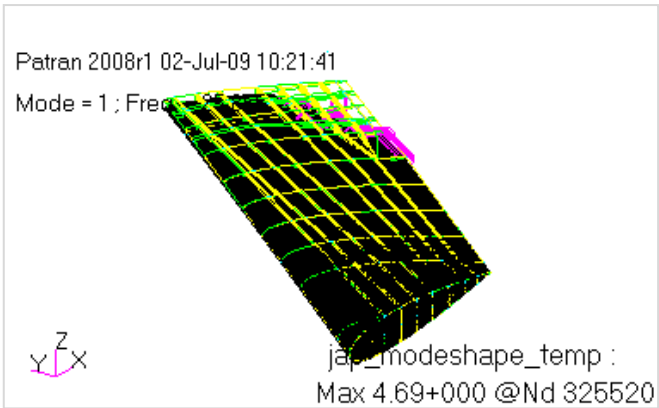


Bending mode: 125 Hz

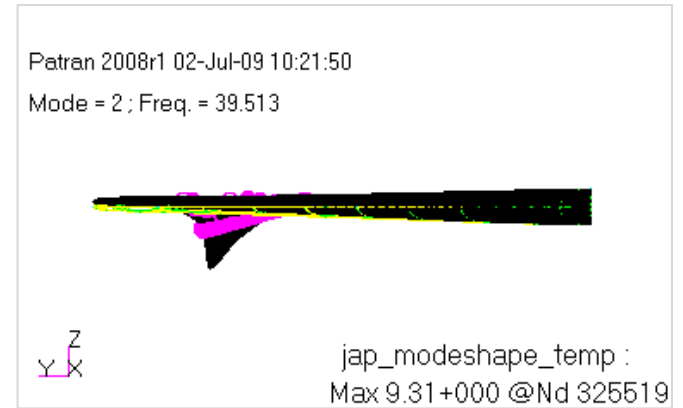


Torsional mode: 131.3 Hz

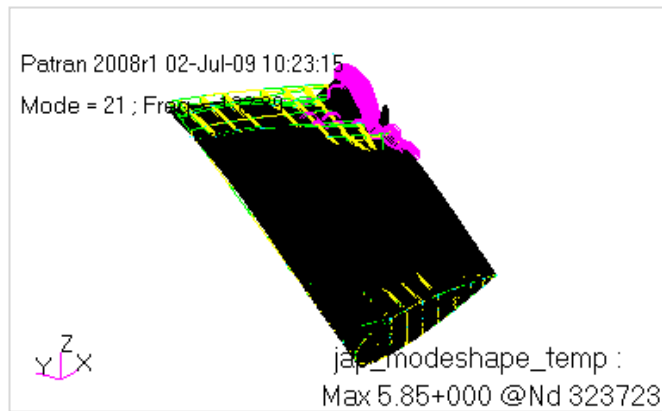
Figure 6.18 Normal modes of SAW Model-3 with Carbon/epoxy skin



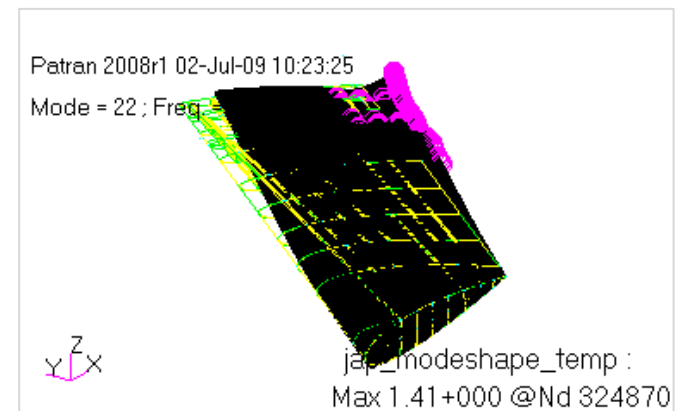
First Bending; 25.86 Hz



TE local bending mode; 39.51 Hz



Bending-Torsion coupling: 132.9 Hz



In-planed Bending: 162.5 Hz

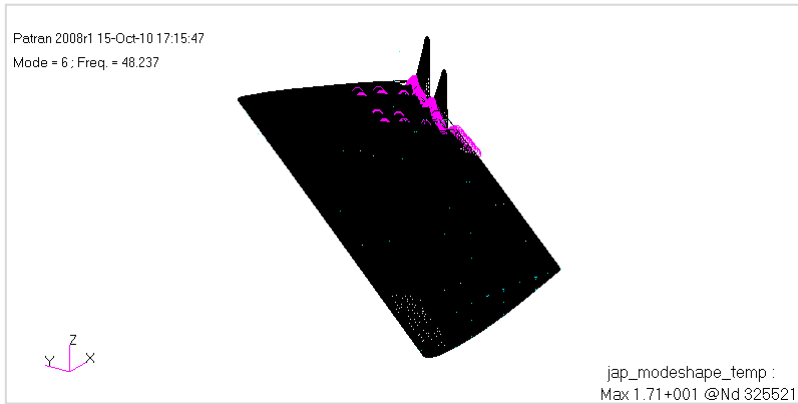
Figure 6.19 Normal modes of SAW Model-2 with Carbon/epoxy skin



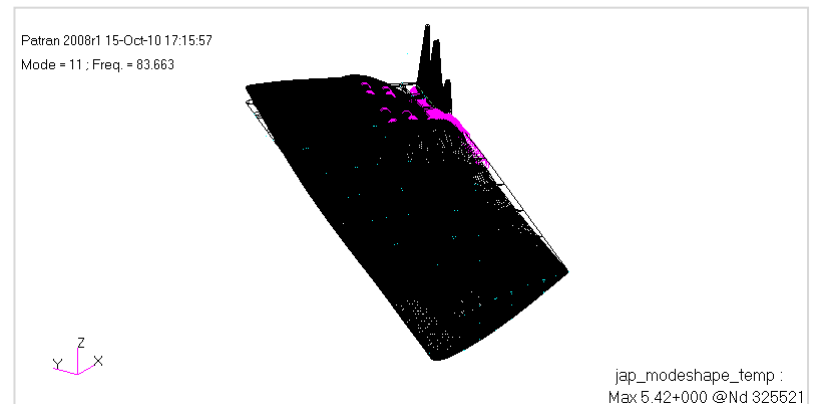
First Bending ; 16.9 Hz



TE local Bending ; 23.8 Hz

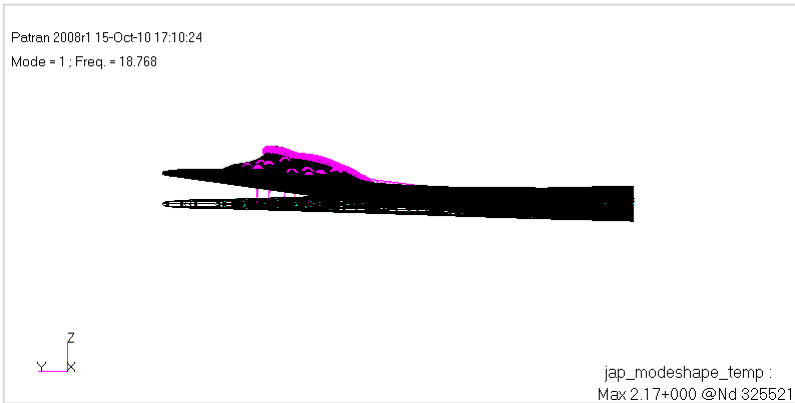


TE Bending; 48.2 Hz

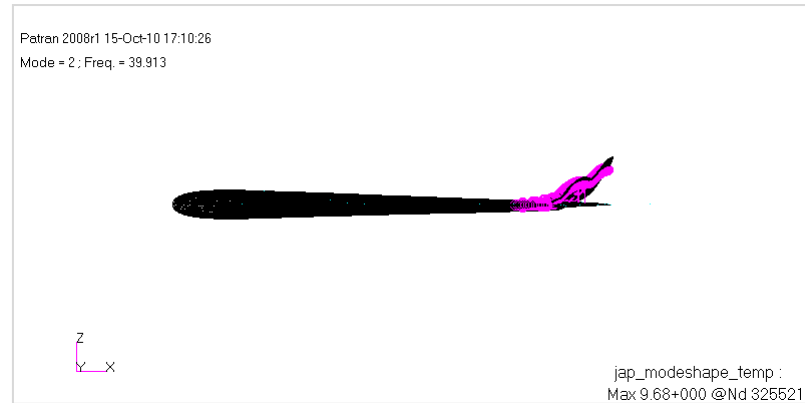


Bending-Torsion coupling; 83.7 Hz

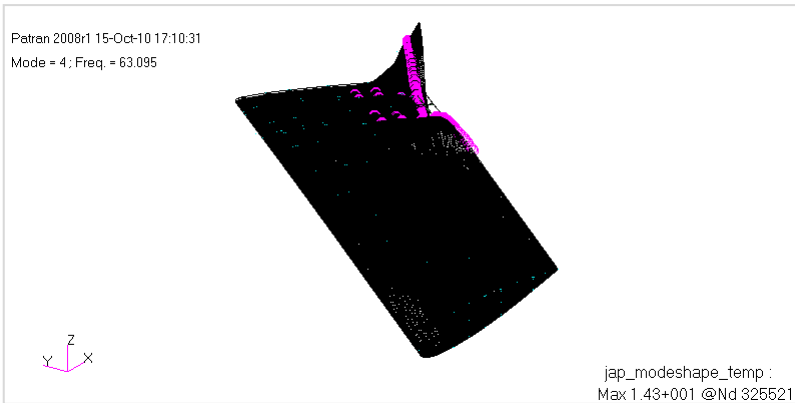
Figure 6.20 Normal modes of SAW Model-2 with E-Glass/epoxy skin



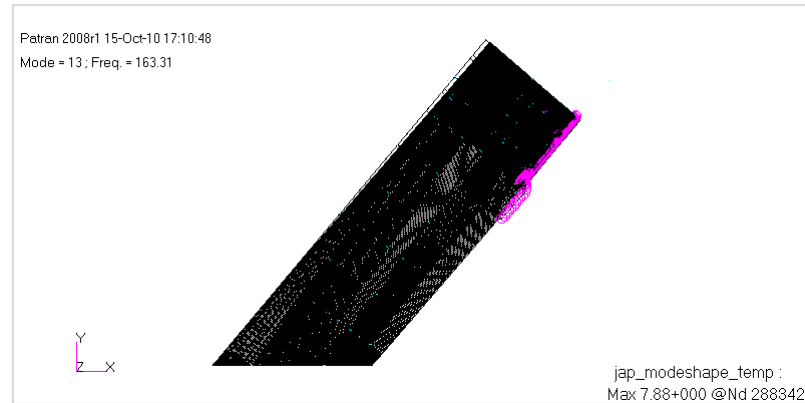
First Bending: 18.8 Hz



TE Local Bending: 39.9 Hz



Bending-Torsion Coupling: 63.1 Hz



In-Plane Bending: 163.3 Hz

Figure 6.21 Normal modes of SAW Model-2 with E-Glass/epoxy skin (without Rubber insert at the TE)

Table 6.3 Fundamental Bending and Torsion Frequencies for the Carbon/Epoxy skin Case

	Model-1 Frequencies (Hz)	Model-2 Frequencies (Hz)	Model-3 Frequencies (Hz)
1 st Bending	31	26	31
TE Bending	-	39	79
2 nd Bending	128	-	125
Bending-Torsion	139	133	131
In-Plane Bending	163	162.5	-

Table 6.3 summarises the Eigen values obtained for the first few resonant frequencies of each SAW FE models with the Carbon/Epoxy skin using MSC/NASTRAN. The baseline model (Model-1) was used to compare the frequencies obtained from Model 2 and 3 which represents the proposed SAW design integrated with an open TE. The results indicate that the open TE models behave in a similar manner to the baseline model with a closed TE. After close inspection of the mode shapes of the SAW models, it was found that the fundamental mode at 31 and 26 Hz are representative of the 1st bending mode for the baseline model and the proposed SAW models respectively. An additional second mode was present for the open TE models where the flexible control surface is present. The frequency for this mode for Model-2 is significantly low compared to that of Model-3. This is mainly due to the modelling of the TE structure with a rubber insert in Model-2, whereas in Model-3 the open TE gap remains empty with no material inserts and is modelled using a rigid connection (RBE2), which adds additional stiffness to the structure at the TE. The mode at 125 Hz represents the 2nd bending mode. The mode at approximately 139 and 130 Hz represents the bending-torsion coupling mode for the baseline model and the SAW open TE models respectively.

Table 6.4 Fundamental Bending and Torsion Frequencies for the E-Glass/Epoxy skin Case

	Model-2 Frequencies (Hz)	Model- 2 (without rubber) Frequencies (Hz)
1 st Bending	16.9	18.8
TE Bending	23.8	39.9
2 nd Bending	-	-
Bending-Torsion	83.7	63.1
In-Plane Bending	-	163.3

Table 6.4 summarises the Eigen values obtained for the first few resonant frequencies of the SAW model-2 with E-Glass/Epoxy skin using MSC/NASTRAN. Model-2 was analysed with and without the rubber insert to see the effect of this additional mass due to rubber at the TE. The first bending mode of these two models showed not much difference. However, the TE bending frequency was significantly higher for the model without rubber compared to the TE with rubber. The more beneficial effect comes from the bending-torsion mode where the frequency was higher for the model with the TE rubber insert as oppose to the model without the rubber insert.

6.4 SAW Flutter Analysis

In this section, the flutter analysis of the SAW wing models was carried out for the baseline wing model with a closed TE and the other two wing model representing an open TE. Both material properties and the laminate lay-up for both Carbon/epoxy and the optimised E-glass/epoxy skins remained the same. The flutter speed was calculated using the finite element package MSC/NASTRAN. The aerodynamic coefficient matrix was evaluated by means of the Doublet-Lattice Method (DLM). The interconnection of the structural grids with the aerodynamic grids was done using the theory of surface splines (SPLINE I card).

The flutter analysis was performed using solution 145 on the SAW FE models created in PATRAN. The analysis was carried out using the first ten vibration modes (PARAM

LMODES 4) of the model. As described in Chapter 3, the flutter solution method used was the PK method. The relation of the flight velocity versus the total damping (structural and aerodynamic damping) and frequency were taken from the output of the PK method and plotted using Microsoft EXCEL program.

6.4.1 Aerodynamic Modelling

The first ten vibration modes shown in the previous section were used in the flutter analysis. Within the aerodynamic model, relevant flight and geometric parameters are specified on the AERO card for the dynamic aeroelastic analysis. The aerodynamic element meshes and the locations of the root and tip leading edges were controlled and located using the CAEROI card which was used for the DLM.

An aerodynamic coordinates system was created using CORD2R card with the X-axis being parallel and positive in the direction of the flow, Y-axis was along the span and Z-axis pointing positive upwards. A total of 60 aerodynamic elements, ten elements along the semi-span and six elements along the chord with a reduced frequency (k) range from 0.001 to 1.0. The aerodynamic and structural grids are connected through the use of the surface SPLINE I and SET I cards. All the aerodynamic elements were used in the interpolation with the selected structural grids.

A reference chord of 783 mm (chord at root of the wing), reference density at sea level were specified through the AERO card for the entire model. The aerodynamic conditions, which are listed in the MKAEROI card, were used to specify the Mach number (0.14) and the reduced frequency range.

6.4.2 Flutter Results

The flutter speeds obtained for the closed and open TE SAW models are shown in the subsequent sections and summarised in Table 6.5 at the end of this section.

SAW Model 1

Figure 6.22 and Figure 6.23 are the V-g and frequency vs. velocity curves for the baseline model (Model 1) with the Carbon/Epoxy skin respectively. The damping of mode one increases with speed up to 1100 m/s and begins to decrease with increasing speed with no change in damping sign. The frequency of this mode eventually decreases to zero around the 1100 m/s speed. The damping of the second mode shows that it increases slightly with increasing speed and decreases until it intersect the curve at 640 m/s for zero damping and continues to increase in the positive damping region of the curve. The corresponding frequency for this mode was approximately 100 Hz as can be seen from Figure 6.23. Mode three and seven show similar trends by increasing with increasing speed. Figure 6.22 shows that the corresponding frequency for mode three increases slightly from 130 Hz to 175 Hz, while for mode seven the frequency decreases from 230 Hz to 175 Hz with increasing speed. The damping of the fifth and sixth modes were very small compared to the rest and changed from being negative to positive damping at 800 m/s and 1100 m/s respectively^a. The frequencies for these two modes were almost constant with increasing speed. Modes eight, nine and ten followed a similar trend where the damping was significantly small and corresponding frequencies remained constant throughout the entire speed range as can be seen from the figures below.

Figure 6.24 and Figure 6.25 summarise damping and frequency against the velocity respectively for each mode considered for the base line SAW model with the optimised E-Glass/Epoxy skin. The damping and frequency trends with varying speed for each mode remain precisely the same as for the carbon/epoxy model. The only difference is that the magnitudes of the damping have increased whilst the frequencies have reduced as a result of reduced stiffness of the E-Glass/Epoxy model. From the V-g plots (i.e. Figure 6.22 and Figure 6.24) it can be seen that the flutter speed were 645 m/s and 370 m/s for the Carbon/epoxy and optimised E-Glass/Epoxy skin models respectively.

^a This is not visible in Figure 6.22 due to the scale of the damping axis.

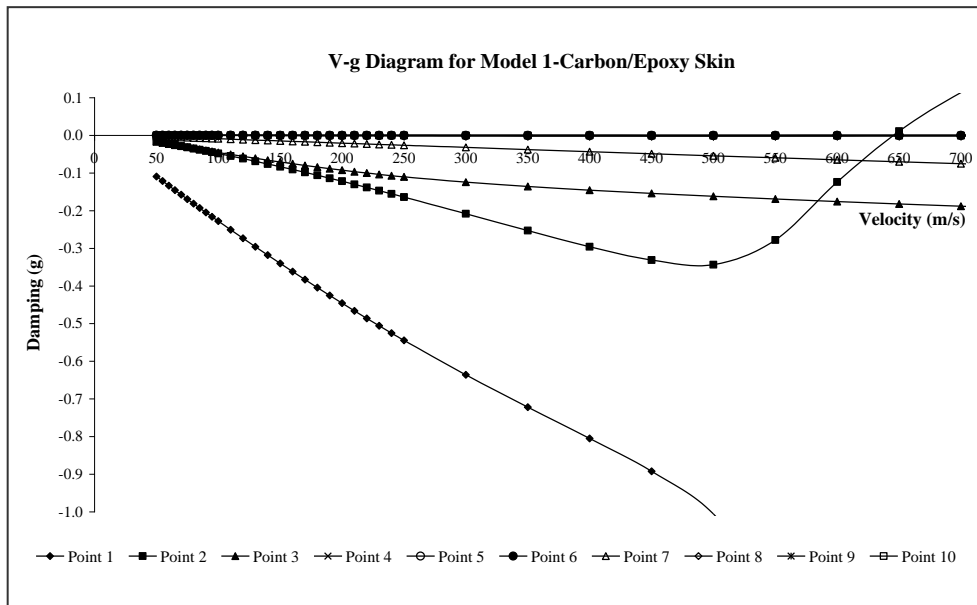


Figure 6.22 Velocity vs Damping (g) of Model 1-Carbon/Epoxy skin

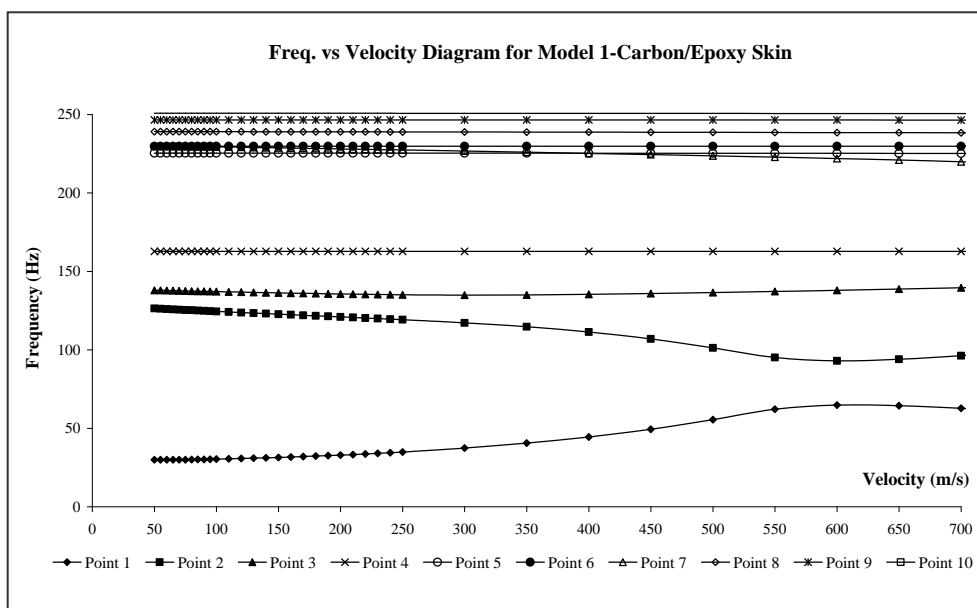


Figure 6.23 Velocity vs Frequency (ω) of Model 1-Carbon/Epoxy skin

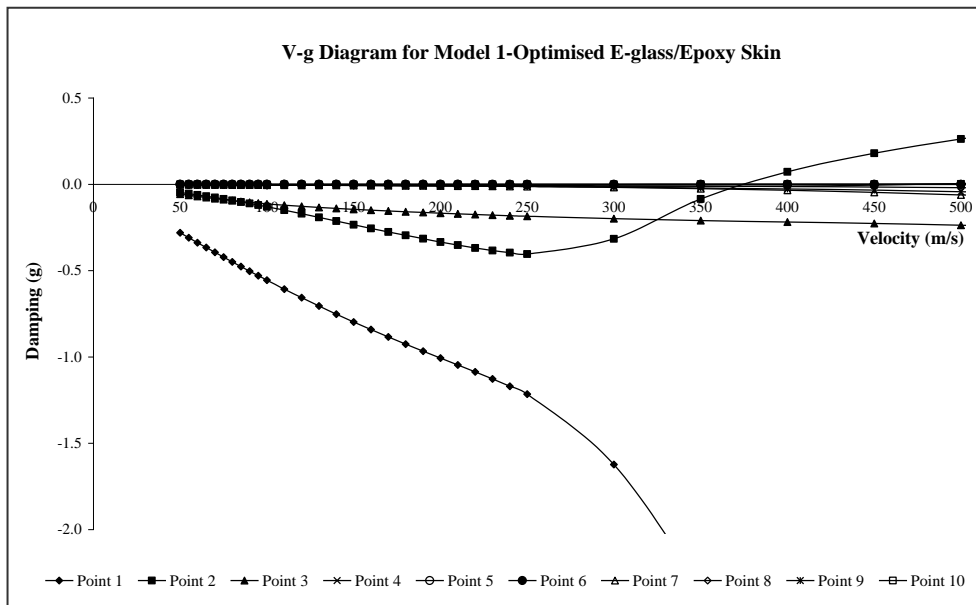


Figure 6.24 Velocity vs Damping (g) of Model 1-Optimised E-Glass/Epoxy skin

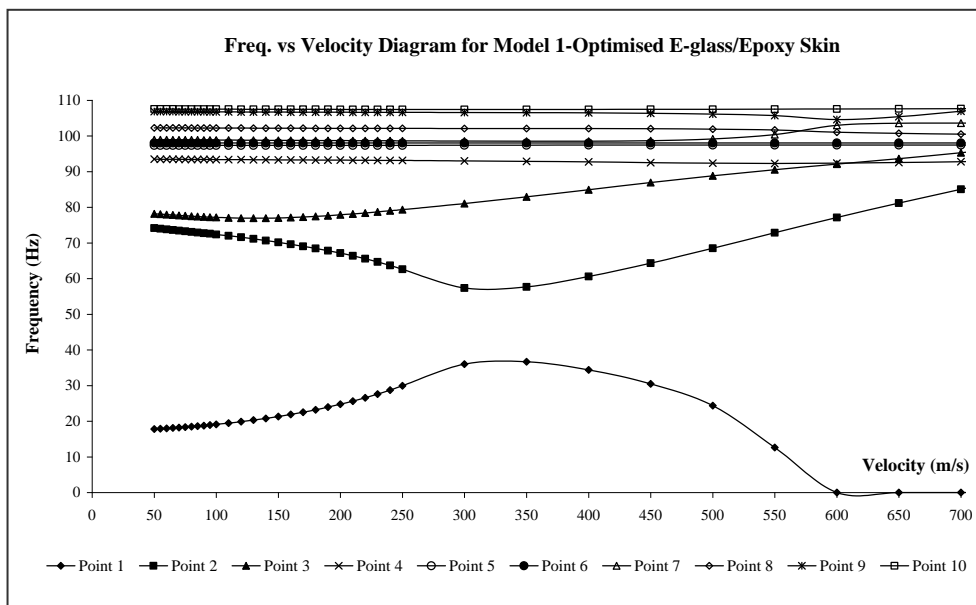


Figure 6.25 Velocity vs Frequency (ω) of Model 1-Optimised E-Glass/Epoxy skin

SAW Model 2

Figure 6.26 and Figure 6.27 are the V-g and frequency vs. velocity curves for the SAW model with the open TE (Model 2) with the Carbon/Epoxy skin respectively. Although it has not been plotted in the V-g curve the damping of mode one and two increases significantly with increasing speed with no change in damping sign. The corresponding frequency of the first mode increases and the frequency of mode two eventually decreased to zero with increasing speed. The damping of the fifth mode shows that it increases with increasing speed and decreases until it intersect the curve at 205 m/s for zero damping and continues to increase in the positive damping region of the curve. The corresponding frequency for this mode was approximately 69 Hz as can be seen from Figure 6.27. Mode six has a similar trend until it intersects the curve at zero damping to the positive region before it goes back to zero damping at higher speeds. Modes 7 -9 exhibit similar trends, where damping being increased with increasing speed and changing signs to positive damping at speeds between 210 – 230 m/s. However, the positive damping tends to change back to negative damping at higher speeds. The frequencies for these two modes were almost constant with increasing speed. The frequencies for these modes remained almost constant with increasing speed as can be seen in Figure 6.27. It can be concluded that the flutter speed of this model is 205 m/s and its corresponding frequency was at 69 Hz.

Figure 6.28 and Figure 6.29 summarise damping and frequency against the velocity respectively for each mode considered for the SAW model with the open TE (Model 2) with the optimised E-Glass/Epoxy skin. As before, damping and frequency trends with varying speed for each mode remain precisely the same as for the carbon/epoxy skin model. The only difference is that the magnitudes of the damping have increased whilst the frequencies have reduced as a result of reduced stiffness of the E-Glass/Epoxy skin model. It can be seen that the flutter for this case occurs at a 120 m/s, which is noticeably reduced compared to that of the Carbon/Epoxy model. This is mainly due to the reduced stiffness of the E-Glass/Epoxy material and the reduction in the torsional stiffness due to an open TE mechanism. The corresponding flutter frequency was at 38 Hz.

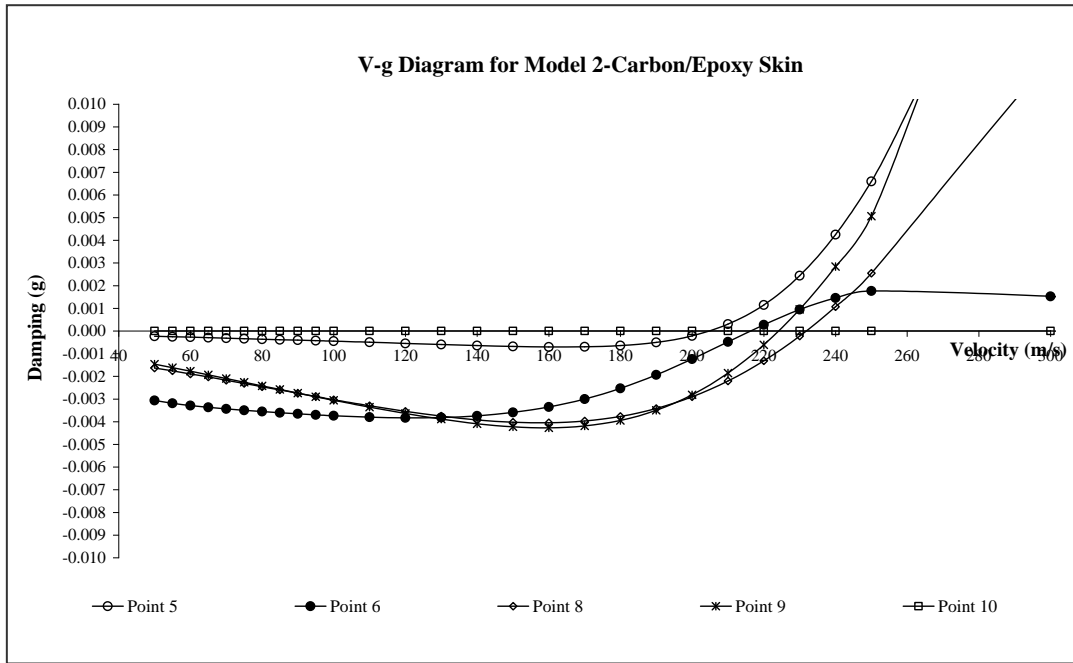


Figure 6.26 Velocity vs Damping (g) of Model 2- Carbon/Epoxy skin

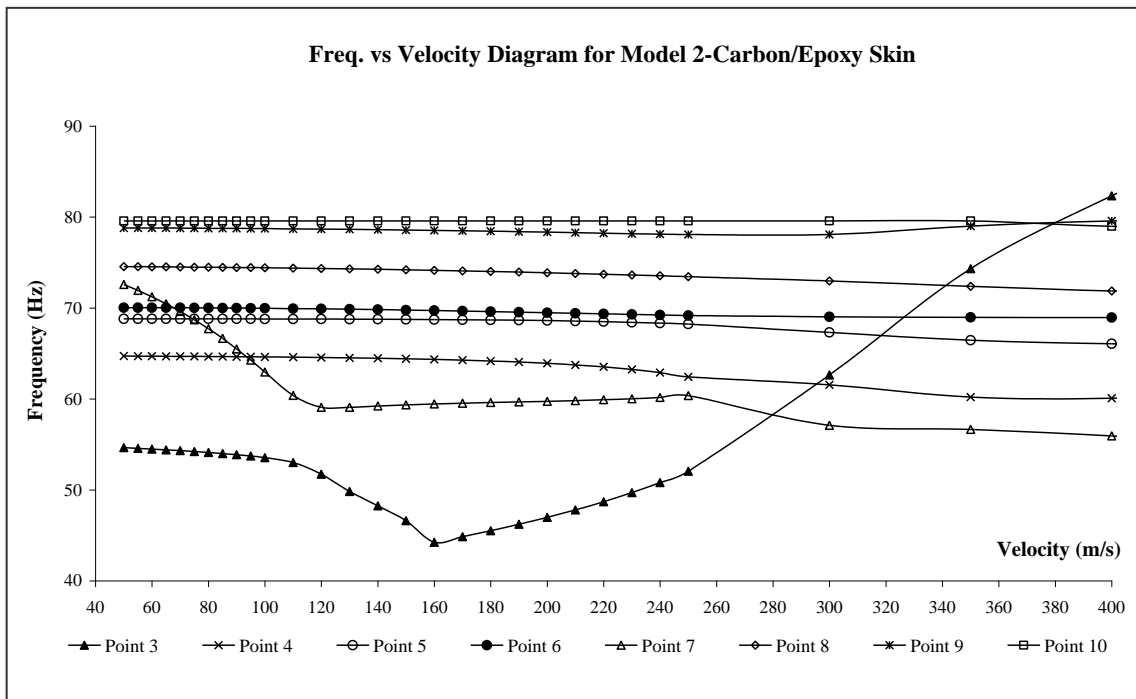


Figure 6.27 Velocity vs Frequency (ω) of Model 2-Carbon/Epoxy skin

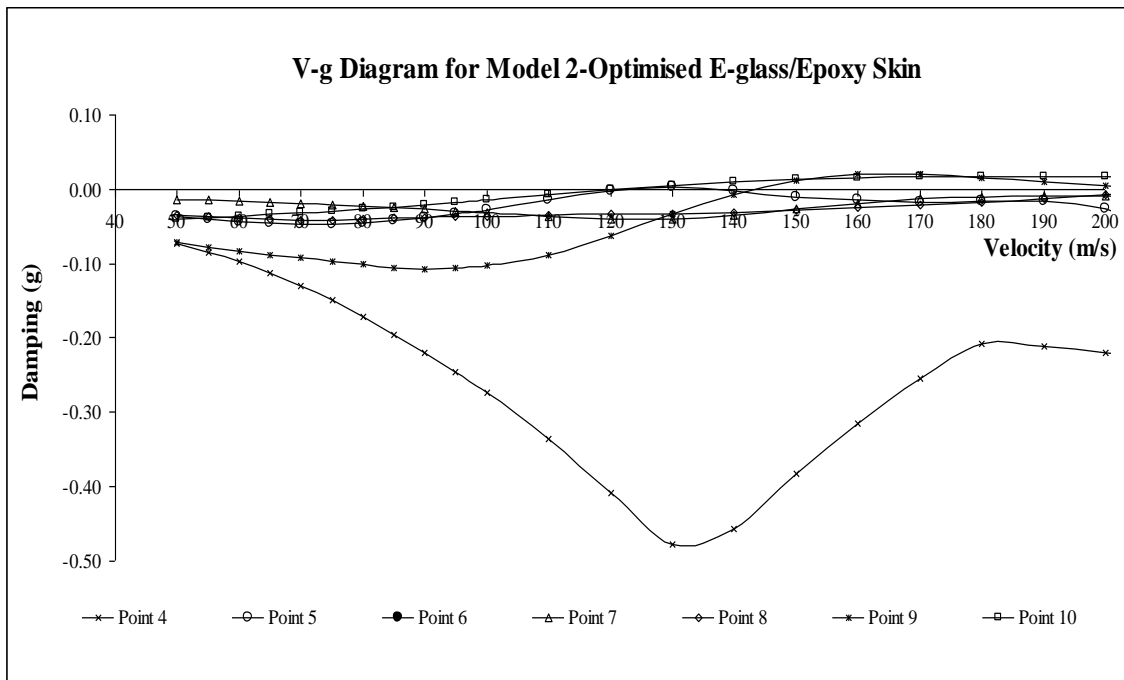


Figure 6.28 Velocity vs Damping (g) of Model 2- Optimised E-Glass/Epoxy skin

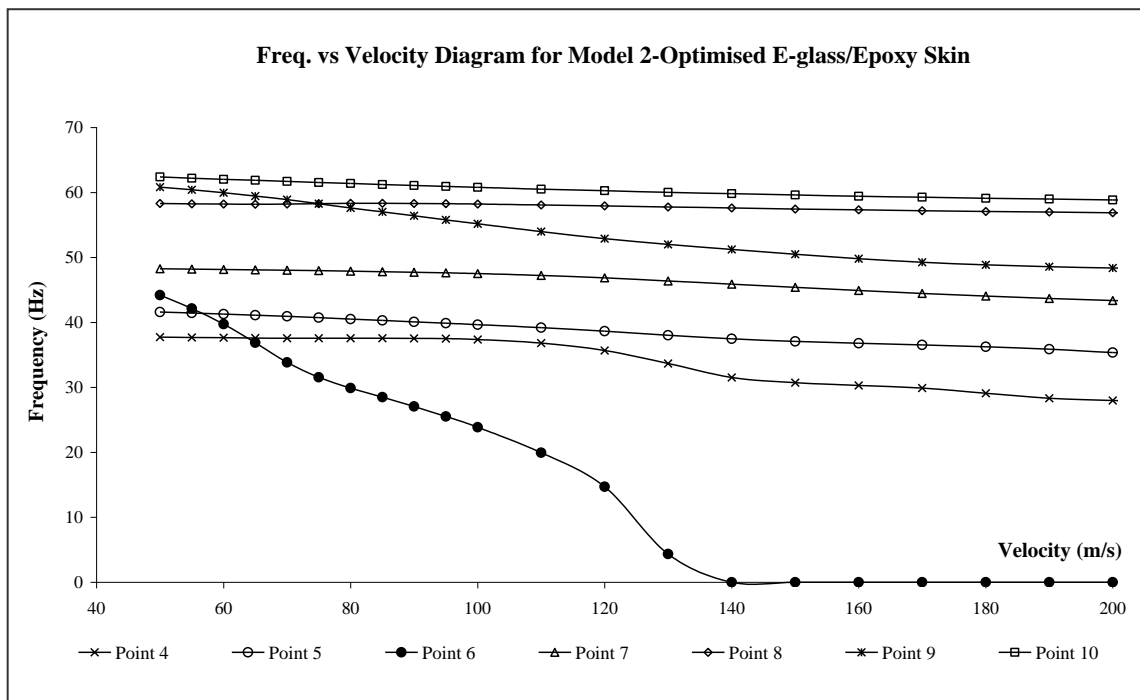


Figure 6.29 Velocity vs Frequency (ω) of Model 2- Optimised E-Glass /Epoxy skin

Figure 6.30 and Figure 6.31 are the V-g and frequency vs. velocity curves for the SAW model with the open TE (Model 2) with the E-Glass/Epoxy skin, without the elastic material (rubber) at the TE section. This was carried out in line with the normal modes analysis to see the effect of the additional mass due to rubber at the TE on the SAW aeroelastic characteristics. From the normal mode analysis it was seen that the SAW with the rubber resulted in a higher bending-torsion coupling frequency compared to the model without. This effect is evident from the V-g plot (Figure 6.30), which shows a significantly lower flutter speed for the model without the rubber insert at mode 4.

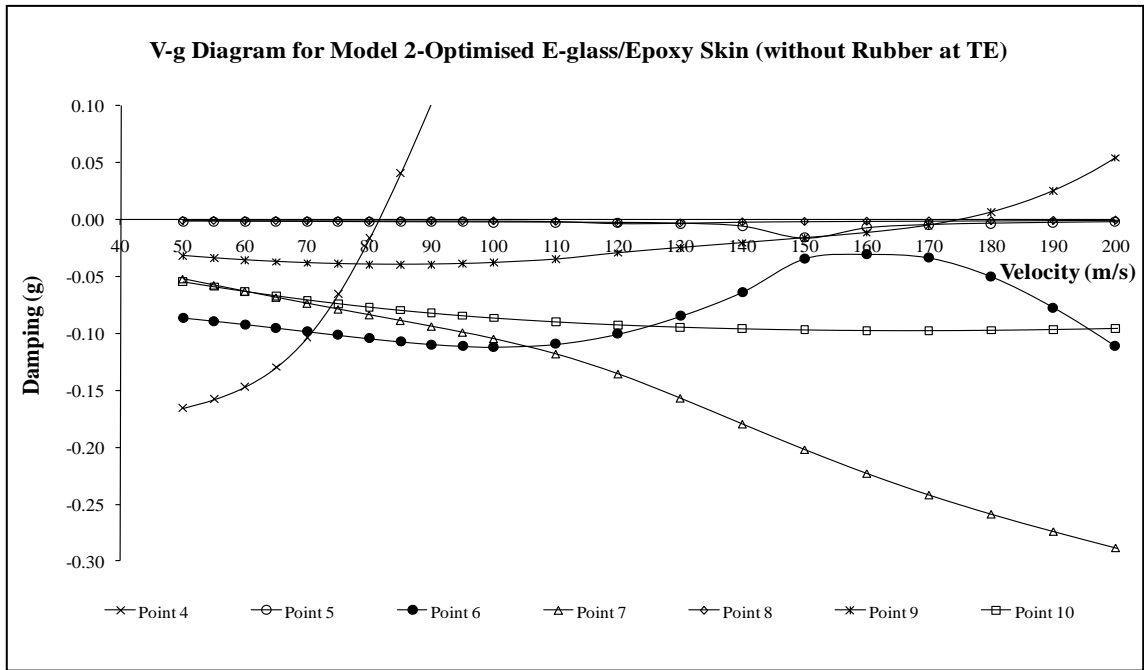


Figure 6.30 Velocity vs Damping (g) of Model 2- Optimised E-Glass/Epoxy skin (without TE Rubber)

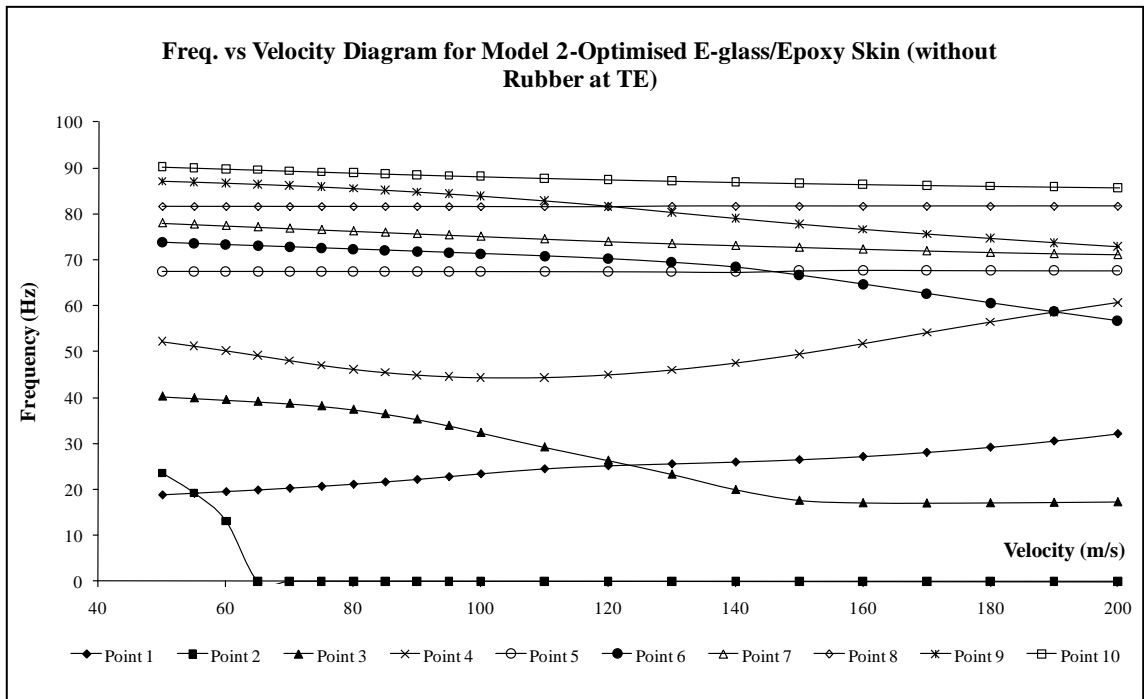


Figure 6.31 Velocity vs Frequency (ω) of Model 2- Optimised E-Glass /Epoxy skin (without TE Rubber)

SAW Model 3

The V-g and frequency vs. velocity curves for the SAW model with the open TE (Model 3) with the Carbon/Epoxy skin are shown in Figure 6.32 and Figure 6.33 respectively. The damping of mode one and two decreases with increasing speed until it crosses the x-axis and change sign from being negative to positive. The corresponding frequencies for these two modes, however, become zero at the speeds the damping of these modes change sign. The damping of the third mode shows that it increases with increasing speed and decreases until it intersect the curve at 290 m/s for zero damping and continues to increase in the positive damping region of the curve. The corresponding frequency for this mode was approximately 80 Hz as can be seen from Figure 6.33. The damping of modes 5, 8 and 10 stays in the negative region with increasing speed and does not cross the zero damping line to exhibit instability. As expected the corresponding frequencies remain constant throughout the speed range considered. Modes 6, 7 and 9 follow a similar trend where they all change sign from negative damping to positive damping at 275 m/s and 240 m/s respectively. The frequencies of these modes remain constant at 95 Hz, 110 Hz and 130 Hz throughout the speed range. It can be concluded that the flutter speed of this model is 275 m/s and its corresponding frequency was at 95 Hz.

Damping and frequency variations of the first ten natural frequencies as a function of flight speed for the SAW model with the open TE (Model 3) with the optimised E-Glass/Epoxy skin are shown in Figure 6.34 and Figure 6.35 respectively. As before, damping and frequency trends with varying speed for each mode remain precisely the same as for the carbon/epoxy skin model. The only difference is that the magnitudes of the damping have increased whilst the frequencies have reduced as a result of reduced stiffness of the E-Glass/Epoxy skin model.

As can be seen from Figure 6.34 damping of modes 3, 5 and 8 have similar trends, which remains in the negative region of the curve with increasing speed and the corresponding frequency remains constant. The damping of the fourth mode shows that it increases with increasing speed and decreases until it intersect the curve at 158 m/s for zero damping and continues to increase in the positive damping region of the curve.

The corresponding frequency for this mode was approximately 30 Hz as can be seen from Figure 6.35. The damping of mode 6 and 10 remains close to zero and crosses to being positive damping at 115 m/s and 160 m/s respectively with increasing speed. As expected the corresponding frequencies remain constant throughout the speed range considered for modes 6 and 10. Modes 7 and 9 changes sign from negative damping to positive damping at 142 m/s and 145 m/s respectively. The frequency of mode 7 starts at 42 Hz and sees a slight decrease around speed of 140 m/s to 40 Hz before increasing steadily with increasing speed. The corresponding frequency of mode 9 on the other hand, starts off at 58 Hz and begins to decrease around the 140 m/s point and remains constant at 45 Hz with increasing speed. It can be concluded that the flutter speed of this model is approximately 140 m/s and its corresponding frequency was at 40 Hz.

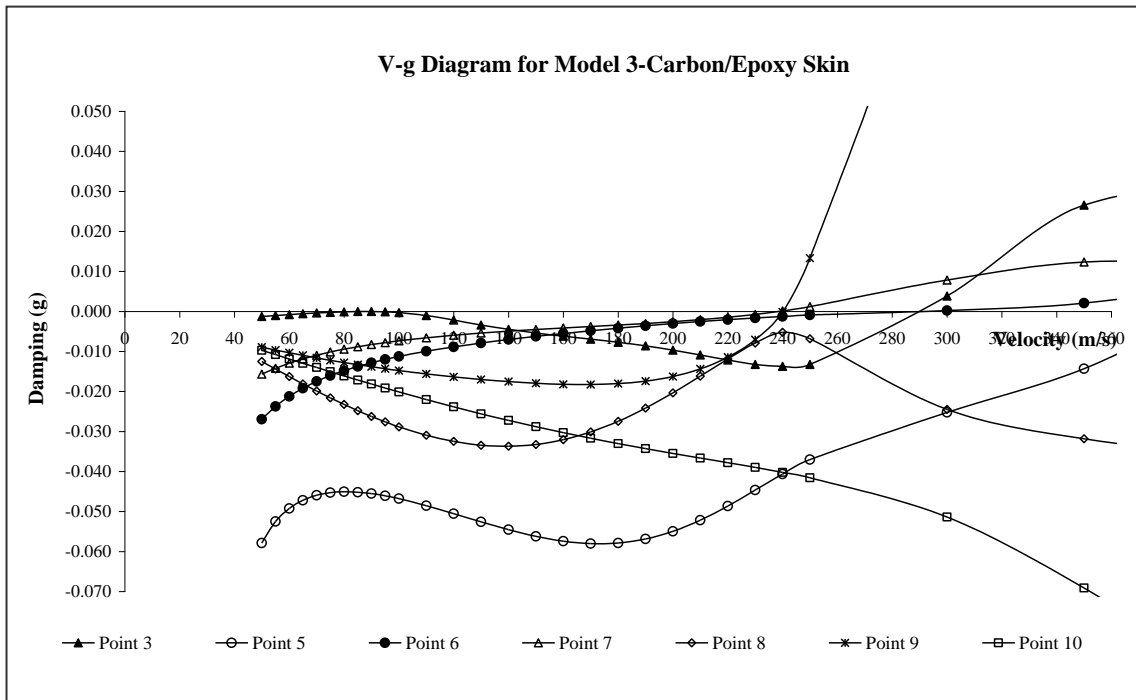


Figure 6.32 Velocity vs Damping (g) of Model 3- Carbon/Epoxy skin

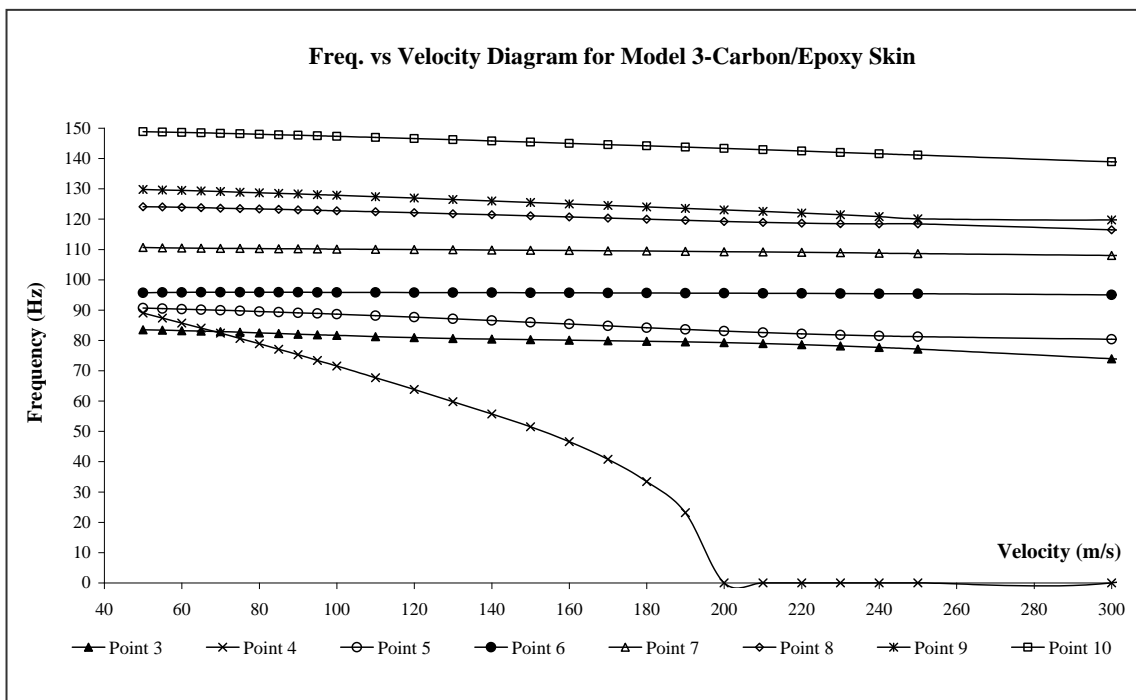


Figure 6.33 Velocity vs Frequency (ω) of Model 3-Carbon/Epoxy skin

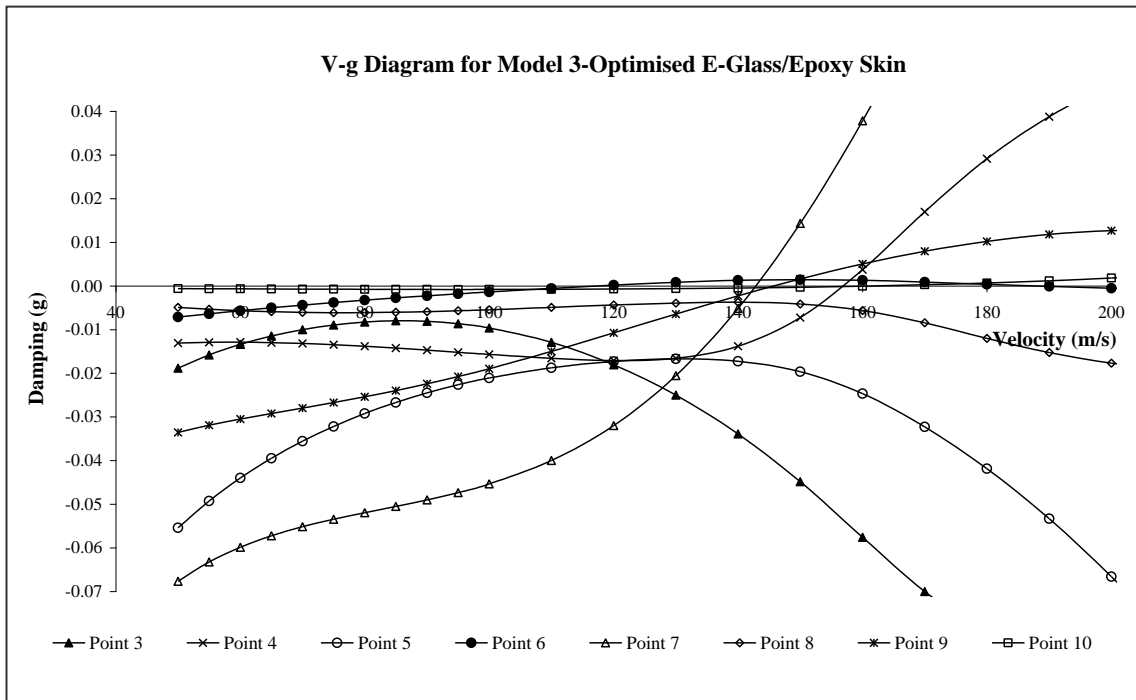


Figure 6.34 Velocity vs Damping (g) of Model 3- Optimised E-Glass/Epoxy skin

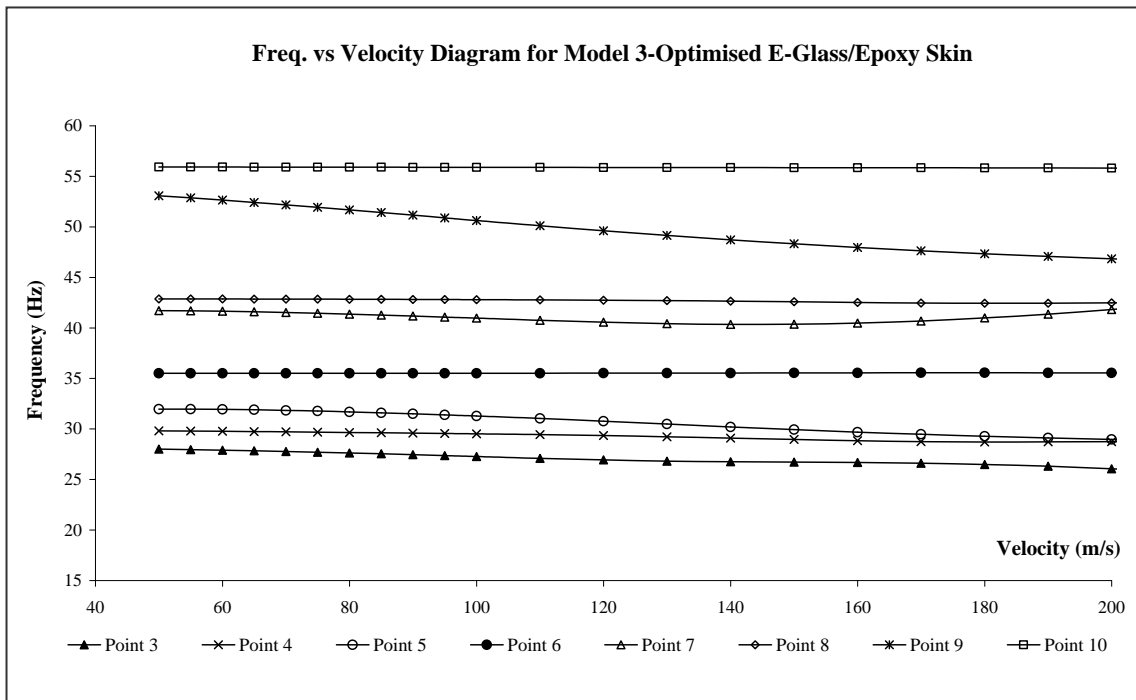


Figure 6.35 Velocity vs Frequency (ω) of Model 3- Optimised E-Glass /Epoxy skin

Table 6.5 Summary of Flutter Speeds

	Mode 1		Mode 2		Model 3	
	Case 1	Case 2.3	Case 1	Case 2.3	Case 1	Case 2.3
V_f (m/s)	645	370	205	120	275	142
ω_f (Hz)	94	60	69	38	95	42

The carbon fibre models resulted in a higher flutter speed compared to that of the E-Glass fibre model. Also, the open TE models resulted in a lower flutter speed compared to that of the closed TE model, as a result of the reduction in torsional stiffness of the whole wing due to the open TE. With regard to the two open TE models, model-2 and model-3, the flutter speed for model-3 is higher compared to model-2. as mentioned before, this is mainly due to the modelling of the open TE section in model-3, which has been represented by rigid element connections to maintain a gap of 1 mm. the rigid elements used in the FE model adds additional stiffness to the model which results in a higher flutter speed. Model-3 has been used to show the benefit of a design such as model-2, in terms of aeroelastic stability. The V-g plots for model-3 (Figure 6.32 and Figure 6.34) shows instability at almost all the modes of the structure. However, even for the worst case, having two layers of E-Glass Fibre with an open TE, flutter speeds obtained are greater than $1.2V_{Dive}$ and satisfy the JAR-VLA (629-aeroelastic requirement).

6.5 Dynamic Response Analysis

Transient-response analyses were carried out for the open SAW FE model with the optimised E-Glass/epoxy skin laminate. As illustrated in Figure 6.36 a spring element (CELAS1) was added to the root of the eccentuator beams in the FE model to represent the actuator stiffness obtained from the experimental results from section 4.4.4. The spring was added to the R_x (rotational degree of freedom in x).

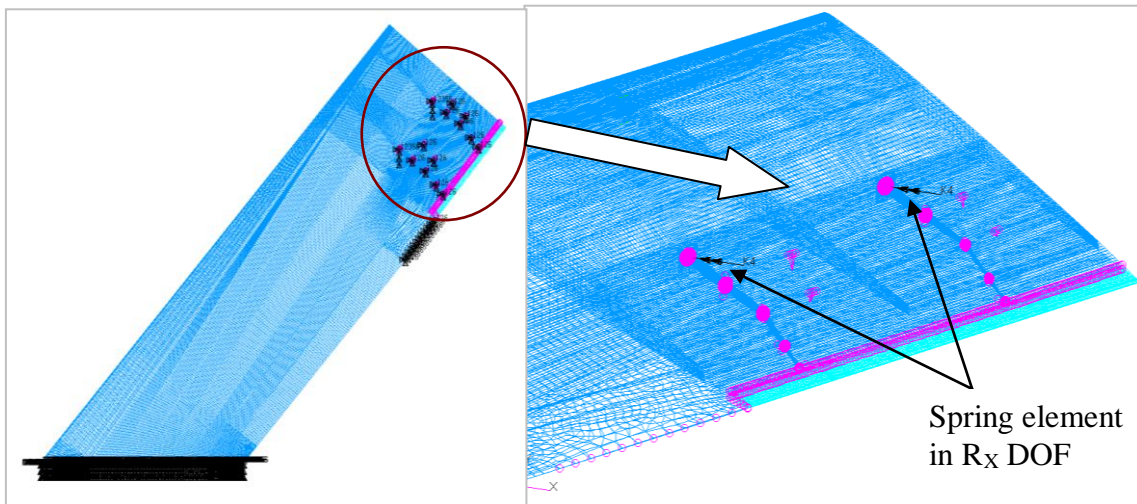


Figure 6.36 Spring element to represent actuator stiffness

The transient-response analysis of the SAW was obtained for a time-varying excitation due to the change in aerodynamic load at 5° TE deflection. (Appendix 6-A provides details of the pressure distribution at the spanwise location, where the eccentuator are present). The distributed loads were applied along the TE section varying at 5 - 20Hz as shown in Figure 6.37. This time dependent loads are applied for duration of specific time period depending on the applied frequencies. Structural damping was assumed to be 0.06 and was converted to equivalent viscous damping at 5 - 20Hz respectively at each frequency input. The resulting wing responses at the LE and TE of the wing tip region are shown in Figure 6.38 - Figure 6.40.

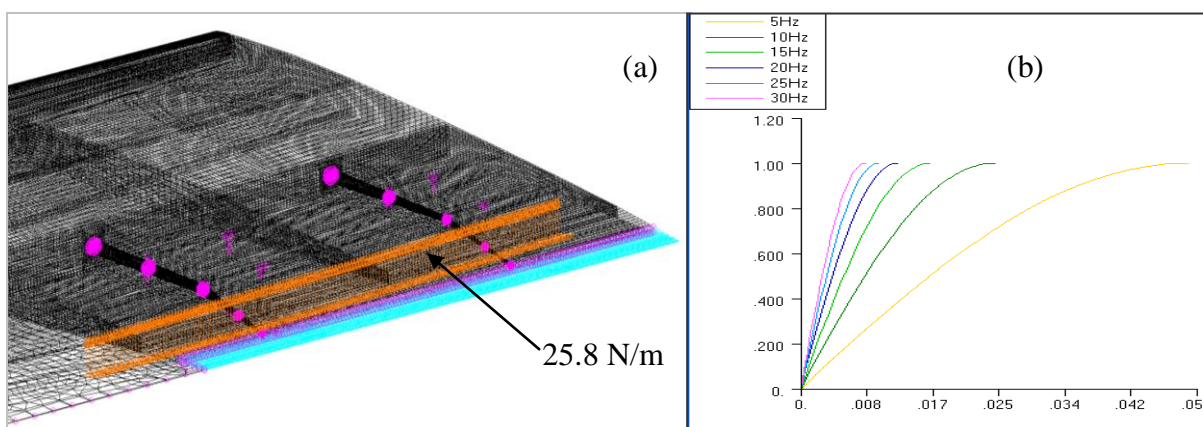


Figure 6.37 (a) Dynamic Response Loading location; (b) Input loading at 5 -20 Hz

6.5.1 Dynamic Response Results

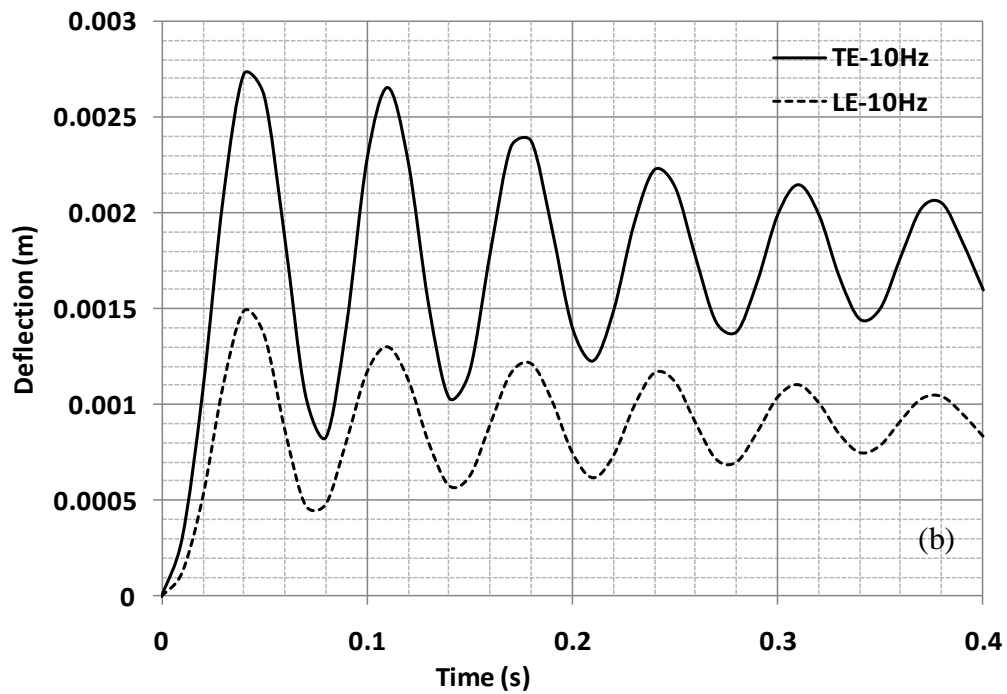
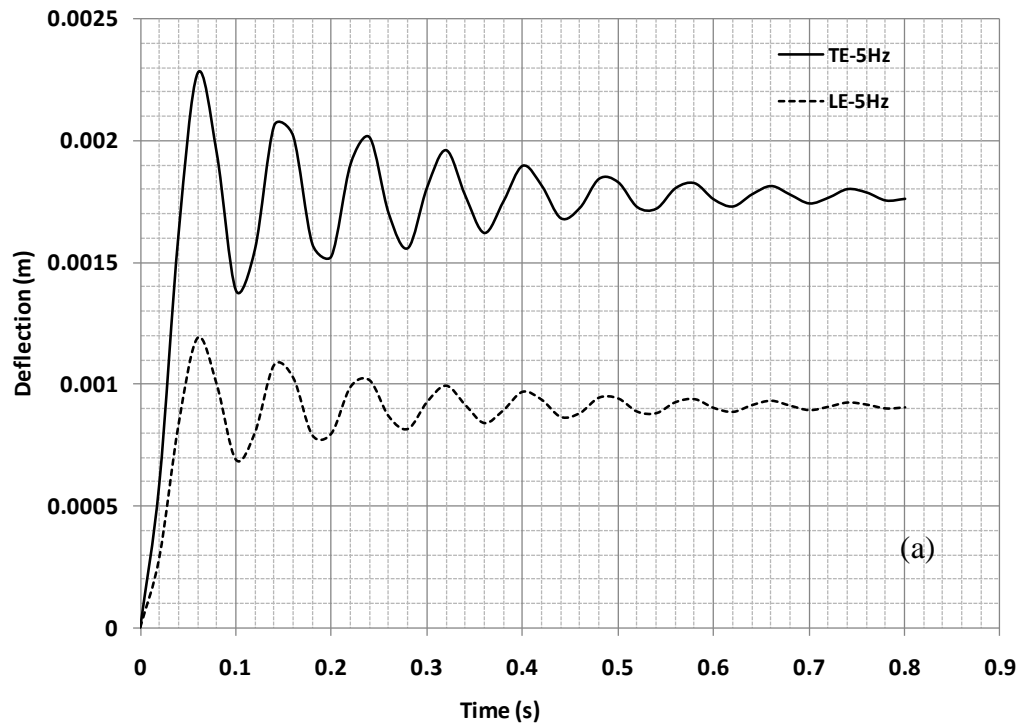


Figure 6.38 Transient Response of (a) Model 2 – 5Hz; (b) Model 2 – 10Hz

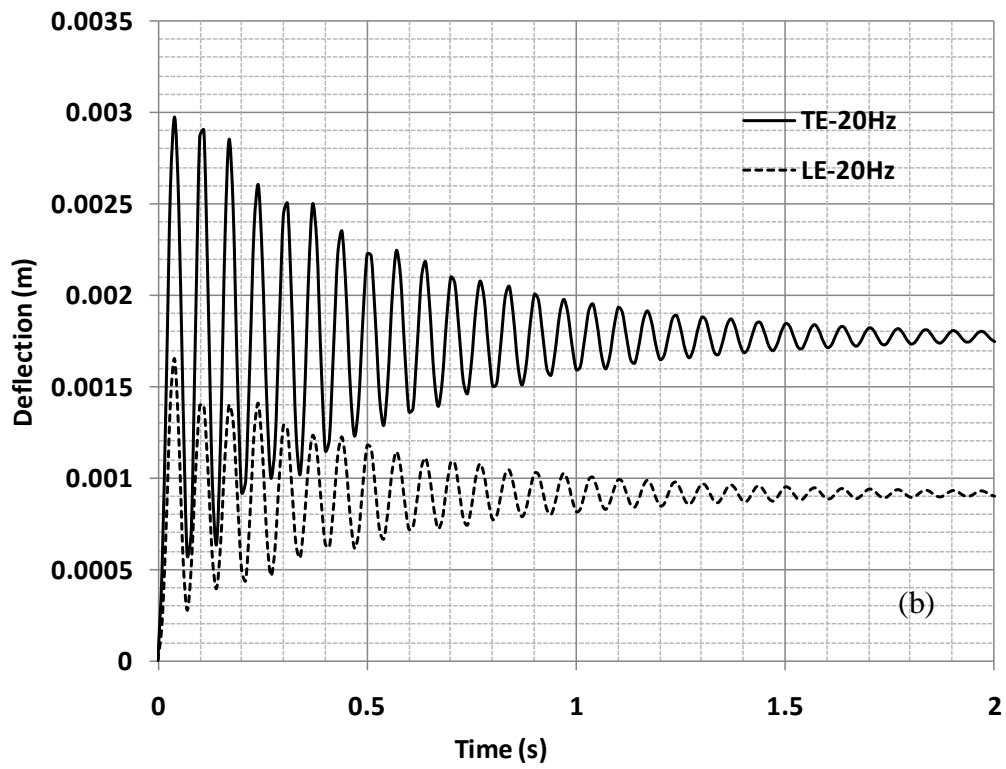
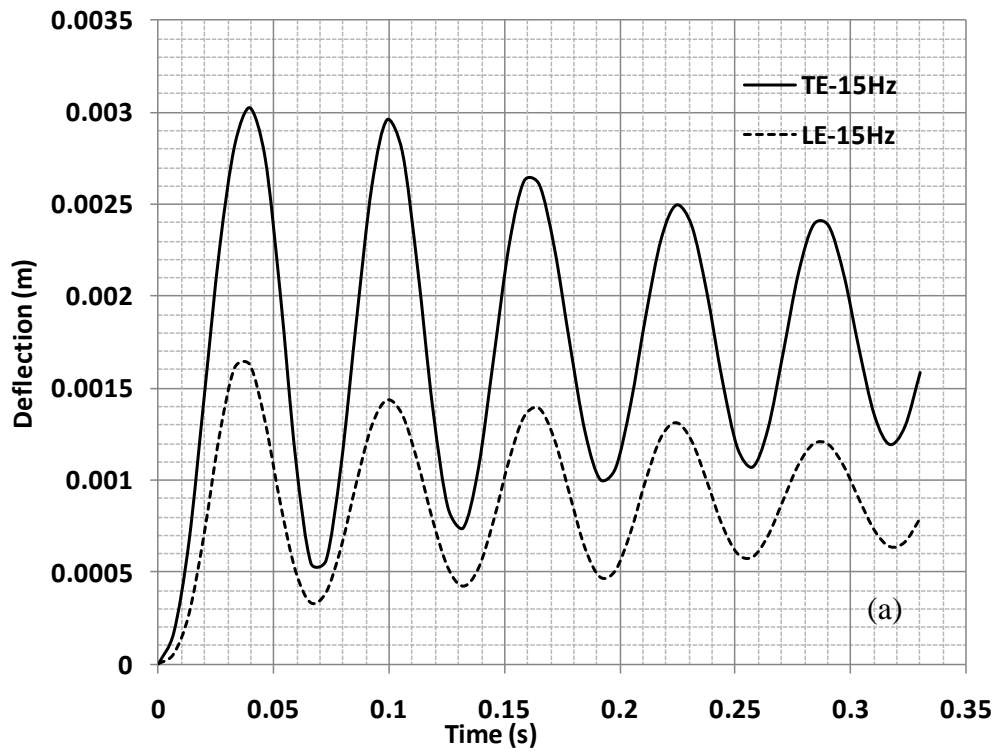


Figure 6.39 Transient Response of (a) Model 2 – 15Hz; (b) Model 2 – 20Hz

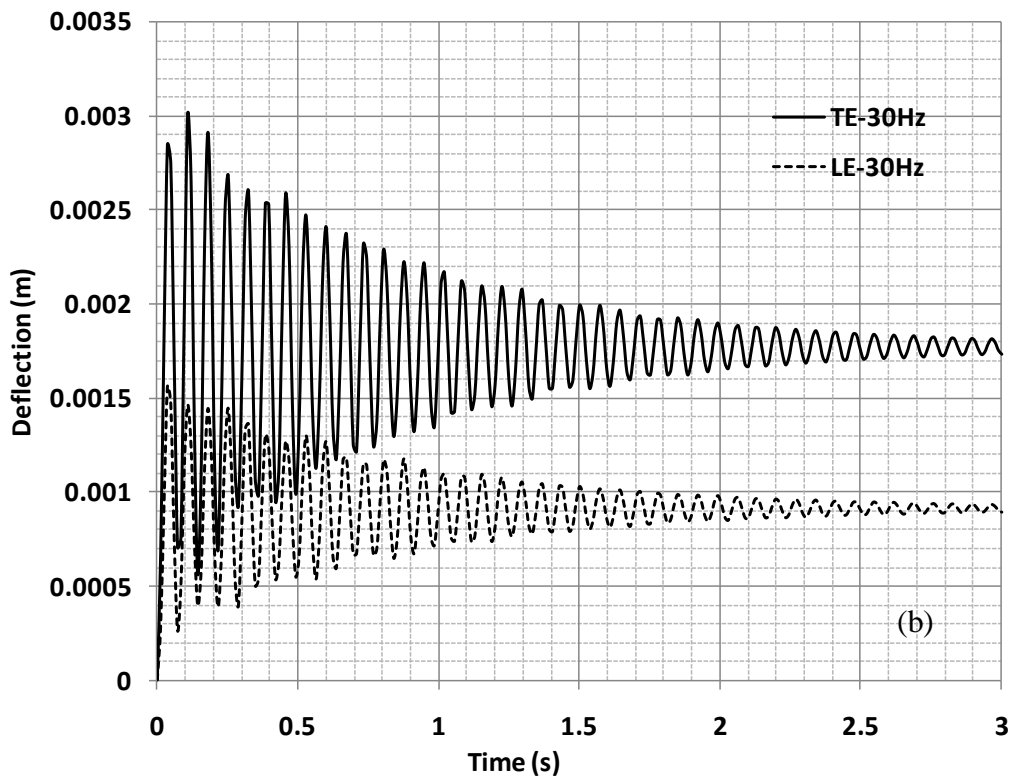
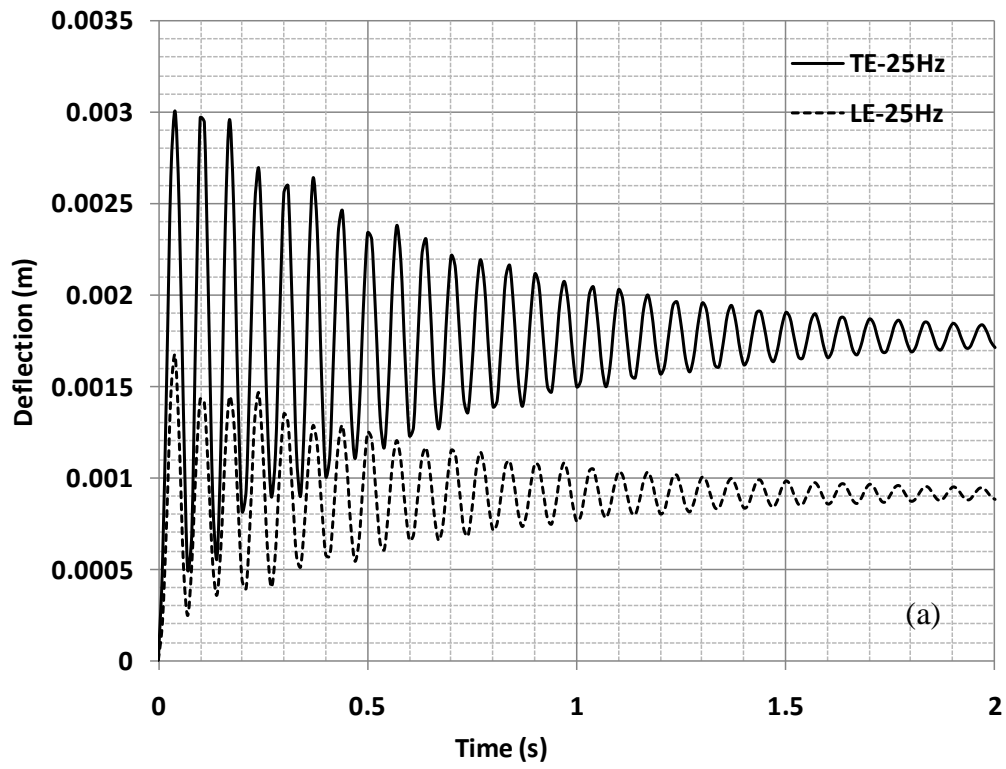


Figure 6.40 Transient Response of (a) Model 2 – 25Hz; (b) Model 2 – 30Hz

From the results presented the response of the structure was checked after the loading has been applied and the structure had returned to being stable. The results show that the response matches very well with the first bending frequency of this model, which was 16 Hz. The loading at 5 Hz, resulted in a slightly lower frequency of 11.5 Hz for the response once the loading was removed. The resulting displacement due to the sudden aerodynamic load remained significantly small. As expected the smallest deflection of 2.3 mm was seen for the lowest frequency input at the TE section. Whereas the larger displacement of 3.05 mm was seen for the 15 Hz load input, this coincides with the structural natural frequency of 16 Hz. However, the response of the structure has converged. The response of the LE sections is smaller compared to the TE, however, behaves in a similar pattern to the TE section. Even at higher frequency inputs of the load the structure remains stable and the maximum deflection at the TE remains at 3 mm.

The results show that the proposed actuation mechanism provides adequate stiffness to the trailing edge structure to overcome the aerodynamic pressure even at higher frequency. It also maintains a high degree of stability in the event of sudden aerodynamic loading due to the TE deflection.

7 Concluding Remarks

The primary aim of this research was to design a Seamless Aeroelastic Wing (SAW) structure applicable to a lightweight UAV. Therefore the study focused on an optimal design of a SAW structure. Although similar to the AAW and relevant to the FLAVIIR, the major difference between them is that a SAW will function as an integrated one piece lifting and control surface. It is designed to produce a desirable wing camber for control by deflecting a hinge-less flexible trailing edge (TE) part instead of a traditional control surface or unconventional coanda jet flow.

Hence the need for a more effective and feasible actuation mechanism was identified within this research study. Attention was firstly paid on the design of a hinge-less flexible trailing edge control surface and the actuation mechanism applicable to a light-weight aircraft (UAV). The proposed mechanism in presented is Chapter four. Two innovative design features have been created in the SAW TE section: an open sliding TE and a curved beam and disc actuation mechanism. This type of actuated TE section allows for the SAW having a camber change in a desirable shape with minimum control power demand. This design concept has been simulated numerically and its feasibility has been demonstrated by a test model. Mechanically the design provides a simple and feasible actuation solution. Structurally, it allows for a significant reduction of structural weight without compromising the strength.

From the study of existing and current design of an aeroelastic wing structure, the following conclusions can be drawn.

- Only the current SAW design of an open TE structure has the potential of deflection in adequate amount and required shape to gain maximum aerodynamic efficiency;
- The actuation power demand for deflecting the TE of the new SAW design is significantly reduced compared to a conventional closed TE design. The open TE design only required approximately 7% of the total force applied for the closed TE design in order to achieve the same deflection at the TE. This load requirement to elastically deform the TE section of the proposed SAW structure is achievable with the available actuators;

- Essentially one disc could provide continuous curvature to the skins (although it would not provide sufficient intermediate support);
- The actuation mechanism for the proposed SAW TE structure can be much simpler and lighter than a conventional closed TE design.

Therefore the proposed SAW TE structure can be applied to wing structures of small scale aircraft such as UAVs, missiles or even Formula one racing cars. It can also be extended to leading edge structure design to achieve LE deformations. Aeroservoelastic stability is not expected to be worse than a classical hinged flap design since the TE structural stiffness will make contribution on top of the servomechanism.

The case studies from Chapter five show that for the design of a UAV wing box especially a large swept back angle wing the aeroelastic effect is much more critical than the structural strength. A significant reduction of wing box weight can be achieved from the structural strength point of view. Because of the relatively low stress level at the 4.2g ultimate load factor, the structural strength has enough safety margin for even two layers of glass/epoxy skin laminate. However the reduced wing stiffness and negative aeroelastic effect lead to a significant reduction of flutter speed and control effectiveness. This is the main challenge to further reduction of the wing structure weight.

An aeroelastic tailoring performance was conducted to optimise the wing box structure for a maximum bending, torsional stiffness and flutter speed. This was achieved by optimising the wing box laminates by using a gradient-based deterministic optimisation method. Furthermore, the improved wing box configuration in chapter five (with the spars and stiffeners relocated to reduce the sweep angle) proved to be better in terms of aeroelastic stability, especially control effectiveness.

It was found that both the flutter and control reversal speeds are dominated by the torsional stiffness. It was also noted that the large sweep angle has negative aeroelastic effect on both flutter speed and control effectiveness due to the large negative bending-torsional coupling. Therefore the bending stiffness of the SAW of this particular wing

planform also plays a very important role in the aeroelastic stability i.e. control effectiveness and has been taken into consideration in the optimisation process.

The optimised E-Glass fibre wing box structure integrated with the SAW actuation mechanism was used for detailed analysis. The analysis was carried out using the finite element code MSC/NASTRAN. Three different FE models were generated, to represent a baseline conventional wing model and two other models with an open TE and the curved beam plus disc actuation mechanism to represent the SAW model. The maximum stress under the maximum aerodynamic loading for all three FE models occur at the root of the rear spar. As expected the SAW with the E-Glass fibre skin resulted in a higher stress value compared to the carbon/epoxy skin model for the baseline and open TE models. The most noticeable difference is that the open TE SAW design results in low stress values compared to the baseline design. This shows that the addition of an open TE changes the standard load path and results in a lower stress at the wing root. The comparison between the deflections and the stresses indicates that even the open TE design has enough strength under the maximum aerodynamic loading.

The normal mode analysis indicates that the open TE models behave in a similar manner to the baseline model with a closed TE. The open TE model with the rubber insert proved to be more beneficial by having a higher bending-torsion frequency as oppose to the open TE model without the rubber insert.

From the flutter analysis carried out on these three FE models, it can be concluded that the carbon fibre models resulted in a higher flutter speed compared to that of the E-Glass fibre model. Also, the open TE models resulted in a lower flutter speed compared to that of the closed TE model, as a result of the reduction in torsional stiffness of the whole wing due to the open TE. However, even for the E-Glass/Epoxy model with an open TE, the flutter speeds obtained are greater than $1.2V_{Dive}$ and satisfy the JAR-VLA (629-aeroelastic requirement).

Finally transient response analysis was carried out on the SAW open TE design with E-Glass/epoxy skin. The effective stiffness of the actuation system evaluated by using

vibration test data was incorporated in the SAW FE model. The dynamic response analysis results show that the SAW skin structure integrated with the actuation system is stable under the transient load representing a rapid change of aerodynamic load produced by the TE control operation.

7.1 Future Work

- The work presented in this research work has reached a limit in terms of passive aeroelastic tailoring for maximising the SAW aeroelastic characteristics, such as flutter and more importantly control reversal. Based on previous work, an initial 2D aerodynamic study showed the potential improvement in static aeroelastic phenomena, control reversal with the use of both leading and trailing edge control surfaces. From the aerodynamic and control point of view, a positive LE or TE deflection will produce a more positive C_m . thus, a possible solution from an active control point of view would be to initially have a negative TE deflection until the required C_L is achieved, and turn the TE back to neutral and make a positive LE deflection to maintain the C_L and control effectiveness. Hence the need for further research on the effect of combining the active aeroelastic control element to the passive aeroelastic tailoring work carried out to maximise the aeroelastic beneficial effect.
- Fluid-structural coupling analysis could be used for a detailed study on the effect of structural deformation and resulting aerodynamic load on aeroelastic behaviour of the wing structure. More detailed CFD modelling should be incorporated to model the 3D aerodynamics to be coupled to the structural model.
- On the design side, more design improvements proposed under open TE design needs to be tested for its feasibility. The proposed elastic skin design has been implemented in the SAW FE model. However, a detailed model with a honeycomb core to replace the ribs should be analysed and included in the numerical model to assess the extra actuation power demand.

- The experimental model built should be used to carry out further structural testing. A wind tunnel test would provide more confidence in the curved beam actuation mechanism and would allow addressing any issues related to the strength of the mechanism under an applied aerodynamic load.

8 Reference

- 1 Shanley, F. R. Weight-Strength analysis of aircraft structures. Dover Publications, 1960.
- 2 Shirk, M. H., Hertz, T. J. and Weisshaar, T. A. Aeroelastic tailoring- Theory, Practice and promise, Journal of Aircraft, vol. 23, no. 1, p 6-18, 1986.
- 3 Battoo, R. S. A beginner's guide to literature in the field of aeroelasticity. Cranfield University, College of Aeronautics, Report no. 9712, 1997.
- 4 Souahi, A. Structural optimization of aircraft lifting surfaces to satisfy flutter requirements, PhD thesis, Cranfield University, 1986.
- 5 Freberg, C. R. and Kemler, E. N. Aircraft vibration and flutter, John Wiley and Sons, Inc., New York, 1944.
- 6 Garrick, I. E. and Reed III, W. H. Historical development of aircraft flutter, Journal of Aircraft, vol. 18, no. 11, p 897-912, 1981.
- 7 Fielding, J. P., Mills, A., and Smith, H. Design and manufacture of the DEMON unmanned air vehicle demonstrator vehicle, Proc. IMechE Part G: J. Aerospace Engineering, Vol. 223.
- 8 Yarf-Abbasi, A. and Fielding, J. Design and development of the eclipse and demon demonstrator UAV's. In Proceedings of the 26th Congress of International Council of Aeronautical Sciences (ICAS 2008), Canada, September 2008.
- 9 Bisplinghoff, R. L., Ashley, H. and Halfman, R. L. Aeroelasticity, Dover, 1996.
- 10 Fick, P., Boehm, B., Sanders, M. B. and Petti, C. Static Aeroelastic Response Predictions of the Active Aeroelastic Wing (AAW) Flight Research Vehicle, In Proceedings of the 42nd AIAA/ASME/ASCE/AHS/ASC Structures, Structural Dynamics, and Materials Conference, Seattle, Washington, April 2001.
- 11 Parker, H. F. The Parker Variable Camber Wing, NACA Report Number 77, 1920.
- 12 Varioplane Company, Tragfläche für Flugzeuge, German Patent No. 366693, 1923.
- 13 Hannah, M. O. Expanding Wing for Aero-plane, U.S. Patent No. 1,773,530, August 19, 1930.
- 14 Lyon, D. G. Variable Shaped Airfoil, U.S. Patent No. 3,179,357, April 20, 1965.
- 15 Statkus, F.D. Continuous Skin, Variable Camber Airfoil Edge Actuating

- Mechanism, U.S. Patent No. 4,351,502, 1982.
- 16 Pendleton, Ed, Kenneth E. Griffin, Michael W. Kehoe, and Boyd P. A Flight Research Program for Active Aeroelastic Wing Technology, In Proceedings of the 37th AIAA Structures, Structural Dynamics and Materials Conference, Salt Lake City, Utah, April 15–17, 1996.
 - 17 Zink, P. S., Mavis, D. N., and Raveh, D. E. Maneuver Trim Optimization Techniques for Active Aeroelastic Wing, *Journal of Aircraft*, Vol. 38, No. 6, November 2001.
 - 18 Zink, P. S., Mavis, D. N., and Raveh, D. E. Integrated Trim and Structural Design Process for Active Aeroelastic Wing Technology, *Journal of Aircraft*, Vol. 40, No. 3, May 2003.
 - 19 Voracek, D., Pendleton, Ed., Reichenbach, E., Griffin, K., and Welch, L. The Active Aeroelastic Wing Phase I Flight Research Through January 2003, NASA/TM-2003-210741, April 2003.
 - 20 Pendleton, Ed, Flick, P., Paul, D., Griffin, K., and Reichenbach, E. The X-53 A Summary of The Active Aeroelastic Wing Flight Research Program, In Proceedings of the 48th AIAA/ASME/ASCE/AHS/ASC Structures, Structural Dynamics, and Materials Conference, Honolulu, Hawaii, 23-26 April 2007.
 - 21 Schweiger, J., Suleman, A. The European Research Project Active Aeroelastic Aircraft Structures, CEAS/AIAA/NVvL International Forum on Aeroelasticity and Structural Dynamics, Amsterdam, 2003.
 - 22 Schweiger, J., Suleman, A., Svetlana, I., and Victor, V. MDO Concepts for An European Research Project on Active Aeroelastic Aircraft, In Proceedings of the 9th AIAA/ISSMO Symposium on Multidisciplinary Analysis and Optimisation, Atlanta Georgia, September 2002.
 - 23 Ricci, S., and Terraneo, M. Conceptual Design of an Adaptive Wing for a Three-Surfaces Airplane, In Proceedings of the 46th SME/ASCE/AHS/ASC Structures, Structural Dynamics, and Materials Conference, April 2005.
 - 24 Ricci, S., Scotti, A., and Terraneo, M. Design Manufacturing and Preliminary Test Results of an Adaptive Wing Camber Model, In Proceedings of the 47th AIAA/ASME/ASCE/AHS/ASC Structures, Structural Dynamics and Materials Conference, Newport, Rhode Islands, 1-4 May 2006.

- 25 Ricci, S., Scotti, A., Cecrdle, J., and Maleek, J. Active Control of Three-Surface Aeroelastic Model, *Journal of Aircraft*, Vol. 45, No.3, May-June 2008.
- 26 Kuzmina, S., Amiryants, G., Schweiger, J., Cooper, J., Amprikidis, M., and Sensburg, O. Review and Outlook on Active and Passive Aeroelastic Design Concepts for Future Aircraft, ICAS Congress, Toronto, 2002.
- 27 Simpson, J., Schweiger, J., and Kuzmina, S. Design of an Adaptive Wing Shape Control Concept for Minimum Induced Drag of a Transport Aircraft, International Forum on Aeroelasticity and Structural Dynamics. Amsterdam, June 2003.
- 28 Moulin, B., Feldgun, V., Karpel, M., Anguita, L., Rosich, E., and Climent, H. Alleviation of Dynamic Gust Loads using Special Control Surfaces, EADS/CEAS/DLR/AIAA International Forum on Aeroelasticity and Structural Dynamics, Munich, Germany, 2005.
- 29 Amprikidis, M., and Cooper, J. E. Experimental Investigation of an All-Movable Vertical Tail Model, In Proceedings of the 44th AIAA/ASME/ASCE/AHS/ASC Structures, Structural Dynamics, and Materials Conference, Norfolk, Virginia, April 2003.
- 30 Amprikidis, M., and Cooper, J. E. Development of an Adaptive Stiffness Attachment for an All-Moving Vertical Tail, In Proceedings of the 46th AIAA/ASME/ASCE/AHS/ASC Structures, Structural Dynamics, and Materials Conference, Austin, Texas, April 2005.
- 31 Barrett, R., "Active Aeroelastic Tailoring of an Adaptive Flexspar Stabilator", *Smart Materials & Structures* (0964-1726). Vol. 5, No. 6, August 1996.
- 32 Arters, J. T., and Vinson, J. R., "Preliminary Design of Piezo-Activated Composite Sandwich Fins for Projectile Manoeuvrability, In Proceedings of the 46th AIAA/ASME/ASCE/AHS/ASC Structures, Structural Dynamics and Materials Conference, Austin, Texas. April 2005.
- 33 Monner, H. P., Sachau, D., Breitbach, E. Design Aspects of the Elastic Trailing Edge for an Adaptive Wing, RTO AVT Specialists' Meeting on Structural Aspects of Flexible Aircraft Control, Ottawa, Canada, October 1999.
- 34 Amprikidis M. and Cooper J. E. Development of Smart Spars for Active Aeroelastic Structures, In Proceedings of the 44th AIAA/ASME/ASCE/AHS/ASC

- Structures, Structural Dynamics, and Materials Conference, Norfolk, Virginia, April 2003.
- 35 Amprikidis, M., and Cooper, J. E. Experimental Variation of Wing Twist Control using Adaptive Internal Structures, In Proceedings of the 45th AIAA/ASME/ASCE/AHS/ASC Structures, Structural Dynamics, and Materials Conference, Palm Springs, California, April 2004.
 - 36 Amprikidis, M., and Cooper, J. E. On the Use of Adaptive Internal Structures for Wing Shape Control, In Proceedings of the 46th AIAA/ASME/ASCE/AHS/ASC Structures, Structural Dynamics, and Materials Conference, Austin Texas, April 2005.
 - 37 Amprikidis, M., and Cooper, J. E. On the Use of Adaptive Internal Structures to Optimise Wing Aerodynamic Distribution, In Proceedings of the 47th AIAA/ASME/ASCE/AHS/ASC Structures, Structural Dynamics, and Materials Conference, Newport, Rhode Island, May 2006.
 - 38 Campanile, L. F. and Anders, S. Aerodynamic and Aeroelastic Amplification in Adaptive Belt-Rib Airfoils, *Aerospace Science and Technology*, Elsevier, 55-63, 2005.
 - 39 Campanile, L. F. and Sachau, D. The Belt-rib Concept: A Structronic Approach to Variable Camber, *Journal of Intelligent Material Systems and Structures*, Vol. 11, March 2000.
 - 40 Chopra I. Review of State-of-Art of Smart Structures and Integrated Systems, In Proceedings of the 42nd AIAA/ASME/ASCE/AHS/ASC Structures, Structural Dynamics, and Materials Conference, April 2001.
 - 41 Personal communication with MBDA
 - 42 Stanewsky E. Adaptive Wing and Flow Control Technology, *Progress in Aerospace Sciences*, Vol. 37, 583 – 667, 2001.
 - 43 Giurgiutiu, V. Active-Materials Induced-Strain Actuation for Aeroelastic Vibration Control, *The Shock and Vibration Digest*, Vol. 32, No.5, 355-368, September 2000.
 - 44 Sheta, E.F., Moses, R.W., Huttshell, L. J., Harrand, V. J. Active Control of F/A-18 Vertical Tail Buffeting Using Piezoelectric Actuators, In Proceedings of the 44th AIAA/ASME/ASCE/AHS/ASC Structures, Structural Dynamics and Materials Conference, Norfolk, Virginia, April 2003.

- 45 Forster, E., and Livne, E. Integrated Structure/Actuation Synthesis of Strain Actuated Devices for Shape Control, In Proceedings of the 42nd AIAA/ASME/ASCE/AHS/ASC Structures, Structural Dynamics, and Materials Conference, Seattle, Washington, April 2000.
- 46 Anusonti-Inthra, P., Sarjeant, R., Frecker, M., and Gandhi, F. Design of a Conformable Rotor Airfoil Using Distributed Piezoelectric Actuators, AIAA Journal, Vol. 43, No. 8, August 2005.
- 47 Cho, M., and Sanghaun, K. Structural Morphing using Two-Way Shape Memory Effect of SMA, International Journal of Solid and Structures, Vol. 42, 1759-1776, 2005.
- 48 Icardi, U., and Ferrero, L. Preliminary Study of an Adaptive Wing with Shape Memory Alloy Torsion Actuators, Materials and Design, Vol. 30, pp 4200-4210, 2009.
- 49 Jardine, P. Smart Wing Shape Memory Alloy Actuator Design and Performance, SPIE Vol.3044, pp 48-55, 1997.
- 50 Kudva J. n., Martin C. A., and Scherer L. B. Overview of the DARPA/AFRL/NASA Smart Wing Program, Industrial and Commercial applications of Smart Structure technologies, SPIE Smart Structures and Materials, Vol.3674,pp 230-236, March 1999.
- 51 Jardine, A. P., Bartley-Cho, J., and Flanagan, J. Improved Design and Performance of the SMA Torque Tube for the DARPA Smart Wing Program, Industrial and Commercial applications of Smart Structure technologies, SPIE Smart Structures and Materials, Vol.3674,pp 260-269, March 1999.
- 52 Scherer, L. B., Martin, C. A., and West, M. DARPA/AFRL/NASA Smart Wing Second Wind Tunnel Test Results, SPIE Symposium on Smart Structures and Materials, Newport Beach, California, March 1999.
- 53 Bartley-Cho J. D. , Wang D. P., Martin C. A., Kudva J N. , and West M. N. Development of High-rate, adaptive Trailing Edge Control Surface for the Smart Wing Phase 2 Wind Tunnel Model, Journal of Intelligent Material Systems and Structures, Vol.15, April 2004.

- 54 Strelec J. K., Lagoudas D. C. Fabrication and Testing of a Shape Memory Alloy Actuated Reconfigurable Wing, *Smart Structures and Integrated Systems*, 4701, 2002.
- 55 Strelec J. K., Lagoudas D. C., Khan M. A., and Yen J. Design and Implementation of a Shape Memory Alloy Actuated Reconfigurable Airfoil, *Journal of intelligent Material Systems and Structures* , Vol. 15 , 257-273, April 2004.
- 56 Jae-Sung, Seigler T. M., and Inman D. J. Aerodynamic and Static Aeroelastic Characteristics of a Variable-Span Morphing Wing, *Journal of Aircraft*, Vol.42, No.2, 2005.
- 57 The design of morphing aircraft, 2007, Aerospace Department, University of Bristol, <http://www.aer.bris.ac.uk/research/morphing>, accessed - April 2007.
- 58 Claus B., Martin W., Hans-Friedrich S., and Schurmann H. A New Structural Approach to Variable Camber Wing Technology of Transport Aircraft, AIAA,- 98-1756.
- 59 Monner, H. P. Design of a Smart Droop Nose as Leading Edge High Lift System for Transportation Aircraft, In Proceedings of the 50th AIAA/ASME/ASCE/AHS/ASC Structures, Structural Dynamics, and Materials Conference, Palm Springs, California, May 2009.
- 60 Shirk M. H., Hertz T. J., and Weisshaar T. A. Aeroelastic Tailoring- Theory, Practice and Promise, *Journal of Aircraft*, Vol. 23, No. 1, pp 6 - 18, 1986.
- 61 Weisshaar, T.A. Aeroelasticity's Role in Innovative UAV Design and Optimization- The Way Things Ought To Be, Purdue University West Lafayette, Indiana USA.
- 62 Lynch, R.W. and Rogers, W. A. Aeroelastic Tailoring of Composite Materials to Improve Performance, In Proceedings of the 17th AIAA/ASME/SAE Structures, Structural Dynamics and Materials Conference, King of Prussia, Pennsylvania, May 1976, pp. 61-68.
- 63 Sahoo D. and Cesnik C. E. S. Roll Manoeuvre Control of UCAV wing using Anisotropic Piezoelectric Actuators, In Proceedings of the 43rd AIAA/ASME/ASCE/AHS/ASC Structures, Structural Dynamics, and Materials Conference, April 2002.

- 64 Andersen, G., Forster E., and Kolonay R. Multiple Control Surface Utilization in Active Aeroelastic Wing Technology, *Journal of Aircraft*, Vol. 34, No.4, pp. 552-557, July 1997.
- 65 Zink P. S., Mavis D. N., Love M. H., and Karpel M. Robust Design for Aeroelastically Tailored/Active Aeroelastic Wing, AIAA paper 98-4781, September 1998.
- 66 Weisshaar T. A. Duke D. K. and Dobbins A. Active Aeroelastic Tailoring with Adaptive Continuous Control Surfaces, AIAA paper 2000-1619, 2000.
- 67 Flick P. M. and Love M. H. The Impact of Active Aeroelastic Wing Technology on Conceptual Aircraft Design, Research Technology Organisation Air Vehicle Technology Specialists Meeting on Structural Aspects of Flexible Aircraft Control, Paper RTO MP-36, October 1999.
- 68 Yurkovich R. R. Optimum Wing Shape for an Active Flexible Wing, AIAA paper 95-1220, 1995.
- 69 Dowell E. H., Bliss D. B., and Clark R. L. Aeroelastic wing with Leading- and Trailing-edge Control Surfaces, *Journal of Aircraft*, Vol. 40, No. 3, pp.559-565, May 2003.
- 70 Platanitis G., and Strganac, T.W. Analyses and Experiments of Suppression of control Reversal using a Wing Section with Multiple Control Surfaces, In Proceedings of the 44th AIAA/ASME/ASCE/AHS/ASC Structures, Structural Dynamics and Materials Conference, Norfolk, Virginia, 7-10 April 2003.
- 71 Platanitis G., and Strganac, T.W. Suppression of Control reversal Using leading- and Trailing-Edge Control Surfaces, *Journal of Guidance, control and Dynamics*, Vol.28, No. 3, pp. 452-460, May –June 2005.
- 72 Pendleton, E. Back to the Future – How Active Aeroelastic Wings are a return to aviation’s beginnings and a small step to future bird-like wings, RTO AVT symposium on “active control technology for enhanced performance operational capabilities of military aircraft, land vehicles and sea vehicles”, Germany, May 2000.
- 73 Naranjo, A. G., Cowling, I., Green, J. A., and Qin, N. Aerodynamic Performance benefits of Utilising Camber Morphing Wings for Unmanned Air Vehicles, In

- Proceedings of the 25th Bristol International unmanned Aerial Vehicle Systems conference, 2010.
- 74 Reich, G. and Sanders, B. Introduction to Morphing Aircraft Research, *Journal of Aircraft*, Vol. 44, No. 4, July-August 2007.
 - 75 Thill, C., Etches I., Bond, K., and Weaver, P. Morphing Skins, *The Aeronautical Journal*, March 2008, pp. 117-139.
 - 76 Wlezien, R.W., Horner, G.C., McGowan, A.R., Padula, S.L., Scott, M.A., Silcox, R.J. and Simpson, J.O. The aircraft morphing program. 1998, International Society for Optical Engineering.
 - 77 Sanders, B., Eastep, F., and Forster, E. Aerodynamic and Aeroelastic Characteristics of Wings with Conformal Control Surfaces for Morphing Aircraft, *Journal of aircraft*, Vol.40, No. 1, pp. 94-99, January-February 2003.
 - 78 Sanders, B., Reich, G., Joo, J., and Eastep, F. Air Vehicle Control Using Multiple Control Surfaces, In *Proceedings of the 45th AIAA/ASME/ASCE/AHS/ASC Structures, Structural Dynamics and Materials Conference*, Palm Springs, California, 19-22 April 2004.
 - 79 Carlsson, M., and Cronander, C. Efficient Roll Control using Distributed Control Surfaces and Aeroelastic Effects, *Aerospace Science and Technology*, Vol. 9, 143-150, 2005.
 - 80 Tang, D., Li, A., and Dowell, E. H. Experimental and Theoretical Study on Rolling Effectiveness of Multiple Control Surfaces, *AIAA Journal*, Vol.41, No.2, February 2003, pp. 160-167.
 - 81 Moorhouse, D., Sanders, B., Spakovsky, M., and Butt, J. Benefits and Design Challenges of Adaptive Structures for Morphing Aircraft, *The Aeronautical Journal*, March 2006, pp.157-162.
 - 82 Sofla, A. Y. N., Meguid, S. A., Tan, K. T., and Yeo, W. K. Shape Morphing of aircraft wing: Status and Challenges, *Materials and Design*, Vol.31, 2010, pp.1284-1292.
 - 83 Kollar, L.P. and Springer, G.S. *Mechanics of Composite Structures*, Cambridge University Press, 2003, Chapter 6.
 - 84 Megson T.H.G. *Aircraft Structure for Engineering Students*, Butterworth Heinmann, Third Edition, 1999, Chapter 13.

- 85 Guo, S. User's guide for program TWboxdc. Unpublished document.
- 86 Armanios, E.A., Badir, A.M. Free Vibration Analysis of Anisotropic Thin Walled Closed Cross-Section Beams, *AIAA Journal*, Vol. 33, 1905-1910, 1995.
- 87 Berdichevsky, V., Armanios, E.A. and Badir, A.M. Theory of Anisotropic Thin Walled Closed Cross-Section Beams, *Journal of Composite Engineering*, 1992, 2, 411-432.
- 88 Banerjee, J. R., Williams, F. W. Coupled Bending-Torsional Dynamic Stiffness Matrix for Timoshenko Beam Elements, *Computers & Structures*, Vol. 42, 301–310, 1992.
- 89 Banerjee, J.R., Williams, F.W. Free Vibration of Composite Beams – An Exact Method using Symbolic Computation, *Journal of Aircraft*, Vol. 32, 636–642, 1995.
- 90 Raymond L., Bisplinghoff, Holt Ashley and Robert L. Halfman, *Aeroelasticity*,
- 91 Sitton, G. MSC/NASTRAN Basic Dynamic analysis user's guide, The MacNeal-Schwendler Corporation.
- 92 Komzsik, L. MSC/NASTRAN Numerical Methods user's guide, Chapter 6, The MacNeal-Schwendler Corporation.
- 93 Theodorsen T. General Theory of Aerodynamic Instability and the Mechanism of Flutter, *NACA Technical Report 496*, 413- 433, 1949.
- 94 Y. C. Fung, *An Introduction to the Theory of Aeroelasticity*, John Wiley and Sons, New York, 1955.
- 95 Liani E., and Guo S. Potential-Flow-Based Aerodynamic analysis and test of a Flapping Wing, in proceedings of the 37th AIAA Fluid dynamics Conference, AIAA-2007-4068, 2007.
- 96 Rodden, W. P. and Johnson, E. H. MSC/NASTRAN Aeroelastic analysis user's guide, The MacNeal-Schwendler Corporation.
- 97 Rodden, W. P., Harder, R. L. and Bellinger E. D. Aeroelastic addition to MSC/NASTRAN, *NASA CR 3094*.
- 98 Hess J. L. and Smith A. M. O. Calculation of Potential Flow about Arbitrary Bodies, *Prog. Aeronaut. Sci* 8, 1966.
- 99 Moran J. *An Introduction to Theoretical and Computational Aerodynamics*, John Wiley and Sons.

- 100 Anderson J. D. Fundamentals of Aerodynamics, Third Edition, McGraw-Hill.
- 101 Fox, R.L. Optimization Methods for Engineering Design, Addison Wesley, 1971.
- 102 Vanderplaats, G. N. ADS- A FORTRAN program for Automated Design Synthesis – Version 1.10, NASA Contract Report 177985, September 1985.
- 103 Fletcher, R. and Powell, M.J.D. A Rapidly Convergent Descent Method for Minimisation, Computer Journal, Vol.6, No. 2, pp. 163-168, 1963.
- 104 Computer Program for Estimation of Lift Curve to Maximum Lift for Wing-Fuselage Combinations with High-Lift Devices at Low Speeds, ESDU International, Item No. 99031, 1999.
- 105 Hepperle M. Javafoil – Velocity and Pressure Distribution, Internet. <http://www.mh-aerotoools.de>, Version: February 2005.
- 106 Richard S. S. Fundamentals of Flight, Second Edition, Prentice Hall, 1983.
- 107 Kaz J. and Plotkin A. Low Speed Aerodynamics, Second Edition, Cambridge University Press, 2001.
- 108 Jacobs E. N., Ward K. E., and Pinkerton R. M. The Characteristics of 78 Related Airfoil Sections from Tests in the Variable-Density Wind Tunnel, NACA Report Number 460, 1948.
- 109 Kunz, P. J. Kroo, I. M. Analysis, Design and Testing of Airfoils for use at Ultra-Low Reynolds Numbers, KTH Library.
- 110 Plantanitis, G. Strganac, T. W. Analyses and Experiments of Suppression of Control Reversal using a Wing Section with Multiple Control Surfaces, 44th AIAA/ASME/ASCE/AHS/ASC Structures, Structural Dynamics and Materials Conference, 7-10 April, Norfolk, Virginia, 2003.
- 111 Dowell, E. H. Bliss, D. B. Clark, R. L. Aeroelastic Wing with Leading and Trailing Edge Control Surfaces, Journal of Aircraft, 2003, vol. 40, no. 3, pp. 559-565.
- 112 Plantanitis, G., Strganac, T. W. Suppression of Control Reversal Using Leading- and Trailing-Edge Control Surface, Journal of guidance, control and dynamics, vol.28 (3), May 2005.
- 113 Bartley-Cho J. D. , Wang D. P., Martin C. A., Kudva J N. , and West M. N. Development of High-rate, adaptive Trailing Edge Control Surface for the Smart Wing Phase 2 Wind Tunnel Model, Journal of Intelligent Material Systems and Structures, Vol.15, April 2004.

- 114 Kudva J. N., Martin C. A., and Scherer L. B. Overview of the DARPA/AFRL/NASA Smart Wing Program, Society of Photo-Optical Instrumentation Engineers, SPIE Proceedings, Vol. 3674, 1999, pp.230 -236.
- 115 Musgrove R. G. Unites States Patent 4,286,761, Eccentric Actuator, September 1981.
- 116 Musgrove R. G. Unites States Patent 3,944,170, Apparatus for Producing Pivotal Movement, March 1976
- 117 Pierre, L. Design of an Actuation Mechanism for a Seamless Aeroelastic Wing, MSc Thesis, Cranfield University, 2008.
- 118 Mistry, S. DEMON UAV Configuration Control Document, Issue 2 Draft B, November 2007.
- 119 Banerjee, J. R. Use and Capability of CALFUN”, 1984.
- 120 Banerjee, J. R. Flutter Sensitivity Studies for High Aspect Ratio Aircraft Wings.
- 121 Banerjee, J. R. User’s Guide to the Computer Program CALFUN, 1989.
- 122 Aluminium 2024-T81 properties. *Citing Internet resources* (WWW document). <http://www.matweb.com/search/datasheet.aspx?matguid=6441f805a3bb42758ab5b15752343138&ckck=1>. (Accessed January 2009).
- 123 Guo, S. *Programs for airframe preliminary sizing and stressing*. Unpublished document, 2004.
- 124 Guo, S. AERO-BEAM-SAW V3.1 Manual, Unpublished document, 2008.

Appendix A Aerodynamic Analysis

Case 1

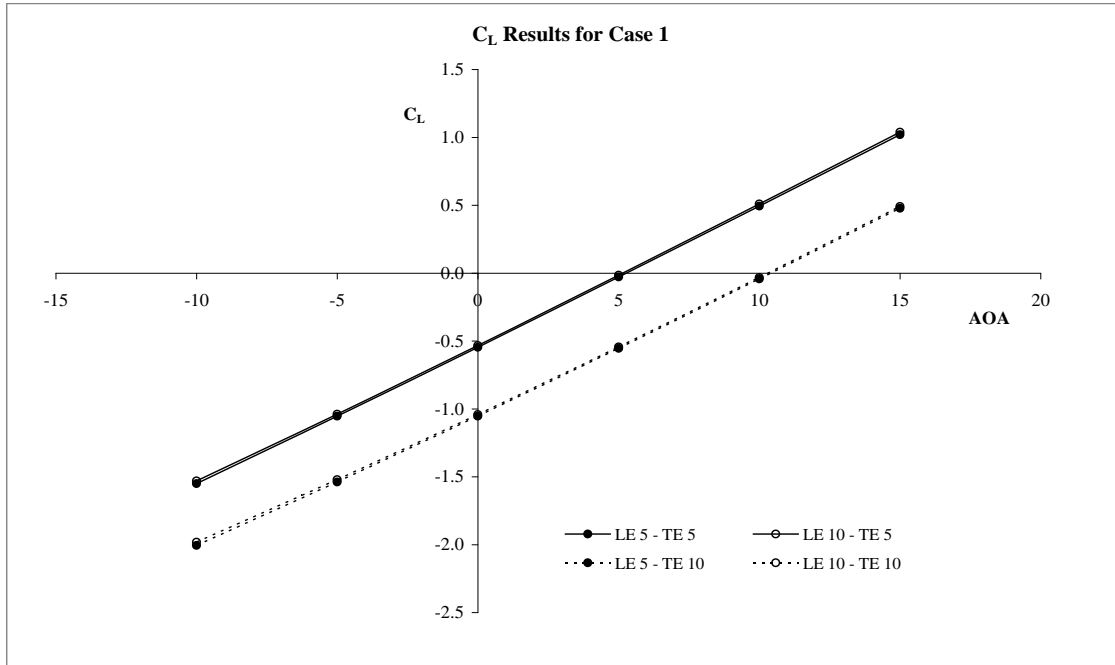


Figure A.1 (a) C_L Comparison for Case *a*

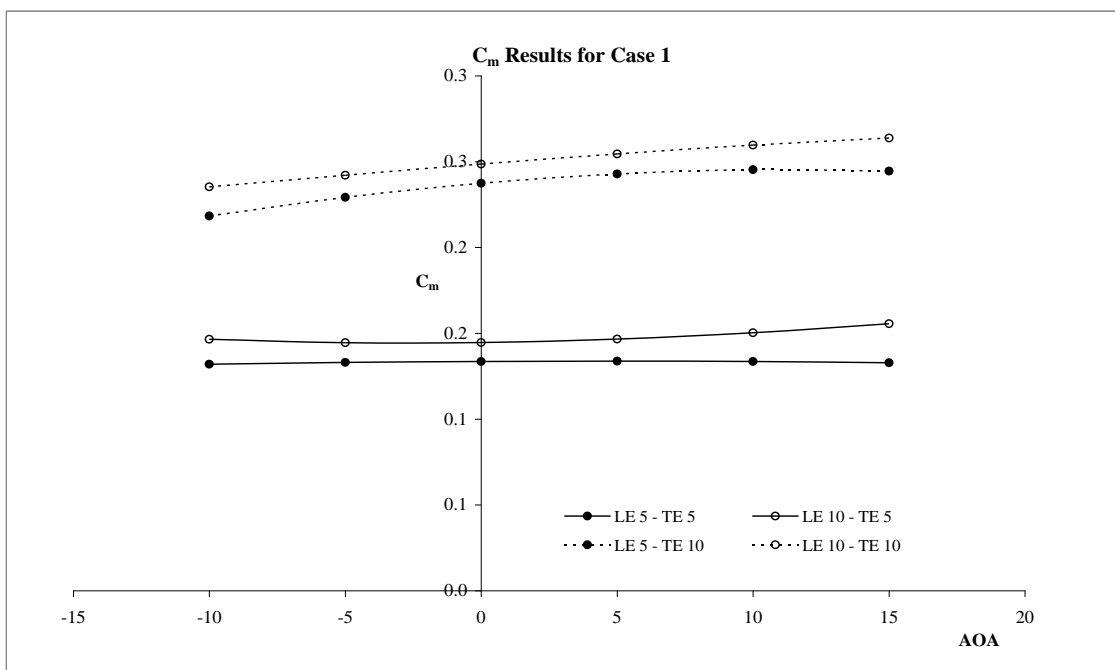


Figure A.1 (b) C_m Comparison for Case 1

Case 2

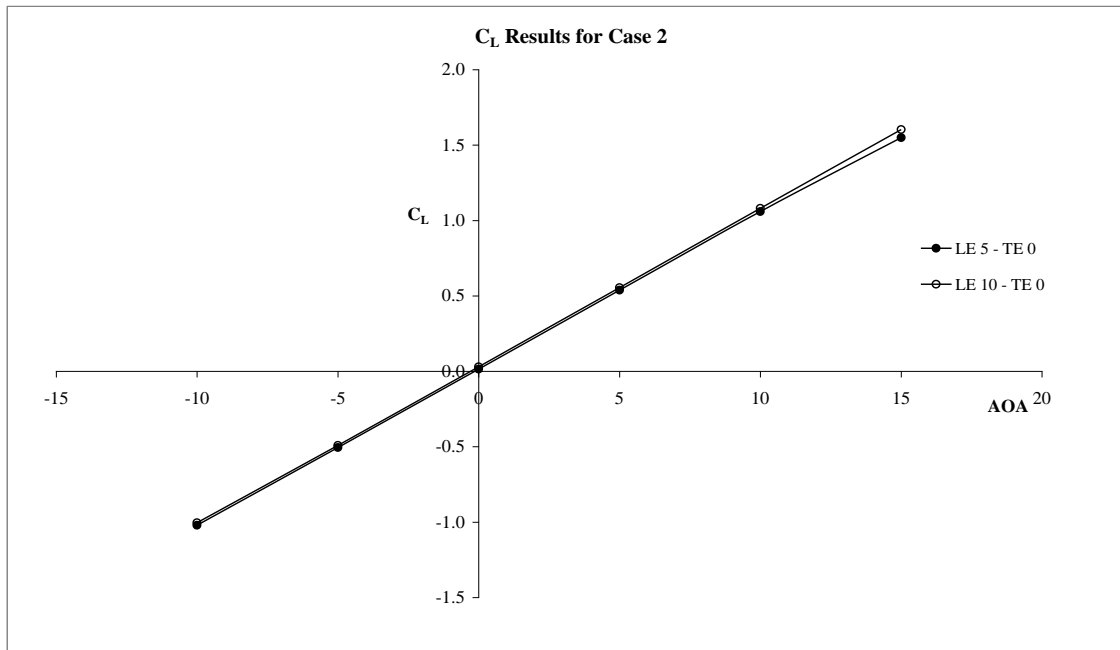


Figure A.2 (a) C_L Comparison for Case 2

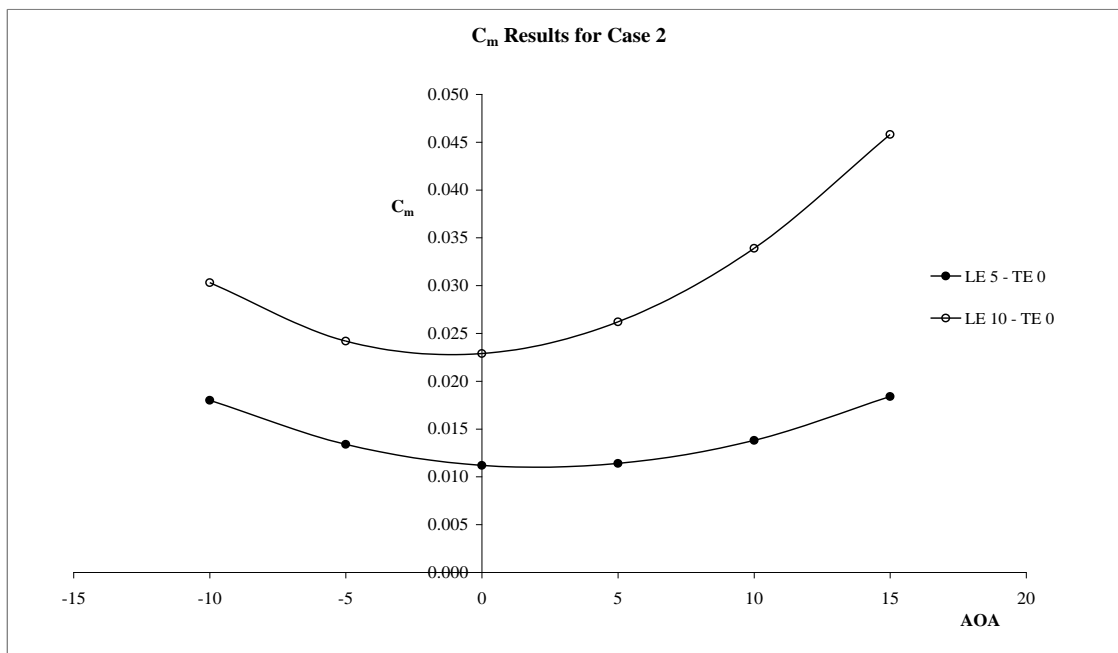


Figure A.2 (b) C_m Comparison for Case 2

Case 3

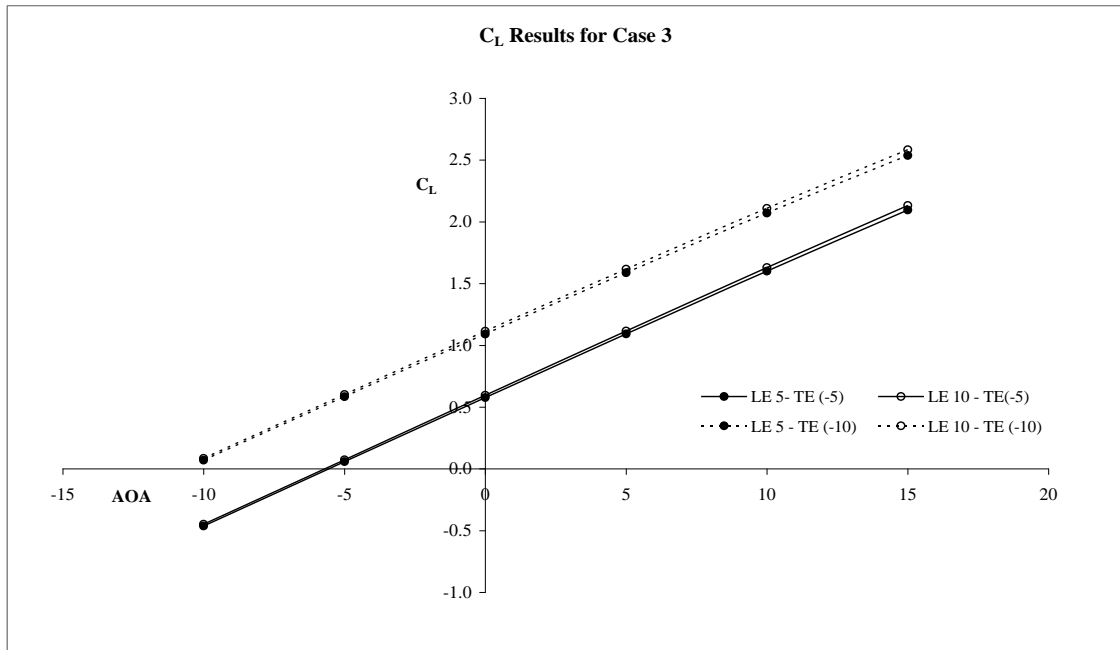


Figure A.3 (a) C_L Comparison for Case 3

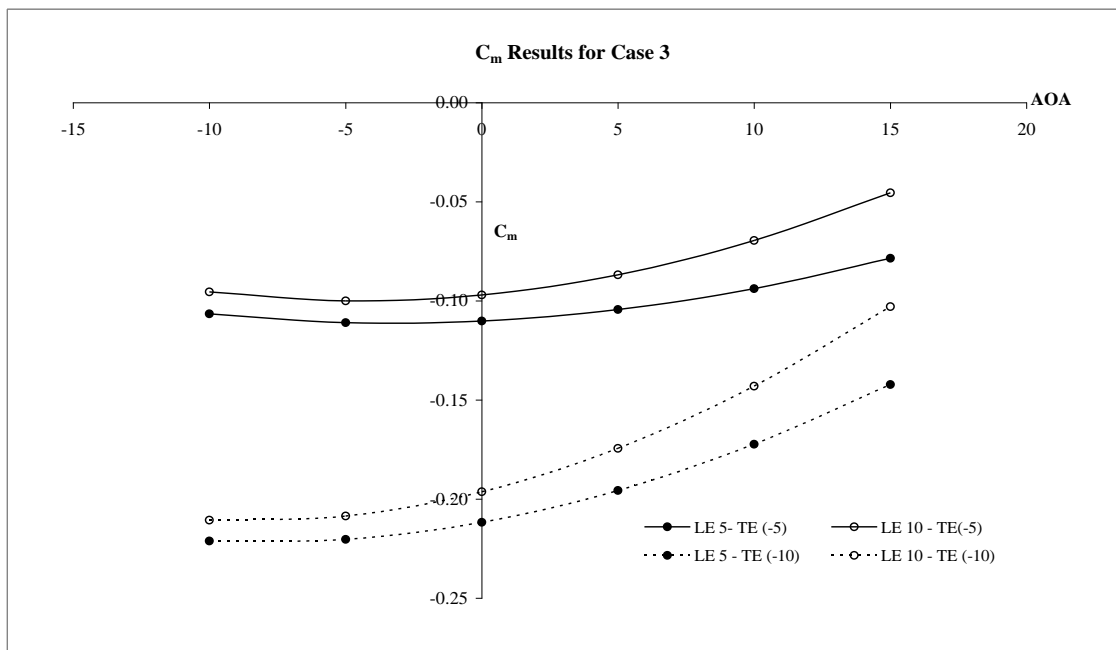


Figure A.3 (b) C_m Comparison for Case 3

Case 4

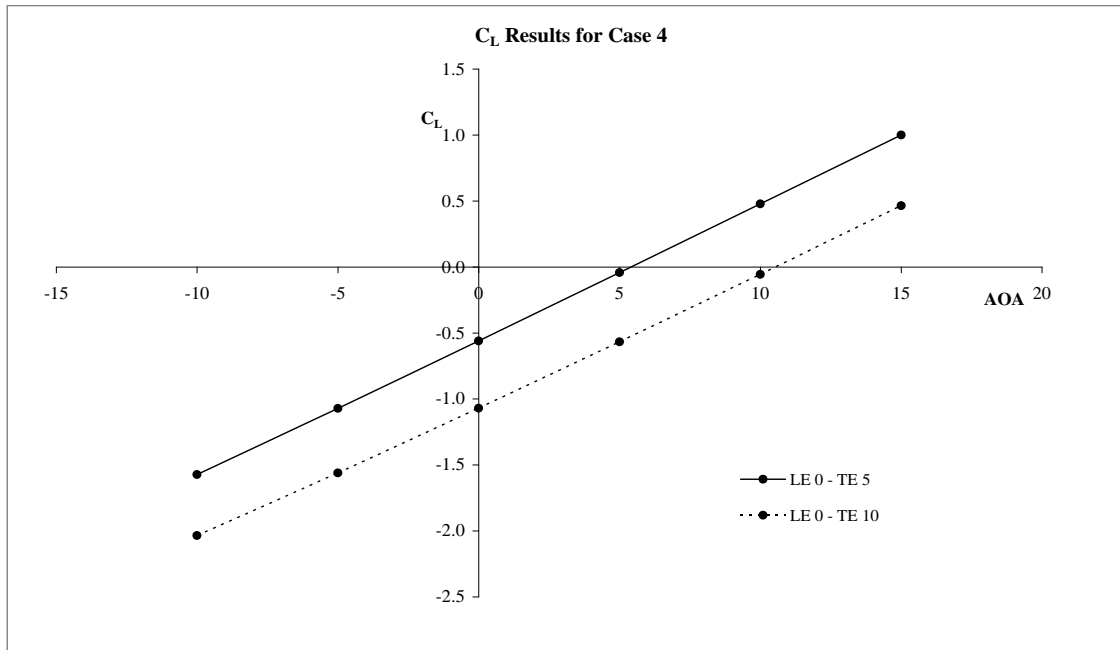


Figure A.4 (a) C_L Comparison for Case 4

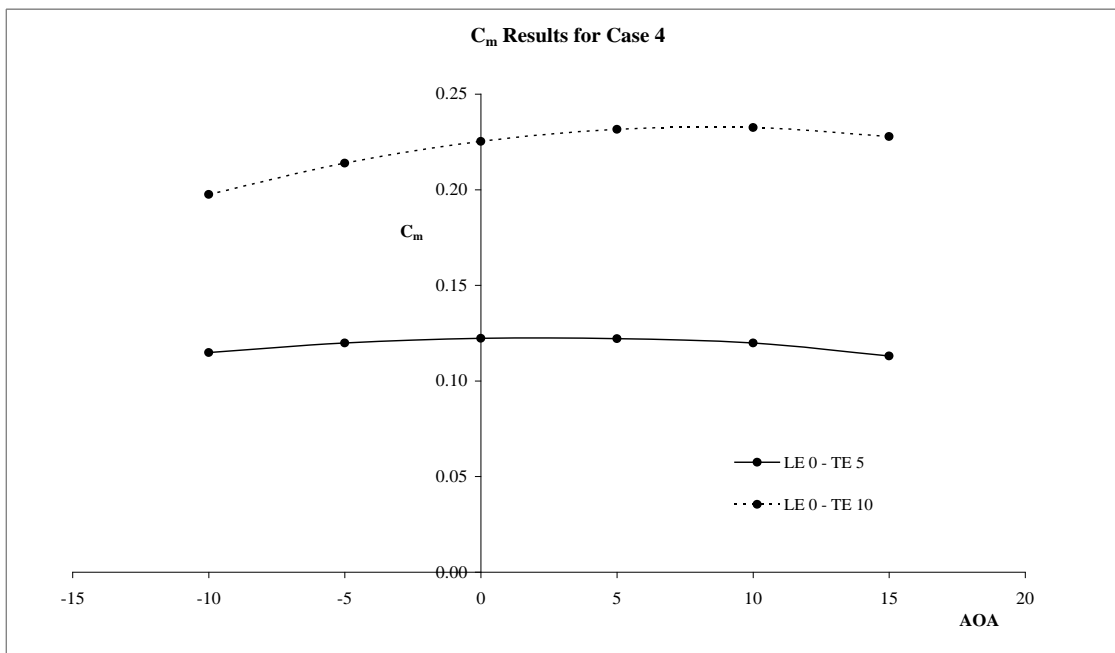


Figure A.4 (b) C_m Comparison for Case 4

Case 5

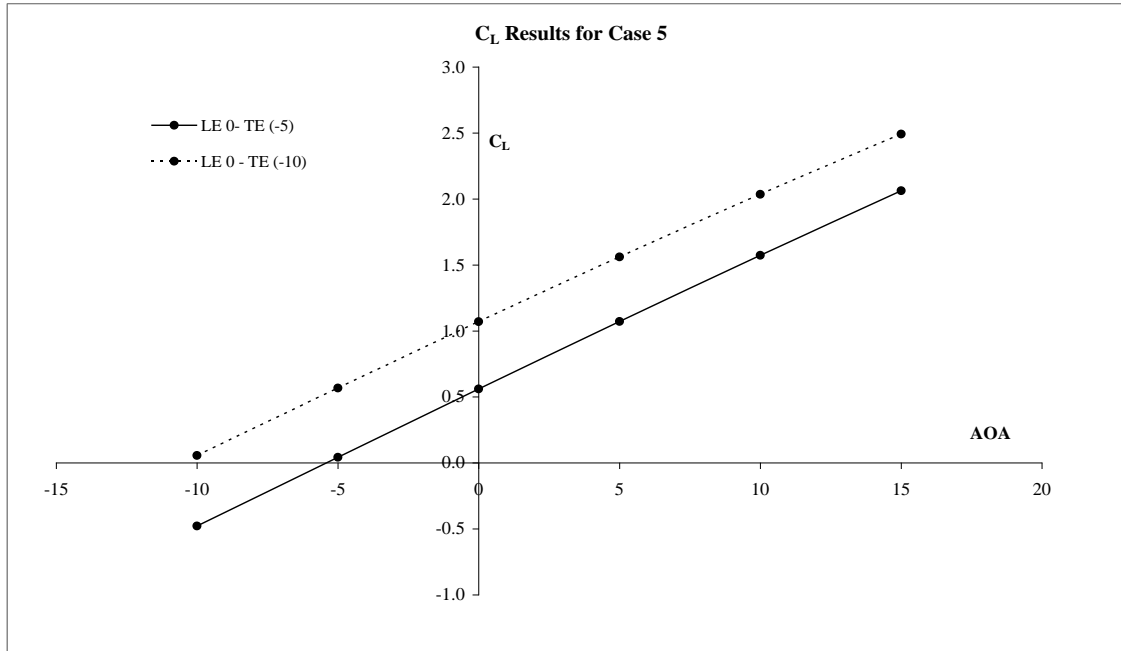


Figure A.5 (a) C_L Comparison for Case 5

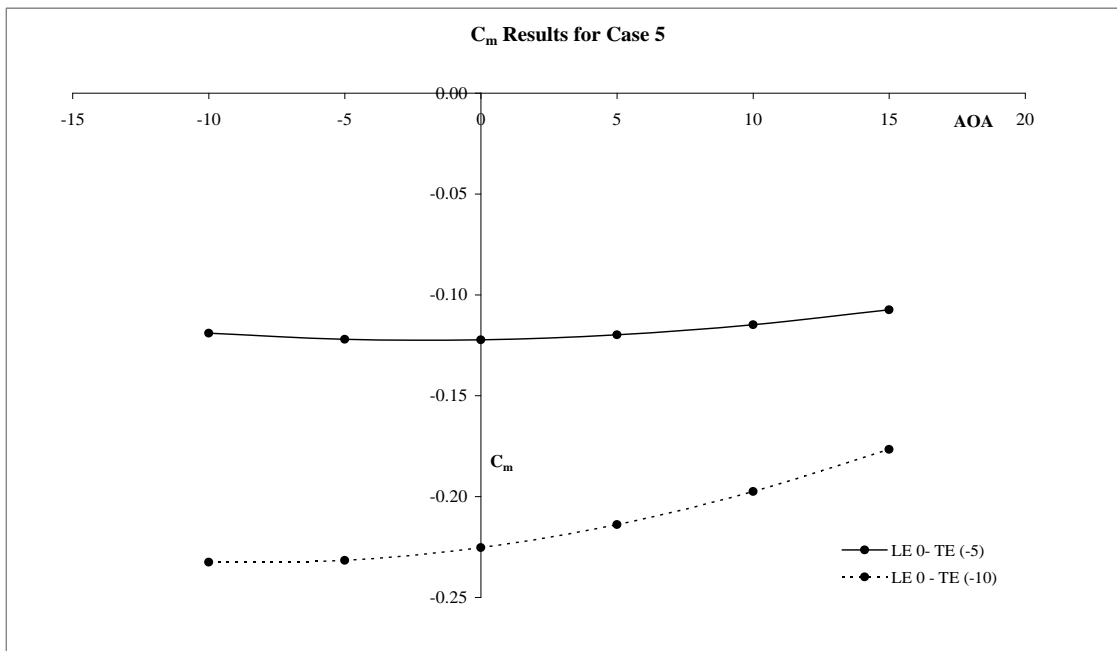


Figure A.5 (b) C_m Comparison for Case 5

Case 6

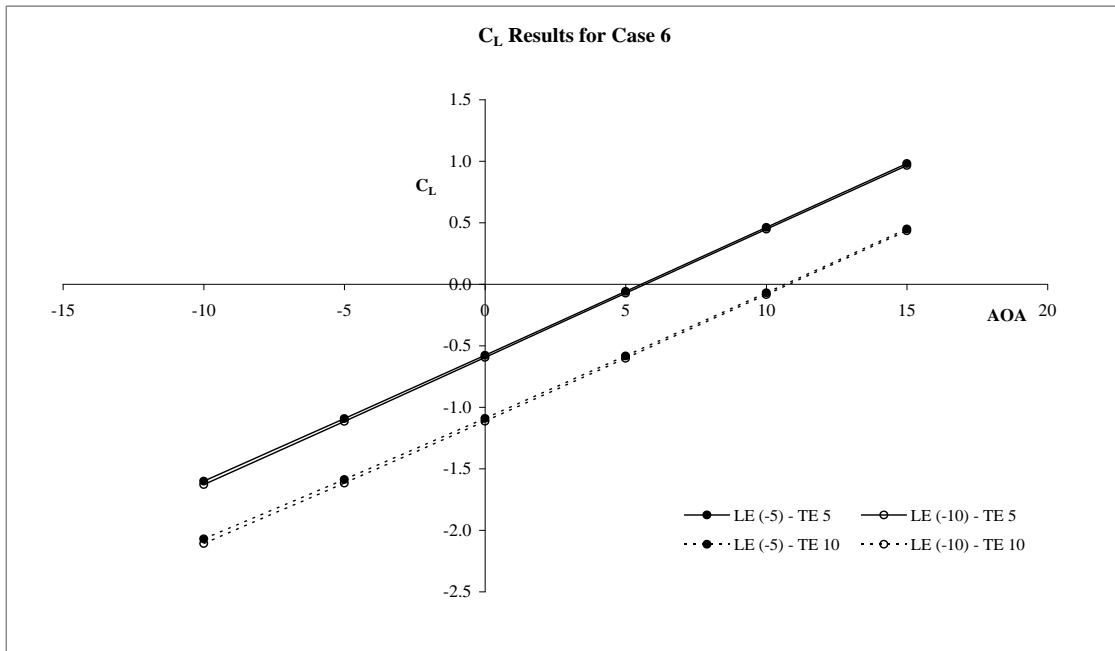


Figure A.6 (a) C_L Comparison for Case 6

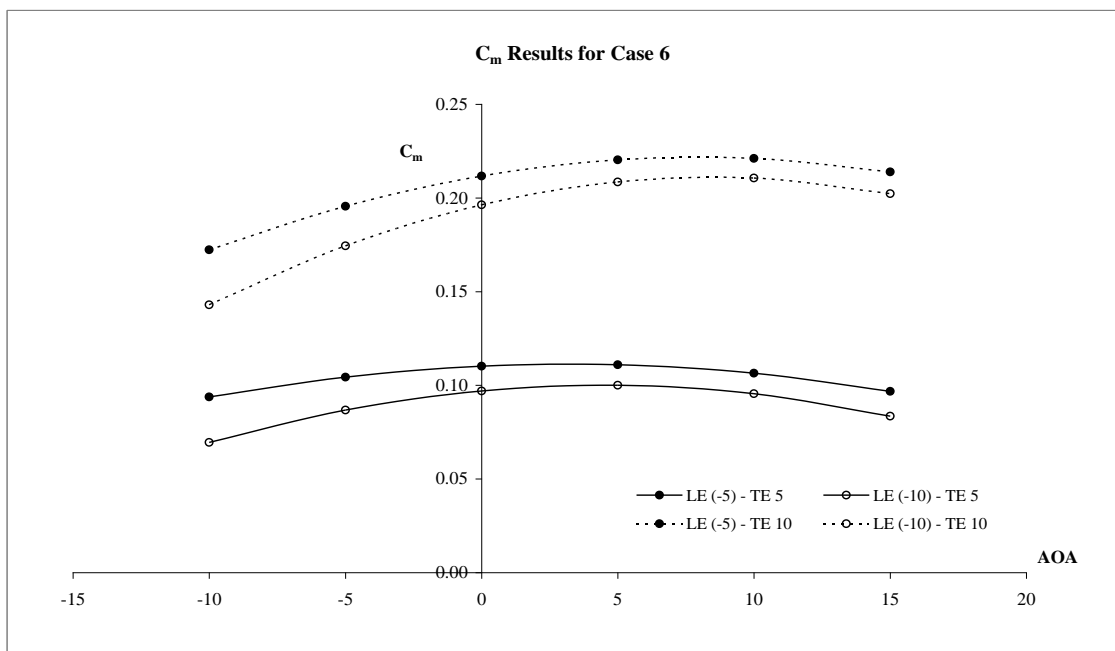


Figure A.6 (b) C_m Comparison for Case 6

Case 7

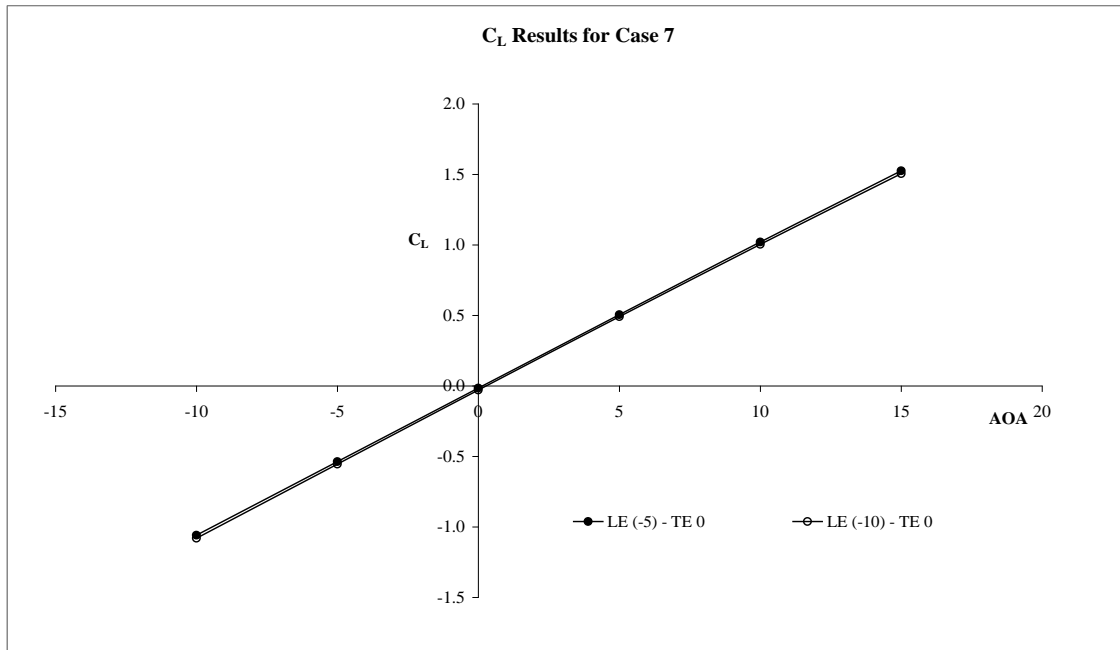


Figure A.7 (a) C_L Comparison for Case 7

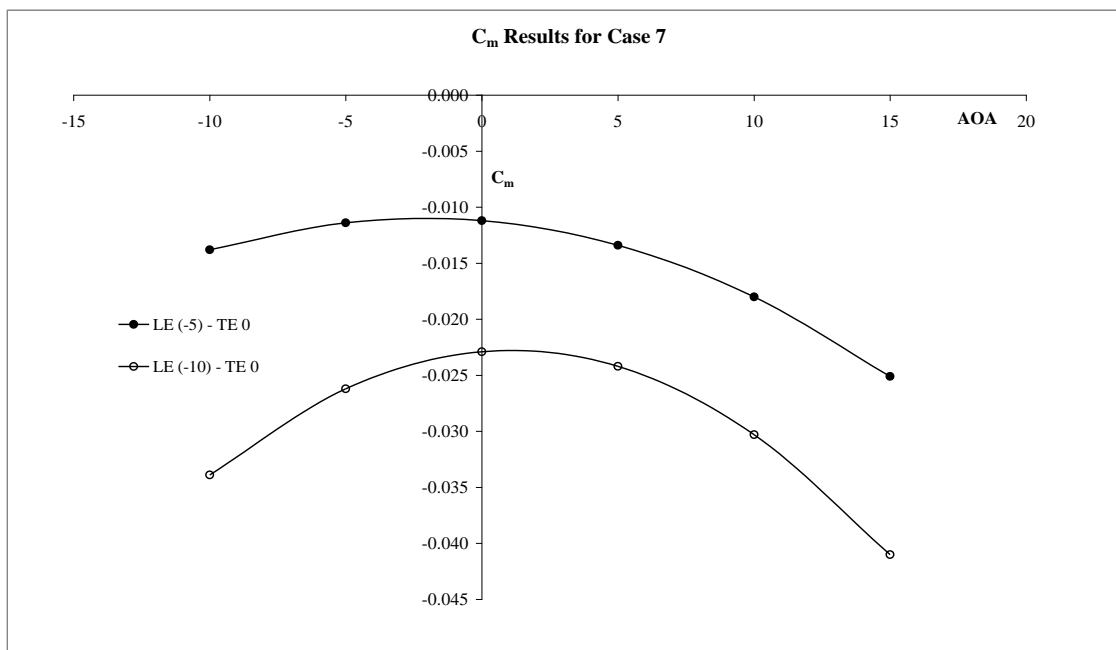


Figure A.7 (b) C_m Comparison for Case 7

Case 8

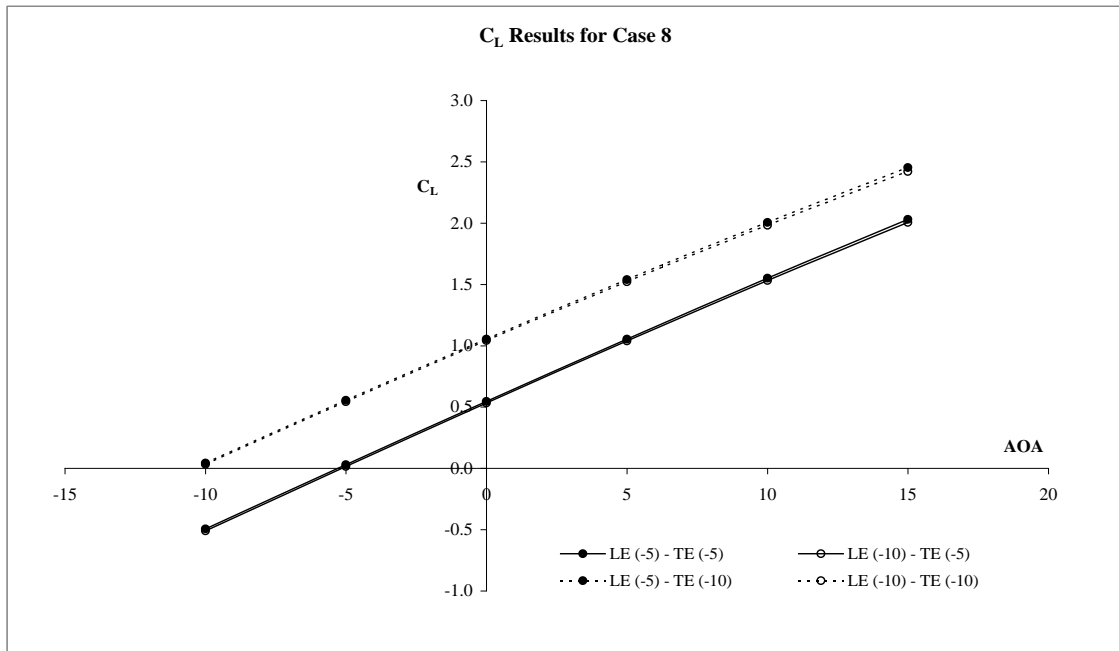


Figure A.8 (a) C_L Comparison for Case 8

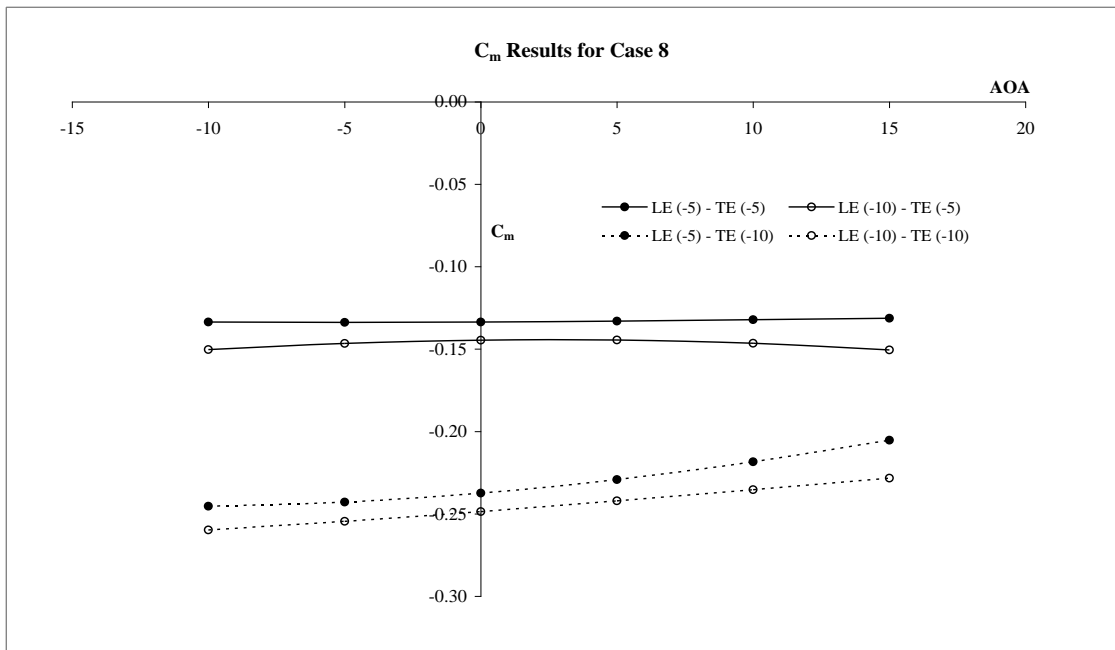


Figure A.8 (b) C_m Comparison for Case 8

Appendix B SAW Disc setting angle

This appendix presents the work carried out in determining a key design feature of the SAW actuation mechanism, which is the setting angle of the discs at each TE location. The work presented here was part of an MSc individual research project completed in year 2007-2008 at Cranfield [117].

Equation of the beam curve

Initially the design consists of determining the equation of the curved beam. It is the key part of the mechanism and will allow the determination of the rest of the parameters. In order to determine the shape two assumptions are made:

- I. Trailing edge maximum deflection, θ , equal to 10 degrees:

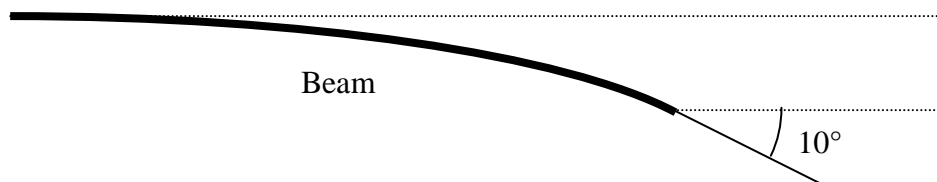


Figure B. 1 TE deflected shape

- II. Equation of the curve corresponds to the deflection of a cantilever beam under tapered distributed pressure:

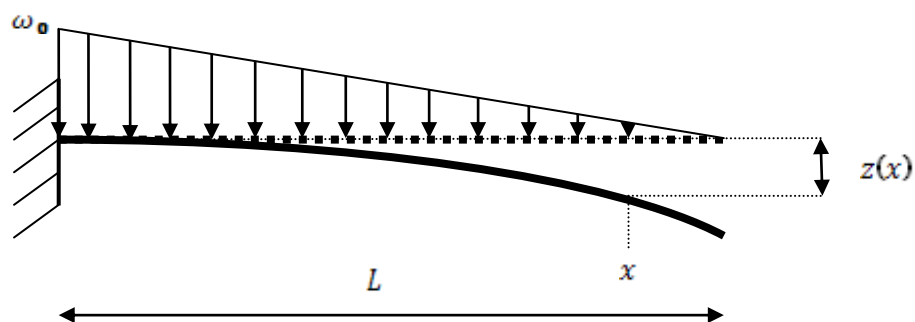


Figure B.2 Cantilever beam under pressure

From basic calculus and mechanics of deformable bodies the beam shape resulting from a distributed moment is;

$$z''(x) = -\frac{M(x)}{EI} \quad (\text{B.1})$$

Where $M(x) = -\int_x^L w(s)(s-x)ds$ and $w(s) = w_0\left(1 - \frac{s}{L}\right)$

The following equation can be obtained;

$$Beam(x_0) = z(x) = \frac{w_0}{EI} \frac{1}{L} \left[\frac{L^3 x^2}{12} - \frac{x^5}{120} - \frac{L^2 x^3}{12} + \frac{Lx^4}{24} \right] \quad (\text{B.2})$$

We also have the deflection angle for small displacements:

$$\theta(x) \approx \tan(\theta(x)) = z'(x) = \frac{w_0}{EI} \frac{1}{L} \left[\frac{L^3 x}{6} - \frac{x^4}{24} - \frac{L^2 x^2}{6} + \frac{Lx^3}{6} \right] \quad (\text{B.3})$$

Hence the maximum vertical displacement at the beam extremity is given by:

$$z_{\max} = z(L) = \frac{w_0}{EI} \frac{L^4}{30} = \frac{24}{30} L \theta_{\max} \quad (\text{B.4})$$

From Eqn. (B.4) the ratio w_0/EI can be determined for a given TE deflection, θ_{\max} and beam length, L .

Disc related equation

In the process of determining the setting angle for the discs, the next step was to express the movement of the extreme point of the disc, w_v . Figure B.1 presents an overview of the geometry and defines the variables used in determining the disc setting angle. The beam is shown in two positions: 0° and 90° rotating up, this rotation angle of the beam is represented by φ . The angle between the plane normal to the curved beam and vertical plane is represented by α .

In this case, the disc is placed at an arbitrary position along the curved beam. It is set at a variable angle, η , to the plane normal to beam curve. A sphere has also been drawn at the extremity of the disc, which is the furthest point from the origin of the curved beam. This point is fixed on the disc and consequently rotates with the curved beam.

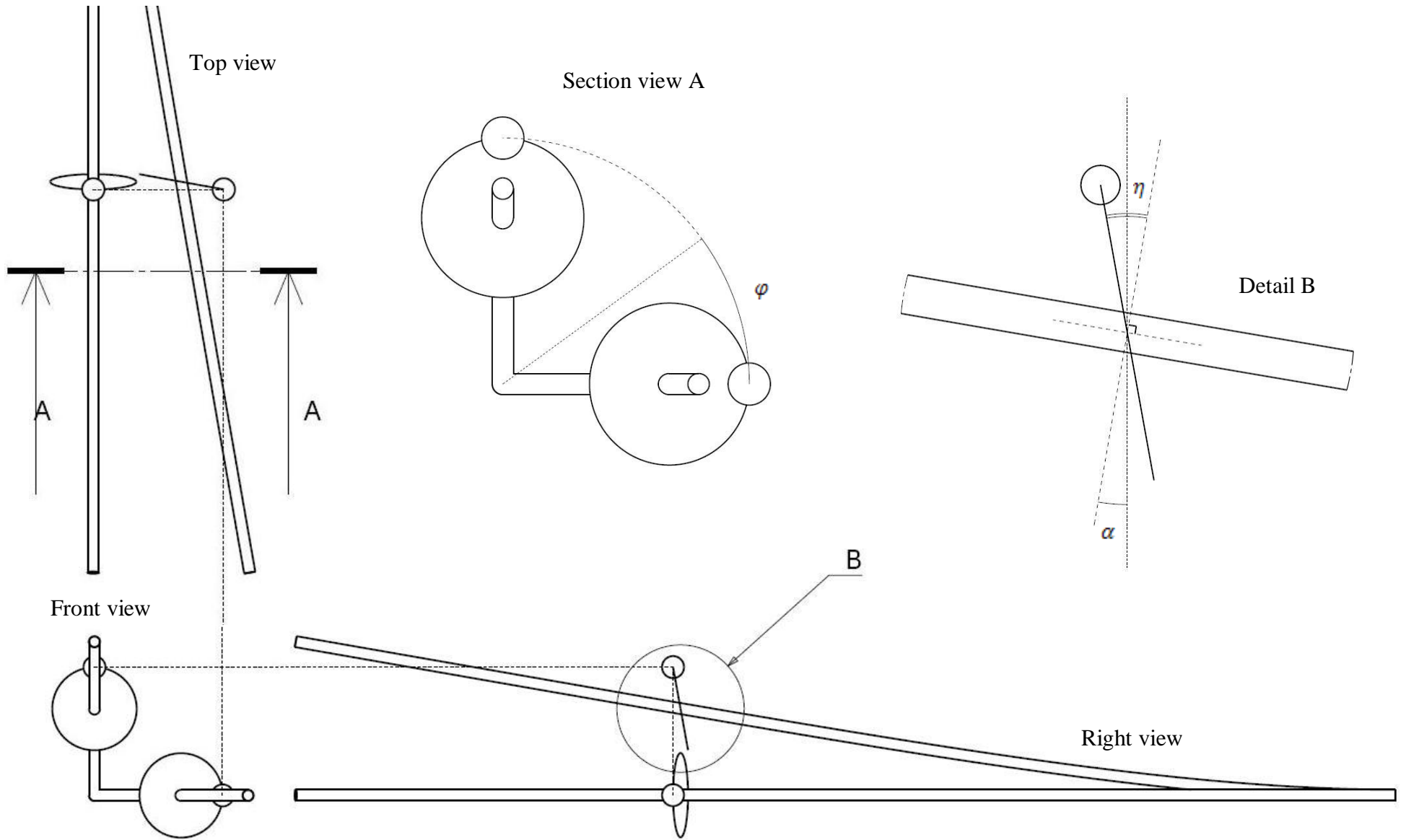


Figure B. 3 Curved Beam at two positions (0° and 90°) with one disc fixed [117]

In order to determine the coordinates of the centre of the disc during rotation, the section view from the Figure B.1 is used.

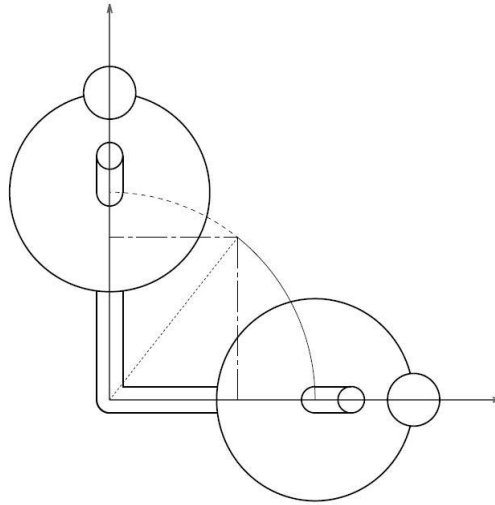


Figure B. 4 Intermediate position I_p for the centre of the disc [117]

If the coordinates of intermediate point, I_p , are (X_0, Y_w, Z_w) , X_0 will be known due to the fact that this will be the location chosen to place the disc along the curved beam. Hence, Y_w and Z_w can be expressed with the use of the curved beam equation, Eqn. (B.2) as:

$$Y_w = Beam(X_0) \cdot \cos(\varphi) \quad (B.5)$$

$$Z_w = Beam(X_0) \cdot \sin(\varphi) \quad (B.6)$$

where $Beam(X_0)$ is the equation of the beam curve and φ is the angle of rotation of the curved beam (varying from 0° to 90°).

The next step was to determine the coordinates of the vertical extreme points of the disc, w_v during rotation. At the maximum angle of rotation, w_v is superimposed with S_p which is the point on the sphere shown in Figure B.2. Figure B.5 (Detail B view of Figure B. 3) is used to obtain the coordinates of S_p by taking the centre of the disc as the new origin.

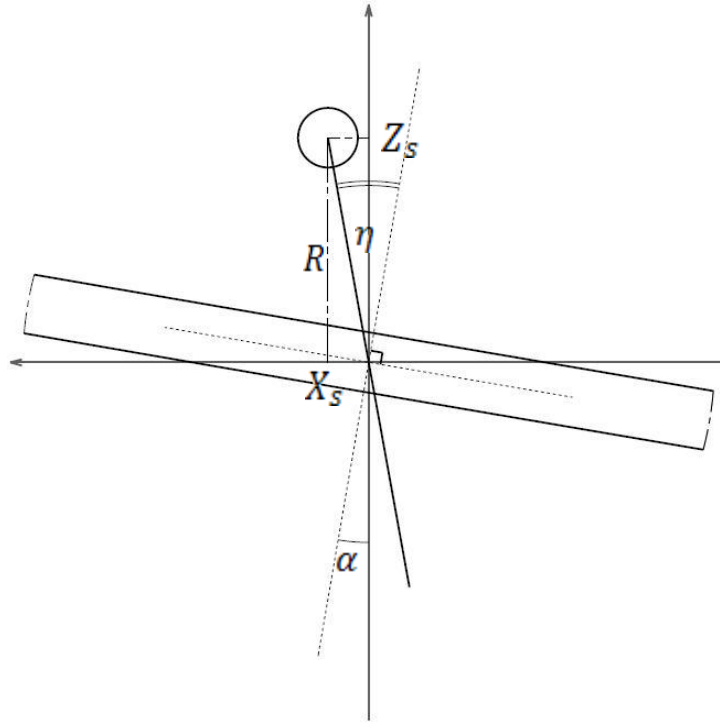


Figure B.5 Coordinates of the Sphere Point, Sp [117]

Hence the coordinates of S_p , (X_s, Y_s, Z_s) at 90° curved beam rotation can be expressed as:

$$X_s = R \cdot \sin(\eta - \alpha) \quad (\text{B.7})$$

$$Y_s = (Y_w)_{\varphi=90^\circ} = 0 \quad (\text{B.8})$$

$$Z_s = R \cdot \cos(\eta - \alpha) \quad (\text{B.9})$$

where R is the radius of the disc, α and η are as before, the angle between the plane normal to the curved beam and the vertical plane and the setting angle (set from the plane normal to the beam) of the disc respectively.

The purpose of the next preceding section is to link the coordinates of w_v to the curved beam angle of rotation φ . The detail view in Figure B. 4 is considered as an intermediate stage during the rotation. It corresponds to a section view of the beam in the plane parallel to the x - z plane which includes the centre of the disc. The new circle indicates the position of w_v . The angle α_i is now variable (from 0 to α) and η is supposed to be null in the following.

The ‘3 sections view’ on the same figure shows three intermediate states for the curved beam which are numbered from 0 to 2. The α_i are present and it can be noted that all the tangents to the beam curve traced from the disc centres at the different positions are concurrent. They all meet at point P. In 3-D, this point corresponds to the intersection between the tangent and the axis of rotation (x-axis).

The α_i can be linked to the coordinates of the disc centres as:

$$\tan(\alpha_i) = \frac{Z_{wi}}{d} \quad (\text{B.10})$$

Using Eqn. (B.5) and assuming that the angle α remains relatively small,

$$\alpha_i \approx \tan(\alpha_i) = \frac{Z_{wi}}{d} = \frac{Beam(X_0) \cdot \sin(\varphi_i)}{d} \quad (\text{B.11})$$

Hence, when

$$\varphi_0 = 0^\circ \text{ then } Z_{w-0} = 0 \text{ and } \alpha_0 = 0^\circ$$

$$\varphi_{90} = 90^\circ \text{ then } Z_{w-90} = Beam(X_0) \text{ and } \tan(\alpha_{90}) = \frac{Beam(X_0)}{d}$$

And at $\varphi_{90} = 90^\circ$, $\alpha_{90} = \alpha_{\max} = \alpha$.

Thus,

$$d = \frac{Beam(X_0)}{\tan(\alpha_{90})} \quad (\text{B.12})$$

Substituting Eqn.(B.12) into Eqn.(B.11) provides a relationship between α_i and φ_i :

$$\alpha_i \approx \tan(\alpha_i) = \tan(\alpha) \cdot \sin(\varphi_i) \quad (\text{B.13})$$

The last step consists of replacing the discrete values of α_i by a continuous variable angle, β which varies from 0 to $\eta - \alpha$.

Because the angles considered are still relatively small, β can be expressed as:

$$\beta \approx \tan(\beta) = \tan(\eta - \alpha) \cdot \sin(\varphi) \quad (\text{B.14})$$

The coordinates of w_v from the centre of the disc (X'_v, Y'_v, Z'_v) can then be determined using Figure B. 4:

$$X'_v = R \cdot \sin(\beta) \quad (\text{B.15})$$

$$Y'_v = 0 \quad (\text{B.16})$$

$$Z'_v = R \cdot \cos(\beta) \quad (\text{B.17})$$

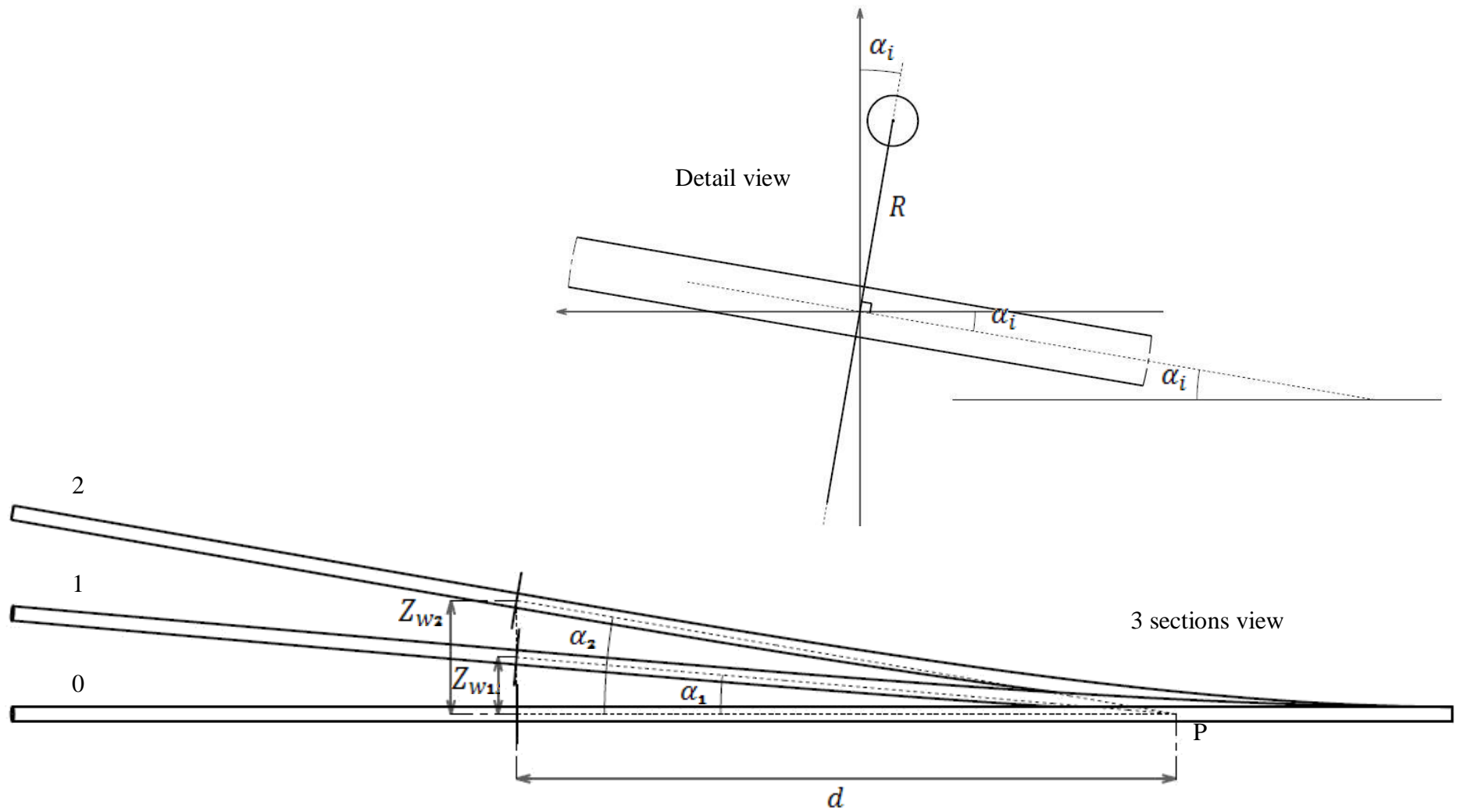


Figure B. 6 Three section views during the beam rotation [117]

The angle α defines the tangent to the beam at X_0 . Hence, α can be expressed as:

$$\tan(\alpha) = D(Beam(X_0)) \quad (B.18)$$

Where $D(Beam(X_0))$ is the derivative of the curved beam definition function $Beam(X_0)$. Thus, for small angles:

$$\alpha \approx \tan(\alpha) = D(Beam(X_0)) \quad (B.19)$$

Hence the coordinates of w_v from the origin of the beam can be expressed as:

$$X_v = X'_v + X_0 \quad (B.20)$$

$$Y_v = Y'_v + Y_w \quad (B.21)$$

$$Z_v = Z'_v + Z_w \quad (B.22)$$

Substituting expressions for (X'_v, Y'_v, Z'_v) and (Y_w, Z_w) from Eqns. (B.15 – B.17) and Eqns. (B.5-B.6) respectively into Eqns. (B.20 - B.22) gives:

$$X_v = R \cdot \sin(\beta) + X_0 \quad (B.23)$$

$$Y_v = Beam(X_0) \cdot \cos(\varphi) \quad (B.24)$$

$$Z_v = R \cdot \cos(\beta) + Beam(X_0) \cdot \sin(\varphi) \quad (B.25)$$

Substituting expressions for α (Eqn.A.19) and β (Eqn. (B.14) into Eqns. (B.23 -24) gives the final expressions for the coordinates of the extreme point on the disc as a function of the disc setting angle, η , and the curved beam rotation angle, φ .

$$X_v = R \cdot \sin(\tan(\eta - D(Beam(X_0))) \cdot \sin(\varphi)) + X_0 \quad (B.26)$$

$$Y_v = Beam(X_0) \cdot \cos(\varphi) \quad (B.27)$$

$$Z_v = R \cdot \cos(\tan(\eta - D(Beam(X_0))) \cdot \sin(\varphi)) + Beam(X_0) \cdot \sin(\varphi) \quad (B.28)$$

Hence if η is set then a 3-D parameterized curve can be plotted at having φ varying from 0° to 90° . This represents the movement of the vertical extreme point of one disc placed at X_0 during the rotation of the curved beam. To have the curve starting at the origin and growing on $y>0$, it is necessary to modify it. Hence if (X_{pc}, Y_{pc}) are the functions for the parameterized curve:

$$X_{pc} = X_v(\varphi) - X_v(0); \quad Y_{pc} = -(Y_v(\varphi) - Y_v(0)) \quad (B.29)$$

$$X_{pc}(\varphi) = R \cdot \sin(\tan(\eta - D(Beam(X_0))) \cdot \sin(\varphi)); \quad Y_{pc}(\varphi) = Beam(X_0) \cdot (1 - \cos(\varphi)) \quad (B.30)$$

Wing related equation

This section deals with the derivation of the warping wing related equation that would follow the same path of point w_v of the disc. The force acting on the wing skins will be coming from the discs pushing the wing surface from the inside, hence only half of the profile will be considered. This half is the one which corresponds to the direction of the disc motion. In the following and as previously, the upward rotation up to 90^0 will be considered for the curved beam. Due to symmetry only the upper half of the wing will be taken into account.

In this section, only one stringer will be considered and it will be assumed that the wing surface keeps its shape while rotating around its own axis. The coordinates of points belonging to the wing surface are represented by Eqn. (B.31) which is for a NACA symmetrical profile.

$$NACA(x) = \frac{t}{0.2} \left(0.2969\sqrt{x} - 0.126x - 0.3516x^2 + 0.2843x^3 - 0.1015x^4 \right) \quad (\text{B.31})$$

Where t is the maximum thickness of the aerofoil as a percentage of the chord, which in this design case is, $t = 0.15c$.

In Eqn. (B.31) x varies from 0 to 1. Hence the results need to be scaled using the chord, c . A new input varying from 0 to c can be used with the following function;

$$z(x) = c \cdot NACA\left(\frac{x}{c}\right) \quad (\text{B.32})$$

It is known that the vertical movement of the wing surface will follow exactly the one of the disc, hence only the horizontal motion needs to be verified.

From Figure B.5 it can be seen that a point (x, z) moves a distance dz and dx upward and forward respectively, depending on the angle of rotation, ϕ . For a given point (x, y) in a bi-dimensional space, the vertical and horizontal variations of its coordinates during rotation can be found only by knowing the angle of rotation, ϕ . In order to find the relation it is necessary to introduce two parameters, r and γ , which are respectively the length of the segment joining the point to the centre of rotation and the angle between the horizontal and the previous segment.

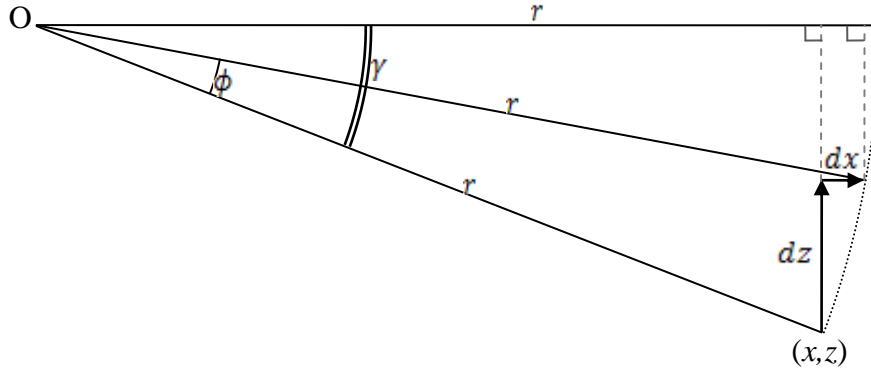


Figure B. 7 Motion of a point fixed to the wing during its morphing [117]

From Figure B. 7,

$$x = r \cos(\gamma) \text{ and } z = r \sin(\gamma) \quad (\text{B.33})$$

Hence, $x + dx = r \cos(\gamma - \phi) \text{ and } z - dz = r \sin(\gamma - \phi)$ (B.34)

Thus,

$$dx = (x + dx) - x = r \cos(\gamma - \phi) - r \cos(\gamma) \quad (\text{B.35})$$

$$dx = r(\cos(\gamma)\cos(\phi) + \sin(\gamma)\sin(\phi)) - r \cos(\gamma) \quad (\text{B.36})$$

$$dx = -r \cos(\gamma)(1 - \cos(\phi)) + r \sin(\gamma)\sin(\phi) \quad (\text{B.37})$$

Substituting expressions for x and z from Eqn. (B.33) gives:

$$dx = -x(1 - \cos(\phi)) + z \sin(\phi) \quad (\text{B.38})$$

Similarly,

$$dz = z - (z - dz) = r \sin(\gamma) - r \sin(\gamma - \phi) \quad (\text{B.39})$$

$$dz = r \sin(\gamma) - r(\sin(\gamma)\cos(\phi) - \sin(\phi)\cos(\gamma)) \quad (\text{B.40})$$

$$dz = r \sin(\gamma)(1 - \cos(\phi)) + r \cos(\gamma)\sin(\phi) \quad (\text{B.41})$$

Substituting expressions for x and z from Eqn. (B.33) gives:

$$dz = z(1 - \cos(\phi)) + x \sin(\phi) \quad (\text{B.42})$$

Therefore dx and dz can be expressed in terms of x , y , and ϕ as:

$$dx = -x(1 - \cos(\phi)) + z \sin(\phi) \quad (\text{B.43})$$

$$dz = x \sin(\phi) + z(1 - \cos(\phi)) \quad (\text{B.44})$$

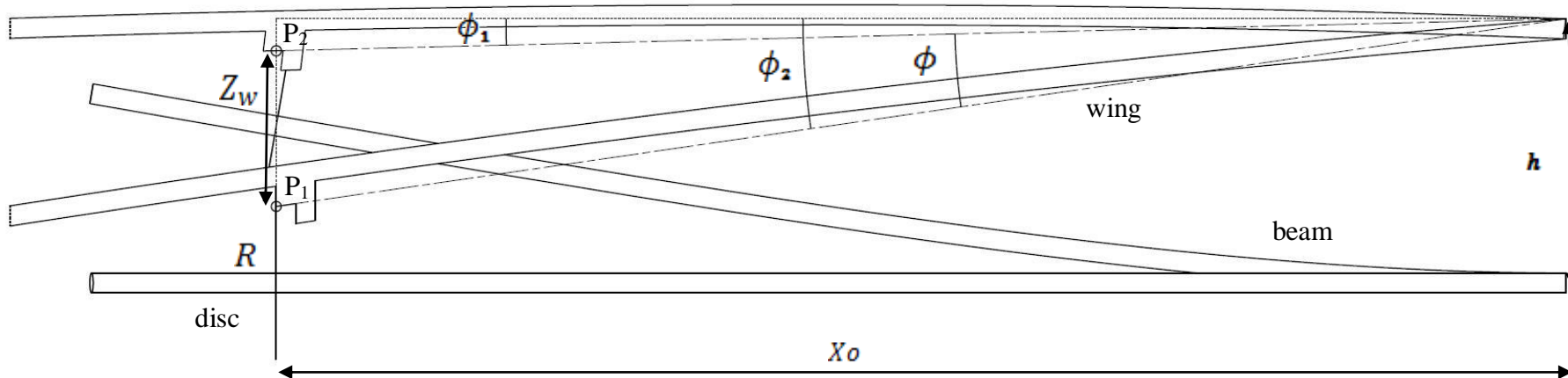


Figure B. 8 Two configurations for the wing when the beam rotates [117]

From the above Figure:

$$\tan(\phi_1) = \frac{h - (R + Z_w)}{X_o}$$

$$\tan(\phi_2) = \frac{h - R}{X_o}$$

$$\phi = \phi_2 - \phi_1$$

The next step was to find a relation between ϕ and φ , which is the angle of rotation of the beam. Then the horizontal movement of the disc, dx , can be linked directly to this angle. Figure B. 8 represents two configurations for the system. Position 1 corresponds to the neutral position for the curved beam ($\varphi = 0$) while position 2 corresponds to an intermediate position. The two points, P₁ and P₂, characterise the vertical position of the stringer during the motion.

At the neutral position, the vertical coordinate of P₁ is equal to R (radius of the disc). At the intermediate position, the stringer has moved as high as the disc ($dz = Z_w$), therefore the vertical coordinate of P₂ is $R + Z_w$.

Now, using the expressions for ϕ_1 and ϕ_2 from **Error! Reference source not found.:**

$$\tan(\phi) = \tan(\phi_2 - \phi_1) = \tan\left(a \tan\left(\frac{h-R}{X_0}\right) - a \tan\left(\frac{h-(R+Z_w)}{X_0}\right)\right) \quad (\text{B.45})$$

$$\tan(\phi) = \frac{\frac{h-R}{X_0} - \frac{h-(R+Z_w)}{X_0}}{1 - \frac{h-R}{X_0} \cdot \frac{h-(R+Z_w)}{X_0}} \quad (\text{B.46})$$

Assuming then that the disc is not too close to the origin of the beam:

$$\frac{h-(R+Z_w)}{X_0} \ll \frac{h-R}{X_0} \ll 1; \quad \frac{h-(R+Z_w)}{X_0} \cdot \frac{h-R}{X_0} \ll \ll 1 \quad (\text{B.47})$$

This leads to:

$$\tan(\phi) \approx \frac{h-R}{X_0} - \frac{h-(R+Z_w)}{X_0} = \frac{Z_w}{X_0} \quad (\text{B.48})$$

Substituting Eqn. (B.6) for Z_w gives;

$$\phi \approx a \tan\left(\frac{BEAM(X_0) \cdot \sin(\varphi)}{X_0}\right) \quad (\text{B.49})$$

In this design case, the initial coordinates of the stringer, from the centre of rotation of the wing, are $(X_0, (h-R))$. Then the equation for the horizontal movement of the stringer can finally be deduced as;

$$dx(\varphi) = -X_0 \left(1 - \cos \left(a \tan \left(\frac{BEAM(X_0) \cdot \sin(\varphi)}{X_0} \right) \right) \right) + (h - R) \sin \left(a \tan \left(\frac{BEAM(X_0) \cdot \sin(\varphi)}{X_0} \right) \right) \quad (\text{B.50})$$

where $h = C \cdot NACA(0.5)$ and $R = C \cdot NACA\left(\frac{X_0 + L}{C}\right)$.

From this result, the same parameterized curve as for the disc $(X_{PC}(\varphi), Y_{PC}(\varphi), \varphi = 0 \dots 90)$ can be plotted. Its corresponding functions for the stringer path are now:

$$X_{PC}(\varphi) = dx(\varphi) \quad (\text{B.51})$$

$$Y_{PC}(\varphi) = -(Y_w(0) - Y_w(\varphi)) \quad (\text{B.52})$$

Appendix C Eccentuator Concept Initial Calculations

Force Requirements

The calculation of the force required to deform the skins to the required deflected shape can be evaluated, which will give an initial estimate for feasibility purposes. Using simple beam bending equations presented in Appendix B it is possible to estimate the force required to achieve the required deflection. Figure C.1 shows the 10⁰ TE equivalent deflected shapes of a cantilever beam of length 300 mm.

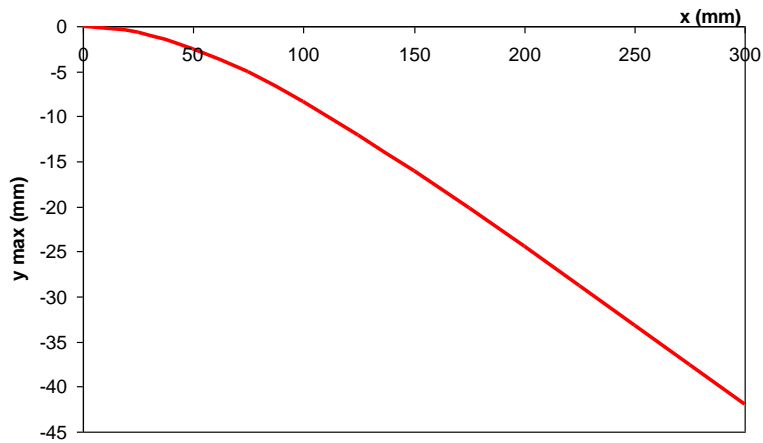


Figure C. 2 Beam bending

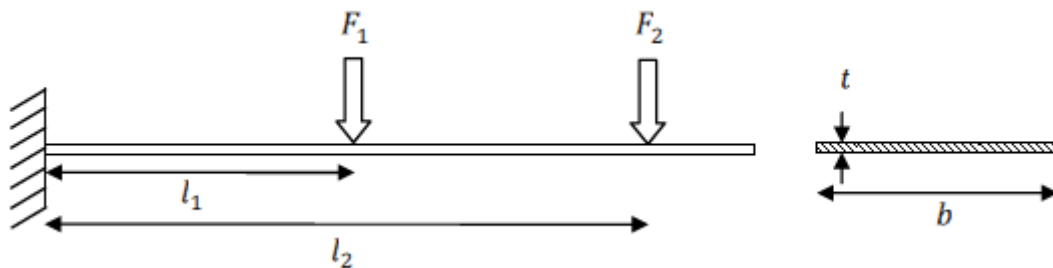


Figure C. 1 Beam Bending – Multiple Point Loads

Where the second moment of area (I) for the skin is given by:

$$I = \frac{b \times t^3}{12} ; b = 300\text{mm (spacing between eccentuators)} \quad (\text{C. 1})$$

The thickness of the skin (t) is driven by the stiffness requirement to prevent deflection under aerodynamic loading conditions, however for this initial appraisal a thickness of 1 mm has been assumed.

$$I = \frac{0.3 \times 0.001^3}{12} = 2.5 \times 10^{-11} m^4$$

If it is assumed that the flexible trailing edge skin surface extends from 50% chord to the tip of the trailing edge, then the length of the flexible trailing edge is:

$$(1 - 0.5) \times 0.6 = 0.3m$$

Essentially one disc could provide continuous curvature to the skins (although it would not provide sufficient intermediate support). An analysis of the Force required to deflect the skin by the required amount to give the necessary shape can be undertaken.

In the extreme case it is assumed that the disc can be located at a point 10mm from the trailing edge. Therefore the distance from the rear spar to the disc location is:

$$L = 600mm - (600 \times 0.5)mm - 10mm = 290mm$$

$$y_{\max} = \frac{PL^3}{3EI} \tag{C. 2}$$

Where: P – Applied Load (N); L – Distance to applied load (m); E - Young's Modulus (Pa).

Rearranging for P:

$$P = \frac{y_{\max} \times 3EI}{L^3} \tag{C. 3}$$

Using Eqn. (B.4) y_{\max} at this location for +10° equivalent deflection was evaluated as approximately 42 mm, therefore the force (P) required to achieve the required deflection is given by:

$$P = \frac{(0.42) \times 3 \times (5.22 \times 10^{10}) \times (2.5 \times 10^{-11})}{0.3^3} = 61N$$

As there are two skins, upper and lower, the force required to deflect the TE section is doubled to (61 N x 2) 122 N.

Appendix D Actuation Force/Power Calculation

Integration of the Surface Pressure Distribution to Obtain the Normal Force

For simplicity, an infinitesimal area on the upper surface of the deflected trailing edge was considered. As a result of the pressure distribution, the infinitesimal area was subject to a normal force acting perpendicular to the flap chord. Summation of all the contributions from these areas on the upper surface, from the trailing edge to the 0.5c location (where the aerofoil is deflected) of the aerofoil, resulted in a force in the normal direction due to the pressure exerted on the upper surface of the aerofoil (subscript u). A similar term was obtained for the resultant pressure in the normal direction action on the lower surface of the aerofoil (subscript l). Thus the total normal force per unit span (N) acting on an aerofoil is given by:

$$N = \int_0^c p_u dx - \int_0^c p_l dx \quad (D.1)$$

The normal force coefficient per unit span can be written as:

$$C_n = \int_0^1 (C_{p,u} - C_{p,l}) d\left(\frac{x}{c}\right) \quad (D.2)$$

Calculating force due to pressure distribution

Initially the area under the C_p vs (x/c) graph was evaluated in order to obtain $C_{n,f}$ using Eqn. (D.2).

$$C_{n,f} = 0.5(C_{p,i} + C_{p,i+1})(x_{i+1} - x_i) \quad (D.3)$$

Then the normal force, N_f , was calculated for the six trailing edge section using Eqn. (D.4).

$$N_f = C_{n,f} \left(\frac{1}{2} \rho V^2 c_f \right) \quad (D.4)$$

Once the normal force acting on each trailing edge section has been evaluated, the bending moment created at each six reference points was calculated using Eqn. (D.5).

$$(BM_i)_p = \sum (N_f)_i \times \text{distance between reference point and geometrical centre} \quad (\text{D.5})$$

where $(i = 1, 2, \dots, 5)$.

Calculating force due to skin bending

Assuming the six trailing edge sections of the aerofoil deforms like the 1mm thick unit span plate described in Appendix B, the force required to bend each trailing edge section was then calculated using the method described in Appendix B. The force required was calculated starting from the 0.5c chordwise location and was assumed that the subsequent trailing edge section would have deformed up to the required trailing edge deflection given by the cantilever beam bending equation in section 4 (Eqn. 4.2). Therefore the force required to bend a subsequent trailing edge section was calculated for the two different trailing edge deflection types.

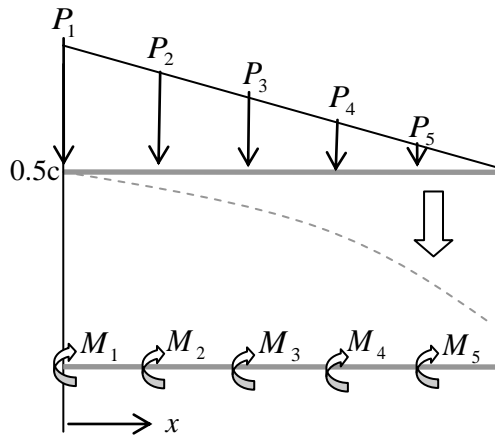


Figure D. 1 Distributed forces and moments

Calculation of the bending force for the flexible trailing edge configuration

From the cantilever bending condition considered, the bending angle for the flexible configuration is given by,

$$\theta = \frac{w_0 L^3}{24EI} \quad (\text{D.6})$$

Using Eqn. (D.6) and the equation for the bending deflection Eqn. (D.7), the force required at the root of the trailing edge section can be formulated as given by Eqn. (D.8).

$$y_{\max} = \frac{24\theta L}{30} = \frac{w_0 L^4}{30EI} \quad (\text{D.7})$$

$$w_0 = \frac{30y_{\max} EI}{L^4} \quad (\text{D.8})$$

Once the force per unit length, w_0 is evaluated, the net force acting at each chordwise section was evaluated by finding the area enclosed (as assumed in section 4).

The bending moment M_i ($i = 1$ to 5) was calculated using Eqn. (D.9).

$$(M_i)_e = \sum P_i \times \Delta x \quad (\text{D.9})$$

Finally the total bending moment created at each chordwise location, i.e. at 0.5c, 0.6c, 0.7c, 0.8c, and 0.9c, was calculated using Eqn. (D.10).

$$(BM)_{total} = (BM_i)_p + (M_i)_e \quad (\text{D.10})$$

The power requirement was then calculated using Eqn. (D.11).

$$P(W) = \frac{\text{Force}(N) \times \text{distance}(m)}{\text{time}(s)} \quad (\text{D.11})$$

Appendix E

The required wing area for the SAW was set as 3.12 m^2 , which was adequate for the MTOW of 70 kg. A SAW as shown in Figure E. 1, which has different planform from the FLAVIIR DEMON wing but produces the required aerodynamic forces was designed and taken as an example. The UAV has a maximum take-off mass of approximately 70 kg, dive speed of 90 m/s and cruise speed of 40 m/s.

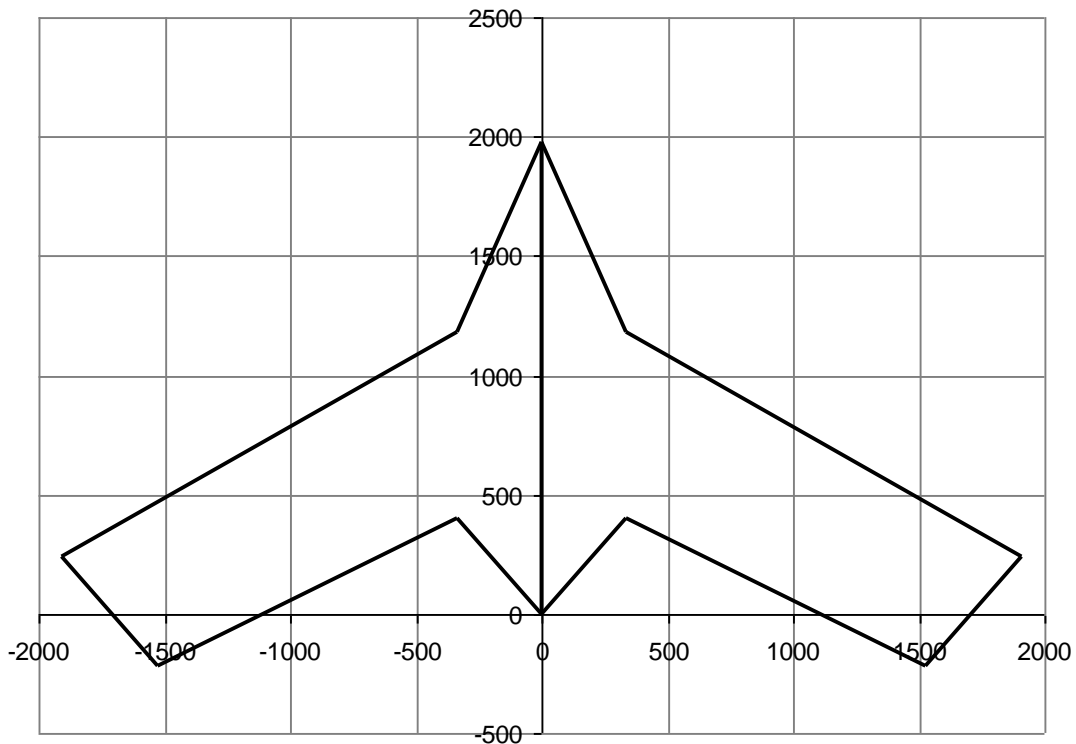


Figure E. 1 SAW planform (dimensions in mm)

The wing aerodynamic loading was then calculated using the program WINGLOADS, which determines the shear force, bending moment and torque of a wing surface section due to lift force acting on it. The shear force (S) is obtained by integration of the spanwise loading. This shear force may be reduced by the inertia force of the wing (self mass), which could reduce the shear force by up to 20%. For this analysis Inertia relief has been taken into account [118].

The wing aerodynamic loading were then calculated using the program Wingloads, which determines the shear force , bending moment and torque of a wing surface section due to lift force acting on it.

The bending moment obtained through this was then converted in to in-plane force using Eqn. (E.1)

$$F = \frac{\text{Bending Moment}}{\text{length in } x\text{-direction}(\text{span})} \quad (\text{E.1})$$

$$F = \frac{193.86Nm}{0.07174m} = 2702.3N$$

The force intensity, N_y were then calculated using Eqn. (E.2)

$$N_y = \frac{F}{c} \quad (\text{E.2})$$

$$N_y = \frac{2702.3N}{0.392m} = 6893.5N / m$$

The force intensity, N_y is calculated at this stage as an input data for the program BOXMEX (see appendix 3 for a sample input file of BOXMEX), in order to run for stiffness parameters such as EI , GJ and CK .

The wing weight takes away 30% of lift, which is roughly 15% of the maximum take off weight (MTOW) for one wing.

Based on this, the force intensity acting on the wing root with a load factor of 4.2 is,

$$N_{y,root} = N_y \times 0.392 \times 4.2 = 11349.5N / m$$

Appendix F

WINGLOADS Program [123]

Wingloads program input and output results for 2D aerodynamic load distribution.

WING LOAD EVALUATION

Dr. S. GUO Aerospace Engineering Cranfield University Nov. 2003
 Determine the shear force, bending moment and torque distribution due to lifting force acting on a wing surface with specified geometry and flight condition (unit: N, m, degree)

Semi-Span	Root Chord
1.6	0.6
L-E Angle	T-E Angle
40	40
A.C. / Chord	E.A. / Chord
0.25	0.35
Section No.	Lifting Cl
8	0.3
Air Speed	Air Density
43	1.225
Lift Distribution 1 -- Yes	RUN

--- DISPLAY LOADING RESULTS ---

Sections	Y-Coord.(m)	Lift (N)	B-Moment (N.m)	Torque (N.m)
0 - 1	.00-.2	40.77	193.86	2.00
1 - 2	.2-.4	40.45	143.47	2.00
2 - 3	.4-.6	39.48	101.20	2.00
3 - 4	.6-.8	37.80	66.93	2.00
4 - 5	.8-1.0	35.31	40.38	2.00
5 - 6	1.0-1.2	31.83	21.14	2.00
6 - 7	1.2-1.4	26.97	8.62	2.00
7 - 8	1.4-1.6	19.74	1.97	1.00
TOTAL LIFT LL=		272.33 (N)		
MAXIMUM B.M. =		193.86 (N.m)		
TOTAL TORQUE TT=		15.00 (N.m)		

246

TW-Box Program [123]

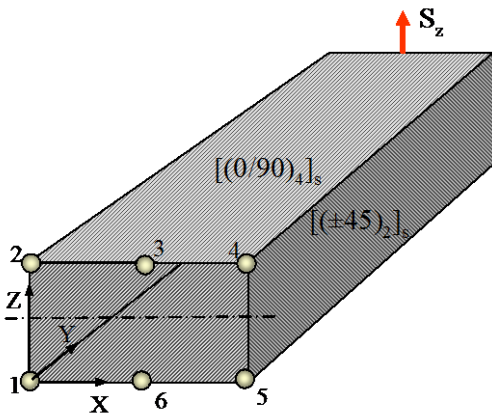


Figure F.1 TWBox Wing Representation

To use TWboxsc3.exe, the box needs to be idealised by converting continuous distributed wall area into discrete concentrated booms (Refer to Section 3.4.4). In this example, only ten booms representing the cross-section areas of their surrounding walls are set along the walls as shown in Figure F.1. As recommended, the coordinate system was placed at the origin at the most left and lowest boom as boom-1 and count the boom number

clockwise from this point. The inboard section is subjected to a bending moment M_x (kNm) due to the shear force S_z (kN) applied at the tip section.

Case 1- Carbon/Epoxy skin

SAW NACA 0015 at $y=500\text{mm}$ 1-cell

10		Number of Booms				
Boom No.	x-coord(mm)	z-coord.(mm)	Boom Area(mm ²)	x-coord(mm)	z-coord(mm)	Ex (N/mm ²)
1	0.0	0.0	114	0.0	0.0	5.22E10
2	0.0	116.4	114	0.0	116.4	5.22E10
3	91.6	104.8	99.75	91.6	104.8	5.22E10
4	179.5	93.7	97.9	179.5	93.7	5.22E10
5	267.4	82.5	96.8	267.4	82.5	5.22E10
6	353.1	71.7	88.7	353.1	71.7	5.22E10
7	353.1	0.0	88.7	353.1	0.0	5.22E10
8	267.4	0.0	96.8	267.4	0.0	5.22E10
9	179.5	0.0	97.9	179.5	0.0	5.22E10
10	91.6	0.0	99.75	91.6	0.0	5.22E10

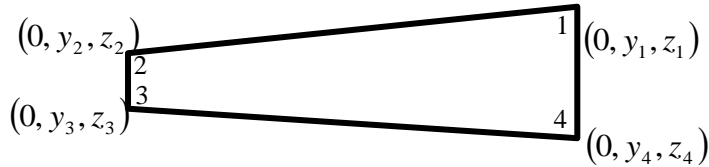
Case 2 –E-Glass/Epoxy skin

SAW NACA 0015 at y=500mm 1-cell

10						
Number of Booms						
Boom No.	x-coord(mm)	z-coord.(mm)	Boom Area(mm ²)	x-coord(mm)	z-coord(mm)	Ex (N/mm ²)
1	0.0	0.0	91.1	0.0	0.0	1.6E10
2	0.0	116.4	91.1	0.0	116.4	1.6E10
3	91.6	104.8	49.9	91.6	104.8	1.6E10
4	179.5	93.7	48.95	179.5	93.7	1.6E10
5	267.4	82.5	48.4	267.4	82.5	1.6E10
6	353.1	71.7	67.3	353.1	71.7	1.6E10
7	353.1	0.0	67.3	353.1	0.0	1.6E10
8	267.4	0.0	48.4	267.4	0.0	1.6E10
9	179.5	0.0	48.95	179.5	0.0	1.6E10
10	91.6	0.0	49.9	91.6	0.0	1.6E10

BOXMEX Program [123]

Wing box (x, y) coordinates at each four points of each spanwise section.



Example of BOXMEX Input File

```

8 8 8 8 (Number of Layers of the ith section of the wing box)
135.0E09 9.50E9 0.3 4.9E09 4.9E09 4.9E09 1600.0 ( $E_1, E_2, \nu_{12}, G_{12}, G_{13}, G_{23}, density$ )
135.0E09 9.50E9 0.3 4.9E09 4.9E09 4.9E09 1600.0
135.0E09 9.50E9 0.3 4.9E09 4.9E09 4.9E09 1600.0
135.0E09 9.50E9 0.3 4.9E09 4.9E09 4.9E09 1600.0
0.0 45 90 -45 -45 90 45 0.0 (Fibre Direction)
0.0 45 90 -45 -45 90 45 0.0
0.0 45 90 -45 -45 90 45 0.0
0.0 45 90 -45 -45 90 45 0.0
0.125E-3 0.125E-3 0.125E-3 0.125E-3 0.125E-3 0.125E-3 0.125E-3 0.125E-3 (Layer thickness)
0.125E-3 0.125E-3 0.125E-3 0.125E-3 0.125E-3 0.125E-3 0.125E-3 0.125E-3
0.125E-3 0.125E-3 0.125E-3 0.125E-3 0.125E-3 0.125E-3 0.125E-3 0.125E-3
0.125E-3 0.125E-3 0.125E-3 0.125E-3 0.125E-3 0.125E-3 0.125E-3 0.125E-3
0.0 -0.135 0.01065 (x, y, z coordinates of the nodes)
0.0 0.135 0.0159
0.0 0.135 -0.0159
0.0 -0.135 -0.01065
0.6 0.114 1.6 (Width, Depth and the total length of the wing box)
21150 0.0 3.235E3 0.0 0.0 0.0 0.0 ( $N_{y,root}$ , in-plane force in y-axis, in-plane force in xy
(shear), moment about x, moment about y and torque
applied at each laminate)
1.68E+9 1.1E+9 0.61E+08 0.244E+09 0.9E+08 (Tensile and compressive strength in
fibre direction 1, Tensile and
compressive strength in fibre direction
2 and shear strength in 1-2 direction)

```

OPTBOXFSC Program [123]

Example of Optboxfsc Input File

```

6                               (number of normal modes used in the analysis)
1 2 3 4 5 6                     (mode numbers)
40                              (sweep angle of the wing-in degrees)
8                               (Total number of elements of wing)
8 1                               }
1 8 1 2 3 4 5 6 7 8             } (control factors)
4 2 1 1                           }
1
8 8 8 8                         (From BOXMEX input for each of the 8 sections)
135.0E09 9.50E9 0.3 4.9E09 4.9E09 4.9E09 1600.0
135.0E09 9.50E9 0.3 4.9E09 4.9E09 4.9E09 1600.0
135.0E09 9.50E9 0.3 4.9E09 4.9E09 4.9E09 1600.0
135.0E09 9.50E9 0.3 4.9E09 4.9E09 4.9E09 1600.0
0.0 45 90 -45 -45 90 45 0.0
0.0 45 90 -45 -45 90 45 0.0
0.0 45 90 -45 -45 90 45 0.0
0.0 45 90 -45 -45 90 45 0.0
0.125E-3 0.125E-3 0.125E-3 0.125E-3 0.125E-3 0.125E-3 0.125E-3 0.125E-3
0.125E-3 0.125E-3 0.125E-3 0.125E-3 0.125E-3 0.125E-3 0.125E-3 0.125E-3
0.125E-3 0.125E-3 0.125E-3 0.125E-3 0.125E-3 0.125E-3 0.125E-3 0.125E-3
0.125E-3 0.125E-3 0.125E-3 0.125E-3 0.125E-3 0.125E-3 0.125E-3 0.125E-3
0.0 -0.135 0.01065
0.0 0.135 0.0159
0.0 0.135 -0.0159
0.0 -0.135 -0.01065
2
.
.
0.6 0.2 1.6
      EI      GJ      CK      M/L      Ip/L      X      Xp      Yp
1      8.968E+03 1.120E+04 1.000E-03 9.0600 0.1831 -0.142 0.15 0.20
2      1.357E+04 1.630E+04 1.000E-03 10.38000.1584 -0.124 0.15 0.20

```

3	1.918E+04	2.230E+04	1.000E-03	12.60800.1434	-0.107	0.15	0.20
4	2.578E+04	2.910E+04	1.000E-03	14.20400.1145	-0.090	0.15	0.20
5	3.344E+04	3.650E+04	1.000E-03	15.35000.0815	-0.073	0.15	0.20
6	4.215E+04	4.470E+04	1.000E-03	16.11900.0505	-0.056	0.15	0.20
7	5.200E+04	5.340E+04	1.000E-03	16.56500.0253	-0.039	0.15	0.20
8	8.986E+04	9.480E+04	1.000E-03	16.71300.0083	-0.022	0.15	0.20

0

1 0. 0. 0. 0.0 0.0 0.0

Node No. b(semi-chord) a(non-dim.)

1	0.3	-0.474
2	0.3	-0.412
3	0.3	-0.356
4	0.3	-0.299
5	0.3	-0.243
6	0.3	-0.187
7	0.3	-0.130
8	0.3	-0.074
9	0.3	-0.050

1

Starting Frequency Step length Maximum Frequency (rad/s)

2	1	300
---	---	-----

Starting Air Speed Step Length Maximum Air Speed (m/s)

20	2	800
----	---	-----

1 2

0.5 0.5

1 1 1 1

0.5 10 10

0

2

2

3441

}
 }
 (Control Factors)

AERO-BEAM-SAW Program [124]

This program needs two input data files: Winggeom.dat and sbeam3d.in, and produces three output files: Aeroforce.out, Aero-cl-cp.out and Beam3d.out.

It works first as a pre-processor to;

1. Interpolate the $Y_j(X_j)$ at specified 'NINTP' number of X_j point along the rear chord and replace the original (X_i, Y_i) coordinates by the nearest interpolating X_j points (to keep the original 'NP' number of geometry data).
2. Based on the original aerofoil (X_i, Y_i) and use specified TE angle, calculate a set of new Y_j of a deformed aerofoil along the rear chord according to the 3 options for the deformed shape definition.

-- NOPT=1 assumes that the aerofoil deforms like a cantilever beam under tapered distributed pressure ($XITA=W0*L^3/24EI$; $Y=24*XITA*L/30$) based on user given input angle (deg) at the TE. A 'RATIO'= $W0/EI = XITA*24/L^3$ can be calculated. The XITA and Y at any X_j along the rear chord C can then be calculated from the above two equations;

-- NOPT=2 – assumes that the aerofoil deforms with a bending angle in proportion to the length ($XITA=RATIO*L$; $Y=24*XITA*L/30$). It also assumes that the shape keeps the same as NOPT=1; it should be a sum of Y_j along the section.

-- NOPT=3 –assumes a rigid flap rotation ($XITA=RATIO$; $Y=XITA*L$).

And then calculate aero-coefficients by using the program 'UNSPM' followed by structural deformation by using the program 'BEAM-3D' in a loop.

Line-1: CRTE, CRLE – Deformable TE and LE root location measured from the LE as a percentage against chord (e.g. CRTE=0.6 for TE control surface starts from 60% of chord measured from LE; CRLE=0.3 for LE ends at 30% of chord);

Line-2: INTPTE, INTPLE – Number of points within the deformable TE and LE region for calculating the deformed TE and LE geometry;

Line-3-4: XINT(J) – Input the X_i at the above INTPTE points and those X_i at the INTPLE points counted from TE forward (in the same anticlockwise order as aerofoil input data), where the original X_j and Y_j at the nearest points to them will be replaced by these interpolated values (input INTPTE plus INTPLE number of data);

Line-5: ANGTE, ANGLE – TE and LE deflected angle in degrees;

Line-6: NTEOPT, NLEOPT – TE and LE deformation shape option (refer to option details above);

Line-7: AOA, CMREF – the aerofoil AOA and reference point in chord (e.g. 0.25) for C_m ;

Line-8: AIRDENS, SPEEDV – Air density and speed for aerodynamic force calculation;

Line-9: NSECTION, NACTSEC – number of sections divided along wing span counting from root to tip for aerodynamic force calculation (NSECTION=Total wing beam nodes – Root node) and the NACTSEC is the section number where the active TE/LE is present;

Line-10: SECHORD(I), SECSPAN(I) – chord and length of the wing section;

Line-11: NP – Number of coordinate points to define the aerofoil geometry;

Line-12: XAIRF(I), YAIRF(I) – Aerofoil geometry coordinates. The input aerofoil data starts anticlockwise from TE with $X_i=1.0$ (origin at LE). It contains the same number of Y_i on upper and lower skins corresponding to the same X_i .

Example file of Winggeom.dat file

```

50 1.25          -- SPEEDV, AIRDENS
4 0.25          -- AOA, CMREF
0.6 0.3         -- CRTE, CRLE (e.g. 0.6 for 60%C from LE);
0.0 0.0         -- ANGTE, ANGLE (deg)
40.0 0.0        -- SWEPTA, DIHLA (deg)
1 1            -- NTEOPT, NLEOPT
5 7            -- INTPTE, INTPLE
1.0           -- XINT(J)
                ...
0.9
0.8
0.7
0.6
0.3
0.25
0.2
0.15

```

```

0.1
0.05
0.0
8 8          -- NSECTION, NACTSEC
0.60 0.2    -- SECHORD(I), SECSPAN(I)
0.60 0.2
0.60 0.2
0.60 0.2
0.60 0.2
0.60 0.2
0.60 0.2
0.60 0.2
0.60 0.2
0.35          -- EAR
20 0.05      -- NITERAT, AEDIFF

121          -- NP
1.00000000  0.00000000  -- XAIRF(I), YAIRF(I)
0.99931477  0.00007273  ...
0.99726095  0.00029034

.            .
.            .
.            .

0.99726095  -0.00029034
0.99931477  -0.00007273
1.00000000  0.00000000

```

Example of Beam-3D input file

NN, ICK, IUNIT, ISMA, IPR

NN – Total Number of Node/Stations ($1 \leq NN \leq 40$ for the current version);

ICK- Control Marker for Stiffness Coupling (ICK=1 to include coupling; =0 for no stiffness coupling);

IUNIT - Control Marker for UNIT System (=1 for SI UNIT; =2 the input data in SI will be converted to IMP. UNIT within the program);

ISMA - Control Marker for Analysis (=1 for static; =2 for vibration analysis);

IPR - Control Marker for Print Results (=0 for end results only; =1, 2 to print the system and element stiffness/mass matrices);

NI -- The Nth Node/Station;

NW(NI, J), (J=1-6) – Freedom indicator for the displacements $u, w, \Phi, v, \theta, \psi$ at the node (=0 for constrained; >0 for free DOF);

PAM(NI, J) – Mass, mass moments and inertias at the node

$M_I, M_{X_I}, M_{Y_I}, M_{Z_I}, I_{XXI}, I_{YYI}, I_{ZZI}, I_{XXI}, I_{YYI}, I_{ZZI}$
 (e.g. $M_{X_I} = M_I(X_m - X_I), I_{XXI} = M_I[(Y_m - Y_I)^2 + (Z_m - Z_I)^2]$)

COR(NI,J), J=1-3 – X, Y, Z-coordinates of the node NI;

(the above data will repeat NN times)

ITY, NE – constants 2, 1

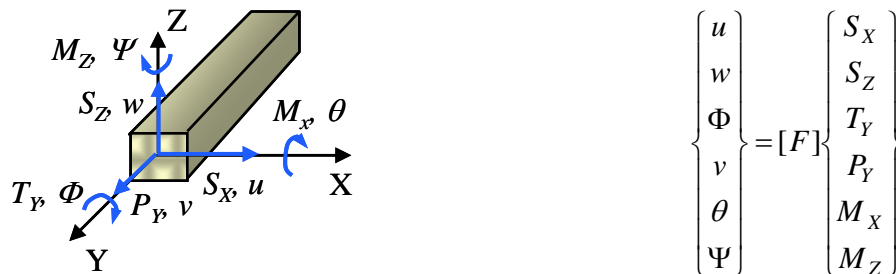
PAK(NI, J) – 15 Properties $E, I_{XX1}, I_{XX2}, I_{ZZ1}, I_{ZZ2}, G, J_1, J_2, A_1, A_2, A_{SX1}, A_{SX2}, A_{SZ1}, A_{SZ2}$,

CK

N12(NI,J) – The node No. at the ends of the element, and ICY and tan(a) to indicate the orientation and incidence of the beam respectively;

(the above data will repeat NN-1 times)

MEND=-1 – End of data file marker;



The figure shows the definition of the directions and order of the forces, moments and displacements

```

9 0 1 1 3 1      --- NN, ICK, IUNIT, ISMA, NR, IPR
1                --- NS – Node No. 1
0 0 0 0 0        --- NW
1.67130 0.19593 0.01332 0.0 0.00011 0.02297 0.02307 0.00156 0.0 0.0

                --  $M_I, MX_I, MY_I, MZ_I, I_{XXI}, I_{YYI}, I_{ZZI}, I_{XYI}, I_{YZI}, I_{XZI}$ 
0      0      0      -- X,Y,Z-Coordinates of Node-I
2
1 2 3 4 5 6
3.32780 0.29871 0.04833 0.0 0.00070 0.02681 0.02751 0.00434 0.0 0.0
0.1678  0.1999  0
3
1 2 3 4 5 6
3.26840 0.29338 0.06888 0.0 0.00145 0.02633 0.02779 0.00618 0.0 0.0
0.3355  0.3999  0
4
1 2 3 4 5 6
3.14690 0.28247 0.08694 0.0 0.00240 0.02535 0.02776 0.00780 0.0 0.0
0.5033  0.5998  0
5
1 2 3 4 5 6
2.95540 0.26528 0.10102 0.0 0.00345 0.02381 0.02726 0.00907 0.0 0.0
0.6711  0.7998  0
6
1 2 3 4 5 6
2.68120 0.24067 0.10921 0.0 0.00445 0.02160 0.02605 0.00980 0.0 0.0
0.8388  0.9997  0
7
1 2 3 4 5 6
2.29880 0.20634 0.10870 0.0 0.00514 0.01852 0.02366 0.00976 0.0 0.0
1.0066  1.1996  0
8
1 2 3 4 5 6
1.94400 0.17450 0.10466 0.0 0.00563 0.01566 0.02130 0.00939 0.0 0.0
1.1744  1.3996  0
9
1 2 3 4 5 6
0.9060 0.08132 0.05471 0.0 3.3042E-03 7.2997E-03 1.0604E-02 4.9112E-03 0.0 0.0
1.3421  1.5995  0
1 9
2 1                --- ITY, NE

```

1.60E+10 1.46E-06 1.27E-06 5.62E-04 2.31E-04 4.00E+09 2.46E-06 2.22E-06 5.02E-04 4.73E-04
5.02E-04 4.73E-04 5.02E-04 4.73E-04 2.15E-20

-- $E, I_{XX1}, I_{XX2}, I_{ZZ1}, I_{ZZ2}, G, J_1, J_2, A_1, A_2, A_{SX1}, A_{SX2}, A_{SZ1}, A_{SZ2}, CK$
-- The node No. at the ends of the element, and ICY and tan(a) to
indicate the orientation and incidence of the beam respectively

1 2 0 0

2 1

1.60E+10 1.27E-06 1.02E-06 2.31E-04 2.10E-04 4.00E+09 2.22E-06 1.84E-06 4.73E-04 4.57E-04
4.73E-04 4.57E-04 4.73E-04 4.57E-04 5.62E-21

2 3 0 0

2 1

1.60E+10 1.02E-06 7.98E-07 2.10E-04 1.88E-04 4.00E+09 1.84E-06 1.49E-06 4.57E-04 4.41E-04
4.57E-04 4.41E-04 4.57E-04 4.41E-04 1.70E-20

3 4 0 0

2 1

1.60E+10 7.98E-07 6.11E-07 1.88E-04 1.67E-04 4.00E+09 1.49E-06 1.18E-06 4.41E-04 4.25E-04
4.41E-04 4.25E-04 4.41E-04 4.25E-04 1.22E-20

4 5 0 0

2 1

1.60E+10 6.11E-07 4.52E-07 1.67E-04 1.45E-04 4.00E+09 1.18E-06 9.07E-07 4.25E-04 4.09E-04
4.25E-04 4.09E-04 4.25E-04 4.09E-04 -1.92E-21

5 6 0 0

2 1

1.60E+10 4.52E-07 3.21E-07 1.45E-04 1.24E-04 4.00E+09 9.07E-07 6.68E-07 4.09E-04 3.93E-04
4.09E-04 3.93E-04 4.09E-04 3.93E-04 5.90E-21

6 7 0 0

2 1

1.60E+10 3.21E-07 1.44E-07 1.24E-04 1.02E-04 4.00E+09 6.68E-07 2.77E-07 3.93E-04 3.77E-04
3.93E-04 3.77E-04 3.93E-04 3.77E-04 -1.41E-22

7 8 0 0

2 1

1.60E+10 1.44E-07 8.69E-08 1.02E-04 8.10E-05 4.00E+09 2.77E-07 1.78E-07 3.77E-04 3.61E-04
3.77E-04 3.61E-04 3.77E-04 3.61E-04 3.26E-21

8 9 0 0

-1

Appendix G

Pressure distribution of the SAW spanwise location where the eccentuator are present. The curves show the additional lift generated by the deflection of the SAW TE section to achieve 5° equivalent flap deflection.

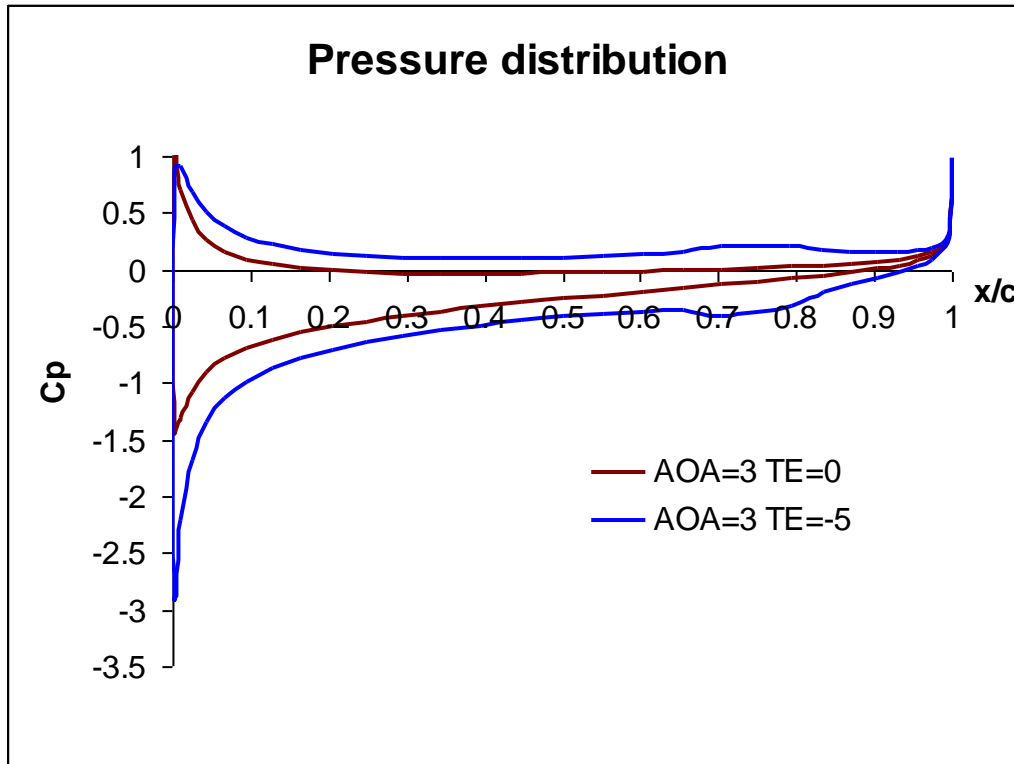


Figure G. 1 Summary of pressure distribution at 0° and 5° TE deflection

The table below summarises the calculation of the additional aerodynamic load due to a 5° TE deflection angle.

Numerical integration trapezoidal rule.		Xi	Cp diff	CLi	Li	Mi=c*(Xi-0.5)*Li
Load from 50% chord		0.5	-0.52486			
rho (kg/m^3)	1.225	0.55226	-0.50725	0.02697	1.96	0.03
V (m/s)	43	0.60396	-0.50172	0.02608	1.89	0.06
b (m)	0.4269	0.65451	-0.51239	0.02563	1.86	0.09
chord (m)	0.3	0.70337	-0.60797	0.02737	1.98	0.12
S (m^2)	0.12807	0.79214	-0.53807	0.05087	3.69	0.32
		0.83292	-0.37142	0.01854	1.34	0.13
		0.87005	-0.29372	0.01235	0.90	0.10
		0.90309	-0.23199	0.00868	0.63	0.08
		0.9317	-0.18074	0.00590	0.43	0.06
		0.95555	-0.13613	0.00378	0.27	0.04
		0.97439	-0.09657	0.00219	0.16	0.02
		0.98799	-0.06127	0.00107	0.08	0.01
		0.99621	-0.03559	0.00040	0.03	0.00
		0.99896	0	0.00005	0.00	0.00
					L (N)	M (Nm)
					15.22	1.06
Centre of Lift from 50% datum					0.07	m

AOA=3 TE=0deg		AOA=3 TE=-5deg	
Wing box +LE Lift (N)	20.08	Wing box +LE Lift (N)	33.88
TE Lift (N)	4.42	TE Lift (N)	15.22

Lift acting on Wing box-stringer 1 (A.C) (N)	14
Lift acting on TE-stringer 2 (N)	11

Numerical integration trapezoidal rule.		Xi	Cp diff	CLi	Li	Mi=c*(Xi-0.5)*Li
Load from 50% chord		0	-1.35281			
rho (kg/m^3)	1.225	0.00274	-3.77309	0.00702	0.51	-0.08
V (m/s)	43	0.01093	-3.12495	0.02825	2.05	-0.30
b (m)	0.4269	0.02447	-2.36288	0.03715	2.69	-0.38
chord (m)	0.3	0.04323	-1.85465	0.03956	2.87	-0.39
S (m^2)	0.12807	0.06699	-1.51261	0.04000	2.90	-0.38
		0.09549	-1.271	0.03967	2.88	-0.35
		0.12843	-1.09247	0.03893	2.82	-0.31
		0.16543	-0.95573	0.03789	2.75	-0.28
		0.20611	-0.84811	0.03669	2.66	-0.23
		0.25	-0.76177	0.03533	2.56	-0.19
		0.29663	-0.69172	0.03389	2.46	-0.15
		0.34549	-0.6347	0.03240	2.35	-0.11
		0.39604	-0.58859	0.03092	2.24	-0.07
		0.44774	-0.55213	0.02949	2.14	-0.03
					L (N)	M (Nm)
					33.88	-3.26
Centre of Lift from 50% datum					-0.10	m

Appendix H Mechanics of Laminated Composites

The following assumptions are made for the next section as long as the laminate is not damaged and undergoes small deflection:

- i. The laminate thickness is very small compared to its other dimensions.
- ii. The lamina (layers) of the laminate are perfectly bonded.
- iii. Line perpendicular to the surface of the laminate remains straight and perpendicular to the surface after deformation.
- iv. The laminate is linear elastic.
- v. Through thickness stresses and strains are negligible.

Definition of Strains and Displacements

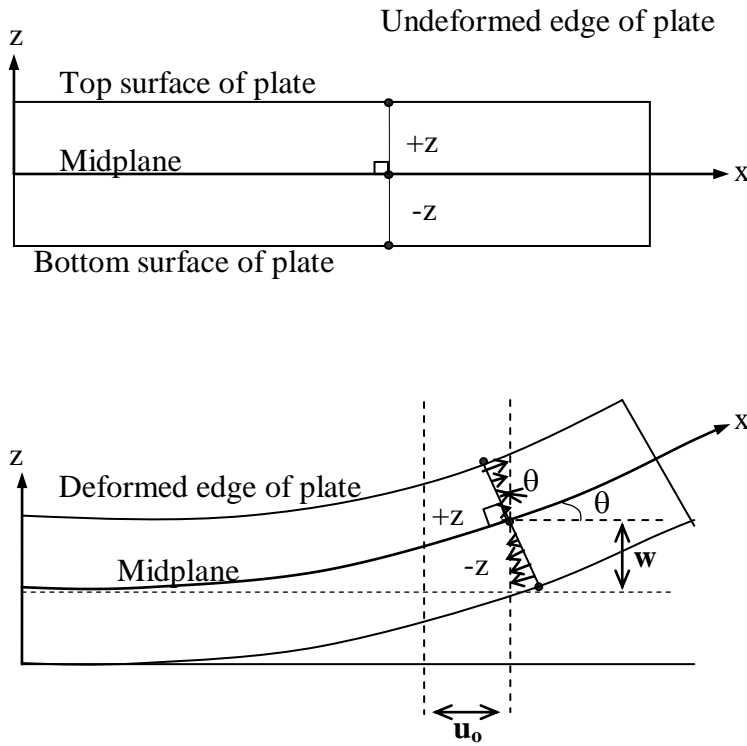
A displacement of the plate in the x , y and z -direction are denoted by u , v and w respectively. Thus the strains are defined as:

$$\varepsilon_x \equiv \frac{\partial u}{\partial x}; \quad \varepsilon_y \equiv \frac{\partial v}{\partial y}; \quad \gamma_{xy} \equiv \left(\frac{\partial u}{\partial y} + \frac{\partial v}{\partial x} \right) \quad (\text{H.1})$$

From Figure H.1 the total in-plane displacement at any point in the plate is the sum of the normal displacements introduced by bending. Denoting the displacements of the midplane of the plate for the x and y directions as u_0 and v_0 respectively, the total displacement can be defined as:

$$u = u_0 - z \frac{\partial w}{\partial x}; \quad v = v_0 - z \frac{\partial w}{\partial y} \quad (\text{H.1})$$

where $\frac{\partial w}{\partial x}$ and $\frac{\partial w}{\partial y}$ are the slopes of the plate in bending along the x and y directions respectively.



$$\theta = \text{Slope} = \frac{\partial w}{\partial x} \text{ for small } \theta$$

Displacement along z-direction is $\sin\theta.z$. Since θ is small $\sin\theta = \theta$. Therefore the displacement is $-z\theta$ where Negative is compression and positive is tension.

Figure H.1 Total Displacements in a Plate

From Eqs. (F.1) and (F.2):

$$\varepsilon_x = \frac{\partial u}{\partial x} = \frac{\partial u_0}{\partial x} - z \frac{\partial^2 w}{\partial x^2}; \varepsilon_y = \frac{\partial v}{\partial y} = \frac{\partial v_0}{\partial y} - z \frac{\partial^2 w}{\partial y^2}; \gamma_{xy} = \left(\frac{\partial u}{\partial y} + \frac{\partial v}{\partial x} \right) = \frac{\partial u_0}{\partial y} + \frac{\partial v_0}{\partial x} - 2z \frac{\partial^2 w}{\partial x \partial y} \quad (\text{H. 2})$$

Defining $\frac{\partial u_0}{\partial x_0}$ as ε_x^0 ; $\frac{\partial v_0}{\partial y_0}$ as ε_y^0 ; and $\frac{\partial u_0}{\partial y_0} + \frac{\partial v_0}{\partial x_0}$ as γ_{xy}^0 to be the midplane strains and

defining $-\frac{\partial^2 w}{\partial x^2}$ as K_x ; $-\frac{\partial^2 w}{\partial y^2}$ as K_y ; and $-2\frac{\partial^2 w}{\partial x \partial y}$ as K_{xy} to be the plate curvatures. The

plate curvatures K_x and K_y are the rate of change of slope of the bending plate in x and y directions respectively. K_{xy} is the amount of bending in the x -direction along the y -axis (i.e. twisting).Eq. (H.3) can be written in matrix form as:

$$\begin{bmatrix} \varepsilon_x \\ \varepsilon_y \\ \varepsilon_{xy} \end{bmatrix} = \begin{bmatrix} \varepsilon_x^0 \\ \varepsilon_y^0 \\ \gamma_{xy}^0 \end{bmatrix} + z \begin{bmatrix} K_x \\ K_y \\ K_{xy} \end{bmatrix} \quad (\text{H.4})$$

From Eq. (3.24) the stresses in each ply of the laminate can be determined using Eq. (H.4):

$$\begin{bmatrix} \sigma_x \\ \sigma_y \\ \tau_{xy} \end{bmatrix} = \begin{bmatrix} \bar{Q}_{11} & \bar{Q}_{12} & \bar{Q}_{16} \\ \bar{Q}_{12} & \bar{Q}_{22} & \bar{Q}_{26} \\ \bar{Q}_{16} & \bar{Q}_{26} & \bar{Q}_{66} \end{bmatrix} \begin{bmatrix} \varepsilon_x^0 \\ \varepsilon_y^0 \\ \gamma_{xy}^0 \end{bmatrix} + z \begin{bmatrix} \bar{Q}_{11} & \bar{Q}_{12} & \bar{Q}_{16} \\ \bar{Q}_{12} & \bar{Q}_{22} & \bar{Q}_{26} \\ \bar{Q}_{16} & \bar{Q}_{26} & \bar{Q}_{66} \end{bmatrix} \begin{bmatrix} K_x \\ K_y \\ K_{xy} \end{bmatrix} \quad (\text{H.5})$$

Definition of Stress and Moments

Since the stress in each ply varies through the thickness of the laminate, the stress will be defined in terms of equivalent forces acting at the middle surface. As can be seen from Figure H.2, the stresses acting on an edge can be broken into increments and summed. The resulting integral is defined as the stress resultant and is denoted by N_i , where the i subscript denotes the direction.

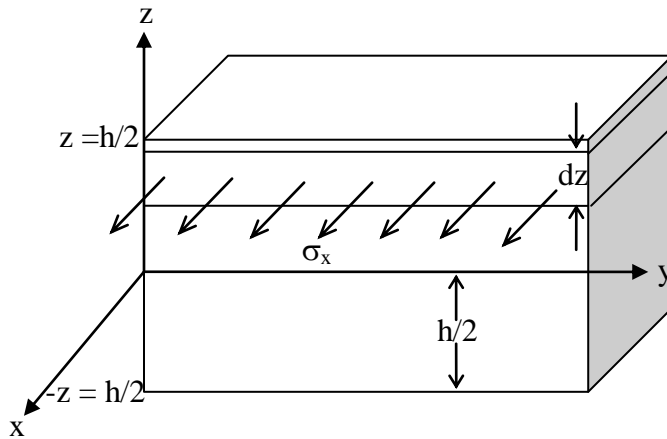


Figure H.2 Definition of Stress Resultant.

$$\text{Total Force in } x \text{ - direction} = \sum \sigma_x (dz)(y)$$

$$\text{As } dz \rightarrow 0, \sum \sigma_x (dz)(y) = y \int_{-h/2}^{h/2} \sigma_x dz$$

$$N_x \equiv \int_{-h/2}^{h/2} \sigma_x dz$$

Similarly the y-direction stress and shear stress resultants can be formed as:

$$N_x \equiv \int_{-h/2}^{h/2} \sigma_x dz; \quad N_y \equiv \int_{-h/2}^{h/2} \sigma_y dz; \quad \text{and} \quad N_{xy} \equiv \int_{-h/2}^{h/2} \sigma_{xy} dz \quad (\text{H.6})$$

As can be seen from Figure H.2, the stress acting on an edge produces a moment about the midplane. The force is $\sigma_x (dz)(y)$ as denoted in Figure H.2. The moment arm is at a distance z from the midplane. Following the same procedure as for the stress resultants, the moment resultants can be defined as:

$$M_x \equiv \int_{-h/2}^{h/2} \sigma_x z dz; \quad M_y \equiv \int_{-h/2}^{h/2} \sigma_y z dz; \quad \text{and} \quad M_{xy} \equiv \int_{-h/2}^{h/2} \sigma_{xy} z dz \quad (\text{H.7})$$

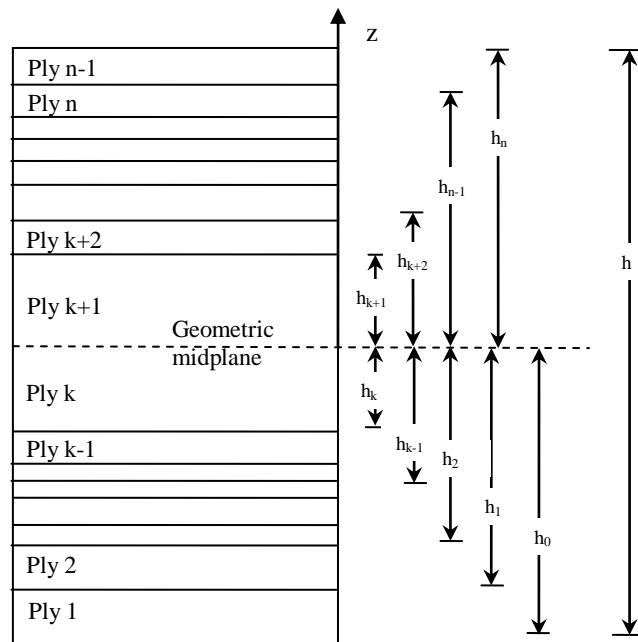
Putting Eq. (H.6) and (H.7) in matrix form gives:

$$\begin{bmatrix} N_x \\ N_y \\ N_{xy} \end{bmatrix} = \int_{-h/2}^{h/2} \begin{bmatrix} \sigma_x \\ \sigma_y \\ \sigma_{xy} \end{bmatrix} dz \quad \text{and} \quad \begin{bmatrix} M_x \\ M_y \\ M_{xy} \end{bmatrix} = \int_{-h/2}^{h/2} \begin{bmatrix} \sigma_x \\ \sigma_y \\ \sigma_{xy} \end{bmatrix} z dz \quad (\text{H.8})-(\text{H.9})$$

The integrals in Eqs. (H.8—H.9) must be performed over each ply and then summed.

Using the schematic of a laminate in Figure H.3 Eqs. (H.8—H.9) are written as:

$$\begin{bmatrix} N_x \\ N_y \\ N_{xy} \end{bmatrix} = \sum_{k=1}^n \int_{h_{k-1}}^{h_k} \begin{bmatrix} \sigma_x \\ \sigma_y \\ \sigma_{xy} \end{bmatrix}_k dz \quad \text{and} \quad \begin{bmatrix} M_x \\ M_y \\ M_{xy} \end{bmatrix} = \sum_{k=1}^n \int_{h_{k-1}}^{h_k} \begin{bmatrix} \sigma_x \\ \sigma_y \\ \sigma_{xy} \end{bmatrix}_k z dz \quad (\text{H.10})-(\text{H.11})$$



Note that ply k and ply k+1 are the same layer, but are separated into two plies by the geometric midplane

Figure H.3 Cross-section of Lamina

Now Eq. (H.6) can be substituted to Eq. (3.24), which then can be substituted into Eqs. (H.10) and (H.11) to give:

$$\begin{bmatrix} N_x \\ N_y \\ N_{xy} \end{bmatrix} = \sum_{k=1}^n \left\{ \int_{h_{k-1}}^{h_k} \begin{bmatrix} \bar{Q}_{11} & \bar{Q}_{12} & \bar{Q}_{16} \\ \bar{Q}_{12} & \bar{Q}_{22} & \bar{Q}_{26} \\ \bar{Q}_{16} & \bar{Q}_{26} & \bar{Q}_{66} \end{bmatrix}_k \begin{bmatrix} \varepsilon_x^0 \\ \varepsilon_y^0 \\ \gamma_{xy}^0 \end{bmatrix} dz + \int_{h_{k-1}}^{h_k} \begin{bmatrix} \bar{Q}_{11} & \bar{Q}_{12} & \bar{Q}_{16} \\ \bar{Q}_{12} & \bar{Q}_{22} & \bar{Q}_{26} \\ \bar{Q}_{16} & \bar{Q}_{26} & \bar{Q}_{66} \end{bmatrix}_k \begin{bmatrix} K_x \\ K_y \\ K_{xy} \end{bmatrix} z dz \right\} \quad (\text{H.12})$$

$$\begin{bmatrix} M_x \\ M_y \\ M_{xy} \end{bmatrix} = \sum_{k=1}^n \left\{ \int_{h_{k-1}}^{h_k} \begin{bmatrix} \bar{Q}_{11} & \bar{Q}_{12} & \bar{Q}_{16} \\ \bar{Q}_{12} & \bar{Q}_{22} & \bar{Q}_{26} \\ \bar{Q}_{16} & \bar{Q}_{26} & \bar{Q}_{66} \end{bmatrix}_k \begin{bmatrix} \varepsilon_x^0 \\ \varepsilon_y^0 \\ \gamma_{xy}^0 \end{bmatrix} z dz + \int_{h_{k-1}}^{h_k} \begin{bmatrix} \bar{Q}_{11} & \bar{Q}_{12} & \bar{Q}_{16} \\ \bar{Q}_{12} & \bar{Q}_{22} & \bar{Q}_{26} \\ \bar{Q}_{16} & \bar{Q}_{26} & \bar{Q}_{66} \end{bmatrix}_k \begin{bmatrix} K_x \\ K_y \\ K_{xy} \end{bmatrix} z^2 dz \right\} \quad (\text{H.13})$$

Since the middle surface strains and curvatures are not a function of z they will be considered to be constants along with the laminate stiffness matrix for a given ply over the integration of a lamina thickness. Hence performing the integration gives:

$$\begin{bmatrix} N_x \\ N_y \\ N_{xy} \end{bmatrix} = \sum_{k=1}^n \left\{ \begin{array}{l} \begin{bmatrix} \bar{Q}_{11} & \bar{Q}_{12} & \bar{Q}_{16} \\ \bar{Q}_{12} & \bar{Q}_{22} & \bar{Q}_{26} \\ \bar{Q}_{16} & \bar{Q}_{26} & \bar{Q}_{66} \end{bmatrix}_k \begin{bmatrix} \varepsilon_x^0 \\ \varepsilon_y^0 \\ \gamma_{xy}^0 \end{bmatrix} (h_k - h_{k-1}) \\ + \begin{bmatrix} \bar{Q}_{11} & \bar{Q}_{12} & \bar{Q}_{16} \\ \bar{Q}_{12} & \bar{Q}_{22} & \bar{Q}_{26} \\ \bar{Q}_{16} & \bar{Q}_{26} & \bar{Q}_{66} \end{bmatrix}_k \begin{bmatrix} K_x \\ K_y \\ K_{xy} \end{bmatrix} \frac{1}{2} (h_k^2 - h_{k-1}^2) \end{array} \right\} \quad (\text{H.14})$$

$$\begin{bmatrix} N_x \\ N_y \\ N_{xy} \end{bmatrix} = \sum_{k=1}^n \left\{ \begin{array}{l} \begin{bmatrix} \bar{Q}_{11} & \bar{Q}_{12} & \bar{Q}_{16} \\ \bar{Q}_{12} & \bar{Q}_{22} & \bar{Q}_{26} \\ \bar{Q}_{16} & \bar{Q}_{26} & \bar{Q}_{66} \end{bmatrix}_k \begin{bmatrix} \varepsilon_x^0 \\ \varepsilon_y^0 \\ \gamma_{xy}^0 \end{bmatrix} \frac{1}{2} (h_k^2 - h_{k-1}^2) \\ + \begin{bmatrix} \bar{Q}_{11} & \bar{Q}_{12} & \bar{Q}_{16} \\ \bar{Q}_{12} & \bar{Q}_{22} & \bar{Q}_{26} \\ \bar{Q}_{16} & \bar{Q}_{26} & \bar{Q}_{66} \end{bmatrix}_k \begin{bmatrix} K_x \\ K_y \\ K_{xy} \end{bmatrix} \frac{1}{3} (h_k^3 - h_{k-1}^3) \end{array} \right\} \quad (\text{H.15})$$